

Electronic Thesis and Dissertation Repository

---

7-21-2016 12:00 AM

## A Novel Composite Material-based Computational Model for Left Ventricle Biomechanics Simulation

Seyyed Mohammad Hassan Haddad  
*The University of Western Ontario*

Supervisor

Dr. Abbas Samani

*The University of Western Ontario*

Graduate Program in Biomedical Engineering

A thesis submitted in partial fulfillment of the requirements for the degree in Doctor of Philosophy

© Seyyed Mohammad Hassan Haddad 2016

Follow this and additional works at: <https://ir.lib.uwo.ca/etd>



Part of the [Biomechanics and Biotransport Commons](#)

---

### Recommended Citation

Haddad, Seyyed Mohammad Hassan, "A Novel Composite Material-based Computational Model for Left Ventricle Biomechanics Simulation" (2016). *Electronic Thesis and Dissertation Repository*. 3870.

<https://ir.lib.uwo.ca/etd/3870>

This Dissertation/Thesis is brought to you for free and open access by Scholarship@Western. It has been accepted for inclusion in Electronic Thesis and Dissertation Repository by an authorized administrator of Scholarship@Western. For more information, please contact [wlsadmin@uwo.ca](mailto:wlsadmin@uwo.ca).

## Abstract

To model cardiac mechanics effectively, various mechanical characteristics of cardiac muscle tissue including anisotropy, hyperelasticity, and tissue active contraction characteristics must be considered. Some of these features cannot be implemented using commercial finite element (FE) solvers unless additional custom-developed computer codes/subroutines are appended. Such codes/subroutines are unavailable for the research community. Accordingly, the overarching objective of this research is to develop a novel LV mechanics model which is implementable in commercial FE solvers and can be used effectively within inverse FE frameworks towards cardiac disease diagnosis and therapy. This was broken down into a number of objectives. The first objective is to develop a novel cardiac tissue mechanical model. This model was constructed of microstructural cardiac tissue constituents while their associated volume contributions and mechanical properties were incorporated into the model. These constituents were organized in small FE tissue specimen models consistent with the normal/pathological cardiac tissue microstructure. *In silico* biaxial/uniaxial mechanical tests were conducted on the specimen models and corresponding stress-strain data were validated by comparing them with cardiac tissue data reported in the literature. Another objective of this research is developing a novel FE-based mechanical model of the LV which is fully implementable using commercial FE solvers without requiring further coding, potentially leading to a computationally efficient model which is easily adaptable to diverse pathological conditions. This was achieved through considering a novel composite material model of the cardiac tissue while all aspects of the cardiac mechanics including hyperelasticity, anisotropy, and active tissue responses were preserved. The model was applied to an *in silico* geometry of a canine LV under both normal and pathological conditions and systolic/diastolic responses of the model were compared with corresponding data of other LV mechanical models and LV contraction measurements. To test the suitability of the proposed cardiac model for FE inversion-based algorithms, the model was utilized for LV diastolic mechanical simulation to estimate the tissue stiffness and blood pressure using an ad-hoc optimization scheme. This led to reasonable tissue stiffness and blood pressure values falling within the range of LV measurements of healthy subjects, confirming the efficacy of this model for inversion-based diagnosis applications.

## Keywords

Biomechanical Modeling of the Left Ventricle, Active and Passive Cardiac Mechanics, Nonlinear Finite Element Simulation, Hyperelasticity, Hyperelastic Parameters, Anisotropy, Transverse Isotropy, Active Myofibers' Contraction Forces, Cardiac Cycle, Systolic Cycle, Diastolic Cycle, Cardiac Tissue Modeling, Cardiac Tissue Microstructural Mechanics, Cardiac Fibrous Structure, Myocardium.

## Co-Authorship Statement

This thesis has been written by Seyyed Mohammad Hassan Haddad under supervision of Dr. Abbas Samani. Parts of the material presented in this thesis have been submitted to several peer-reviewed journal papers as listed below. The research materials presented in different chapters of this thesis have been conducted by the principal author and guided by the thesis supervisor in collaboration with the underlined authors who are graduate students in the supervisor's research laboratory.

The material presented in Chapter 2 is entitled “A novel micro-to-macro approach for cardiac tissue mechanics.” It was authored by S. M. H. Haddad and A. Samani and it is now in Press at the Journal of *Computer Methods in Biomechanics and Biomedical Engineering*.

The material presented in Chapter 3 is entitled “A novel biomechanical computational model of the left ventricle using a composite material approach.” It was authored by S. M. H. Haddad and A. Samani, and has been submitted to the *International Journal of Engineering Science* and is currently peer reviewed by the journal.

The material presented in Chapter 4 is entitled “A biomechanical model of pathological left ventricle using a composite material approach.” It was authored by S. M. H. Haddad and A. Samani, and has been submitted to the Journal of *Medical Engineering and Physics* and is currently peer reviewed by the journal.

The material presented in Chapter 5 is entitled: “Human left ventricle biomechanics using medical imaging data and composite material mechanics approach.” It was authored by: S. M. H. Haddad, E. Karami, and A. Samani.

## **Acknowledgments**

I would like to seize this opportunity to thank individuals without their supports, this achievement would not have been realized.

My first and foremost gratitude belongs to my supervisor, Dr. Abbas Samani, for his forward and continuous encouragements during my PhD studies. I would like to express my gratitude and highest appreciations for him due to his kind guidance, his timely and calculated advices, his constructive comments, in addition to his effortless contributions throughout these years.

I also appreciate the input provided by members of my advisory committee, Dr. Drangova and Dr. White. I also thank my colleagues here at Western for their support and frequent constructive comments they provided which often inspired me to move forward with my PhD project.

My highest love and gratitude goes to my wife who has been a major inspiration and greatest source of strength for me towards realizing my academic and non-academic achievements throughout our marriage. My deepest gratitude goes to my kind family, specially my parents for their constant supports and encouragements since my childhood. At the end, I would like to express my love to my little daughter, Melika, who greatly inspired me during the last steps of my PhD work when I needed her presence in my life the most.

# Table of Contents

<b>Abstract</b> .....	i
<b>Co-Authorship Statement</b> .....	iii
<b>Table of Contents</b> .....	v
<b>List of Tables</b> .....	viii
<b>List of Figures</b> .....	x
<b>List of Acronyms and Abbreviations</b> .....	xvi
<b>List of Appendices</b> .....	xvii
<b>Chapter 1</b> .....	1
<b>1 Introduction</b> .....	1
1.1 Background and Motivation .....	1
1.2 Anatomy, Microstructure, and Physiology .....	4
1.3 Theory .....	15
1.3.1 Finite Elasticity .....	15
1.3.2 Mechanical Modeling of Cardiac Tissue .....	25
1.3.3 Active Contraction Models .....	28
1.4 Literature Review.....	32
1.4.1 Cardiac Tissue Passive Mechanical Properties.....	32
1.4.2 Left Ventricle Mechanical Modeling.....	36
1.4.3 Diastolic Heart Mechanics.....	41
1.5 Objectives .....	43
1.6 Thesis Outline .....	44
1.6.1 Chapter 2.....	45
1.6.2 Chapter 3.....	45
1.6.3 Chapter 4.....	46
1.6.4 Chapter 5.....	47
1.6.5 Chapter 6.....	48
1.7 Contributions of Thesis.....	48
<b>References</b> .....	50
<b>Chapter 2</b> .....	61
<b>2 A Novel Micro-to-Macro Approach for Cardiac Tissue Mechanics</b> .....	61
2.1 Introduction.....	61
2.2 Materials and Methods.....	63
2.2.1 Major Myocardial Tissue Constituents.....	63
2.2.2 Finite Element Modeling of Cardiac Tissue Samples.....	65
2.2.3 Normal Cardiac Tissue Modeling.....	69
2.2.4 Infarcted Cardiac Tissue Hyperelastic Model.....	73
2.2.5 Sensitivity Analysis .....	75
2.3 Results.....	76
2.3.1 Normal Cardiac Tissue Modeling.....	76
2.3.2 Infarcted Cardiac Tissue Modeling.....	79
2.4 Discussion and Conclusions .....	83
<b>References</b> .....	87
<b>Chapter 3</b> .....	92
<b>3 A Novel Biomechanical Computational Model of the Left Ventricle using a Composite Material Approach</b> .....	92
3.1 Introduction.....	92

3.2	Materials and Methods.....	94
3.2.1	Composite Material Model .....	94
3.2.2	Major Elements of the LV Model.....	95
3.2.3	Contraction Model and Elasticity Theory.....	97
3.2.4	Calculation of LV Stresses under Initial Stress Condition .....	98
3.2.5	<i>In silico</i> LV modeling .....	102
3.3	Results.....	104
3.3.1	Passive Inflation during Diastolic Phase.....	104
3.3.2	Systolic LV Mechanics .....	107
3.4	Discussion and Conclusions .....	109
	<b>References</b> .....	113
	<b>Chapter 4</b> .....	117
4	<b>A Biomechanical Model of the Pathological Left Ventricle using a Composite Material Approach</b> .....	117
4.1	Introduction.....	117
4.2	Materials and Methods.....	119
4.2.1	Composite Material Model .....	119
4.2.2	Major Elements of the LV Model.....	121
4.2.3	Contraction Model and Elasticity Theory.....	123
4.2.4	Finite Element Analysis of LV under Incremental Initial Stresses.....	125
4.2.5	<i>In silico</i> Infarcted LV Modeling .....	128
4.3	Results.....	130
4.4	Discussion and Conclusions .....	136
	<b>References</b> .....	141
	<b>Chapter 5</b> .....	146
5	<b>Human Left Ventricle Biomechanics using Medical Imaging Data and Composite Material Mechanics Approach</b> .....	146
5.1	Introduction.....	146
5.2	Materials and Method .....	148
5.2.1	Image Acquisition.....	148
5.2.2	Left Ventricle Model Construction.....	149
5.2.3	Composite Material Model of the Cardiac Tissue .....	151
5.2.4	Major Elements of the Left Ventricle Model.....	152
5.2.5	Anisotropy of the FE-based Left Ventricle Model .....	154
5.2.6	Ad-hoc Inversion-based Approach for End-diastolic LV Blood Pressure Estimation .....	155
5.2.7	Performance Evaluation of the LV Mechanical Model at End Diastole .....	156
5.3	Results.....	156
5.3.1	Ad-hoc Optimization .....	156
5.3.2	Diastolic LV Mechanical Model with Optimum Parameters .....	158
5.4	Discussion and Conclusions .....	164
	<b>References</b> .....	169
	<b>Chapter 6</b> .....	173
6	<b>Conclusion and Future Work</b> .....	173
6.1	Conclusion .....	173
6.1.1	Chapter 2: A Novel Micro-to-Macro Approach for Cardiac Tissue Mechanics .....	175

6.1.2	Chapter 3: A Novel Biomechanical Computational Model of the Left Ventricle using a Composite Material Approach.....	177
6.1.3	Chapter 4: A Biomechanical Model of the Pathological Left Ventricle using a Composite Material Approach .....	179
6.1.4	Chapter 5: Human Left Ventricle Biomechanics Using Medical Imaging Data and Composite Material Mechanics Approach .....	181
6.2	Future Directions .....	183
6.3	Closing Remarks .....	184
	<b>Appendices</b> .....	186
7	<b>Curriculum Vitae</b> .....	187



# List of Tables

**Table 2.1:** Major constituents of the normal myocardial tissue with their volume percentage ..... 65

**Table 2.2:** Yeoh hyperelastic parameters of the background tissue constituents obtained through fitting procedure ..... 71

**Table 2.3:** Major constituents of the infarcted myocardial tissue with their volume percentage ..... 73

**Table 2.4:** Second order Ogden hyperelastic parameters of the background tissue and myofibrils ..... 76

**Table 2.5:** Hyperelastic parameters of normal cardiac tissue calculated from the equibiaxial stress-strain data obtained from FE simulation compared to parameters given in [11]..... 77

**Table 2.6:** Percentage variations of hyperelastic parameters of normal cardiac tissue obtained by varying volume percentages (VPs) of each tissue constituent..... 79

**Table 2.7:** Yeoh hyperelastic parameters of the collagen fibers in the infarcted cardiac tissue ..... 79

**Table 2.8:** Fifth order Ogden hyperelastic model parameters of the background tissue and myofibril ..... 80

**Table 2.9:** Hyperelastic parameters of the infarcted cardiac tissue..... 81

**Table 2.10:** Percentage variations of infarcted cardiac tissue hyperelastic parameters due to alterations of volume percentage (VP) of collagen fibers ..... 82

**Table 4.1:** End-systolic radial, circumferential, and longitudinal strains in normal LV..... 130

**Table 4.2:** Transmural variations of end-systolic radial, circumferential, longitudinal, and fiber stresses in normal LV ..... 130

<b>Table 4.3:</b> Hyperelastic parameters of the 2 <sup>nd</sup> order Ogden model used for normal tissue mechanical simulation .....	131
<b>Table 4.4:</b> Hyperelastic parameters of the 2 <sup>nd</sup> order Ogden model used for infarcted tissue mechanical simulation .....	131
<b>Table 4.5:</b> Average values of end-systolic radial, circumferential, and longitudinal strains at the three regions of the infarcted LV .....	133
<b>Table 4.6:</b> Average values of end-systolic circumferential strains in the three regions of infarcted LV [24] .....	133
<b>Table 4.7:</b> End-systolic average values of the fiber stress in the three regions of infarcted LV .....	136
<b>Table 5.1:</b> Optimum hyperelastic parameters of the 2 <sup>nd</sup> order Ogden model used for diastolic LV mechanical simulation .....	157
<b>Table 5.2:</b> Variations of the surface matching errors obtained from the ICP algorithm with variable end-diastolic blood pressure values .....	157

# List of Figures

<b>Figure 1.1:</b> Major parts of the mammalian heart. ....	3
<b>Figure 1.2:</b> Chambers of the heart. ....	6
<b>Figure 1.3:</b> Geometry of the LV at mid-diastole state obtained from segmentation of the MR images. ....	7
<b>Figure 1.4:</b> Helix angle ( $\alpha$ ) model representing fiber orientation through the LV model [22]. .....	8
<b>Figure 1.5:</b> Helix angle ( $\alpha$ ) model describes fiber orientations as discrete bundles of the fibers with the same direction while they are in the same depth in the LV wall [23]. ....	8
<b>Figure 1.6:</b> Laminar structure of myofiber distribution in the LV model [30]. ....	9
<b>Figure 1.7:</b> Microstructure of the cardiac muscle cells [38]. ....	12
<b>Figure 1.8:</b> Structure of the myofibrils made by basic elements, i.e. sarcomeres (a), sarcomeres composed of thin filament, actin, and thick filament, myosin (b). ....	14
<b>Figure 1.9:</b> A general elastic geometry at its reference state (time $t_0$ ) and at its deformed state (time $t$ ) [46]. ....	15
<b>Figure 1.10:</b> Components of the Cauchy stress acting on a material when a very small cubic particle within the material has been considered. ....	20
<b>Figure 1.11:</b> Hill's model for cardiac tissue mechanical modeling. ....	26
<b>Figure 2.1:</b> Flowchart illustrating the proposed cardiac tissue modeling approach. ....	67
<b>Figure 2.2:</b> FE cylindrical sample of the background cardiac tissue which is composed of three types of elements: mitochondrion, fibroblast, and collagen. ....	68
<b>Figure 2.3:</b> FE cylindrical and sheet samples of the whole cardiac tissue which is composed of two types of elements: myofibril and background tissue. ....	69

<b>Figure 2.4:</b> (a): Stress-strain curve for a 3D matrix of type I collagen fiber reported in [33], (b): Stress-strain curve for an intact cardiac myofibril reported in [39]. .....	71
<b>Figure 2.5:</b> Stress-strain curve of background tissue of normal myocardium obtained from the proposed method. ....	76
<b>Figure 2.6:</b> Stress-strain data of normal myocardial tissue along fiber direction (a) and cross-fiber direction (b) obtained from the equibiaxial test FE simulation compared to measurements reported in the literature [11]. ....	77
<b>Figure 2.7:</b> Stress-strain data of normal myocardial tissue along fiber direction vs. change in volume percentages (VP) of the tissue constituents (U: upper bound of VP, L: lower bound of VP). Change in VP of the myofibril and mitochondrion (a) and change in VP of the fibroblast and collagen fiber (b). ....	78
<b>Figure 2.8:</b> Stress-strain data of normal myocardial tissue along cross-fiber direction vs. Change in volume percentages (VP) of the tissue constituents (U: upper bound of VP, L: lower bound of VP). Change in VP of the myofibril and mitochondrion (a) and change in VP of the fibroblast and collagen fiber (b). ....	79
<b>Figure 2.9:</b> Stress-strain curve of background tissue of infarcted myocardium obtained from the proposed method. ....	80
<b>Figure 2.10:</b> (a): Stress-strain data of infarcted myocardial tissue obtained from uniaxial simulation, (b): Stress-strain curve of infarcted myocardial tissue obtained from the proposed method compared to corresponding measurements. ....	81
<b>Figure 2.11:</b> Stress-strain data of infarcted myocardial tissue while the volume percentages (VP) of the collagen was changed (U: upper bound of VP, L: lower bound of VP). ....	82
<b>Figure 3.1:</b> Schematic of composite model of cardiac tissue including two parts: myofibers and background while active contractile myofiber forces generate stresses in both parts of the tissue to maintain equilibrium according to the momentum balance principle (a), three- element Hill's model for cardiac tissue (b). ....	95
<b>Figure 3.2:</b> Flow chart illustrating biomechanical simulation of the LV. ....	96

<b>Figure 3.3:</b> The rebar and background tissue in the reference state before contraction (a) and after contraction (b).....	102
<b>Figure 3.4:</b> The <i>In silico</i> LV model constructed using finite elements (a), and blood pressure variations during a cardiac cycle [35-36].....	103
<b>Figure 3.5:</b> LV pressure-volume variations in diastolic phase. ....	105
<b>Figure 3.6:</b> Transmural variations of the passive strain components at the LV equatorial area from endocardium (indicated by 0) towards epicardium (indicated by 100) when a diastolic blood pressure of 1 kPa was applied to the LV model. The strains are referenced w.r.t the zero-stress unloaded configuration. ....	106
<b>Figure 3.7:</b> Transmural variations of the diastolic stress components within the background at the LV equatorial area from endocardium towards epicardium when a diastolic blood pressure of 1 kPa was applied to the LV model. Maximum principle stress (panel a), radial stress (panel b), circumferential stress (panel c), and longitudinal stress (panel d) are shown. ....	106
<b>Figure 3.8:</b> Transmural variations of end-diastolic fibers stress at the equatorial area (a), transmural variations of end-diastolic fibers stress near the base (b), and transmural variations of end-diastolic fibers stress near the apex (c). ....	107
<b>Figure 3.9:</b> Transmural variations of end-systolic strain components at the LV equatorial area from endocardium (indicated by 0) towards epicardium (indicated by 100) when time-variable active stress and blood pressure were applied to the LV model. The strains are referenced w.r.t end diastole. ....	108
<b>Figure 3.10:</b> Transmural variations of end-systolic stress components within the background at the LV equatorial area from endocardium towards epicardium when time-variable active stress and blood pressure were applied to the LV model. Maximum principle stress (panel a), radial stress (panel b), circumferential stress (panel c), and longitudinal stress (panel d) are shown. ....	109

<b>Figure 3.11:</b> Transmural variations of end-systolic fibers stress at the equatorial area (a), transmural variations of end-systolic fibers stress near the base (b), and transmural variations of end-systolic fibers stress near the apex (c). .....	109
<b>Figure 4.1:</b> Three-element Hill’s model for cardiac tissue. ....	121
<b>Figure 4.2:</b> Flow chart illustrating biomechanical simulation of the LV.....	121
<b>Figure 4.3:</b> <i>In silico</i> normal and infarcted LV models constructed using finite elements: normal LV model (a), infarcted LV model with a circular infarcted region and border zone (b), and cross-section of the infarcted LV model with myocardial thinning from different views (c,d).....	122
<b>Figure 4.4:</b> Infarcted region with lower volume percentage of myofibers surrounded by normal cardiac tissue with higher volume percentage of myofibers. ....	129
<b>Figure 4.5:</b> Blood pressure variations during a cardiac cycle [35]......	130
<b>Figure 4.6:</b> End-systolic strain distribution through the infarcted LV model. The strains are referenced w.r.t end diastole. Radial strain distribution (a), cross sectional view of the radial strain distribution at midventricular area (b), circumferential strain distribution (c), cross sectional view of the circumferential strain distribution at midventricular area (d), longitudinal strain distribution (e), cross sectional view of the longitudinal strain distribution at midventricular area (f). ....	132
<b>Figure 4.7:</b> Circumferential strain variations with respect to the circumference of the LV at the equatorial area of the infarcted and normal models. ....	134
<b>Figure 4.8:</b> Longitudinal strain variations with respect to the circumference of the LV at the equatorial area of the infarcted and normal models.....	134
<b>Figure 4.9:</b> Transmural variations of end-systolic stress components within the background at the LV equatorial area from endocardium towards epicardium when time-variable active stress and blood pressure were applied to the infarcted LV model. Maximum principle stress (a), radial stress (b), circumferential stress (c), and longitudinal stress (d) are shown.....	135

<b>Figure 4.10:</b> Transmural variations of end-systolic fibers stress: within the infarct region (a), within the border zone (b), and within the healthy region (c). .....	136
<b>Figure 5.1:</b> 3D Cardiac MR image of a healthy human subject at the start-diastole: coronal view (a), sagittal view (b), and axial view (c).....	149
<b>Figure 5.2:</b> 3D surface model of the healthy subject’s LV obtained from MR image slices segmentation (shown using green color) which is superimposed onto arbitrary 3 orthogonal slices of the 3D MR image pertaining to start diastole.....	150
<b>Figure 5.3:</b> 3D LV model of the healthy subject at start diastole constructed by MR image segmentation. ....	150
<b>Figure 5.4:</b> FE model of the human subject LV: whole LV model view (a) and the model’s short axis cross section view (b). ....	151
<b>Figure 5.5:</b> Flow chart illustrating biomechanical simulation of the LV at the diastolic phase. ....	154
<b>Figure 5.6:</b> Active stress variations along a sarcomere of length $1.7 \mu m$ during a cardiac cycle [28]. ....	154
<b>Figure 5.7:</b> Surfaces of the calculated and measure LV geometries at the end-diastolic state corresponding to the best match achieved through ad-hoc optimization.....	158
<b>Figure 5.8:</b> Normal strains distributions through the LV volume at the end-diastolic state: cross-sectional views of the radial strain distribution (a) along with the whole radial strain distribution (b), cross-sectional view of the circumferential strain distribution (c) along with the whole circumferential strain distribution (d), cross-sectional view of the longitudinal strain distribution (e) along with the whole longitudinal strain distribution (f). ....	160
<b>Figure 5.9:</b> Shear strains distributions through the LV volume at the end-diastolic state: cross-sectional view of the rad-circ. strain distribution (a) along with the whole rad-circ. strain distribution (b), cross-sectional view of the rad-long strain distribution (c) along with the whole rad-long strain distribution (d), cross-sectional view of the circ.-long strain distribution (e) along with the whole circ.-long strain distribution (f). ....	162

**Figure 5.10:** Distribution of the background tissue stresses through the LV model at the end-diastolic state: cross-sectional view of the maximum principal stress distribution (a) along with the whole maximum principal stress distribution (b), cross-sectional view of the radial stress distribution (c) along with the whole radial stress distribution (d), cross-sectional view of the circumferential stress distribution (e) along with the whole circumferential stress distribution (f), cross-sectional view of the longitudinal stress distribution (g) along with the whole longitudinal stress distribution (h). ..... 164



## List of Acronyms and Abbreviations

<b>1D</b>	One-dimensional or one dimension
<b>2D</b>	Two-dimensional or two dimensions
<b>3D</b>	Three-dimensional or three dimensions
<b>3D-MRI</b>	Three-dimensional MRI
<b>4D-MRI</b>	Four-dimensional MRI
<b>ATP</b>	Adenosine Triphosphate
<b>AV</b>	Atrioventricular
<b>CE-MRI</b>	Contrast Enhanced MRI
<b>CT</b>	Computed Tomography
<b>CVD</b>	Cardiovascular Disease
<b>DT-MRI</b>	Diffusion Tensor MRI
<b>ECC</b>	Excitation-Contraction Coupling
<b>ECG</b>	Electrocardiogram
<b>ECM</b>	Extracellular Matrix
<b>EF</b>	Ejection Fraction
<b>FE</b>	Finite Element
<b>FEM</b>	Finite Element Method
<b>FFD</b>	Free-Form Deformation
<b>LV</b>	Left Ventricle
<b>LSE</b>	Least Squares Error
<b>MI</b>	Myocardial Infraction
<b>MR</b>	Magnetic Resonance
<b>MRI</b>	Magnetic Resonance Imaging
<b>PK</b>	Piola-Kirchhoff
<b>RV</b>	Right Ventricle
<b>SFEM</b>	Statistical FEM
<b>STD</b>	Standard Deviation
<b>SV</b>	Stroke Volume
<b>US</b>	Ultrasound

# List of Appendices

# Chapter 1

## Introduction

### 1.1 Background and Motivation

**T**HE heart is a fundamental muscular organ in the body which pumps blood through the whole body via the circulatory system, supplying oxygen and nutrients such as water, sugar (glucose), salt, proteins, etc. to the different organs including all types of tissues (cells), and removing carbon dioxide and other metabolic waste materials from them. The crucial importance of the heart lies in the fact that without enough nutrition and wastes removal none of the cells in the body can remain viable, hence none of the tissues in the body can continue their physiological activities unless the heart performs its function properly. As such, any defect or impairment in the heart function can influence organs, affecting the overall body health quite significantly.

The heart is located in the middle compartment of the mediastinum behind the breastbone in the chest. The mammalian heart has four chambers: two upper chambers (the atria) and two lower ones (the ventricles). The right atrium and right ventricle constitute the “right heart” and the left atrium and left ventricle form the “left heart.” These two parts of the heart are separated by a muscular wall called the septum. The heart is enclosed by a strong sac called the pericardium. The heart is protected and retained firmly in the chest by this sac. The pericardium has two major sacs: the outer sac (the parietal pericardium) and the inner sac (the serous pericardium). There is a liquid between these two sacs called the

pericardial fluid which lubricates the heart during its contraction in addition to lubricating its contact surface with the lungs. The heart's outer wall consists of three layers including the epicardium, myocardium and endocardium. The epicardium is the outermost wall layer which forms the inner part of the pericardium. The myocardium is the middle layer which is the muscular part of the heart containing the myofibers that generate the heart contraction. Finally, the endocardium is the inner layer which is the heart's inner coating touching the blood [1].

As shown in Figure 1.1, the heart has a number of valves which are: 1) Atrioventricular (AV) valves including the tricuspid valve and the mitral valve which control the blood flow between the atria and the ventricles, 2) the pulmonary semi-lunar valve which separates the right ventricle from the pulmonary artery and 3) the aortic valve which separates the left ventricle from the aorta. The valves are attached to the heart muscle via heartstrings or chordae tendinae [1]. The sinoatrial node is another important anatomical part of the heart which generates the action potential that stimulates myofibers contractions and regulates heart rhythm through a precise electrophysiological procedure.

The heart pumps blood through two pathways: the pulmonary circuit and the systemic circuit. In the pulmonary circuit, deoxygenated blood is transferred from the right ventricle to the lungs via the pulmonary artery and then oxygenated blood is guided to the left atrium via the pulmonary vein. In the systemic circuit, the heart's function of pumping oxygenated blood to the body is accomplished by the left ventricle (LV) which is a strong muscular part of the heart. The blood is pushed out of the LV cavity and flows via the aorta before it is distributed to all organs through arterial networks. The deoxygenated blood is also directed from tissues and via veins to the venae cavae and then to the heart's right atrium [1]. The abovementioned description of the heart and blood circulation system reveals the significance of the left ventricle, as the largest, most vigorous, and most muscular chamber of the heart, supplying most of the heart's pumping power.

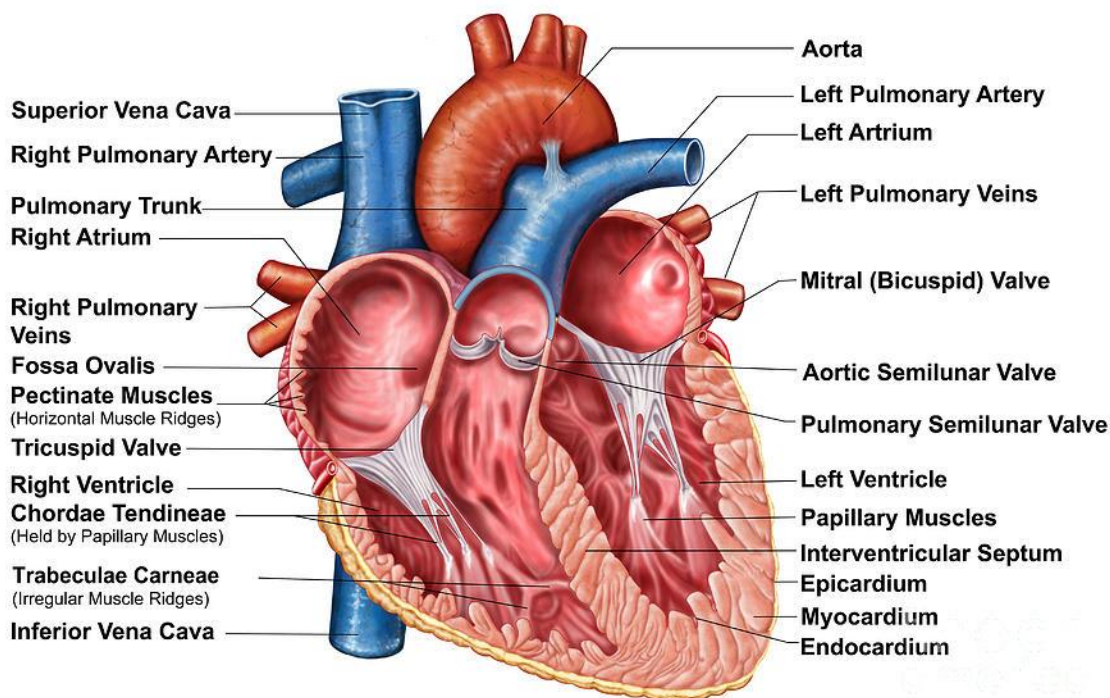


**Figure 1.1:** Major parts of the mammalian heart.

There is a wide and prevalent range of diseases that are related to the heart, as a crucial organ in the body. Cardiovascular diseases (CVD) are the leading cause of death worldwide. They include ischemic heart disease (coronary heart disease), hypertensive heart disease, inflammatory heart disease, rheumatic heart disease, and congenital heart disease. They also include heart diseases caused by drugs, unhealthy diet, trauma, toxins, and alcohol, accounting for more than 67% of all CVD-related deaths [1]. In 2012, there were more than 17.5 million deaths due to CVD in addition to almost 11.2 million other deaths related to heart diseases [2]. These appalling statistics reinforces the importance of research in the area of cardiac mechanics in order to devise more effective diagnostic and therapeutic techniques to manage diverse cardiac conditions. Due to complexity of the cardiovascular system's physiology and complex pathology, however, accurate heart diseases diagnosis and treatment are associated with many challenges. In most cases, cardiologists need a wide range of data acquired from various clinical testing and imaging techniques to be able to determine patients' cardiac pathology necessary to adopt appropriate therapy plans [3-5]. Advances in science, technology and computation have

led to adaptation of a new paradigm of utilizing biophysical based models of the myocardium. Such models have three major advantages. Firstly, these computational models serve the interests of clinicians to gain insight into heart physiology, i.e. both heart mechano- and electrophysiology, as well as diverse cardiac pathological pathways. This has motivated considerable amount of progress in mechanical and electromechanical models of the heart to simulate the heart under physiological and pathological conditions [6-11]. Secondly, such models can provide invaluable supplementary information for cardiologists to achieve more precise prognosis of cardiac conditions [12-14]. This is indisputably quite vital since it prevents patients from receiving unnecessary and/or ineffective therapeutic procedures that may not only have some side-effects but may also impose unjustified expenses to already strained health care systems. Thirdly, it has been demonstrated in some research works that electromechanical models have a great potential to be combined with other non-invasive tools such as medical imaging for more efficient patient-specific therapy planning [15-17]. For instance, while cardiac computed tomography (CT) perfusion and contrasts-enhanced magnetic resonance imaging (CE-MRI) techniques can specify ischemic tissue portions within the myocardium with less blood flow, they do not provide any information about their mechanical characteristics (e.g. stiffness and contractile ability). From a diagnostic point of view, it is highly advantageous to obtain such information using computer assisted tool involving patient-specific mechanical models of the heart to be fused with medical imaging data. Such fused data can enable more detailed assessment of the intensity and extension of ischemia through different parts of the myocardium. Considering the abovementioned merits of electromechanical models of the heart, this research is geared towards developing a novel and effective computational technique for mechanical modeling of the LV. The technique is designed to describe the LV mechanophysiology characteristics necessary for quantification of local contraction forces, which can be used as a direct mechanical measure of the functionality of the cardiac tissue.

## 1.2 Anatomy, Microstructure, and Physiology

An adult heart has a mass of ~300 grams (~10.5 oz). The human heart is typically the size of a fist: 12 cm in length, 8 cm wide, and 6 cm in thickness. As described earlier, the heart

includes four chambers as shown in Figure 1.2. The two upper chambers are the atria and the two lower chambers are the ventricles. The thickness of the four chambers varies consistently with their specific functions. The atria are typically thin-walled because they transfer blood into the adjacent ventricles while the ventricles are normally muscular and thick-walled as they pump blood through farther distances. The right and left ventricles operate as two separate pumps working simultaneously, however, the right one has a much smaller workload. The right ventricle only drives blood to the lungs, which are located close to the right ventricle, withstanding only small vascular resistance to blood flow. In contrast, the LV pumps blood to the whole body through much farther distances, hence facing much higher vascular resistance to blood flow. As such, the LV must work harder to establish sufficient blood flow throughout the body. The anatomy of the ventricular walls are influenced by their related workloads, therefore, the muscular LV wall is substantially thicker than that of the right ventricle [1]. As illustrated in Figure 1.2, while the LV has an ellipsoidal shape similar to a bullet, the right ventricle appears triangular from longitudinal view and crescent from transversal view. A human LV geometry obtained from processed medical image is illustrated in Figure 1.3. As shown in this figure, it has three major parts of lower part or apex, middle part which is called midventricular or equatorial area, and upper part which is referred to as base. The LV has two major surfaces, an inner surface which is called endocardium and an outer surface which is called epicardium. The length of the human LV from base to apex is  $\sim 7.5$  cm [18]. The diameter of the LV typically refers to the maximum transverse (left-to-right) internal (luminal) distance, excluding thickness of the walls [19]. For different individuals, it ranges from  $\sim 36$  mm to  $\sim 56$  mm depending on the level of their activities, their diets, and health conditions [20]. The LV wall thickness is not uniform through the whole LV and it decreases from base to apex. It also varies among different individuals ranging from  $\sim 8.9$  mm to  $\sim 9.6$  mm within the midventricular area at end-diastolic state. It is noteworthy that when a normal LV contracts, its LV wall thickness increases significantly and varies from  $\sim 13.9$  mm to  $\sim 15.7$  mm at end-systolic state. This phenomenon is well-known in the LV contraction process and called LV wall thickening [21].

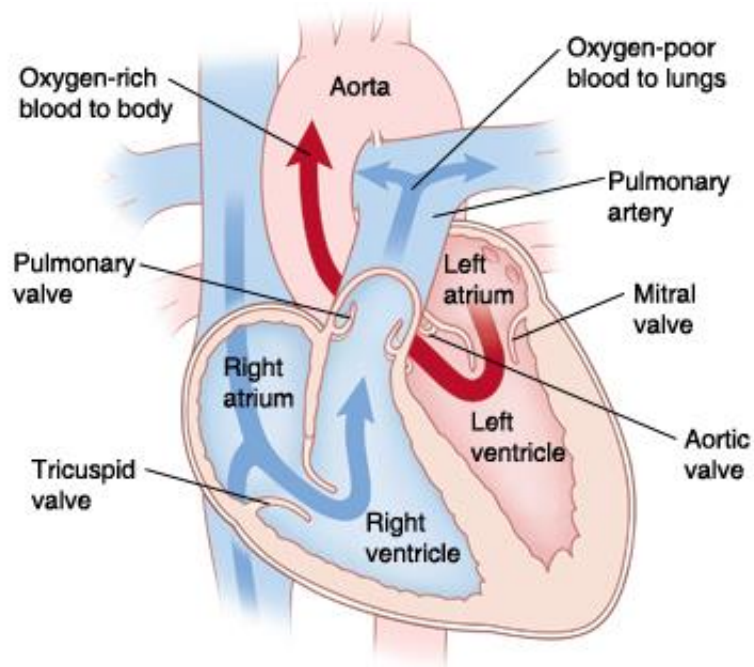


**Figure 1.2:** Chambers of the heart.

The most important mechanical feature of the cardiac tissue and especially LV is its fibrous structure [22-24]. Myofibers are the active part of the cardiac tissue that generate contraction forces. Given their specific orientation within the LV volume, they lead to the well-known anisotropy of cardiac tissue. While the contraction of each individual myofiber may not be significant, superposition of the contractions of the myofibers distributed throughout the LV volume generates a considerable net contraction leading to a strong pumping characteristic for the LV. Fiber orientations of the LV can be represented by a complex network of the different bundles of the muscle fiber within the LV. This anisotropic structure plays an essential role in developing the LV mechanical characteristics, including the stress and strain distribution through the LV and contraction pattern, and in particular its torsional motion during ejection. According to ex-vivo morphological studies on LV wall tissue samples, which were performed using light microscopy [22-23], fiber orientation of the LV typically varies continuously when moving from endocardium towards epicardium. These studies suggest that the LV fiber orientation can be described using the helix angle ( $\alpha$ ) as shown in Figure 1.4. The helix angle is measured in the plane which is parallel to the epicardial surface with respect to the latitudinal line. Measured with respect to the epicardium, fiber angles are assumed to be



positive in the upper right quadrant and negative in the lower right quadrant. A zero helix angle means that, in the local system, the fiber is directed circumferentially. Also,  $+90^\circ$  helix angle means that the fiber is oriented longitudinally from apex to base, while  $-90^\circ$  helix angle means that the fiber is oriented longitudinally from base to apex. Based on morphological studies involving tissue samples from different parts of the LV, the helix angle on average varies from  $+60^\circ$  at epicardium to  $-60^\circ$  at endocardium [22-23]. These studies suggest that the fiber orientation is almost circumferential at mid-wall. These morphological measurements demonstrated a spiral network of fibers through the LV volume which is quantified by the helix angle such that discrete bundles of fibers located in the same depth along the LV wall thickness have similar helix angle (see Figure 1.5) [22-24]. Almost all LV mechanical models, which consider transverse isotropy, used this description of fiber orientation through the LV. They concluded that, from stress analysis perspective, this description can provide reasonable results as compared to measurements of the LV contraction [25-27]. While most LV models consider a linear change in the helix angle by moving from endocardium to epicardium, some models considered more accurate nonlinear variations which were fitted to measured data [22,28].

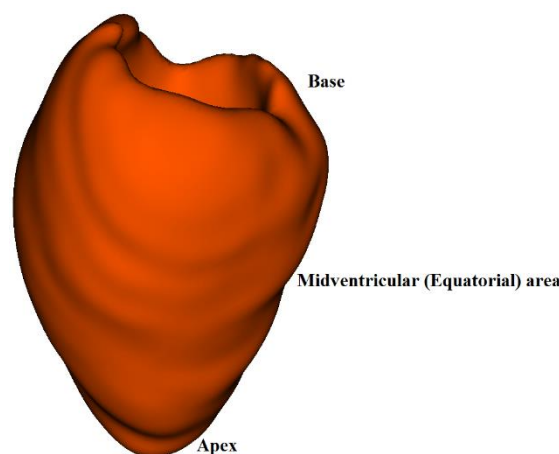


**Figure 1.3:** Geometry of the LV at mid-diastole state obtained from segmentation of the MR images.

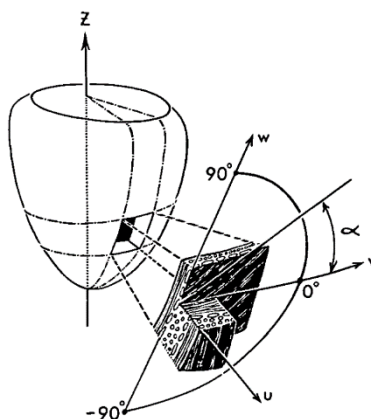


**Figure 1.4:** Helix angle ( $\alpha$ ) model representing fiber orientation through the LV model [22].

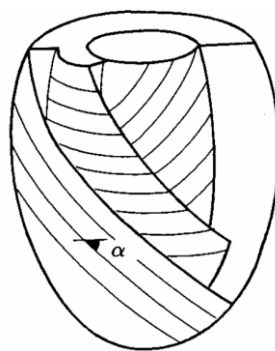


**Figure 1.5:** Helix angle ( $\alpha$ ) model describes fiber orientations as discrete bundles of the fibers with the same direction while they are in the same depth in the LV wall [23].

More recent studies suggest that cardiac tissue is composed of discrete layers of myofibers tightly bound by endomysial collagen, as depicted in Figure 1.6 [29-30]. These myofiber laminae have the capability to slide over each other and even produce complex rearrangements at different time instances during a cardiac cycle. These rearrangements are believed to reinforce the pumping characteristic of the LV. The thickness of each lamina is about four to six cells which is continuously divided in different branches (directions) throughout the LV wall. The orientation of each lamina is perpendicular to the LV surface except for subendocardial and subepicardial laminae which are almost parallel to the LV surface. This information agrees with previous studies which assume transverse isotropy, since they concluded that the fiber network is almost aligned with the LV surface near epicardial and endocardial surfaces. Based on the laminar structure of the fiber orientation within the LV model, three distinct material axes can be identified at each specific point within the muscle including: 1) the fiber axis which is along the muscle fiber

direction, 2) the sheet axis which is transverse to the plane of the fiber layer, and 3) the sheet-normal axis which is perpendicular to the plane of the fiber layer. This assumption results in a more complex and higher level of anisotropy of the LV which can be characterized using an orthotropic material model as used in some of studies dealing with mechanical modeling of the heart [31-32].

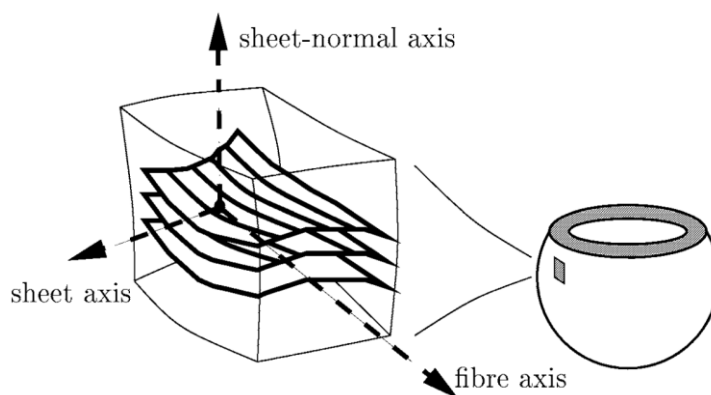


**Figure 1.6:** Laminar structure of myofiber distribution in the LV model [30].

Other recent studies use newer technologies such as the diffusion tensor magnetic resonance imaging (DT-MRI) technique to quantify fiber orientation more accurately [33-35]. These studies focus on building a statistical atlas of the cardiac fiber architectures using human or animal datasets [33-35]. These atlases are useful for 1) providing an average quantification of the fiber orientation within the LV and myocardium for a specific specimen (animal or human) and 2) assisting clinicians and biomedical engineers to estimate fiber orientation variability in a given population [33-34]. In [33] the fiber architecture of the human heart has been studied and the results have shown that there is a good agreement between previous studies based on light microscopy with those based on DT-MRI measurements. This study follows fiber orientation models based on light microscopy which suggest that fiber helix angle varies with respect to the LV wall thickness while it starts from positive values (apex to base direction) at the endocardium and ends at the negative values at the epicardium (base to apex direction). In [35] canine cardiac fiber architecture has been studied and it was concluded that fiber orientation angle varies smoothly from endocardium towards epicardium while fiber transverse and sheet angles, which were described in the laminar model, involve significant variations at the

basal region especially at the positions where two populations of the fibers sheets intersect with each other. At these regions DT-MRI can provide more accurate estimation of fiber orientations through the myocardium [35].

More recently, the problem of quantifying fiber orientation within the myocardium was tackled using a very interesting mathematical approach [36]. For this purpose, the generalized helicoid, which was derived based on a special form of minimal surfaces, was utilized. This approach made it possible to describe fiber orientation variations through the myocardium using only three curvature parameters. The advantage of this mathematical form is that it provides a continuous network of fibers throughout the myocardium. In conjunction with mechanical models of the heart, this more realistic network continuity is expected to lead to improved overall modeling accuracy and, consequently, higher result reliability. This model was proven to provide accurate description of the cardiac fiber orientations in various species such as dog, human, and rat as validated by DT-MRI data [36]. In a more recent study relevant to this approach, the first order models of smooth frame fields were utilized to provide direct measurement of myofibers helix and transverse angles variations. This method was also used to measure the amount of the heart wall curvature and myocytes fanning and twisting using statistical analysis of the DT-MRI data [37].

Myocardial tissue has a very complex microstructure including two major parts: cardiac muscle cells (cardiomyocytes) and extracellular matrix (ECM). Cardiomyocytes are the major constituents of the cardiac tissue from the prospect of volume percentage and are composed of different constituents such as myofibrils, mitochondria, sarcolemma, sarcoplasmic reticulum, intercalated disk, nucleus, T-tubules, etc. (see Figure 1.7). Cardiomyocytes have a length of 120  $\mu\text{m}$  and a diameter of 20–30  $\mu\text{m}$  in a normal adult heart [38]. Each muscle cell has one or two large nuclei typically located in its central part. Cardiomyocytes are branched at their ends such that the branched adjacent cells are tightly bound together by complex junctions called the intercalated discs [38]. As demonstrated in Figure 1.7, the major constituent of cardiomyocytes is the myofibril. It is the active contractile part of the cardiac tissue that generates cardiac contraction forces [38]. Myofibrils are organized structurally into very basic contractile units called sarcomeres

that are located along the myofibrils. A sarcomere is composed of myosin and actin, two well-known types of proteins. The interaction of these proteins is responsible for active force generation as illustrated in Figure 1.8. The actin filaments are thin, causing the lighter bands (I bands) in the striated muscle while the myosin filaments are thicker, causing darker bands (A bands) under electron microscopy [38]. Adjacent sarcomeres are isolated from each other by z-discs. Each cardiomyocyte is enclosed in a membrane called sarcolemma. A T-tubule (or transverse tubule) is a deep invagination of the sarcolemma, which is the main location for the coupling of excitation and contraction where the distributed depolarization is converted into force by basic contractile elements, i.e. sarcomeres [38]. A tubular membrane-bound that encloses the myofibrils is sarcoplasmic reticulum which is a plexus for storage, release, and reaccumulation of calcium ions as the stimulators of active contraction and relaxation sequences in the cardiac cycle [38]. A major part in the cardiomyocyte is mitochondrion which is a cell organelle that produces adenosine triphosphate (ATP) as the source of chemical energy for the muscle cells. Myofibrils utilize ATP for their contraction and other cellular activities within the cardiomyocytes [38]. As such, mitochondria are known as the power plants of the cardiomyocytes [38]. The large mitochondria, with their dense folds in the inner membrane (cristae), reveal the high level of cellular metabolism of cardiac muscles. The volume contribution of mitochondria in cardiac muscle is even higher than that in the skeletal muscle cells [38]. Cardiomyocytes require considerable amount of oxygen for their cellular activities and, as such, high levels of myoglobin and a rich network of capillaries are present surrounding the myofibrils. It is noteworthy that from volume percentage perspective, myofibril and mitochondrion are the major constituents of the cardiac myocytes occupying ~90% of the volume of the cardiomyocytes [39]. Furthermore, mechanically, these two major constituents are very essential. Myofibrils are the active part of the tissue that generates contraction forces, hence is they form the main component necessary to achieve the active mechanical response of cardiac tissue. Its passive characteristics are also important, as it is built by the well-bounded protein chains [38] with considerable stiffness necessary to withstand external forces. This high stiffness is reflected in the stress-strain characteristics of the cardiac tissue along the fiber direction indicated in the literature frequently [40-41]. The mitochondria are also important from mechanical

stiffness perspective since they can be assumed as fairly large spherical/elliptical shape particles filled with special fluid and distributed throughout the whole cardiac tissue as illustrated in Figure 1.7. Essentially, the mitochondria can be assumed isovolumic (incompressible) during mechanical deformation due to the presence of fluid in their structure [42].

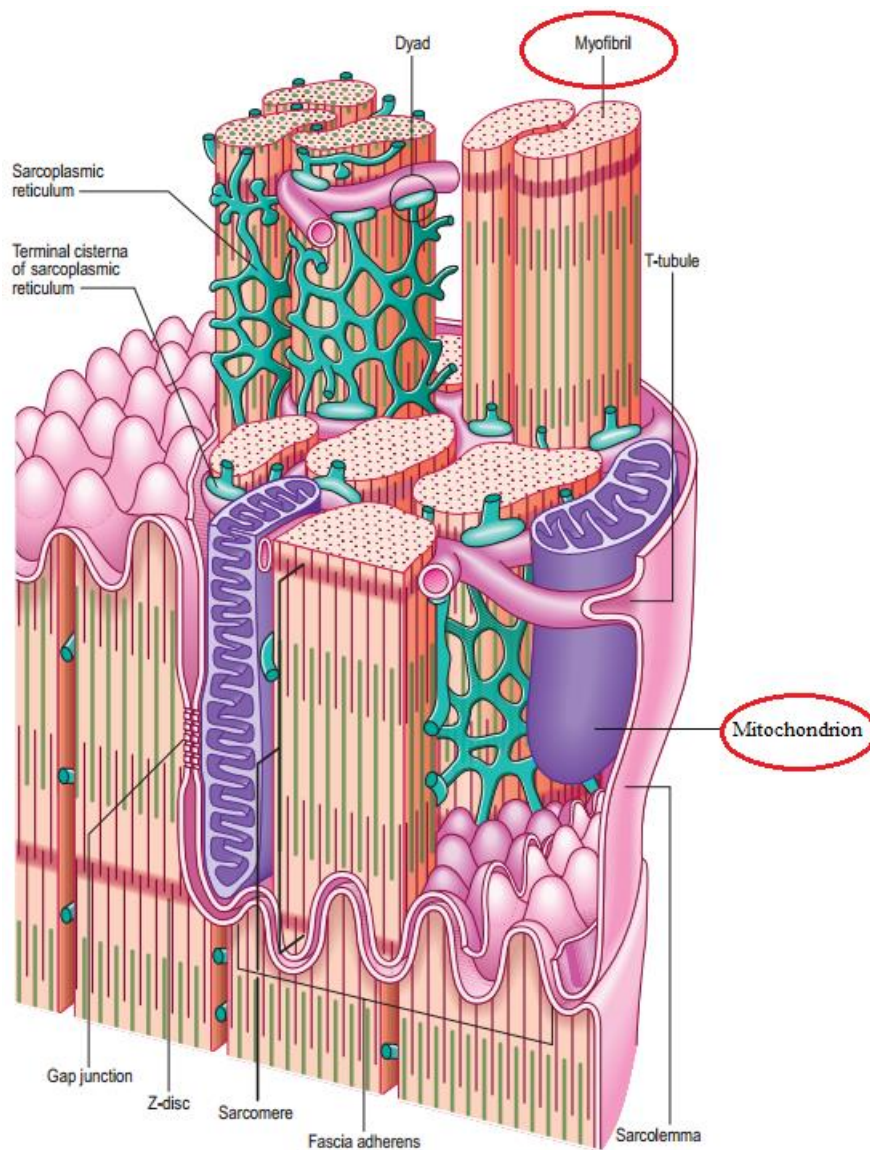


**Figure 1.7:** Microstructure of the cardiac muscle cells [38].

The other essential part of the myocardial tissue is ECM. It consists of various parts such as fibroblasts, connective tissue, glycosaminoglycans, glycoproteins, blood vessels, and nerves [38]. Fibroblasts which are responsible for synthesis of ECM specifically collagen

fibers are the most abundant cells in the myocardial tissue composition. They are a fundamental constituent of the normal ECM in terms of volume contribution. They occupy about 10% of the myocardial tissue. Connective tissue is another ECM constituent which is composed of collagen (mainly collagen type I) and insignificant amounts of fibronectin, laminin, and elastin [43]. Connective tissue plays an important role in joining the cardiac muscle cells to each other to preserve the integrity of the cardiac tissue such that it can properly accomplish the major function of the myocardium contraction. Collagen is an essential constituent of the connective tissue and cardiac ECM [38]. While the volume contribution of the collagen is not very high, from the mechanical function perspective it is a fundamental part of tissue microstructure. It contributes very significantly to stiffness, especially under tension while it provides structural support for the cardiac tissue. Glycosaminoglycans are long unbranched polysaccharides consisting of a repeating disaccharide unit. This repeating unit is made up of an amino sugar along with a uronic sugar or galactose. Glycosaminoglycans are highly polar molecules and thus have a high tendency to absorb water. Consequently, their major role in the cardiac tissue is that they act as a lubricant or as a shock absorber that is quite vital to preserve the elasticity of the myocardium while it contracts as well as contacts other parts of the body such as lungs during its function. Glycoproteins are located in cell walls and connective tissues in cardiac ECM. These proteins may also adhere to cells and enable development of functional tissues. They also give structural support to cells, serve as a constitutional component in production of the connective tissue, and facilitate digestion process of some nutrition by the muscle cells [38]. Blood vessels and nerves are the other cardiac ECM constituents with small volume contributions to the tissue structure. Their influences on the whole cardiac tissue mechanical function is also insignificant due to their low stiffness. From tissue mechanics perspective, it can be concluded that the major constituents of the cardiac ECM are fibroblast and collagen fibers.

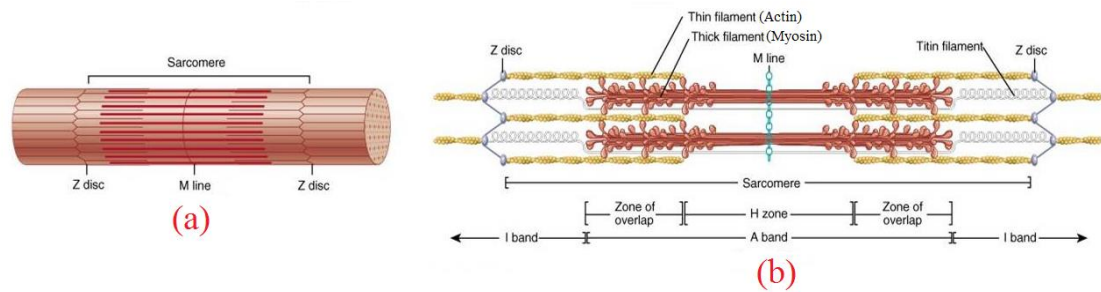


**Figure 1.8:** Structure of the myofibrils made by basic elements, i.e. sarcomeres (a), sarcomeres composed of thin filament, actin, and thick filament, myosin (b).

As indicated previously, the myofibrils have distinct, repeating micro-anatomical units, called sarcomeres, which are considered as the basic contractile elements of cardiomyocytes as shown in Figure 1.8. A sarcomere is composed of thick filament (myosin) and thin filament (actin). Its length is defined as the space between two consecutive z-discs and it ranges from about 1.6  $\mu\text{m}$  to 2.2  $\mu\text{m}$  in the human heart. Electrochemical interactions between the actin and myosin in a single sarcomere results in shortening of the sarcomere, and in a larger scale the myocyte within the well-known process of excitation-contraction coupling (ECC). ECC is the process whereby a myocyte contracts by propagation of action potential. When an action potential depolarizes a cardiomyocyte, calcium ions ( $\text{Ca}^{2+}$ ) enter the cardiac myocyte by distribution of the action potential via L-type calcium channels located on the sarcolemma. The calcium ions accumulated in the sarcoplasmic reticulum are released by the newly-entered calcium ions. The calcium released by sarcoplasmic reticulum binds to troponin-C (TN-C) that is part of the actin protein in sarcomeres. This triggers a conformational change in a regulatory complex such that troponin-I (TN-I) opens a new location on the actin molecule that has the capability to bind to the myosin ATPase which is situated on the myosin head. ATP hydrolysis occurs due to this binding that provides energy for a conformational alteration in the sarcomere, leading to ratcheting between the myosin heads and the actin forming cross-bridges between these filaments and eventually leading to the contraction of the sarcomere. The activation of the TN-C propagates to the adjacent sarcomeres generating successive sarcomere contractions which continues as long as the concentration of the calcium ions is maintained above a minimum level [38]. From macroscopic view, at this stage isovolumetric contraction of the LV occurs and continues until the cavity blood



pressure evolves beyond the aortic pressure which opens the aortic valve and pumps the blood out of the LV cavity [44].

During sarcomere relaxation phase, an ATP-dependent calcium mechanism in sarcoplasmic reticulum sequesters calcium ions from the myofibrils. Hence the calcium ion concentration is gradually reduced and eventually washed out from the TN-C. When intracellular calcium ion concentration is reduced to a minimum level, a conformational alteration is prompted in the actin complex, leading to removal of the TN-I from the actin binding site and untangling myosin and actin from each other. At the end of the relaxation cycle, a new ATP is attached to the myosin head which replaces the hydrolyzed ATP (ADP), and sarcomere length returns to its initial state [38]. Macroscopically, this time coincides with the LV isovolumetric relaxation. This relaxation carries on until the LV cavity pressure descends to a lower level of the left atrium pressure opening the mitral valve. This is the time when the LV diastolic filling starts [45].

## 1.3 Theory

### 1.3.1 Finite Elasticity

The theory of elasticity deals with the deformation of elastic materials. It relates deformation of the material to external forces applied to it based on its stiffness (mechanical) properties. To start, as illustrated in Figure 1.9, we consider an elastic object geometry at its reference state at time  $t_0$  when no deformation has occurred. Then we assume that the deformed geometry is at time  $t$  when a displacement field  $\mathbf{u}(\mathbf{X}, t)$  is generated throughout the object's domain.

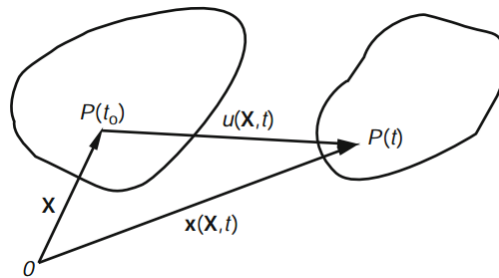


**Figure 1.9:** A general elastic geometry at its reference state (time  $t_0$ ) and at its deformed state (time  $t$ ) [46].

With this assumption we can relate each point such as  $P(t_0)$  at position  $\mathbf{X}$  in the reference geometry to the corresponding point in the deformed geometry,  $P(t)$ , at its new position  $\mathbf{x}$  through the following Equation [46]:

$$\mathbf{x}(\mathbf{X}, t) = \mathbf{X} + \mathbf{u}(\mathbf{X}, t) \quad (1.1)$$

Considering the previous equation and using differential calculus principles, we can obtain the following relation [46]:

$$d\mathbf{x} = d\mathbf{X} + (\nabla \mathbf{u})d\mathbf{X} \quad (1.2)$$

where  $\nabla \mathbf{u}$  is the displacement gradient which can be defined as follows:

$$\nabla \mathbf{u} = \begin{pmatrix} \frac{\partial u_1}{\partial X_1} & \frac{\partial u_1}{\partial X_2} & \frac{\partial u_1}{\partial X_3} \\ \frac{\partial u_2}{\partial X_1} & \frac{\partial u_2}{\partial X_2} & \frac{\partial u_2}{\partial X_3} \\ \frac{\partial u_3}{\partial X_1} & \frac{\partial u_3}{\partial X_2} & \frac{\partial u_3}{\partial X_3} \end{pmatrix} \quad (1.3)$$

In tensor notation Equation (1.2) can be rewritten as:

$$d\mathbf{x} = \mathbf{F}d\mathbf{X} \quad (1.4)$$

where  $\mathbf{F}$  is the deformation gradient tensor which can be defined as:

$$\mathbf{F} = \mathbf{I} + \nabla \mathbf{u} \quad (1.5)$$

where  $\mathbf{I}$  is the identity tensor. To define the relationship between the length of  $d\mathbf{x}$ ,  $ds$ , in the deformed configuration and the length of  $d\mathbf{X}$ ,  $dS$ , in the reference configuration, we use the dot product of Equation (1.4) which leads to the following Equation:

$$ds^2 = d\mathbf{x} \cdot d\mathbf{x} = d\mathbf{X} \cdot \mathbf{C} d\mathbf{X} \quad (1.6)$$

where  $\mathbf{C}$  is the right Cauchy-Green deformation tensor which is defined based on the deformation gradient tensor as:

$$\mathbf{C} = \mathbf{F}^T \mathbf{F} \quad (1.7)$$

Note that according to the Equation (1.6) when  $\mathbf{C} = \mathbf{I}$ ,  $ds^2 = d\mathbf{S}^2$  which means that there is rigid body motion (translation and/or rotation). Using Equation (1.5) in conjunction with tensor calculus principles, the following relation for the right Cauchy-Green deformation tensor in terms of the displacement gradient can be obtained [46]:

$$\mathbf{C} = \mathbf{I} + \nabla \mathbf{u} + (\nabla \mathbf{u})^T + (\nabla \mathbf{u})^T (\nabla \mathbf{u}) \quad (1.8)$$

This can be written in the form:

$$\mathbf{C} = \mathbf{I} + 2\mathbf{E} \quad (1.9)$$

where tensor  $\mathbf{E}$  is the famous Green-Lagrange strain tensor which is related to the displacement gradient as:

$$\mathbf{E} = \frac{1}{2} \left[ \nabla \mathbf{u} + (\nabla \mathbf{u})^T + (\nabla \mathbf{u})^T (\nabla \mathbf{u}) \right] \quad (1.10)$$

Using Equation (1.9) and (1.7) the following Equation for the Green-Lagrange strain tensor in terms of the deformation gradient can be obtained:

$$\mathbf{E} = \frac{1}{2} \left[ \mathbf{F}^T \mathbf{F} - \mathbf{I} \right] \quad (1.11)$$

### 1.3.1.1 Infinitesimal Deformation

We start with the assumption that the displacement vector and its partial derivatives are very small (mathematically infinitesimal), then all the components of the tensor  $(\nabla \mathbf{u})^T (\nabla \mathbf{u})$  will be an infinitesimal value of higher order which may be ignored to simplify the relation (1.10) to:

$$\boldsymbol{\varepsilon} = \frac{1}{2} \left[ \nabla \mathbf{u} + (\nabla \mathbf{u})^T \right] \quad (1.12)$$

Tensor  $\boldsymbol{\varepsilon}$  is the well-known infinitesimal strain tensor where its components can be written in terms of the displacement components in Cartesian coordinates as [46]:

$$\varepsilon_{ij} = \frac{1}{2} \left( \frac{\partial u_i}{\partial X_j} + \frac{\partial u_j}{\partial X_i} \right) \quad (1.13)$$

This is the type of strain we used for all finite element (FE) simulations when there are not nonlinear geometric and intrinsic nonlinearity effects during the deformation process of the elastic solid [47]. When ABAQUS uses this measure for strain it means that the FE simulation deals with a linear elastic material that undergoes infinitesimal deformations while geometric nonlinearity is insignificant [47].

### 1.3.1.2 Finite (Large) Deformation

When we deal with a material which involves large displacements values during its deformation resulting from external or internal mechanical loads, Equation (1.10) and (1.11) cannot be simplified, hence they are used in their original forms. This means that the term  $(\nabla \mathbf{u})^T (\nabla \mathbf{u})$  cannot be ignored, hence the proper strain measure will be the Green-Lagrange strain tensor  $\mathbf{E}$ . This is the strain measure that is used by ABAQUS software when we deal with FE simulations which involve large deformations with either elastic or non-linear elastic materials [47]. Components of the Green-Lagrange strain tensor in its general form based on Equation (1.10) can be written in the Cartesian coordinates system as follows [46]:

$$E_{ij} = \frac{1}{2} \left( \frac{\partial u_i}{\partial X_j} + \frac{\partial u_j}{\partial X_i} \right) + \frac{1}{2} \frac{\partial u_m}{\partial X_i} \frac{\partial u_m}{\partial X_j}, \quad m = 1, 2, 3 \quad (1.14)$$

Using Equation (1.11) to describe the strain is highly advantageous as it involves the term  $\mathbf{F}^T \mathbf{F}$  which was taken on the reference body configuration instead of the current one,

rendering all calculations in ABAQUS to be straightforward. For comparison, one can see Equations (1.6) and (1.7) which are written based on the reference configuration. Another important feature of  $\mathbf{E}$  is that it can be calculated easily from the deformation gradient without any need to obtain principle directions and principle stretches. These important merits make the Green-Lagrange strain tensor computationally attractive for FE and other types of mechanical simulations where finite deformation is involved.

### 1.3.1.3 Stress Tensor and Principle of Linear Momentum

The internal traction vector,  $\mathbf{t}$ , is defined as the force per unit area acting on a plane. As such the internal traction can be given as [46]:

$$\mathbf{t} = \frac{d\mathbf{F}}{dA} \quad (1.15)$$

where  $d\mathbf{F}$  denotes the force applied to  $dA$  which is a very small differential area over the surface. The components of the Cauchy stress (true stress),  $\sigma_{ij}$ , can be mathematically expressed based on the traction vectors,  $\mathbf{t}_{e_i}$ s, applied to the faces of a very small differential volume of the material (see Figure 1.10) using the following Equations [46]:

$$\begin{cases} \mathbf{t}_{e_1} = \sigma_{11}\mathbf{e}_1 + \sigma_{12}\mathbf{e}_2 + \sigma_{13}\mathbf{e}_3 \\ \mathbf{t}_{e_2} = \sigma_{21}\mathbf{e}_1 + \sigma_{22}\mathbf{e}_2 + \sigma_{23}\mathbf{e}_3 \\ \mathbf{t}_{e_3} = \sigma_{31}\mathbf{e}_1 + \sigma_{32}\mathbf{e}_2 + \sigma_{33}\mathbf{e}_3 \end{cases} \quad (1.16)$$

Which can be written in a simpler form as:

$$\mathbf{t}_{e_i} = \sigma_{ij}\mathbf{e}_j, \quad j = 1, 2, 3 \quad (1.17)$$

where  $\mathbf{e}_j$  denotes the unit vectors defined locally as normal to the faces of the infinitesimal cubic volume shown in Figure 1.10. After introducing the components of the Cauchy stress, we are going to derive the differential equations of motion for any continuum in motion based on the equilibrium of forces for a very small infinitesimal volume of the continuum material undergoing deformations. Newton's law of motion must be satisfied for the small

volume of continuum. The stress vectors that act on the faces of a small volume of the continuum material are shown in Figure 1.10. We also assume that vector  $\mathbf{B}$  is the body force per unit mass through the continuum,  $\rho$  is the mass density at position  $\mathbf{x}_i$  representing the cube, and  $\mathbf{a}$  is the acceleration vector at point  $\mathbf{x}_i$ .

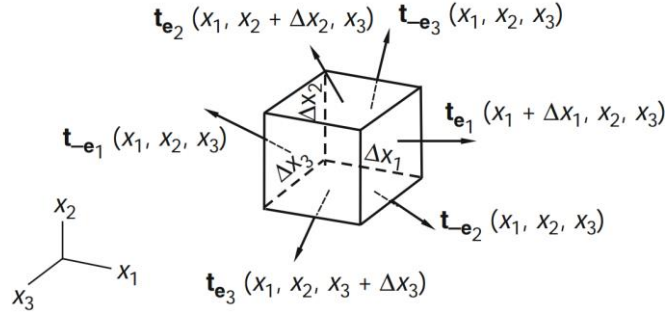


**Figure 1.10:** Components of the Cauchy stress acting on a material when a very small cubic particle within the material has been considered.

Writing Newton's law of motion in Cartesian coordinate systems for the cubic volume and assuming that  $\Delta x_i \rightarrow 0$ , leads to the following equation:

$$\frac{\partial \mathbf{t}_{e_1}}{\partial x_1} + \frac{\partial \mathbf{t}_{e_2}}{\partial x_2} + \frac{\partial \mathbf{t}_{e_3}}{\partial x_3} + \rho \mathbf{B} = \rho \mathbf{a} \quad \text{or} \quad \frac{\partial \mathbf{t}_{e_j}}{\partial x_j} + \rho B_j \mathbf{e}_j = \rho a_j \mathbf{e}_j \quad (1.18)$$

By considering Equation (1.16), the above equation can be written based on the Cauchy stress tensor components as follows [46]:

$$\frac{\partial \sigma_{ij}}{\partial x_j} + \rho B_i = \rho a_i \quad (1.19)$$

The equivalent form of the above Equation in tensor form is:

$$\text{div } \boldsymbol{\sigma} + \rho \mathbf{B} = \rho \mathbf{a} \quad (1.20)$$

Equation (1.20) (or its equivalent form (1.19)) is referred to as the well-known Cauchy's equation of motion which is an essential equation for describing the deformation of a continuum body.

### 1.3.1.4 Linear Elastic Material

To describe the mechanical response of a material due to a given loading and specific boundary conditions, we must utilize five fundamental principles of continuum physics including the principle of conservation of mass, the principle of linear momentum, the principle of moment of momentum, the principle of conservation of energy, and the entropy inequality [46]. All these principles are valid for every continuum undergoing deformation since their derivations do not depend on the mechanical behavior of the material. However, the mentioned principles are not adequate to determine the mechanical response of the material. In addition to the mentioned continuum mechanics principles, we must have sufficient information about the intrinsic mechanical properties of the material such as its stiffness and compressibility as well as its active response to determine its deformation pattern due to a specific loading condition. In continuum mechanics, the intrinsic material mechanical behavior is typically determined through a relation between stresses and strains generated in the continuum body which is known as *constitutive law* [46]. The constitutive law for the simplest material model in continuum mechanics, i.e. a linear elastic material, is given by *Hooke's law* which relates the Cauchy stresses,  $\sigma_{ij}$ , introduced in Equation (1.17) to the infinitesimal strain tensor components,  $\varepsilon_{kl}$ , introduced in Equation (1.13) within the material through a linear equation as follows:

$$\sigma_{ij} = C_{ijkl} \varepsilon_{kl} \quad (1.21)$$

where  $C_{ijkl}$ 's, are components of the fourth-order tensor known as *the elasticity tensor*. This tensor is a matrix with 81 coefficients in general, while it can be demonstrated that based on the continuum mechanics principles and symmetry it can be fully characterized by 21 independent coefficients. For an *isotropic linear elastic material*, Hooke's law reduces to a simpler form as:

$$\sigma_{ij} = \lambda \varepsilon_{kk} \delta_{ij} + 2\mu \varepsilon_{ij} \quad (1.22)$$

where  $\lambda$  and  $\mu$  are *Lame's constants* and  $\delta_{ij}$  is Kronecker delta. The equivalent form of Equation (1.22) in tensor form is [46]:

$$\boldsymbol{\sigma} = \lambda \varepsilon_{kk} \mathbf{I} + 2\mu \boldsymbol{\varepsilon} \quad (1.23)$$

Lame's constants can be written in terms of *Poisson's ratio* and Young's Modulus as follows [46]:

$$\lambda = \frac{\nu E}{(1+\nu)(1-2\nu)}, \quad \mu = \frac{E}{2(1+\nu)} \quad (1.24)$$

Equation (1.23) in addition to the Cauchy's Equation of motion (Equation (1.20)) describe the mechanical response of an isotropic linear elastic material under a specific loading condition.

### 1.3.1.5 Hyperelastic Material

There can be two major types of nonlinearity in a material's mechanical behavior. One is intrinsic nonlinearity which arises from intrinsic mechanical properties of the materials constituents. This leads to a nonlinear characteristic curve between stress and strain within the material. The other source of nonlinearity pertains to the geometric nonlinearity which is defined as the change of material stiff due to change of its geometry. This results in the redistribution of the internal forces within the material which typically occurs when large deformations (strain over 5%) are encountered. The latter is called intrinsic nonlinearity and can be encountered even if the material is linear elastic [48]. Hyperelastic materials are used to idealize materials that involve both type of nonlinearities.

Theoretically, a hyperelastic material is defined based on this postulation that a *Helmholtz free-energy function* such as  $U$  exists which is defined as strain energy per unit volume of the reference geometry of the material. For cases where this energy function solely depends on the deformation gradient tensor ( $\mathbf{F}$ ), other forms of strain tensors, or strain scalar invariants, it is referred to as *the strain energy function* which is typically shown as  $U(\mathbf{F})$ . This strain energy function characterizes the mechanical behavior of the material and its



constitutive law which is derived accordingly. The Cauchy stress tensor (true stress) can be derived based on the strain energy function for a homogenous hyperelastic material as:

$$\boldsymbol{\sigma} = J^{-1} \mathbf{F} \frac{dU(\mathbf{F})}{d\mathbf{F}} \quad (1.25)$$

where  $J$  is the volume ratio which can be obtained based on the deformation gradient tensor as:

$$J = \det(\mathbf{F}) \quad (1.26)$$

For the case of an incompressible hyperelastic material the relation (1.25) takes the following form [46]:

$$\boldsymbol{\sigma} = -p\mathbf{I} + \mathbf{F} \frac{dU(\mathbf{F})}{d\mathbf{F}}, \quad \det(\mathbf{F}) = 1 \quad (1.27)$$

where  $p$  is an indeterminate Lagrange multiplier which can be characterized as a hydrostatic pressure. It is noteworthy that  $p$  can be determined based on the equilibrium equations and boundary conditions defined for the hyperelastic material.

Throughout this thesis, we merely deal with isotropic hyperelastic materials that are modeled in ABAQUS software. Note that LV tissue anisotropy will be modeled following a novel approach which utilizes isotropic hyperelastic materials, leading to a self-contained anisotropy model. For isotropic hyperelastic material, the following constitutive law can be derived based on the strain energy function [46]:

$$\boldsymbol{\sigma} = 2J^{-1} \left[ I_3 \frac{\partial U}{\partial I_3} \mathbf{I} + \left( \frac{\partial U}{\partial I_1} + I_1 \frac{\partial U}{\partial I_2} \right) \mathbf{B} - \frac{\partial U}{\partial I_2} \mathbf{B}^2 \right] \quad (1.28)$$

The above Equation is considered as the basis for deriving various constitutive laws for different hyperelastic models. In the above Equation, the strain energy function is in the form of  $U(I_1, I_2, I_3)$  which depends on first to third scalar invariants, i.e.  $I_1$ ,  $I_2$ , and  $I_3$  defined as:

$$I_1 = \text{tr}(\mathbf{B}) = \lambda_1^2 + \lambda_2^2 + \lambda_3^2 \quad (1.29\text{-a})$$

$$I_2 = \frac{1}{2} \left[ (\text{tr}(\mathbf{B}))^2 - \text{tr}(\mathbf{B}^2) \right] = \lambda_1^2 \lambda_2^2 + \lambda_1^2 \lambda_3^2 + \lambda_2^2 \lambda_3^2 \quad (1.29\text{-b})$$

$$I_3 = \det(\mathbf{B}) = J^2 = \lambda_1^2 \lambda_2^2 \lambda_3^2 \quad (1.29\text{-c})$$

where  $\lambda_1$ ,  $\lambda_2$ , and  $\lambda_3$  are the principle stretches and  $\mathbf{B}$  is the left Cauchy-Green deformation tensor defined as:

$$\mathbf{B} = \mathbf{F}\mathbf{F}^T \quad (1.30)$$

Equation (1.28) can be used for derivation of constitutive law of isotropic hyperelastic materials provided that the strain energy function is known. There are a number of hyperelastic models that are implemented in the ABAQUS software such as Arruda-Boyce, Marlow, Mooney-Rivlin, Neo-Hookean, Ogden, Polynomial, Reduced polynomial, Van der Waals, and Yeoh. Here, we describe strain energy functions of two hyperelastic models which were used more frequently in this project for modeling various parts of cardiac tissue. The first model is Yeoh model which is described using the following strain energy function [47]:

$$U = \sum_{i=1}^3 \left( C_i (I_1 - 3)^i + \frac{1}{D_i} (J - 1)^{2i} \right) \quad (1.31)$$

where  $C_i$ 's are the material hyperelastic parameters, and  $D_i$ 's are the compressibility coefficients. Given the known incompressibility of tissue in the context of this research,  $C_i$ 's are the only parameters that are determined based on stress-strain data which can be achieved through mechanical testing (e.g. uniaxial, biaxial or indentation). The second hyperelastic model that was also used frequently in this research is Ogden model which is described as [47]:

$$U = \sum_{i=1}^N \left( \frac{2\mu_i}{\alpha_i^2} (\lambda_1^{-\alpha_i} + \lambda_2^{-\alpha_i} + \lambda_3^{-\alpha_i} - 3) + \frac{1}{D_i} (J - 1)^{2i} \right) \quad (1.32)$$

where  $\alpha_i$  and  $\mu_i$  are hyperelastic coefficients,  $\lambda_i$ 's are the principal stretches, and  $D_i$ 's are the compressibility coefficients. Once more,  $\alpha_i$  and  $\mu_i$  are the only parameters that are needed to be determined based on stress-strain data.

### 1.3.2 Mechanical Modeling of Cardiac Tissue

Myocardial tissue has a complex mechanical behavior characterized by passive mechanical properties and active response. Passive behavior of cardiac tissue includes two major features: hyperelasticity and anisotropy [49]. It is well-known that the elastic behavior of cardiac tissue is nonlinear. Its intrinsic nonlinearity arises from cardiac tissue microstructural constituents, especially the diverse protein types present in the tissue such as collagen, elastin, actin, myosin, etc. [38]. As cardiac tissue undergoes large strains typically exceeding 20% in a majority portion of the myocardium during contraction, the other source of nonlinearity is geometric nonlinearity [50-51]. As such cardiac tissue behavior can be modelled effectively using hyperelastic models [49]. Another important feature of cardiac tissue is its anisotropy due to its fibrous structure which was described in Section 1.2. As such, anisotropic models must be employed to model cardiac tissue mechanical behavior accurately [49]. For modeling of the passive behavior of cardiac tissue we require mechanical models which are capable of mathematically accounting for both hyperelasticity and anisotropy. The other mechanical aspect of the cardiac tissue which adds to its mechanical complexity, is its active response. Myofibers are the active part of the cardiac tissue that generate cardiac contraction forces by propagation of the action potential through the heart muscle [52]. It is noteworthy that, microscopically, part of the cardiac tissue volume is not active as there is a non-myofiber part which does not contribute to contraction force generation. Throughout this thesis this part will be referred to as background tissue [53-54]. Based on the abovementioned description of cardiac tissue mechanics, models were proposed for simulating its mechanical behavior. One of these models is *Hill's model* which forms the basis of all mechanical models of the LV and heart in the literature [53-54]. This tissue model is shown in Figure 1.11. In this model the myocardial tissue is simulated using two parallel elements (parts): the active element (myofiber) and the passive elastic element (non-myofiber part). The active and elastic elements represent the myofibers while the passive element mimics both the background

myofibers. According to Hill's model, active contractile stress is developed within the active elements. This leads to contraction to both of the active (element connected in series) and passive elements (connected in parallel) since there is a bond between the fibers and background part which prevents slipping along interfaces of the tissue ultrastructural constituents. This contraction creates stresses in both of the fibers and background parts such that mechanical equilibrium is maintained according to the momentum balance principle.

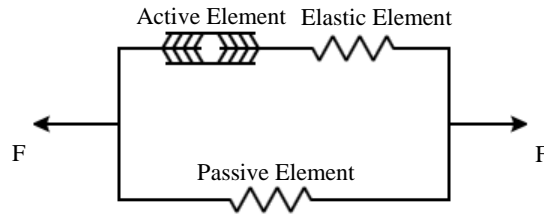


**Figure 1.11:** Hill's model for cardiac tissue mechanical modeling.

The Hill's model provides a realistic description of cardiac tissue which considers both passive and active mechanics aspects of the tissue. As indicated earlier, two types of stress are developed in the tissue: active stress which is generated only in the myofibers and passive stress which is generated in both parts of the tissue. The active stress is controlled by active contraction model parameters such as time, action potential, length of the contractile elements (sarcomeres), etc. as discussed in active contraction models section. The passive stresses are distributed in both parts of the tissue such that mechanical equilibrium is established according to the conservation of linear momentum principle. This conceptual description of the Hill's model leads to the fundamental idea of superimposing passive and active stresses at each cardiac tissue point to derive the governing constitutive law of cardiac tissue. To our knowledge, this is the basis of all mechanical models that are presented in the literature. If the passive part of the Cauchy stress is  $\sigma_p$ , and the active part of the Cauchy stress is  $\sigma_a$ , then the total stress within the cardiac tissue ( $\sigma_t$ ) is [55]:

$$\sigma_t = \sigma_p + \sigma_a \quad (1.33)$$

There are some cases that the total stress is written based on another well-known measure of the stress, the *Second Piola-Kirchhoff* ( $2^{\text{nd}}$  PK) stress tensor which is denoted by  $\mathbf{S}$  throughout this thesis. For these cases Equation (1.33) can be rewritten as [56]:

$$\mathbf{S} = \mathbf{S}_p + \mathbf{S}_a \quad (1.34)$$

where  $\mathbf{S}_p$  and  $\mathbf{S}_a$  denote passive and active  $2^{\text{nd}}$  PK stresses within the cardiac tissue respectively. In Equation (1.33 or 1.34) the passive stress,  $\boldsymbol{\sigma}_p(\mathbf{S}_p)$ , can be calculated based on a strain energy function (typically based on a hyperelastic anisotropic model) which has been considered for the cardiac tissue while the active stress,  $\boldsymbol{\sigma}_a(\mathbf{S}_a)$ , can be derived based on the active contraction models considered for myofibers (sarcomeres). It is noteworthy that the  $2^{\text{nd}}$  PK stress is related to the deformation gradient tensor,  $\mathbf{F}$ , and Cauchy stress,  $\boldsymbol{\sigma}$ , using the following Equation:

$$\mathbf{S} = \mathbf{J}\mathbf{F}^{-1}\boldsymbol{\sigma}\mathbf{F}^{-T} \quad (1.35)$$

### 1.3.2.1 Cardiac Passive Mechanics Models

In this section a commonly used constitutive law for passive modeling of the cardiac tissue will be introduced. As indicated earlier, such model must consider both hyperelasticity and anisotropy of cardiac tissue. The model was presented in [57-58] by J. D. Humphry et al. where the cardiac tissue is considered as a transversely isotropic material with the mechanical properties merely changing in fiber direction. The strain energy function for this model is as follows:

$$U(I_1, \alpha) = c_1(\beta - 1)^2 + c_2(\alpha - 1)^3 + c_3(I_1 - 3) + c_4(I_1 - 3)(\alpha - 1) + c_5(I_1 - 3)^2 \quad (1.36)$$

where  $I_1$  is first scalar strain invariant and  $\alpha$  is defined as follows [57-58]:

$$\alpha^2 = I_4 = \mathbf{N}\mathbf{C}\mathbf{N}^T \quad (1.37)$$

In the above relation  $\mathbf{C}$  is the right Cauchy-Green deformation tensor and  $\mathbf{N}$  is a unit vector coincident with the local muscle fiber direction. In the equation  $I_4$  can be interpreted as *the fourth scalar invariant* which appears in the strain energy functions of anisotropic hyperelastic models. Based on the strain energy function presented in (1.36) and assuming incompressibility for the tissue, the following constitutive law can be derived for Cauchy stress [57-58]:

$$\mathbf{T} = -p\mathbf{I} + 2W_1\mathbf{B} + (W_\alpha / \alpha)\mathbf{FN} \otimes \mathbf{NF}^T \quad (1.38)$$

where  $p$  is a Lagrange multiplier enforcing incompressibility on the myocardial tissue, and  $W_1$  and  $W_\alpha$  are derivatives of the strain energy function given in the following [57-58]:

$$W_1 = \partial W / \partial I_1 \quad (1.39-a)$$

$$W_\alpha = \partial W / \partial \alpha \quad (1.39-b)$$

In Equation (1.38), the mathematical operation  $\otimes$  denotes dyadic product of two vectors. Coefficients  $c_1$  through  $c_3$  in Equation (1.36) are hyperelastic parameters which are determined through a fitting procedure by matching experimental biaxial stress-strain data pertaining to heart specimens [57-58].

### 1.3.3 Active Contraction Models

In this section, three mathematical models of *active contraction of the sarcomeres* are presented [59-60]. These models consider the sarcomere's active stress as a function of peak intercellular calcium ion concentration, time after onset of contraction, sarcomere length history, and sarcomere velocity. If we assume that active stress is generated merely in the fibers direction with the Y-axis representing the sarcomere longitudinal direction, then the active Cauchy stress tensor may be written as follows:

$$\boldsymbol{\sigma}_a = \begin{bmatrix} 0 & 0 & 0 \\ 0 & T & 0 \\ 0 & 0 & 0 \end{bmatrix} \quad (1.40)$$

where  $T$  is the sarcomere active stress which is governed by the following general Equation:

$$T = T_0 C_v \quad (1.41)$$

where  $T_0$  denotes *the isometric active stress* and  $C_v$  is *force-velocity function* which incorporates the effect of the sarcomere velocity into the active stress generation process. Equation (1.41) is the basis for the following three different active stress models:

1) *Deactivation Model*: This is the most complex model of active stress development presented in [59-60]. In this model isometric tension is governed by the following Equation:

$$T_0 = A_c p(0) \frac{f}{f + g(0)} \quad (1.42)$$

where  $A_c$  and  $f$  are constants and  $p(0)$  is the value of the  $p(x)$  at  $x=0$  with  $p(x)$  as the *Hill's hyperbolic function* of force in terms of velocity. It is worth noting that  $x$  is the displacement of an attached cross-bridge and  $x=0$  denotes the point of attachment where the sarcomere contraction begins. A positive value of  $x$  represents sarcomere shortening.  $p(x)$  is also described mathematically as follows:

$$p(x) = p_0 (e^{-\lambda(x-x_l)} - 1) \quad (1.43)$$

In the above Equation  $p_0$ ,  $\lambda$ , and  $x_l$  are constants.  $g(0)$  in Equation (1.42) is the value of  $g(x)$ , which is a *piecewise cross-bridge detachment function*, at  $x=0$ .  $g(x)$  is also given as:

$$g(x) = \begin{cases} \infty & \text{when } x < D_L, \\ g_L & \text{when } D_L \leq x < 0, \\ g_0 & \text{when } 0 \leq x < x_l, \\ g_s & \text{when } x_l \leq x < D_s, \\ \infty & \text{when } D_s < x, \end{cases} \quad (1.44)$$

where  $D_L$  and  $D_s$  are constants. This function enforces that the detachment rate of the cross-bridge is constant and finite between a yield point in lengthening,  $D_L$ , and a working stroke for shortening,  $D_s$ , otherwise it is infinite. It is consistent with the physiology of the cross-bridge formation within a sarcomere during its contraction. The force-velocity function,  $C_v$ , during shortening of the sarcomere is given by the following Equation:

$$C_v = \frac{(f + g_0) \left[ \frac{1}{g_0} + \frac{1}{g_0 + \lambda v} e^{\lambda x_l} + \frac{(g_0^2 - g_s^2) \lambda v + (g_s - g_0) \lambda^2 v^2}{g_0 g_s (g_0 + \lambda v) (g_s + \lambda v)} e^{-\frac{g_0}{v} x_l} \right]}{(e^{\lambda x_l} - 1) \left\{ 1 + f \left[ \frac{1}{g_0} - \frac{g_s - g_0}{g_0 g_s} e^{-\frac{g_0}{v} x_l} - \frac{1}{g_s} e^{-\frac{1}{v} [g_0 x_l + g_s (D_s - x_l)]} \right] \right\}} + \frac{(f + g_0) \left[ \frac{1}{g_s} e^{-\frac{1}{v} [g_0 x_l + g_s (D_s - x_l)]} - \frac{1}{g_s + \lambda v} e^{-\left[ \lambda (D_s - x_l) + \frac{1}{v} [g_0 x_l + g_s (D_s - x_l)] \right]} \right]}{(e^{\lambda x_l} - 1) \left\{ 1 + f \left[ \frac{1}{g_0} - \frac{g_s - g_0}{g_0 g_s} e^{-\frac{g_0}{v} x_l} - \frac{1}{g_s} e^{-\frac{1}{v} [g_0 x_l + g_s (D_s - x_l)]} \right] \right\}} \quad (1.45)$$

During lengthening of the sarcomeres,  $C_v$  is given by the following Equation:

$$C_v = \frac{(f + g_L) \left\{ \frac{g_L}{\lambda} \left[ e^{\lambda x_l} (1 - e^{-(\lambda + \frac{g_L}{v}) D_L}) + 1 - e^{-\frac{g_L}{v} D_L} \right] - v \left( 1 - e^{-\frac{g_L}{v} D_L} \right) \right\}}{(e^{\lambda x_l} - 1) \left[ g_L + f (1 - e^{-\frac{g_L}{v} D_L}) \right] \left( \frac{g_L}{\lambda} + v \right)} \quad (1.46)$$

In Equations (1.45) and (1.46), there are several parameters which are related to the active model of the sarcomeres. More details of these parameters, their values and their physical interpretation are provided in [59-60]. We just focus on important parameter  $v$  which is the sarcomere velocity during its contraction. In fact Equations (1.45) and (1.46) only describe the dependence of active force generation on sarcomere velocity.

- 2) *Hill Model*: In the Hill model,  $C_v$  is given by Equations (1.45) and (1.46) but it is described based on a phenomenological model instead of a structural model. In fact the Hill model takes into account the effect of sarcomere length on the duration of the



isometric twitch. This model is a function of internal variable  $C_t$  which is a function of time after onset of contraction  $t$ , and sarcomere length  $l$ . The following equation was derived based on Hill assumptions of the sarcomere contraction:

$$T_0 = T_{\max} \frac{Ca_0^2}{Ca_0^2 + ECa_{50}^2} C_t \quad (1.47)$$

where  $T_{\max}$  is the isometric tension at the longest sarcomere length and  $Ca_0$  denotes the intercellular calcium concentration.  $ECa_{50}$  is also a length-dependent calcium sensitivity function which is given by:

$$ECa_{50} = \frac{(Ca_0)_{\max}}{\sqrt{\exp[B(l-l_0)]-1}} \quad (1.48)$$

In the above equation  $B$  is a constant and  $l_0$  is the sarcomere length at which no active tension develops. Internal variable  $C_t$  in Equation (1.47) is governed by:

$$C_t = \frac{1}{2}(1 - \cos \omega) \quad (1.49)$$

where  $\omega$  is a time dependent variable which shows the dependence of active stress to time and it is governed by the following equation:

$$\omega = \begin{cases} \pi \frac{t}{t_0} & \text{when } 0 \leq t < t_0 \\ \pi \frac{t-t_0+t_r}{t_r} & \text{when } t_0 \leq t < t_0+t_r \\ 0 & \text{when } t_0+t_r \leq t \end{cases} \quad (1.50)$$

where  $t_0$  and  $t_r$  are time-to-peak tension which denote a constant and duration of relaxation, respectively. Duration of relaxation is a linear function of sarcomere length,  $l$ , as follows:

$$t_r = ml + b \quad (1.51)$$

where  $m$  and  $b$  are constants. The sarcomere length can also be described as a function of strain in the sarcomere longitudinal (fiber) direction,  $E_{11}$ , and the stress-free sarcomere length (reference sarcomere length),  $l_R$ , as follows:

$$l = l_R \sqrt{2E_{11} + 1} \quad (1.52)$$

- 3) *Elastance Model*: In this model, which is a simpler model of sarcomere contraction, the dependence of the contraction with respect to the sarcomere velocity is removed by setting  $C_v$ , force-velocity function, to unity [59-60]. The main Equation which describes active stress generation within the sarcomere is given by Equation (1.47) similar to the Hill model. This model has been used for mechanical modeling of the heart and LV more frequently than the other models and it has demonstrated its effectiveness for such simulations [61-62]. As such, we used it for modeling active contraction of the sarcomeres (myofibers) in our LV mechanical model development.

## 1.4 Literature Review

### 1.4.1 Cardiac Tissue Passive Mechanical Properties

Computational models of cardiac mechanics and electrophysiology are regarded as effective techniques for simulating the contractile behavior of the heart. This computational simulation is beneficial for understanding underlying mechanisms of the heart's function and its related pathological conditions. These biophysical-based models may be employed by clinicians as effective tools for planning successful patient-specific therapies [63-65]. One of the essential inputs of cardiac mechanics computational models is the intrinsic passive cardiac tissue mechanical properties. As such, accurate quantification of these properties is highly important for achieving simulation realism. A traditional approach for measuring cardiac tissue mechanical properties uses mechanical testing to acquire stress-strain data necessary for fitting tissue constitutive models with varying complexities ranging from isotropic and linear elastic to anisotropic and hyperelastic. Another approach develops constitutive models based on cardiac tissue microstructure. Overall response of the heart calculated using computational cardiac mechanics models may enable gaining insight into the cardiac tissue microstructure and constituents using an inverse problem

framework. For example abnormally small LV deformation at diastole may indicate tissue stiffening resulting from pathological changes of the tissue ultrastructure. In addition to being effective in modeling various tissue related pathologies, the latter approach of developing a cardiac tissue constitutive model is suitable for modeling cardiac tissue treated using tissue engineering methods as the cardiac tissue microstructure may undergo extensive alterations in both cases [66-70].

In the context of myocardial infarction, the necrotic myocytes are cleared from the injured area within hours before being replaced by newly synthesized ECM which serves as a scaffold for deposition of new collagen fibers. ECM and collagen fibers generation ensue until the termination of the cardiac fibrotic phase when a heavily collagenous scar remains in the healed infarcted zone [71-72]. Another example of cardiac tissue microstructural changes occurs in dilated cardiomyopathy. In this case, the healthy ventricular myofibers stretch to contract more vigorously and compensate for the non-contractile injured part within the myocardium. When the cardiac scar is chronic and extensive, abnormal myofibers' extension is prolonged, resulting in a dilated thin-walled flabby ventricles with new composition of tissue constituents which cannot pump the blood effectively [73]. Cardiac arrhythmias are also caused by pathological changes in tissue microstructure such as depressed coupling in gap junctions, myocardial fibrosis in cardiac injuries, and excessive amounts of ECM constituents especially collagen fibers amongst the bundles of the heart's electrical conduction system [74]. These examples reveal that the overall intrinsic mechanical properties of the tissue is strongly dependent on the tissue microstructure, more specifically its constituents and their arrangements within the tissue [75-78]. Accordingly several studies investigated the influences of tissue microstructure and constituents on the macroscopic mechanical behavior of the tissue through developing tissue mechanics models based on its microstructure. These models are classified under three main categories: phenomenological, continuum, and structural tissue models [79]. In the phenomenological approach, the mechanical behavior of the tissue is delineated by a strain energy based constitutive equation. In this approach the stress-strain curves obtained from measurements are fitted to a constitutive equation to quantify unknown coefficients involved in the equation [80-82]. Phenomenological strategies are used extensively for characterization of the tissue passive behavior. However, a major limitation with them is

that the outcome of the fitting procedure is merely valid for the tissue specimens that were used in mechanical testing. Another drawback with methods derived from this approach is that they are not adaptable to account for tissue inhomogeneity, especially for cases with complex microstructural compositions [83-86]. Another approach employs continuum methods for tissue characterization which accounts for the tissue's complex microstructure. This approach takes into account all tissue microstructural elements, including solid and liquid phases, ions, cells, etc. to obtain the macroscopic response of the tissue [87-88]. A limitation with this approach is that its theoretical and mathematical complexities may hinder application of their derived methods for tissue mechanics identification, especially when dealing with highly complex microstructure [79,89]. It is noteworthy that even these limitations, the approach is often used to derive accurate tissue mechanics model based on microstructure. The structural approach is another alternative for tissue mechanics characterization. This approach is based on the premise that the overall mechanical response of tissue is the result of the sum of mechanical responses of its microstructural constituents. Based on this assumption, tissue constituents and their individual responses are incorporated into the tissue mechanical model to derive a macroscopic constitutive law for the tissue [79,89]. A problem with such methods derived based on this strategy is that constitutive formulations developed using them require cost-effective superposition algorithms to integrate their tissue constituents' responses for obtaining the overall tissue macroscopic response. Nevertheless, these approaches are of interest within the research community due to their relatively simple mathematical description compared to the continuum approaches [79,89].

The structural approach has been widely used to derive mechanical models for various types of tissues with different mechanical characteristics and compositions. Anisotropic properties of tissues have been studied in [90-91] based on their microstructure. A structural constitutive law was presented in [90-91] that considers angular distribution of collagen fibers within the tissue. This structural constitutive law was utilized to simulate biaxial mechanical responses of the arterial walls and aortic valve which both contain dense collagen fibers in their structure. In some research studies [79,89], finite element method (FEM) was employed to develop a computational model for simulating tissue microscopic structure such as a fine network of collagen fibers. In [79,89] the tissue volume was divided

into a number of finite elements. A fine microscopic collagen fiber network was considered in each element of the tissue model, leading to a 3D structure of collagen gel consisting of type I collagen which was simulated using this approach. By applying an appropriate mechanical loading and boundary conditions to the constructed 3D structure, macroscopic deformation of the collagen network was calculated. The approaches presented in [79,89] provide evidence that the FE technique is able to effectively integrate micro-responses of individual tissue constituents. Cardiac tissue microstructural mechanics have been also studied using structural approaches. Changes in mechanical properties of the right ventricular (RV) tissue due to hypertension was investigated in [92] where a biomechanical model, including two tissue constituents: myofibers and collagen fibers, was developed to obtain a constitutive law for the ventricular tissue. Parameters of the model were determined by fitting stress-strain data obtained from biaxial mechanical tests pertaining to ventricular tissue specimens to the derived constitutive law. In [92], it was concluded that the constitutive law in conjunction with the calculated parameters indicate presence of stiffer myofibers in the ventricular tissue as well as longitudinal reorientation of the myofibers and collagen fibers due to hypertension. Alterations of the RV tissue mechanical properties due to decellularization was also investigated in [93]. Numerous biaxial mechanical tests were conducted on several RV tissue specimens in [93]. It was inferred that neither anisotropy nor heterogeneity were altered due to decellularization of the RV tissue samples. In another research study [94], biaxial mechanical properties of various specimens of the murine RV were investigated by developing a novel anisotropic structural constitutive law. Extensive structural morphological analysis on the myofibers and collagen networks were also conducted using light microscopy. The study concluded that overall tissue mechanical properties show strong correlation with the orientations of myofibers and collagen fibers in the tissue which were measured by morphological studies. In chapter 2, we present a novel hyperelastic and anisotropic constitutive model of normal and pathological cardiac tissue. This model was developed based on the microstructural constituents of the cardiac tissue and their mechanical properties. The microscopic constituent's composition and mechanical properties are incorporated directly into the presented tissue model to estimate overall macroscopic tissue passive response. Our method takes all major constituents of the cardiac tissue into consideration, while some

recent studies have incorporated only limited numbers of major tissue constituents, i.e. myofibers and collagen fibers [92]. In our strategy, as many tissue constituents as required can be incorporated into the overall tissue model without affecting the computational complexities and efficiency of our algorithm. This competence makes it feasible to achieve very accurate tissue models with numerous microstructural constituents. Our approach can also be effectively used for modeling pathological cardiac tissue. It is well-known that various cardiac pathologies are often associated with substantial alterations in the tissue's composition and their related mechanical properties. These changes can be easily incorporated in our model with the abovementioned adaptability feature to derive structurally-based constitutive laws. Such pathological tissue mechanical properties are of great importance to conduct mechanical simulations of pathological myocardium since they are utilized as the major inputs for such simulations.

#### 1.4.2 Left Ventricle Mechanical Modeling

Simulation of cardiac contraction and motion under normal as well as diverse pathophysiological conditions has attracted clinicians' and cardiologists' attentions over the past few decades. Recent technological and scientific advances in various fields (e.g. computer graphics, cardiac medical imaging, high-speed computer processors, computerized image processing algorithms, and cardiac microstructural mechanics) have enabled medical engineers and physicists to design realistic mechanical and electrophysiological models of the myocardium. These models can provide clinicians and scientists invaluable insight into the physiology of the heart such as heart's electromechanics, blood pressure and cardiac tissue interactions, propagation of the electrical stimuli through the myocardium, development of active contraction forces in the myofibers, blood flow and perfusion mechanism through the myocardium etc. [25-27,95]. In this section, we focus on biomechanical-based models of the myocardium. Apart from their importance in understanding the heart's function as a mechanical pump which pumps out the blood through all organs in the body, these models can be utilized to simulate various cardiac pathological conditions to understand their complications from mechanics perspective. The heart's mechanical performance is affected by cardiac pathological condition. Resulting alterations can be quantified in terms of different mechanical

measures such as displacement, normal and shear strains and stresses, cardiac stroke volume, etc. The most prevalent cardiac disease is cardiac ischemia which typically happens by occlusion of the blood vessels within the heart muscle due to various adverse phenomena such as atherosclerosis and thrombosis leading to cardiac ischemic scars with shortage of blood flow and oxygen in some portions of the myocardium. This can lead to myocardial infarction (MI) in severe continual ischemic cases. MI pathology results in mechanical alterations of infarct regions. For instance, infarct areas do not show considerable active mechanical response and thus have fragile contractile power [96-98]. Infarct regions also have substantially higher stiffness due to myocardial fibrosis which typically occurs by deposition of stiffer myofibers and collagen fibers. Stiff collagenous scars undergo much higher mechanical stresses during contraction of the myocardium which are typically followed by abnormal tensile strains [96-97]. The situation can be even aggravated by cardiac remodeling and eventually heart failure as the worst scenario [96-97]. Mechanical simulations have been used extensively to simulate the abovementioned mechanical alterations due to cardiac ischemia and MI [16,99-100]. For instance, myocardial infarction mechanics at its early stages in a canine left ventricle (LV) was studied in [99]. Early infarction was modeled by depressing the contractility within the ischemic region of the LV FE model. It was observed that LV geometrical variations are proportional to the extent and acuteness of ischemia [99]. It was also inferred that the ejection fraction (EF) and stroke volume of the LV model decreases considerably as a result of the ischemia. Dilated cardiomyopathy is another example of cardiac disease which is accompanied by alterations of the heart's mechanical function. During this disease, ventricular walls become thinner with considerable stretching during myocardial contraction. Over time, cardiac mass and volume increase due to these biophysical changes. The major mechanical complication of dilated cardiomyopathy emerges with reduction of the myocardial systolic strains in all three directions: circumferential, radial, and longitudinal [101-102]. Another instance is prolonged hypertension which imposes extra mechanical loads to the myocardium, making the ventricular walls thicker known as ventricular hypertrophy. These pathological changes lead to remarkable increase in the systolic wall stresses whereas myofibers' shortening decreases [103]. All the abovementioned samples exemplify alterations in cardiac mechanical measures due to

specific pathological condition. Hence, accurate quantifications of these alterations in mechanical responses (stress, strain, displacement, ejection fraction, etc.) can be exploited in the clinic as effective diagnostic data pertaining to cardiac pathologies. These mechanical measures can be quantified as outputs of mechanical models of pathological myocardium, reflecting their clinical relevance for diagnostic purposes.

Another major advantage of myocardial mechanical models is that they can be utilized for new therapy planning to combat various cardiac diseases. This can be achieved by modeling alterations (e.g. using cardiac tissue graft) using cardiac mechanical simulation framework to test the relevant therapeutic strategy through assessing pathology treatment outcome obtained from the model. Ischemic cardiomyopathy is a heart condition that is gradually aggravated by ventricular remodeling which is often followed by heart failure. The Dor procedure is a novel surgical treatment method for size, shape, and wall stress restoration of the ventricles which involves planting a circular patch plasty within the ventricular walls exactly where the MI has occurred. The mechanical outcomes of the Dor procedure for a male sheep's infarcted LV were studied using the LV mechanical modeling of replacing the infarct region with patch plasty [104]. Simulation results of the study confirmed the effectiveness of this procedure similar to what was observed in the animal model experiment. Another therapeutic approach to prevent cardiac remodeling involves injecting biocompatible hydrogels in the LV wall where the MI occurred. The mechanical outcomes of this procedure was investigated in a number of research works by mechanical modeling of the infarcted LV [105-106]. These studies concluded that the average wall stresses in both infarcted and remote healthy regions were reduced by the injection of hydrogels, confirming the procedure's effectiveness to size, shape, and wall stress restoration of the infarcted LV.

The main and probably most recent application of cardiac mechanical models pertains to patient-specific clinical diagnosis and therapy planning. Such models can be personalized and along with other diagnostic tools (e.g. cardiac medical imaging, electrocardiography (ECG), blood works) may help provide valuable data to diagnose heart diseases, adopt appropriate therapies, and even optimize the outcome of these therapies by using the models to adjust their parameters [64,107-108]. To this end, personalized cardiac



mechanics models can be developed based on data obtained from imaging techniques to simulate normal and pathological heart's contractile and passive functions more realistically [61-62,109-114]. Cardiac imaging techniques are utilized within two major strategic frameworks. In one framework, cardiac imaging techniques such as ultrasound or MR along with advanced image processing algorithms are utilized to obtain some image-based features pertaining to myocardial function parameters. These features include myocardial wall motion and deformation, size, mass, geometry, and cardiac output evaluators such as stroke volume and EF. Acquired with predetermined diagnosis for a significantly large patient cohort, these features can be processed using machine learning algorithms to determine a set of threshold values which can be used to guide diagnosis in patients not included in the cohort [109-112]. The other framework benefits from available underlying science which relates image data to various pathologies quantitatively. In this framework, mechanical modeling of the myocardium is utilized in conjunction with inverse FE algorithm to attain accurate diagnosis [61-62,113-114]. For instance, in [61-62] an inverse problem algorithm was developed which uses an FE based mechanical model of infarcted LV as its forward model. The algorithm adjusts the active response of healthy and border zone tissues in the FE model systematically until the volume and strains obtained by the LV FE model is in agreement with those obtained from corresponding MR image analysis. Similar to [61-62], in [113-114] the active response of cardiac tissue was varied using a similar inverse FE framework where a non-homogeneous high resolution distribution of tissue active response was adjusted systematically to achieve better matching with the measurements obtained from imaging data. It is noteworthy that a major requirement of all inversion-based FE algorithms is a patient-specific forward cardiac mechanical model which is run iteratively to solve an optimization problem where regional cardiac passive and active mechanical characteristics are adjusted such that a realistic agreement is achieved between parameters obtained from cardiac mechanics model and imaging counterpart. Evidently, the forward cardiac mechanics model must provide sufficient realism, be computationally efficient and easily adaptable to various cardiac conditions.

Over the past decade, different mechanical models of the myocardium have been introduced to simulate both passive and active aspects of cardiac mechanics. Simpler

models have considered tissue linearity and isotropy to develop cardiac mechanics models [115-117]. Recently, more realistic models have been developed where hyperelasticity and anisotropy, leading to nonlinear FE with higher degree of realism [118-120]. In these models, a single strain energy based constitutive law is often assumed for the entire myocardium to build the passive properties including anisotropy and hyperelasticity into the model [83,86,121-122]. The constitutive law is typically achieved by fitting the mathematical form corresponding to the hyperelastic and isotropic model to available biaxial / uniaxial test data pertaining to cardiac tissue specimens [57-58]. Considering a single constitutive law for the entire myocardium is problematic since the myocardial tissue has a complex microstructure with different tissue constituents as indicated in Section 1.2 of this chapter [38]. Furthermore, different cardiac pathologies may alter the type and composition of the tissue constituents which may lead to substantial changes in the overall tissue passive mechanical properties [71-72,123]. As such, different constitutive laws were considered for pathological parts of the myocardium in more recent studies. For instance, different constitutive laws were assigned to areas with cardiac ischemia within the left ventricle model in [61-62]. Furthermore, with ischemic and MI scars within the myocardial walls, new developed biomaterials are typically used to substitute the pathological region [104-106]. Such biomaterials typically have different mechanical properties, hence their simulation using FE models requires assigning different parameters. Another major issue with FE-based cardiac mechanics models is that they often require complex non-linear FE algorithms which can be implemented by custom-developed FE computer codes [61-62, 121-122]. In addition to not being available to the research and end-users communities, such codes are usually not optimized for computational efficiency and are likely to encounter numerical instability. Recently, endeavors have been made to implement realistic cardiac mechanics models in both diastole and systole using available off-the-shelf FE software packages [124-125]. While valuable, these models require user-defined subroutines which may again suffer from similar issues. To tackle these issues, in Chapter 3 of this thesis, we propose a novel LV mechanics model which takes into account cardiac anisotropy, hyperelasticity, and active fiber's contraction forces. An important feature of the proposed model is that while it can be implemented using available libraries of commercial FEM software packages, it is adaptive as it can simulate both normal and

pathological LV's contraction scenarios. The novel aspect of the model lies in the approach of modelling the myofibers and their contraction forces. This model treats the myocardial tissue as a composite material, including a background tissue through which microscopic reinforcement bars are distributed to undergo variable contraction forces. These bars simulate the fibers within the myocardial tissue whereas their orientations are in accordance with the fibrous cardiac anatomy, leading to a self-contained anisotropic model. Both of the background tissue and myofibers are also considered as hyperelastic materials. As a result of applying contraction forces to the bars while blood pressure is applied to the LV endocardial surface, LV contraction occurs. This model can be developed and solved using many off-the-shelf FE software packages. It does not require highly sophisticated custom-developed computer codes while it incorporates all necessary mechanical complexities of the myocardial tissue. Moreover, it is anticipated that the proposed model is more computationally efficient and less prone to divergence and instability issues compared to custom-developed FE codes as commercial FE solvers are usually optimized to achieve high computational performance for diverse applications. The qualities of the proposed model cast it as a desirable forward model within inverse problem frameworks where the model is run iteratively. In Chapter 3, this model has been utilized to simulate normal LV mechanical behavior. To prove the capacity of our model for pathological LV modeling, in Chapter 4 it was applied to infarcted LV geometry. In the infarcted LV model, three different regions including healthy region, infarcted region, and border zone consistent with the pathology of the MI were considered while different passive mechanical properties and active responses were assigned to each region. The performance of both normal and infarcted LV models were compared with the *in vivo* and *ex-vivo* measurements and other validated mechanical models of the LV.

### 1.4.3 Diastolic Heart Mechanics

A complete cardiac cycle includes two major phases of passive diastolic phase followed by active-passive systolic phase. These two cycles are different from the cardiac mechanical behavior perspective. In diastole the myocardium is enlarged while its ventricular cavities are filled with blood. In contrast, the systolic phase involves strong contraction of the myocardium resulting from the superposition of contraction of individual

myocytes organized through the volume of the heart muscle. For comprehensive understanding of various heart diseases, it is essential to develop understanding of underlying mechanics of each of these phases as some cardiac pathological conditions are known to alter the mechanical characteristics of one phase only [126-128]. These phase-dependent mechanical changes can be quantified using patient-specific cardiac mechanics model framework which can be used to determine the underlying mechanical causes of observed symptoms pertaining to the pathological condition [126-128]. Heart failure, which is a common cardiac disease with high mortality rate, is a good instance of such condition which can be caused by both systolic and diastolic dysfunctions. Heart failure occurs in ~2% of adults while it is even more common in people older than 65 years where the incidence rate is 6–10% [129-130]. Mortal heart failures are often caused by systolic dysfunctions where the heart cannot pump enough blood to appropriately nourish all organs in the body [7,131]. Surprisingly, more than 50% of heart failures occur when diastolic dysfunctions are observed without any symptoms of systolic dysfunctions [7,131]. In such cases abnormal LV relaxation, filling, or diastolic stiffness typically lead to diastolic heart failure where the LV diastolic capacity is suppressed. The latter is typically followed by subsequent LV EF reduction in the systolic phase under prolonged chronic conditions [128,132]. Diastolic stiffness can be considered as an essential mechanism among the abovementioned diastolic abnormalities. This mechanism can be effectively quantified by patient-specific inversion-based FE cardiac mechanics algorithms. The diastolic LV deformation data acquired using imaging technique can be processed within such inverse problem algorithms to determine the cardiac tissue stiffness such that the best tissue deformation match is attained between the patient-specific cardiac mechanics simulation and corresponding imaging based measurement. A computationally efficient forward cardiac mechanics model is essential as the core of such inversion-based algorithms as it must be run iteratively to determine blood pressure and cardiac tissue stiffness parameters. In Chapters 3 and 4, a forward cardiac mechanics model was presented. This model is anticipated to be computationally efficient and straight forward to be developed and utilized as it is implementable using off-the-shelf FE solvers. These features render the presented model appropriate for inversion-based strategies such as diastolic cardiac tissue stiffness estimations. In Chapter 5 the performance of the model presented in Chapters 3

and 4 was investigated to simulate the diastolic phase of cardiac cycle. In this chapter, MR image-based LV geometry of a healthy human volunteer was utilized to construct a subject-specific cardiac mechanics model. The model was used to estimate the end-diastolic blood pressure and cardiac tissue stiffness properties using an ad-hoc optimization framework.

## 1.5 Objectives

The overarching objective of the research presented in this thesis is to develop and validate a novel LV mechanics model which can be effectively used within inverse FE frameworks aimed at improved cardiac disease and therapy. This was broken down into a number of objectives. The first objective is to develop a novel mechanical model of the cardiac tissue. Details of this model are presented in Chapter 2. The main feature of this tissue mechanical model is that it is built based on cardiac tissue microstructural constituents and their volume contribution in the cardiac tissue. These constituents and their associated mechanical properties are incorporated into FE model of small cardiac tissue samples. This approach was used for modelling intrinsic properties of both normal and pathological (infarcted) cardiac tissues. Uniaxial and biaxial mechanical test simulations were performed on those cardiac tissue sample models to generate their characteristic stress-strain data which describe their passive mechanical properties. These data was fitted to known hyperelastic models to obtain corresponding coefficients. To validate the proposed technique, data obtained from this study was compared with corresponding data acquired from mechanical testing of normal and infarcted cardiac tissues.

Another objective of our research is development of a novel FE-based mechanical model of the LV which is presented in Chapter 3. This model has two main features: 1) it is implementable using an off-the-shelf FE software package and 2) it is computationally efficient since it does not require custom-developed computer codes, and is optimally implemented using efficient and well-tested algorithms. The latter feature is quite important as it renders the presented LV model suitable for FE inversion-based algorithms in which the LV mechanical model must be run iteratively. A novel aspect of our LV model, which made its implementation using off-the-shelf FE software package possible, is that it is implemented using a composite model of the cardiac tissue which considers two main tissue parts of myofibers and background tissue. The model in Chapter 3 was applied

to an *in silico* geometry of a canine LV and systolic and diastolic responses of the model were compared with other LV mechanical models and with LV contraction measurements available in the literature.

The LV mechanics model presented in Chapter 3 has another important feature. It is easily adaptable with various cardiac pathological conditions due to the novel composite material model used in the FE model development. This cardiac tissue decomposition make it feasible to assign different passive and active mechanical properties to each part of the tissue, i.e. background tissue and myofibers, in accordance with the specific cardiac disease considered in the simulation. This capability of our model was tested in Chapter 4 by applying the model to an *in silico* geometry of an infarcted LV. For validation, the results of the FE simulations of the infarcted LV model including stress and strain distributions were compared to measured data pertaining to infarcted LV as well as to other validated LV mechanical simulations.

In chapter 5, the performance of the LV forward mechanical model presented in Chapters 3 and 4 was investigated towards implementation of a simplified inversion-based FE algorithm solved by an ad-hoc optimization procedure. As such, the model presented in Chapters 3 and 4 was applied to an LV geometry obtained from start-diastolic human MR image data to simulate diastolic inflation of the LV. Next, the diastolic cardiac stiffness properties and blood pressure were adjusted within an ad-hoc optimization framework. The target of this optimization framework was to minimize the difference between the calculated LV geometry (determined using the LV diastolic mechanical simulation displacements output) and the measured geometry obtained from segmenting the corresponding MR image. The results of this ad-hoc optimization were cardiac tissue stiffness properties and blood pressure which were within the normal range of human LV according to measurements of the LV diastolic function, lending credit to the reliability of the proposed model towards inversion-based algorithms' implementations.

## 1.6 Thesis Outline

Based on the thesis objectives described above, we organized our thesis within five chapters which will be discussed in more details as follows:

### 1.6.1 Chapter 2

In Chapter 2 a novel approach for mechanical modeling of cardiac tissue using FE approach is presented. This model considers all major myocardial tissue constituents which are distributed consistent with the cardiac tissue microstructure, anatomy and quantity throughout FE models of tissue samples. The mechanical properties of each cardiac tissue constituent was input to the FE model based on data pertaining to the constituent's mechanical measurements. In this study, two important features are noteworthy. One is that the tissue sample FE models were constructed such that the fibrous structure of the cardiac tissue is preserved. As such the fibers were modeled as continuous bars to mimic the tissue anisotropy. The second is that for all tissue constituents, hyperelastic models were considered to in order to model cardiac tissue large deformations expected during the heartbeat with high degree of realism. To demonstrate the capability of the proposed approach for modeling normal cardiac tissue, strains up to 40% were applied to cylindrical and sheet FE samples of the cardiac tissue to simulate uniaxial and biaxial mechanical tests while corresponding stress-strain data of the tissue samples were generated. The resultant stress-strain data were then compared to those obtained from biaxial and uniaxial testing of cardiac tissue which confirmed accuracy of the presented approach. The cardiac tissue model was also utilized for simulating intrinsic mechanical behavior of pathological cardiac tissue. For this purpose infarcted cardiac tissue was chosen. Volume percentage and type of the cardiac tissue constituents were altered consistent with a realistic infarcted cardiac tissue. Biaxial and uniaxial mechanical testing was simulated on the infarcted tissue sample models similar to the normal cardiac tissue. Finally, the resultant stress-strain data generated by the simulations were validated by comparing them corresponding data obtained from actual mechanical testing of infected cardiac tissue.

### 1.6.2 Chapter 3

Chapter 3 introduces a new mechanical model of the LV. In this model, a composite material model consistent with its anisotropy was developed for the cardiac tissue. This composite model has two major parts: background tissue and rebars (myofibers). The active stress was generated in the myofibers based on the elastance model while the background tissue is passive. This tissue decomposition is realistic and consistent with the

cardiac tissue physiology. Moreover, it is also consistent with well-known cardiac tissue models such as Hill's model. In this model, the myofibers are distributed through the tissue volume such that it is consistent with the fibrous structure of the LV. Hyperelastic passive mechanical properties are considered for both tissue parts: myofibers and background tissue to account for large deformation of the LV model under physiological conditions. This model was implemented using a commercial FE software package and does not require any additional custom-developed nonlinear FE codes or subroutines. As such, it can be widely available to the research community for use in biomedical applications and further development. The model was applied to normal healthy LV *in silico*. The FE model output, including diastolic and systolic stress and strain distributions through the LV geometry and passive LV diastolic pressure-volume curve, were compared with corresponding data obtained from experimental measurements and other validated LV mechanical models, confirming validity of the proposed approach.

### 1.6.3 Chapter 4

In Chapter 4, the LV mechanical model introduced in Chapter 3 is applied for pathological LV modeling. As described in Section 1.4.2 of this chapter, mechanical modeling of pathological myocardium is quite important to understand the mechanical characteristics pertaining to cardiac diseases or to devise patient-specific therapeutic and diagnostic tools. To demonstrate effectiveness of our approach for modeling cardiac pathologies, it was applied for simulating transmural infarction at the mid-ventricular area. Again, the composite material model described in the previous section was used to model the cardiac tissue. For the pathological (infarct) region, the mechanical properties of the background tissue and reinforcement rebars (myofibers) were altered consistent with known cardiac infarction microstructure alteration. It is noteworthy that the fibers orientation within the infarcted region was also adjusted in the model according to the MI pathology. We considered no active contraction within the infarcted region assuming that viable and active myocytes are not present. Consistent with the MI pathology, a border zone region with depressed contractile function was considered surrounding the infarct region. The active and passive properties of the healthy cardiac tissue was kept the same as those used with the normal LV model presented in Chapter 3. The performance of the proposed FE model



in this context was assessed by comparing stress and strain distributions through the infarct and healthy regions obtained from the model with those of experimental measurements and other relevant computational LV models presented in the literature. These comparisons demonstrated very good agreement, consolidating the proposed approach validity. It is noteworthy that there is some overlap between materials presented in Chapters 3 and 4. The reader can skip reading sections 4.2.1, the first part of 4.2.2, 4.2.3, and 4.2.4 without major disruption in this chapter's comprehension.

#### 1.6.4 Chapter 5

An important feature of the FE LV mechanical model presented in Chapters 3 and 4 is that it is easy to develop while it is anticipated to be computationally efficient and less prone to divergence since it is fully implementable using commercial FE solvers. These important characteristics make this model attractive for inversion-based strategies. To test this model for inverse problem applications within a preliminary simplified framework, the model was applied for estimation of the cardiac tissue passive stiffness mechanical properties as well as diastolic LV blood pressure. To this end, the model was applied to simulate diastolic inflation of the human LV. The start-diastolic LV geometry was obtained from MR image data segmentation of a healthy human volunteer. The LV geometry was discretized using FE meshing software, while similar to Chapters 3 and 4 a composite tissue model was considered for mechanical modeling of the LV muscle tissue. Next, the blood pressure was applied to the LV endocardial surface to dilate the LV model while no significant contraction was considered for the myofibers as the LV was in its passive diastolic phase. To initiate the diastolic LV mechanical simulation within the inversion framework, initial values of LV muscle tissue stiffness parameters and blood pressure were input using values pertaining to healthy subjects as reported in the literature. The mechanical properties and diastolic blood pressure parameters were adjusted through an ad-hoc scheme to achieve the best match between the calculated LV geometry and the one obtained from the corresponding end-diastolic MR image segmentation where maximum LV dilation was observed. The performance of the LV diastolic mechanical simulations using the optimal values of tissue stiffness and blood pressure parameters was validated by comparing the geometrical parameters of the dilated LV model as well as the stress and strain distributions

through the LV model with corresponding values available from reported measurements of the human LV at the end-diastolic state.

### 1.6.5 Chapter 6

This Chapter summarizes the material presented in Chapters 2 through 5. It also suggests possible future directions for the research described in the thesis and finally concludes this dissertation.

## 1.7 Contributions of Thesis

This thesis addresses the challenging computational cardiac mechanics modeling by considering the heart wall as a composite material which is made up of different cardiac tissue constituents with different mechanical properties. These constituents are organized within the cardiac tissue 3D space in accordance with the anatomical microstructure of the heart. In Chapter 2 we present an in-depth microscopic perspective of cardiac tissue mechanics with the aim of characterizing its intrinsic mechanical properties. The strategy taken in this chapter is to explicitly consider the distinct roles played by cardiomyocyte and ECM as the two major parts of cardiac tissue. The cardiomyocytes are mainly comprised of myofibrils and mitochondria while the ECM is comprised largely of fibroblasts and collagen fibers. This leads to a composite mechanical model of the cardiac tissue including two major parts: 1) background tissue as the mechanically passive part of the cardiac tissue with three major constituents of mitochondrion, collagen fiber, and fibroblast and 2) myofibrils as the mechanically active/passive part of the cardiac tissue. Next, the macroscopic passive mechanical properties of this composite tissue model were computed through FE simulations by setting the types and volume percentages of the major constituents of each part in accordance with the given normal and pathological cardiac tissue conditions. This resulted in a very good agreement with mechanical measurements of both normal and pathological cardiac tissue reported in the literature. In Chapters 3, 4, and 5 this composite material approach was utilized to mechanically model the LV diastolic and systolic functions using an FE commercial solver. This composite material model is quite advantageous as it allows using standard libraries of the commercial FE solvers for simulating all cardiac tissue mechanics aspects including anisotropy, hyperelasticity, and

active contraction forces simultaneously without need for further FE coding. Moreover, this model reduces the level of mathematical formulation complexity needed to capture the LV contraction physiology. This was achieved by incorporating the tissue anisotropy as a manifestation of the LV tissue composite model. This follows a totally different approach than the conventional approach of LV mechanics models which incorporates anisotropy and contractility within the tissue strain energy function. This approach led to a good agreement with reported measurements and with current mechanical models of the LV diastolic and systolic functions available in the literature.

## References

- [1] G. J. Tortora and B. Derrickson, [Principles of Anatomy & Physiology], 13th ed., Hoboken, NJ Wiley, 2012.
- [2] World Health Organization (WHO), [www.who.org](http://www.who.org).
- [3] S. Marchesseau, H. Delingette, M. Sermesant, M. Sorine, K. Rhode, S. G. Duckett, C. A. Rinaldi, R. Razavi, and N. Ayache, "Preliminary specificity study of the Bestel-Clement-Sorine electromechanical model of the heart using parameter calibration from medical images," *J. Mech. Behav. Biomed. Mater.*, 20, 259-271, 2013.
- [4] G. Drzewiecki, J. Wang, J. K. -J. Li, J. Kedem, and H. Weiss, "Modeling of mechanical dysfunction in regional stunned myocardium of the left ventricle," *IEEE Trans. Biomed. Eng.*, 43, 12, 1151-1163, 1996.
- [5] S. Goktepe and E. Kuhl, "Electromechanics of the heart: a unified approach to the strongly coupled excitation-contraction problem," *Comput. Mech.*, 45, 2-3, 227-243, 2010.
- [6] H. F. Choi, J. D'hooge, F. E. Rademakers, and P. Claus, "Influence of left-ventricular shape on passive filling properties and end-diastolic fiber stress and strain," *J. Biomech.*, 43, 9, 1745-1753, 2010.
- [7] H. M. Wang, H. Gao, X. Y. Luo, C. Berry, B. E. Griffith, R. W. Ogden, and T. J. Wang, "Structure-based finite strain modelling of the human left ventricle in diastole," *Int. J. Numer. Method. Biomed. Eng.*, 29, 1, 83-103, 2013.
- [8] K. D. Costa, P. J. Hunter, J. S. Wayne, L. K. Waldman, J. M. Guccione, and A. D. McCulloch, "A three-dimensional finite element method for large elastic deformations of ventricular myocardium: II—prolate spheroidal coordinates," *J. Biomech. Eng.*, 118, 4, 464-472, 1996.
- [9] S. K. Kyriacou, A. D. Shah, and J. D. Humphrey, "Myocardial transversely isotropic material parameter estimation from in-silico measurements based on a reduced-order unscented Kalman filter," *J. Mech. Behav. Biomed. Mater.*, 4, 7, 1090-1102, 2011.
- [10] P. Sáez and E. Kuhl, "Computational modeling of acute myocardial infarction," *Comput. Methods Biomech. Biomed. Engin.*, 9:1-9, 2015.
- [11] H. Xia, K. Wong, and X. Zhao, "A fully coupled model for electromechanics of the heart," *Computational and Mathematical Methods in Medicine*, vol. 2012, 10 pages, 2012.
- [12] F. J. C. Gascóá, "Mathematical modeling and simulations to study cardiac arrhythmias," *Rev. Esp. Cardiol.*, 58:6-9, 2005.
- [13] A. Lopez-Perez, R. Sebastian, and J. M. Ferrero, "Three-dimensional cardiac computational modelling: methods, features and applications," *Biomed. Eng. Online.*, 14: 35, 2015.

- [14] R. Mittala, J. H. Seoa, V. Vedulaa, Y. J. Choia, H. Liub, H. H. Huangb, S. Jainc, L. Younesc, T. Abrahamd, and R. T. Geoged, “Computational modeling of cardiac hemodynamics: Current status and future outlook,” *Journal of Computational physics*, 305: 1065–1082, 2016.
- [15] G. M. Fomovsky, J. R. Macadangdang, G. Ailawadi, and J. W. Holmes, “Model-based design of mechanical therapies for myocardial infarction,” *J. Cardiovasc. Transl. Res.*, 4(1): 82-91, 2011.
- [16] L. Gepstein, A. Goldin, J. Lessick, G. Hayam, S. Shpun, Y. Schwartz, G. Hakim, R. Shofty, A. Turgeman, D. Kirshenbaum, and S. A. Ben-Haim, “Electromechanical characterization of chronic myocardial infarction in the canine coronary occlusion model,” *Circulation.*, 98: 2055-2064, 1998.
- [17] M. Sermesant, R. Chabiniok, P. Chinchapatnam, T. Mansi, F. Billet, P. Moireau, J. M. Peyrat, K. Wong, J. Relan, K. Rhode, M. Ginks, P. Lambiase, H. Delingette, M. Sorine, C. A. Rinaldi, D. Chapelle, R. Razavi, and N. Ayache, “Patient-specific electromechanical models of the heart for the prediction of pacing acute effects in CRT: a preliminary clinical validation,” *Med. Image. Anal.*, 16(1):201-15, 2012.
- [18] Anonymous, [Rocky Mountain Medical Review: A Journal of Scientific Medicine and General Science], Vol. 1, Adams and Kimball., 2007.
- [19] S. Grimsgaard, K. H. Bønaa, J. B. Hansen, and E. S. Myhre, “Effects of highly purified eicosapentaenoic acid and docosahexaenoic acid on hemodynamics in humans,” *Am. J. Clin. Nutr.*, 68(1): 52-9, 1998.
- [20] Simon O'Connor, [Examination Medicine (The Examination)], Edinburgh: Churchill Livingstone, 2009.
- [21] J. Lessick J, Y. Fisher, R. Beyar, S. Sideman, M. L. Marcus, and H. Azhari, “Regional three-dimensional geometry of the normal human left ventricle using cine computed tomography,” *Ann. Biomed. Eng.*, 24(5): 583-94, 1996.
- [22] P. H. M. Bovendeerd, T. Arts, J. M. Huyghe, D. H. Van Campen, and R. S. Reneman, “Dependence of local left ventricular wall mechanics on myocardial fiber orientation: a model study,” *Journal of Biomechanics*, 25, 10, 1129-1140, 1992.
- [23] D. D. Jr. Streeter, H. M. Spotnitz, D. P. Patel, J. Jr. Ross, and E. H. Sonnenblick, “Fiber orientation in the canine left ventricle during diastole and systole,” *Circ. Res.*, 24(3): 339-47, 1969.
- [24] R. A. Greenbaum, S. Y. Ho, D. G. Gibson, A. E. Becker, and R. H. Anderson, “Left ventricular fibre architecture in man,” *Br. Heart J.*, 45(3): 248–263, 1981.
- [25] H. F. Choi, J. D'hooge, F. E. Rademakers, and P. Claus, “Distribution of active fiber stress at the beginning of ejection depends on left-ventricular shape,” *Engineering in Medicine and Biology Society (EMBC), Annual International Conference of the IEEE*, Buenos Aires, pp. 2638-2641, 2010.

- [26] R. J. Okamoto, M. J. Moulton, S. J. Peterson, D. D. Li, M. K. Pasque, and J. M. Guccione, "Epicardial suction: a new approach to mechanical testing of the passive ventricular wall," *ASME. J Biomech. Eng.*, 122(5): 479-487, 2000.
- [27] X. Papademetris, A. J. Sinusas, D. P. Dione, R. T. Constable, and J. S. Duncan, "Estimation of 3-D left ventricular deformation from medical images using biomechanical models," *IEEE Trans Med Imaging.*, 21(7): 786-800, 2002.
- [28] T. Arts, P. C. Veenstra, and R. S. Reneman, "Epicardial deformation and left ventricular wall mechanisms during ejection in the dog," *Am. J. Physiol.*, 243(3): H379-90, 1982.
- [29] I. J. LeGrice, B. H. Smaill, L.Z. Chai, S. G. Edgar, J. B. Gavin, and P. J. Hunter, "Laminar structure of the heart: ventricular myocyte arrangement and connective tissue architecture in the dog," *Am. J. Physiol.*, 269(2 Pt 2): H571-82, 1995.
- [30] M. P. Nash, P. J. Hunter, "Computational mechanics of the heart," *Journal of elasticity and the physical science of solids*, vol. 61, iss. 1, pp. 113-141, 2000.
- [31] V. Gurev, T. Lee, J. Constantino, H. Arevalo, and N. A. Trayanova, "Models of cardiac electromechanics based on individual hearts imaging data: image-based electromechanical models of the heart," *Biomech. Model. Mechanobiol.*, 10(3): 295-306, 2011.
- [32] T. P. Usyk, R. Mazhari, and A. D. McCulloch, "Effect of laminar orthotropic myofiber architecture on regional stress and strain in the canine left ventricle," *Journal of elasticity and the physical science of solids*, vol. 61, iss. 1, pp. 143-164, 2000.
- [33] H. Lombaert, J. M. Peyrat, P. Croisille, S. Rapacchi, L. Fanton, F. Cheriet, P. Clarysse, I. Magnin, H. Delingette, and N. Ayache, "Human atlas of the cardiac fiber architecture: study on a healthy population," *IEEE Trans. Med. Imaging.*, 31(7): 1436-47, 2012.
- [34] J. M. Peyrat, M. Sermesant, X. Pennec, H. Delingette, C. Xu, E. R. McVeigh, and N. Ayache, "A computational framework for the statistical analysis of cardiac diffusion tensors: application to a small database of canine hearts," *IEEE Trans. Med. Imaging.*, 26(11): 1500-14, 2007.
- [35] A. P. Benson, S. H. Gilbert, P. Li, S. M. Newton, and A. V. Holden, "Reconstruction and quantification of diffusion tensor imaging-derived cardiac fibre and sheet structure in ventricular regions used in studies of excitation propagation," *Mathematical Modelling of Natural Phenomena*, vol. 3, iss. 6, pp. 101-130, 2008.
- [36] P. Savadjiev, G. J. Strijkers, A. J. Bakermans, E. Piuze, S. W. Zucker, and K. Siddiqi, "Heart wall myofibers are arranged in minimal surfaces to optimize organ function," *Proceedings of the National Academy of Science*, 109(24): 9248-9253, 2012.

- [37] Piuze, E., J. Sparring, and K. Siddiqi, "Maurer-Cartan forms for fields on surfaces: application to heart fiber geometry," *IEEE Transactions On Pattern Analysis and Machine Intelligence*, 37(12): 2492-504, 2015.
- [38] H. Gray, S. Standring, H. Ellis, and B. K. B. Berkovitz, [Gray's Anatomy: The Anatomical Basis of Clinical Practice], Edinburgh: Elsevier Churchill Livingstone, 2005.
- [39] A. M. Gerdes and F. H. Kasten, "Morphometric study of endomyocardium and epimyocardium of the left ventricle in adult dogs," *Am. J. Anat.*, 159, 4, 389-394, 1980.
- [40] L. L. Demer and F. C. Yin, "Passive biaxial mechanical properties of isolated canine myocardium," *J. Physiol.*, 339: 615-630, 1983.
- [41] W. Zhang, Y. Feng, C. H. Lee, K. L. Billiar, and M. S. Sacks, "A generalized method for the analysis of planar biaxial mechanical data using tethered testing configurations," *J. Biomech. Eng.*, 137(6):064501, 2015.
- [42] Y. Yaniv, M. Juhaszova, S. Wang, K. W. Fishbein, D. B. Zorov, and S. J. Sollott, "Analysis of mitochondrial 3D-deformation in cardiomyocytes during active contraction reveals passive structural anisotropy of orthogonal short axes," *PLoS One*, 6, 7, e21985, 2011.
- [43] R. R. de Souza, "Aging of myocardial collagen," *Biogerontology*, 3, 6, 325-335, 2002.
- [44] D. M. Bers, "Cardiac excitation-contraction coupling," *Nature*, vol. 415, no. 6868, pp. 198-205, 2002.
- [45] L. H. Opie, "Fundamental role of angiotensin-converting enzyme inhibitors in the management of congestive heart failure," *Am. J. Cardiol.*, vol. 75, no. 18, pp. 3F-6F, 1995.
- [46] G. A. Holzapfel, [Nonlinear Solid Mechanics: A Continuum Approach for Engineering], Wiley, West Sussex, 2000.
- [47] Hibbit, Karlsson, Sorenson, *ABAQUS Theory Manual*. Pawtucket, RI, June 1998.
- [48] P. S. Wellman, R. D. Howe, N. Dewagan, M. A. Cundari, E. Dalton and K. A. Kern, "Tactile imaging: A method for documenting breast masses," *Annual International Conference of the IEEE Engineering in Medicine and Biology - Proceedings*, 2, 1131, 1999.
- [49] G. A. Holzapfel and R. W. Ogden, "Constitutive modelling of passive myocardium: a structurally based framework for material characterization," *Phil. Trans. R. Soc. A.*, 367: 3445-3475, 2009.
- [50] M. L. Shehata, S. Cheng, N. F. Osman, D. A. Bluemke, and J. A. Lima, "Myocardial tissue tagging with cardiovascular magnetic resonance," *J. Cardiovasc. Magn. Reson.*, 11:55, 2009.

- [51] S. Urheim, T. Edvardsen, H. Torp, B. Angelsen, and O. A. Smiseth, "Myocardial strain by Doppler echocardiography. Validation of a new method to quantify regional myocardial function," *Circulation*. 102(10): 1158-64, 2000.
- [52] M. Sermesant, H. Delingette and N. Ayache, "An electromechanical model of the heart for image analysis and simulation," *IEEE Transactions on Medical Imaging*, vol. 25, no. 5, pp. 612-625, 2006.
- [53] M. P. Nash and A. V. Panfilov, "Electromechanical model of excitable tissue to study reentrant cardiac arrhythmias," *Prog. Biophys. Mol. Biol.*, 85(2-3): 501-22, 2004.
- [54] N. A. Trayanova, "Whole heart modeling: applications to cardiac electrophysiology and electromechanics," *Circulation research*, 108(1): 113-128, 2011.
- [55] R. C. P. Kerckhoffs, P. H. M. Bovendeerd, J. C. S. Kotte, F. W. Prinzen, K. Smits, and T. Arts, "Homogeneity of cardiac contraction despite physiological asynchrony of depolarization: a model study," *Annals of Biomedical Engineering*, vol. 31, iss. 5, pp. 536-547, 2003.
- [56] C. M. Augustin, A. Neic, M. Liebmann, A. J. Prassl, S. A. Niederer, G. Haase, and G. Plank, "Anatomically accurate high resolution modeling of human whole heart electromechanics: A strongly scalable algebraic multigrid solver method for nonlinear deformation," *J. Comput. Phys.*, 15; 305: 622-646, 2016.
- [57] J. D. Humphrey, R. K. Strumpf, and T. C. P. Yin, "Determination of a constitutive relation for passive myocardium: I. – a new functional form," *J. Biomech. Eng.*, 112, pp. 333-339, Aug. 1990.
- [58] J. D. Humphrey, R. K. Strumpf, and T. C. P. Yin, "Determination of a constitutive relation for passive myocardium: II. - parameter estimation," *J. Biomech. Eng.*, 112, pp. 340-346, Aug. 1990.
- [59] J. M. Guccione and A. D. McCulloch, "Mechanics of active contraction in cardiac muscle: Part I--Constitutive relations for fiber stress that describe deactivation," *J. Biomech. Eng.*, 115(1):72-81, 1993.
- [60] J. M. Guccione, L. K. Waldman, and A. D. McCulloch, "Mechanics of active contraction in cardiac muscle: Part II--Cylindrical models of the systolic left ventricle," *J. Biomech. Eng.*, 115(1):82-90, 1993.
- [61] K. Sun, N. Stander, C. S. Jhun, Z. Zhang, T. Suzuki, G. Y. Wang, M. Saeed, A. W. Wallace, E. E. Tseng, A. J. Baker, D. Saloner, D. R. Einstein, M. B. Ratcliffe, and J. M. Guccione, "A computationally efficient formal optimization of regional myocardial contractility in a sheep with left ventricular aneurysm," *Biomech. Eng.*, 131(11): 111001, 2009.
- [62] J. F. Wenk, K. Sun, Z. Zhang, M. Soleimani, L. Ge, D. Saloner, W. A. Wallace, M. B. Ratcliffe, and J. M. Guccione, "Regional Left Ventricular Myocardial Contractility and Stress in a Finite Element Model of Posterobasal Myocardial Infarction," *J. Biomech. Eng.*, 133(4): 044501, 2011.



- [63] M. A. Hassan, M. Hamdi, and A. Noma, "The nonlinear elastic and viscoelastic passive properties of left ventricular papillary muscle of a Guinea pig heart," *J. Mech. Behav. Biomed. Mater.*, 5, 1, 99-109, 2012.
- [64] H. Talbot, S. Marchesseau, C. Duriez, M. Sermesant, S. Cotin, and H. Delingette, "Towards an interactive electromechanical model of the heart," *Interface Focus*, 3 20120091, 2013.
- [65] K. F. Augenstein, B. R. Cowan, I. J. LeGrice, and A. A. Young, "Estimation of cardiac hyperelastic material properties from MRI tissue tagging and diffusion tensor imaging," *Medical Image Computing and Computer-Assisted Intervention – MICCAI*, LNCS 4190, 628-635, 2006.
- [66] A. Virgen-Ortiz, J. L. Marin, A. Elizalde, E. Castro, E. Stefani, L. Toro, and J. Muñiz, "Passive mechanical properties of cardiac tissues in heart hypertrophy during pregnancy," *Journal of Physiological Sciences*, vol. 59, iss. 5, pp. 391-396, 2009.
- [67] T. S. E. Eriksson, A. J. Prassl, G. Plank, and G. A. Holzapfel, "Influence of myocardial fiber/sheet orientations on left ventricular mechanical contraction," *Math. Mech. Solids*, 1-15, May 2013.
- [68] K. B. Gupta, M. B. Ratcliffe, M. A. Fallert, L. H. J. Edmunds, and D. K. Bogen, "Changes in passive mechanical stiffness of myocardial tissue with aneurysm formation," *Circulation*, 89:2315-26, 1994.
- [69] A. Grosberg and M. Gharib, "Modeling the macro-structure of the heart: healthy and diseased," *Med. Biol. Eng. Comput.*, 47, 3, 301-311, 2009.
- [70] P. Zhang, J. M. Guccione, S. I. Nicholas, J. C. Walker, P. C. Crawford, A. Shamal, G. Acevedo-Bolton, M. A. Guttman, C. Ozturk, E. R. McVeigh, D. A. Saloner, A. W. Wallace, and M. B. Ratcliffe, "Endoventricular patch plasty for dyskinetic anteroapical left ventricular aneurysm increases systolic circumferential shortening in sheep," *J. Thorac. Cardiovasc. Surg.*, 134, 4, 1017-1024.e1, 2007.
- [71] J. W. Holmes, T. K. Borg, and J. W. Covell, "Structure and mechanics of healing myocardial infarcts," *Annu. Rev. Biomed. Eng.*, 7, 1, 223-253, 2005.
- [72] G. Ertl and S. Frantz, "Healing after myocardial infarction," *Cardiovasc. Res.*, 66, 1, 22-32, 2005.
- [73] G. Agnoletti, A. Cargnoni, L. Agnoletti, M. Di Marcello, P. Balzarini, E. Pasini, G. Gitti, P. Martina, R. Ardesi, and R. Ferrari, "Experimental ischemic cardiomyopathy: insights into remodeling, physiological adaptation, and humoral response" *Ann. Clin. Lab. Sci.*, 36, 3, 333-340, 2006.
- [74] M. L. Hubbard and C. S. Henriquez, "Microscopic variations in interstitial and intracellular structure modulate the distribution of conduction delays and block in cardiac tissue with source-load mismatch," *Europace*, 14, suppl 5, v3-v9. 2012.
- [75] S. C. Panda and R. Natarajan, "Finite-element method of stress analysis in the human left ventricular layered wall structure," *Med. Biol. Eng. Comput.*, 15, 1, 67-71, 1997.

- [76] D. Dagan, M. Be'ery, and A. Gefen, "Single-trabecula building block for large-scale finite element models of cancellous bone," *Med. Biol. Eng. Comput.*, 42, 4, 549-556, 2004.
- [77] V. Y. Wang, A. J. Wilson, G. B. Sands, A. A. Young, I. J. LeGrice, and M. P. Nash, "Microstructural remodelling and mechanics of hypertensive heart disease," *Functional Imaging and Modeling of the Heart*, 9126, 382-389, 2015.
- [78] D. P. Sokolis, "Passive mechanical properties and constitutive modeling of blood vessels in relation to microstructure," *Med. Biol. Eng. Comput.*, 46, 12, 1187-1199, 2008.
- [79] T. Stylianopoulos and V. H. Barocas, "Volume-averaging theory for the study of the mechanics of collagen networks," *Comput. Methods Appl. Mech. Eng.*, 196, 31, 2981-2990, 2007.
- [80] R. Herbert, "The passive mechanical properties of muscle and their adaptations to altered patterns of use," *Australian Journal of Physiotherapy*, vol. 34, iss. 3, pp. 141-149, 1988.
- [81] D. P. Sokolis, S. Sassani, E. P. Kritharis, and S. Tsangaris, "Differential histomechanical response of carotid artery in relation to species and region: mathematical description accounting for elastin and collagen anisotropy," *Med. Biol. Eng. Comput.*, 49, 8, 867-879, 2011.
- [82] S. M. Klisch and C. Lotz, Jeffrey, "Application of a fiber-reinforced continuum theory to multiple deformations of the annulus fibrosus," *J. Biomech.*, 32, 10, 1027-1036, 1999.
- [83] S. Goktepe, S. N. S. Acharya, J. Wong, and E. Kuhl, "Computational modeling of passive myocardium," *Int. J. Numer. Method. Biomed. Eng.*, 27, 1, 1-12, 2011.
- [84] K. D. Costa, J. W. Holmes, and A. D. McCulloch, "Modelling cardiac mechanical properties in three dimensions," *Phil. Trans. R. Soc. Lond. A*, 359, 1783, 1233-1250, 2001.
- [85] P. H. M. Bovendeerd, T. Arts, J. M. Huyghe, D. H. Van Campen, and R. S. Reneman, "Dependence of local left ventricular wall mechanics on myocardial fiber orientation: a model study," *Journal of Biomechanics*, 25, 10, 1129-1140, 1992.
- [86] R. H. Keldermann, M. P. Nash, H. Gelderblom, V.Y. Wang, and A. V. Panfilov, "Electromechanical wavebreak in a model of the human left ventricle," *Am. J. Physiol. Heart Circ. Physiol.*, 299, 1, H134-H143, 2010.
- [87] V. H. Barocas and R. T. Tranquillo, "An anisotropic biphasic theory of tissue-equivalent mechanics: the interplay among cell traction, fibrillar network deformation, fibril alignment, and cell contact guidance," *J. Biomech. Eng.*, 119, 2, 137-145, 1997.
- [88] V. C. Mow, S. C. Kuei, W. M. Lai, and C. G. Armstrong, "Biphasic creep and stress relaxation of articular cartilage in compression: theory and experiments," *J. Biomech. Eng.*, 102, 1, 73-84, 1980.

- [89] B. Agoram and V. H. Barocas, "Coupled macroscopic and microscopic scale modeling of fibrillar tissues and tissue equivalents," *J. Biomech. Eng.*, 123, 4, 362-369, 2001.
- [90] N. J. Driessen, C. V. Bouten, and F. P. Baaijens, "A structural constitutive model for collagenous cardiovascular tissues incorporating the angular fiber distribution," *J. Biomech. Eng.*, 127, 3, 494-503, 2004.
- [91] K. L. Billiar and M. S. Sacks, "Biaxial mechanical properties of the native and glutaraldehyde-treated aortic valve cusp: part II-a structural constitutive model," *J. Biomech. Eng.*, 122, 4, 327-335, 2000.
- [92] M. R. Hill, M. A. Simon, D. Valdez-Jasso, W. Zhang, H. C. Champion, and M. S. Sacks, "Structural and mechanical adaptations of right ventricle free wall myocardium to pressure overload," *Ann. Biomed. Eng.*, 42, 12, 2451-2465, 2014.
- [93] C. Witzenburg, R. Raghupathy, S. M. Kren, D. A. Taylor, and V. H. Barocas, "Mechanical changes in the rat right ventricle with decellularization," *J. Biomech.*, 45, 5, 842-849, 2012.
- [94] D. Valdez-Jasso, M. A. Simon, H. C. Champion, and M. S. Sacks, "A murine experimental model for the mechanical behaviour of viable right-ventricular myocardium," *J. Physiol. (Lond.)*, 590, 18, 4571-4584, 2012.
- [95] Blase A. Carabello, "Understanding coronary blood flow. The wave of the future," *Circulation.*, 113: 1721-1722, 2006.
- [96] L. C. Lee, M. Genet, A. B. Dang, L. Ge, J. M. Guccione, and M. B. Ratcliffe, "Applications of computational modeling in cardiac surgery," *J. Card. Surg.*, 29(3): 293-302, 2014.
- [97] A. Nehorai and A. Jeremic, "Estimating mechanical properties of the left ventricle using dynamic modeling and magnetic resonance imaging," *Computers in Cardiology*, 25, 257-260, 1998.
- [98] B. P. Cupps, P. Moustakidis, B. J. Pomerantz, G. Vedala, R. P. Scheri, N. T. Kouchoukos, V. Davila-Roman, and M. K. Pasque, "Severe aortic insufficiency and normal systolic function: determining regional left ventricular wall stress by finite-element analysis," *Ann. Thorac. Surg.*, 76, 3, 668-675, 2003.
- [99] M. Perl and A. Horowitz, "Mechanical model for the simulation of ischaemia and infarction of the left ventricle," *Medical and Biological Engineering and Computing*, vol. 25, iss. 3, pp. 284-288, 1987.
- [100] D. Mojsejenko, J. R. McGarvey, S. M. Dorsey, J. H. Gorman, J. A. Burdick, J. J. Pilla, R. C. Gorman, and J. F. Wenk, "Estimating passive mechanical properties in a myocardial infarction using MRI and finite element simulations," *Biomech. Model. Mechanobiol.*, 14(3): 633-47, 2015.
- [101] M. Sermesant, H. Delingette, and N. Ayache, "An electromechanical model of the myocardium for cardiac image analysis and medical simulation," *INRIA Sophia Antipolis*, N° RR-5395, 2004.

- [102] A. I. Veress, W. P. Segars, B. M. W. Tsui, and G. T. Gullberg, "Incorporation of a Left Ventricle Finite Element Model Defining Infarction Into the XCAT Imaging Phantom," *IEEE Transactions on Medical Imaging*, vol. 30, no. 4, pp.915-927, 2011.
- [103] A. Christy, "Left ventricular wall mechanics in hypertension – an echocardiographic study," *Int. J. Biol. Med. Res.*, 3(1): 1267-1272, 2012.
- [104] P. Zhang, J. M. Guccione, S. I. Nicholas, J. C. Walker, P. C. Crawford, A. Shamal, D. A. Saloner, A. W. Wallace, and M. B. Ratcliffe, "Left ventricular volume and function after endoventricular patch plasty for dyskinetic anteroapical left ventricular aneurysm in sheep," *J. Thorac. Cardiovasc. Surg.*, 130(4): 1032-8, 2005.
- [105] X. J. Jiang, T. Wang, X. Y. Li, D. Q. Wu, Z. B. Zheng, J. F. Zhang, J. L. Chen, B. Peng, H. Jiang, C. Huang C, and X. Z. Zhang, "Injection of a novel synthetic hydrogel preserves left ventricle function after myocardial infarction," *J. Biomed. Mater. Res. A.*, 90(2): 472-7, 2009.
- [106] J. F. Wenk, P. Eslami, Z. Zhang, C. Xu, E. Kuhl, J. H. Gorman, J. D. Robb, M. B. Ratcliffe, R. C. Gorman, and J. M. Guccione, "A novel method for quantifying the in-vivo mechanical effect of material injected into a myocardial infarction," *Ann. Thorac. Surg.*, 92(3):935-41, 2011.
- [107] G. Drzewiecki, J. Wang, J. K. J. Li, J. Kedem, and H. Weiss, "Modeling of mechanical dysfunction in regional stunned myocardium of the left ventricle," *IEEE Trans. Biomed. Eng.*, 43, 12, 1151-1163, 1996.
- [108] S. Goktepe and E. Kuhl, "Electromechanics of the heart: a unified approach to the strongly coupled excitation-contraction problem," *Comput. Mech.*, 45, 2-3, 227-243, 2010.
- [109] V. Sudarshan V, U. R. Acharya, E. Y. Ng, C. S. Meng, R. S. Tan, and D. N. Ghista, "Automated identification of infarcted myocardium tissue characterization using ultrasound images: a review," *IEEE Rev. Biomed. Eng.*, 8:86-97, 2015.
- [110] X. Zhang, B. R. Cowan, D. A. Bluemke, J. P. Finn, C. G. Fonseca, A. H. Kadish, D. C. Lee, J. A. Lima, A. Suinesiaputra, A. A. Young, and P. Medrano-Gracia, "Atlas-based quantification of cardiac remodeling due to myocardial infarction," *PLoS One.*, 9(10): e110243, 2014.
- [111] E. Konukoglu, J. Relan, U. Cilingir, B. H. Menze, P. Chinchapatnam, A. Jadidi, H. Cochet, M. Hocini, H. Delingette, P. Jaïs, M. Haïssaguerre, N. Ayache, and M. Sermesant, "Efficient probabilistic model personalization integrating uncertainty on data and parameters: Application to eikonal-diffusion models in cardiac electrophysiology," *Prog. Biophys. Mol. Biol.*, 107(1):134-46, 2011.
- [112] D. Neumann, T. Mansi, B. Georgescu, A. Kamen, E. Kayvanpour, A. Amr, F. Sedaghat-Hamedani, J. Haas, H. Katus, B. Meder, J. Hornegger, D. Comaniciu, and S. less, "Robust image-based estimation of cardiac tissue parameters and their uncertainty from noisy data," *Medical Image Computing and Computer-Assisted Intervention*, 8674: 9-16, 2014.

- [113] C. A. Linte, M. Wierzbicki, T. M. Peters, and A. Samani, "Towards a biomechanics-based technique for assessing myocardial contractility: an inverse problem approach," *Comput. Methods Biomech. Biomed. Engin.*, 11(3): 243-55, 2008.
- [114] L. C. Lee, J. F. Wenk, D. Klepach, Z. Zhang, D. Saloner, A. W. Wallace, L. Ge, M. B. Ratcliffe, and J. M. Guccione, "A novel method for quantifying in-vivo regional left ventricular myocardial contractility in the border zone of a myocardial infarction," *J. Biomech. Eng.*, 133(9): 094506, 2011.
- [115] A. Nehorai and A. Jeremic, "Estimating mechanical properties of the left ventricle using dynamic modeling and magnetic resonance imaging," *Computers in Cardiology*, 25, 257-260, 1998.
- [116] B. P. Cupps, P. Moustakidis, B. J. Pomerantz, G. Vedala, R. P. Scheri, N. T. Kouchoukos, V. Davila-Roman, and M. K. Pasque, "Severe aortic insufficiency and normal systolic function: determining regional left ventricular wall stress by finite-element analysis," *Ann .Thorac. Surg.*, 76, 3, 668-675, 2003.
- [117] Z. Hu, D. Metaxas, and L. Axel, "*In vivo* strain and stress estimation of the heart left and right ventricles from MRI images," *Med. Image Anal.*, 7, 4, 435-444, 2003.
- [118] H. F. Choi, J. D'hooge, F. E. Rademakers, and P. Claus, "Influence of left-ventricular shape on passive filling properties and end-diastolic fiber stress and strain," *J. Biomech.*, 43, 9, 1745-1753, 2010.
- [119] H. M. Wang, H. Gao, X. Y. Luo, C. Berry, B. E. Griffith, R. W. Ogden, and T. J. Wang, "Structure-based finite strain modelling of the human left ventricle in diastole," *Int. J. Nnumer. Method. Biomed. Eng.*, 29, 1, 83-103, 2013.
- [120] K. D. Costa, P. J. Hunter, J. S. Wayne, L. K. Waldman, J. M. Guccione, and A. D. McCulloch, "A three-dimensional finite element method for large elastic deformations of ventricular myocardium: II—prolate spheroidal coordinates," *J. Biomech. Eng.*, 118, 4, 464-472, 1996.
- [121] K. D. Costa, J. W. Holmes, and A. D. Mcculloch, "Modelling cardiac mechanical properties in three dimensions," *Phil. Trans. R. Soc. Lond. A*, 359, 1783, 1233-1250, 2001.
- [122] H. Dal, S. Goktepe, M. Kaliske, and E. Kuhl, "A fully implicit finite element method for bidomain models of cardiac electromechanics," *Comput. Methods Appl. Mech. Eng.*, 253, 323-336, 2013.
- [123] A. M. Katz. *Physiology of the Heart*. Wolters Kluwer Health/Lippincott Williams & Wilkins Health, 2010.
- [124] M. Genet, L. C. Lee, R. Nguyen, H. Haraldsson, G. Acevedo-Bolton, Z. Zhang, L. Ge, K. Ordovas, S. Kozerke, and J. M. Guccione, "Distribution of normal human left ventricular myofiber stress at end diastole and end systole: a target for *in silico* design of heart failure treatments," *Journal of Applied Physiology*, 117 (2) 142-152, 2014.

- [125] M. Genet, L. C. Lee, B. Baillargeon, J. M. Guccione, and E. Kuhl, "Modeling pathologies of diastolic and systolic heart failure," *Annals of Biomedical Engineering*, 44(1): 112-127, 2015.
- [126] A. I. Veress, G. T. Gullberg, and J. A. Weiss, "Measurement of strain in the left ventricle during diastole with cine-MRI and deformable image registration," *J. Biomech. Eng.*, 127(7): 1195-207, 2005.
- [127] S. D. Colan, "Mechanics of left ventricular systolic and diastolic function in physiologic hypertrophy of the athlete heart," *Cardiol Clin.*, 10(2): 227-40, 1992.
- [128] M. R. Zile and D. L. Brutsaert, "New concepts in diastolic dysfunction and diastolic heart failure: Part I: diagnosis, prognosis, and measurements of diastolic function," *Clinical Cardiology: New Frontiers: Circulation.*, 105: 1387-1393, 2002.
- [129] J. J. McMurray and M. A. Pfeffer, "Heart failure," *The Lancet*, vol. 365, iss. 9474, pp. 1877-1889, 2005.
- [130] W. A. Newman, *Dorland's Illustrated Medical Dictionary*. Philadelphia, PA: Saunders, 2007.
- [131] W. J. Paulus, C. Tschöpe, J. E. Sanderson, C. Rusconi, F. A. Flachskampf, F. E. Rademakers, P. Marino, O. A. Smiseth, G. D. Keulenaer, A. F. Leite-Moreira, A. Borbely, I. Edes, M. L. Handoko, S. Heymans, N. Pezzali, B. Pieske, K. Dickstein, A. G. Fraser, and D. L. Brutsaert, "How to diagnose diastolic heart failure: a consensus statement on the diagnosis of heart failure with normal left ventricular ejection fraction by the heart failure and echocardiography associations of the European society of cardiology," *European Heart Journal*, 28 (20): 2539-2550, 2007.
- [132] M. R. Zile and D. L. Brutsaert, "New concepts in diastolic dysfunction and diastolic heart failure: Part II: causal mechanisms and treatment," *Clinical Cardiology: New Frontiers: Circulation.*, 105: 1387-1393, 2002.

## Chapter 2

# A Novel Micro-to-Macro Approach for Cardiac Tissue Mechanics

*The material presented in this chapter is in Press in the Journal of the Computer Methods in Biomechanics and Biomedical Engineering.*

### 2.1 Introduction

**A**CCURATE quantification of the passive mechanical properties of cardiac tissue is an essential prerequisite for cardiac mechanics computational models used to describe its underlying physics of contractile deformation and contraction forces. It also provides a deep comprehension of the passive and active responses of the cardiac tissue as well as alterations of the tissue mechanical properties due to various pathological procedures or tissue engineering treatments [1-5]. It is well known that the overall intrinsic mechanical properties of tissue are functions of its microstructural constituents and their organization within the tissue [6-9]. As such several research studies have been conducted to develop effective approaches to characterize the macroscopic mechanical response of the tissue based on its microstructure and constituents. These approaches can be categorized in three main groups: phenomenological, continuum, and structural [10]. In phenomenological strategies, the mechanical behavior of the tissue is described using a strain energy based constitutive equation while the stress-strain data is fitted to the equation to obtain the unknown parameters of the model [9,11-13]. An essential issue with the phenomenological approach is that the calculated model parameters are valid merely for the tested tissue sample while they lack flexibility to model inhomogeneity arising from variations expected in the tissue microstructure composition [14-17]. The continuum approach incorporates all solid and liquid phases of the tissue including cells, fibers, ions etc. as well as their interactions within the tissue model to derive a comprehensive

constitutive equation for the tissue as an intricate composite structure [18-19]. Although this method is powerful in modeling the details of the microstructure of the tissue, the theoretical complexity of this approach is an essential limitation especially in case of tissues with elaborate composition [10,20]. Finally, the structural approach assumes that the mechanical response of the tissue is characterized by the superposition of the micro-responses of its built-in constituents and thus the constituents and their individual responses can be included directly in the tissue mechanical model [10,21]. This approach leads to methods which are more manageable in terms of mathematical complexities, nonetheless they require cost-effective computational algorithms to connect the tissue constituents and integrate their individual responses to yield the overall tissue response [10,20].

Over the recent few decades diverse structural approaches have been used to provide realistic mechanical models for various types of tissues. For instance, in [21] and [22] a structural constitutive framework was presented that accounts for angular distribution of the collagen fibers within the tissue. This framework was applied to simulate biaxial behavior of the arterial walls and aortic valve. In [10] and [20] a computational finite element (FE) model was developed to simulate tissue microscopic collagen fiber network. In this approach the macroscopic domain of the tissue was discretized into a number of finite elements while in each element a microscopic collagen fiber network was distributed. This method was applied to a 3D structure of type I collagen gels to obtain macroscopic deformation of the gels resulting from a given loading and boundary conditions. Structural approaches have also been utilized for cardiac tissue modeling. In [23] mechanical properties alterations of the right ventricular (RV) tissue in response to pulmonary hypertension (PH) was investigated. There the biomechanical modeling approach considered two major constituents of the tissue, namely myofibers and collagen fibers to derive a constitutive law for the RV tissue. The constitutive law's parameters were then calculated by fitting biaxial stress-strain data obtained using the constitutive law to corresponding measurements pertaining to pathological tissue specimen. The calculated parameters suggested higher stiffness of the myofibers and longitudinal reorientation of the myofibers and collagen fibers within the tissue. Other works took the approach of relating the tissue macroscopic behavior of the cardiac tissue to its ultrastructural constituents. In [24] the biaxial mechanical properties of the various specimens of the murine RV was



quantified and compared to corresponding results obtained from the developed constitutive law. This comparison showed correlation with morphological analysis results of orientations of the myofibers and collagen fibers within the specimens, demonstrating the dependence of the tissue mechanical properties on its microstructure. In [25] changes in the RV tissue mechanical properties due to decellularization was investigated. This was carried out by performing biaxial mechanical testing of RV tissue specimens where they concluded that neither anisotropy nor heterogeneity was altered significantly after decellularization. In this article we present a novel hyperelastic and anisotropic constitutive model of the normal and pathological cardiac tissue which was developed based on its microstructural tissue constituents and mechanical properties. The proposed model incorporates the microscopic constituent's composition and mechanical properties directly into the tissue model to predict its macroscopic mechanical response. While [23] considers only two major constituents of the cardiac tissue, including myofibers and collagen fibers, this method considers all major constituents of the tissue. The method is adaptable to add as many constituents as required along with their mechanical properties to the tissue model to attain accurate constitutive laws for describing tissue mechanical behavior. This adaptability feature is highly important since various cardiac pathologies are often associated with substantial alteration in the tissue's composition and their related mechanical properties, making it possible to attain suitable constitutive model for such pathological tissue by modifying the type and volume fractions of the tissue constituents. Such models are invaluable as they can be input into cardiac mechanics computational models to predict cardiac mechanics under specific pathophysiological conditions. In this investigation, we applied this approach for normal and infarcted cardiac tissues by considering their known constituents to find their corresponding constitutive models. Resulting models led to very good agreement between stress-strain response these models predict and their measured counterparts reported in the literature.

## 2.2 Materials and Methods

### 2.2.1 Major Myocardial Tissue Constituents

Myocardial tissue has a complex microstructure which has been examined using various morphometric techniques such as electron and light microscopy. These techniques aim at

quantifying the volume of myofibrils as the active/passive part and the background tissue constituents as the passive part of the myocardial tissue. Morphological studies of pathological tissue ultrastructure also provide valuable information about alterations in both tissue constituents' type and their volume percentage caused by various pathologies. As such, cardiac morphometric studies are very important for tissue mechanical characterization.

Cardiac morphological studies reveal that myocardial tissue consists of two main parts of cardiac muscle cells or cardiomyocytes and the ECM. Cardiomyocytes have a complicated microstructure including various constituents such as myofibrils, mitochondria, sarcolemma, sarcoplasmic reticulum, intercalated disk, nucleus, T tubes, etc. [26]. Myofibrils are the active/passive part of the myocytes generating the myocardial contraction forces. Mitochondrion is another important cell organelle of the myocytes and it is known as cellular power plants. Since the myocardium consumes considerable energy for its contraction, the volume percentage of the mitochondrion in the heart is higher compared to other organs in the body. According to morphological studies, ~90% of the myocyte's volume is occupied by two cell organelle types including myofibrils and mitochondria [27]. Therefore, we considered myofibrils and mitochondria as the major constituents of the cardiomyocytes in our model. The second part of the myocardial tissue is the ECM. The ECM has various constituents including fibroblast, glycosaminoglycans and glycoproteins, blood vessels, nerves, and proteins, including collagen (mainly collagen type I), in addition to small amounts of fibronectin, laminin, and elastin [28]. Fibroblast is the most abundant cell type in the cardiac tissue and the most important constituent of the normal ECM as it occupies about 10% of the myocardial tissue volume. Due to its high stiffness, especially under tension, collagen is another essential constituent in cardiac ECM despite its small volume contribution in normal cardiac tissue. Hence, we selected fibroblast and collagen as the major constituents of the cardiac ECM. As such, in the proposed model, we consider the four major constituents of myofibril, mitochondrion, fibroblast, and collagen fibers. Table 2.1 shows each constituent's volume percentage in normal cardiac tissue [29-30]. This table indicates that the tissue volume percentage occupied by the stated constituents is ~97%. This shows that the mechanical behavior

expected to result from these major constituents will predominantly determine the macroscopic cardiac tissue mechanics.

**Table 2.1:** Major constituents of the normal myocardial tissue with their volume percentage

Constituent	Myofibril	Mitochondrion	Fibroblast	Collagen Fiber
Volume Percentage	62%	23%	~10%	~2%

## 2.2.2 Finite Element Modeling of Cardiac Tissue Samples

Myocardial tissue can be considered as a composite material including myofibrils and the remaining part through which microscopic myofibrils are distributed. Hereafter, this remaining non-myofibril part will be referred to as background tissue. By considering alignment of the myofibrils in a certain direction within the cardiac tissue volume leads to self-contained tissue anisotropy. Due to bonding between the myofibrils and background tissue, contraction of the myofibrils leads to contraction in the background part, creating stresses in both of the myofibrils and background tissue that maintain mechanical equilibrium. This description of the myocardial tissue is consistent with the renowned Hill's model in which active contractile stress generated by active elements causes contraction in both of the active (element connected in series) and passive elements (connected in parallel).

As stated earlier, cardiac tissue was resolved into two main parts: myofibrils (active/passive part) and background tissue (passive part). The background tissue is composed of three main constituents including mitochondrion, fibroblast, and collagen fiber. This tissue decomposition leads to a composite material model of the myocardial tissue. Our strategy for modeling the passive part of the cardiac tissue is shown in the flowchart illustrated in Figure 2.1. It involves constructing FE models of composite materials pertaining to normal and pathological tissues using known combinations of the described constituents. Using these models, stress vs. strain data of these *in silico* samples can be generated. As illustrated in the flowchart, developing the tissue's FE model involves two steps. In the first step, hyperelastic models are developed for the background and myofibril parts of the cardiac tissue based on their known constituents. This is followed by developing a self-contained

anisotropic hyperelastic model of the whole cardiac tissue consisting of the two background and myofibril parts as described in the following sections.

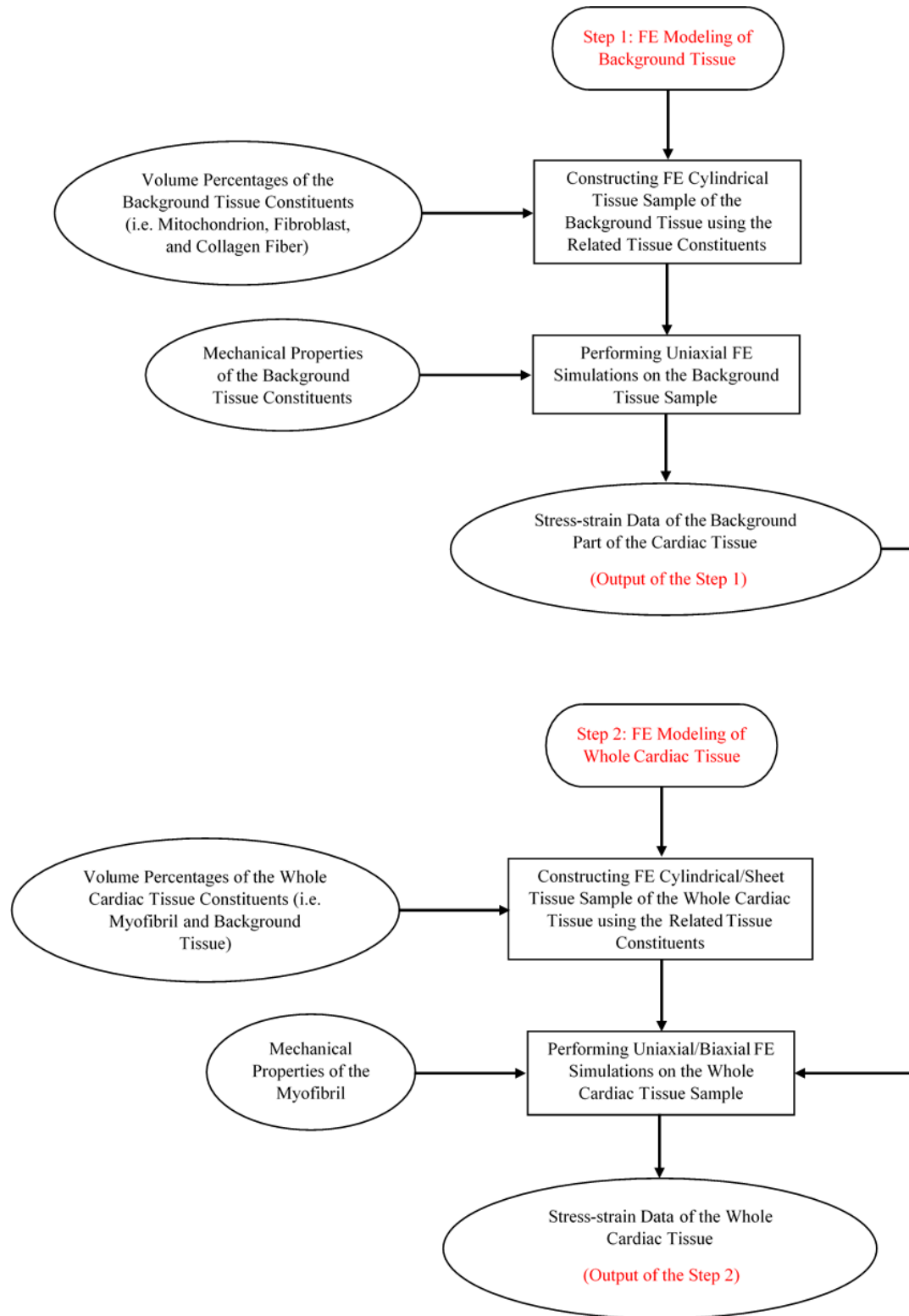


**Figure 2.1:** Flowchart illustrating the proposed cardiac tissue modeling approach.

### 2.2.2.1 Finite Element Modeling of Background Tissue

A cylindrical sample was considered to construct the background tissue's FE model. As indicated in the previous section, the background tissue is a composite structure of three constituents: mitochondria, fibroblasts, and collagen fibers. Thus, the composite background tissue's FE model involves three types of elements corresponding to these three tissue constituents. Each element type within the sample has its own mechanical properties reported in the literature. Fibroblasts and collagen fibers are distributed uniformly throughout the cardiac ECM [31] while mitochondria are dispersed almost uniformly in cardiac myocytes [32]. As such, for constructing the sample's FE model, these three types of element were randomly distributed throughout the sample in consistency with their known volume percentages (i.e. as given in Table 2.1). A cylindrical FE composite model of the background tissue with the three building elements is shown in Figure 2.2.

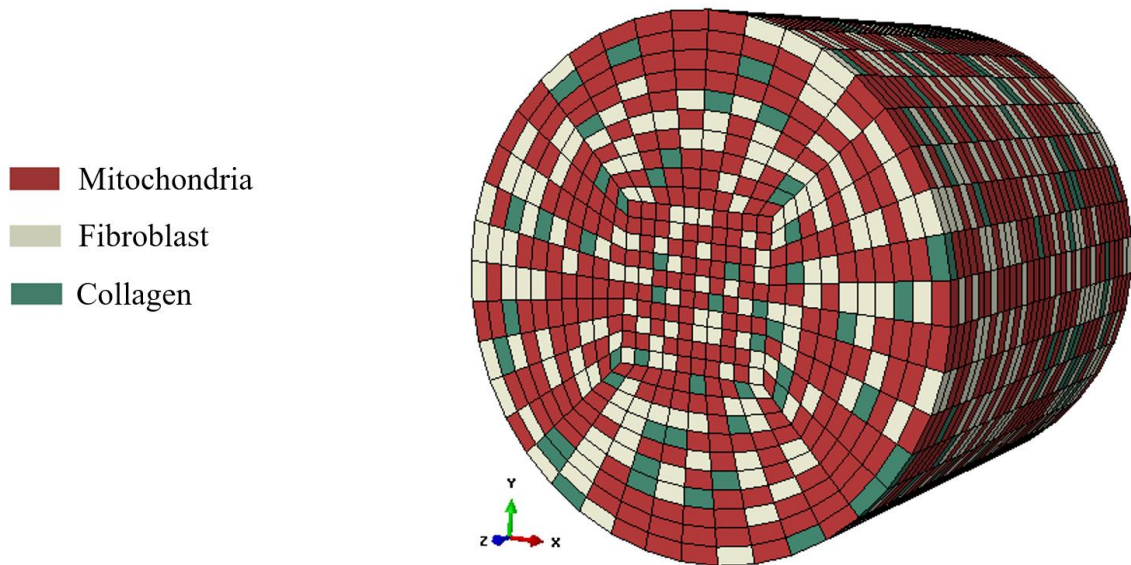


**Figure 2.2:** FE cylindrical sample of the background cardiac tissue which is composed of three types of elements: mitochondrion, fibroblast, and collagen.

### 2.2.2.2 Whole Tissue Sample Construction

We modelled the cardiac tissue as a composite structure containing two main parts: myofibrils and background tissue with the myofibrils distributed uniformly throughout the background tissue. As such, for FE modeling of the whole cardiac tissue, a composite

material model with two distinct parts of background tissue and myofibrils was considered. To construct the corresponding FE model, two element types corresponding to these two tissue parts were used. In this model, the myofibril elements were assembled to form continuous fibers aligned longitudinally within the background tissue in order to preserve the tissue's fibrous structure. Figure 2.3 illustrates FE models of cylindrical and sheet samples of the cardiac tissue with the two types of myofibril and background tissue building elements. The quantity of each element type (material) in the sample was set to be proportional to the corresponding known volume percentage. It is noteworthy that for the sheet FE sample in Figure 2.3 the Y-axis represents the fiber direction while the X-axis coincides with the cross-fiber direction.

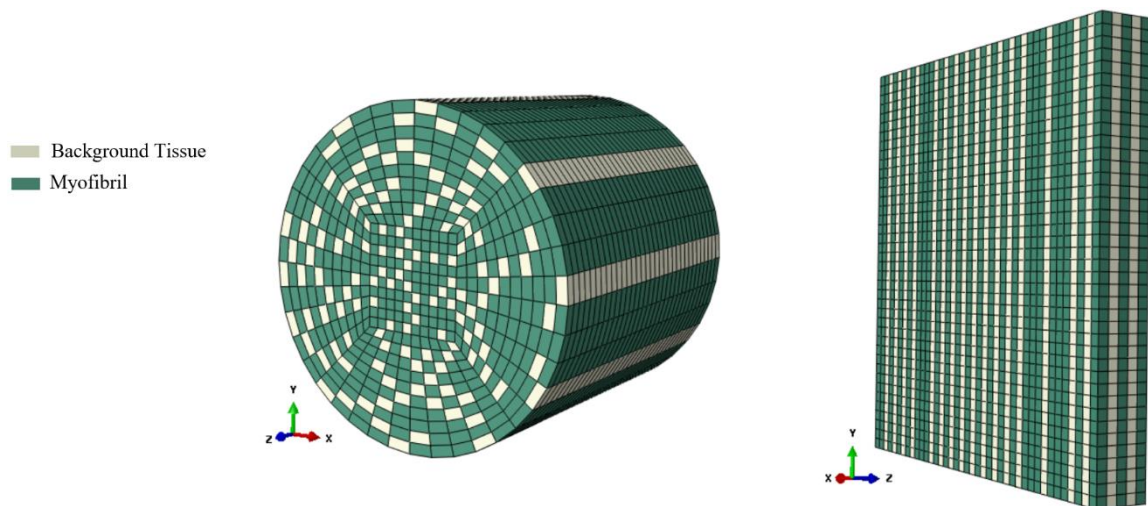


**Figure 2.3:** FE cylindrical and sheet samples of the whole cardiac tissue which is composed of two types of elements: myofibril and background tissue.

### 2.2.3 Normal Cardiac Tissue Modeling

Using the constructed FE models of the cylindrical and sheet samples, uniaxial and equibiaxial tests of normal cardiac tissue were simulated to obtain its mechanical parameters. For this simulation, two steps were performed including background tissue mechanical testing simulation followed by the whole normal tissue mechanical testing simulation using the sample models described in the previous section. It is noteworthy that we tried various hyperelastic model combinations for the tissue constituents of the background tissue (consisting of mitochondrion, fibroblast, and collagen fibers) and the

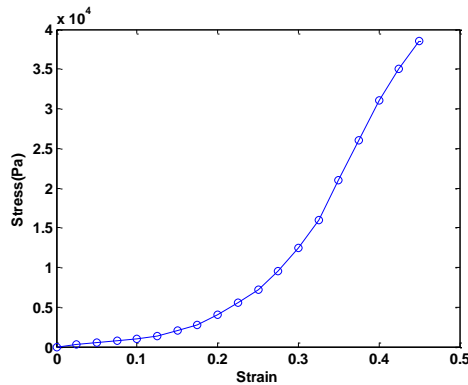
tissue constituents of the whole cardiac tissue (i.e. myofibers and background tissue) before arriving at the given combination which led to the highest accuracy and computational stability.

### 2.2.3.1 Background Tissue Hyperelastic Model

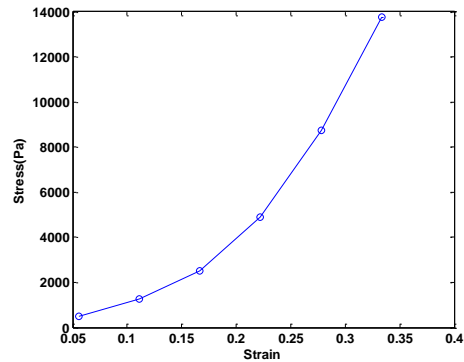
As indicated earlier, the proposed method involves developing a hyperelastic model for the background tissue based on its constituents. A major constituent in the background tissue is collagen fibers. More than 80% of these fibers are collagen type I [31], which act as a scaffold for cardiac ECM while predominantly providing tensile strength to the cardiac tissue. In our model development, we used the stress-strain curve shown in Figure 2.4 (a) which is reported in [33] for a 3D matrix of purified collagen type I. This curve was fitted to Yeoh hyperelastic model form given in the following equation for an incompressible material [34].

$$W = \sum_{i=1}^3 C_i (I_1 - 3)^i \quad (2.1)$$

where  $C_i$  represents the hyperelastic parameters reflecting the intrinsic mechanical properties of the tissue and  $I_1$  is the first scalar invariant. Cardiac fibroblast is another constituent of the background tissue. The initial stiffness of this constituent is characterized by a Young's modulus of  $\sim 5$  kPa [35-36]. To account for large deformation, we again utilized a Yeoh hyperelastic form consistent with the 5 kPa Young's modulus to model the fibroblast cells.



(a)



(b)



**Figure 2.4:** (a): Stress-strain curve for a 3D matrix of type I collagen fiber reported in [33],  
 (b): Stress-strain curve for an intact cardiac myofibril reported in [39].

The third constituent of the background tissue is the mitochondrion. Mitochondria are very small spherical/elliptical shape particles filled with fluid and distributed throughout the cardiac myocyte. Essentially, the mitochondria can be assumed isovolumic during mechanical deformations due to the presence of the fluid in its structure [37]. To our knowledge, stiffness data of mitochondrion has not been reported in the literature. However, given that lipid materials such as phospholipid in addition to proteins are present as structural material in the mitochondrion, especially in its outer membrane [38], the initial Young's modulus of the mitochondria was set to be 3 kPa consistent with the Young's modulus of fat. To account for large deformation, similar to the fibroblast cells, we utilized a Yeoh hyperelastic form consistent with the 3 kPa Young's modulus to model the mitochondria. The calculated Yeoh hyperelastic parameters for three major background tissue constituents including mitochondrion, fibroblast, and collagen fibers are given in Table 2.2.

With the Yeoh hyperelastic parameters of the three background part constituents obtained as described here, FE model of the sample shown in Figure 2.2 was completed for uniaxial test simulation. Uniformly distributed axial strains varying incrementally from 0 to 35% were applied to the cylindrical sample using prescribed displacement boundary conditions, leading to corresponding uniformly distributed axial stresses which were calculated by ABAQUS (Dassault Systèmes Simulia Corp, USA). The maximum 35% strain value was selected based on maximum cardiac tissue strain expected in normal contraction.

**Table 2.2:** Yeoh hyperelastic parameters of the background tissue constituents obtained through fitting procedure

Yeoh Hyperelastic Parameters	Mitochondrion	Fibroblast	Collagen Fiber
$C_1$ (Pa)	500.0	833.3	277.8
$C_2$ (Pa)	2000.0	1600.0	18931.3
$C_3$ (Pa)	0.0	0.0	3146.6

### 2.2.3.2 Normal Cardiac Tissue Hyperelastic Model

To obtain normal cardiac tissue constitutive model, constitutive model of the myofibrils part is required. For this part, we used the stress-strain data shown in Figure 2.4 (b) which

is reported in [39] for an intact cardiac myofibril. With known stress-strain data of both of the background and myofibril parts, FE simulations of equibiaxial tests were performed to obtain equibiaxial stress-strain data of the whole cardiac tissue. It is noteworthy that these simulations were conducted where the stress-strain data of the myofibril and background parts of the tissue were fitted to the hyperelastic models of Arruda–Boyce, Marlow, Mooney-Rivlin, Neo-Hookean, Ogden, Polynomial, Reduced Polynomial, Van der Waals, and Yeoh models. Among them, the second order Ogden hyperelastic model for the tissue constituents (i.e. background tissue and myofibril) of the cardiac tissue led to the highest agreement with the biaxial measurements of the normal cardiac tissue available in the literature as described in the Results section. The Ogden model is described using the following strain energy function for an incompressible material [34]:

$$W = \sum_{p=1}^N \frac{\mu_p}{\alpha_p} (\lambda_1^{\alpha_p} + \lambda_2^{\alpha_p} + \lambda_3^{\alpha_p} - 3) \quad (2.2)$$

where  $N$  is the order of Ogden model,  $\mu$ 's and  $\alpha$ 's are the hyperelastic parameters, and  $\lambda_i$ 's are the principle stretches. To simulate the equibiaxial test, the sheet tissue model was used where equal strains ranging from 0 to 35% along and across the fibers (X and Y) direction were applied. Corresponding stresses in the X and Y directions were calculated using ABAQUS FE solver. Stress-strain data of normal cardiac tissue which were obtained from the equibiaxial test simulation were fitted to the hyperelastic anisotropic model presented in [11] by Humphrey et al. 1990 and corresponding hyperelastic parameters were determined. The anisotropic hyperelastic model is described using the following strain energy function [11]:

$$W(I_1, \alpha) = C_1(\alpha - 1)^2 + C_2(\alpha - 1)^3 + C_3(I_1 - 3) + C_4(I_1 - 3)(\alpha - 1) + C_5(I_1 - 3)^2 \quad (2.3)$$

where  $C_i$ s are hyperelastic parameters,  $I_1$  is the first scalar strain invariant, and  $\alpha$  is a parameter related to the fourth scalar strain invariant as follows:

$$I_4 = \alpha^2 \quad (2.4)$$

This strain energy function results into the following Cauchy stresses under equibiaxial extension experiment [11]:

$$t_{11} = 2(\lambda_1^2 - \lambda_3^2)[C_3 + C_4(\alpha - 1) + 2C_5(I_1 - 3)] + \lambda_1[2C_1(\alpha - 1) + 3C_2(\alpha - 1)^2 + C_4(I_1 - 3)] \quad (2.5)$$

$$t_{22} = 2(\lambda_2^2 - \lambda_3^2)[C_3 + C_4(\alpha - 1) + 2C_5(I_1 - 3)] \quad (2.6)$$

where  $t_{11}$  and  $t_{22}$  denote the stresses in fiber and cross-fiber directions, respectively. Under equibiaxial extension and incompressibility condition the stretches are related such that  $\lambda_1 = \lambda_2 = \lambda$  and  $\lambda_3 = 1/\lambda^2$ . The stress-strain curves obtained from the FE simulations are fitted to the above equations for Cauchy stresses to determine the  $C_i$  parameters.

#### 2.2.4 Infarcted Cardiac Tissue Hyperelastic Model

Similar to normal cardiac tissue, modeling of infarcted cardiac tissue was performed in two steps of modeling the background followed by modelling the whole tissue. Experimental data involving dogs and sheep indicate that 1 to 6 weeks after the onset of myocardial infarction, collagen fibers dilate and start to increase within the infarcted region as part of the healing phase, leading to scar tissue formation. Similar patterns have been observed in human myocardial infraction [40]. This stage of healing, which is known as cardiac fibrosis, leads to a heavily collagenous scar. Table 2.3 presents volume percentages of infarcted scar tissue constituents according to tissue morphology data reported in [41], which shows ~40 times increase in collagen content compared to normal cardiac tissue.

**Table 2.3:** Major constituents of the infarcted myocardial tissue with their volume percentage

Constituent	Myofibril	Mitochondrion	Fibroblast	Collagen Fiber
Volume Percentage	5.26%	1.94%	~10%	80.74%

The FE models of cylindrical and sheet tissue samples were constructed by distributing numbers of finite elements corresponding to each constituent type calculated according to this table.

### 2.2.4.1 Background Tissue Hyperelastic Model

To perform FE simulation of a uniaxial test on the cylindrical sample model of background tissue, similar to the normal tissue, we incorporated the mechanical properties of each constituent into the FE model. For the collagen fiber part, histological studies have shown that collagen type I with higher thickness than in normal cardiac tissue is developed in infarcted region [42,43]. Other studies have also shown that these fibers are denser with more cross-links in infarct regions, leading to stiffer collagen compared to normal cardiac tissue [44,45]. To our knowledge, stiffness characteristics of collagen fibers in infarcted cardiac tissue have not been measured. As such, we assumed that the Yeoh hyperelastic parameters ( $C_i$ 's) of collagen fibers in infarcted cardiac tissue are larger than those of normal cardiac tissue by a constant factor greater than one. This factor was determined using 1D optimization whereby it was changed systematically until the best agreement between calculated and experimental stress-strain data of infarcted cardiac tissue was achieved. We used the nonlinear least square optimization technique to calculate this factor. Cardiac fibroblast and mitochondrion are the two other constituents of the background tissue which we did not alter in comparison to what we used in modeling normal cardiac tissue. Similar to modeling normal cardiac tissue, we used the Yeoh hyperelastic model for all constituents in the background tissue and simulated a uniaxial test using axial strain values ranging from 0 to 35% in conjunction with the cylindrical sample model. Corresponding stresses were calculated using ABAQUS FE solver.

### 2.2.4.2 Whole Tissue Hyperelastic Model

Hyperelastic parameters of infarcted cardiac tissue were determined using the methods described earlier in Section 2.3.2 for normal cardiac tissue. For the myofibrils, we incorporated volume percentage data in Table 2.3 in conjunction with stress-strain data shown in Figure 2.4 (b). FE simulation of uniaxial test was performed using the cylindrical sample model. These simulations were conducted using ABAQUS FE solver with incremental strain values ranging from 0 to 35%. The stress-strain data of the myofibril and background parts were fitted to the hyperelastic models of Arruda–Boyce, Marlow, Mooney-Rivlin, Neo-Hookean, Ogden, Polynomial, Reduced Polynomial, Van der Waals, and Yeoh models. The fifth order Ogden hyperelastic model for both parts led to the highest

agreement with reported measurements of infarcted cardiac tissue. Next, the stress-strain data of infarcted cardiac tissue which were obtained from the uniaxial test FE simulation were fitted to Yeoh, second order Polynomial, and fifth order Ogden hyperelastic models and corresponding hyperelastic parameters of the whole infarcted cardiac tissue were determined.

### 2.2.5 Sensitivity Analysis

We conducted ad-hoc sensitivity analysis to investigate the variations of stress-strain curves, and consequently corresponding hyperelastic parameters, of the cardiac tissue with respect to alterations in the volume percentages of tissue constituents. For this purpose, the volume percentage of each tissue constituent was altered within a range of values reported in morphological studies of cardiac tissue and corresponding range of stress-strain curves was obtained. It is noteworthy that when the volume percentage of each tissue constituent was changed in the model, the volume percentages of the other tissue constituents were accordingly adjusted proportional to their volume contribution in the tissue model. For further sensitivity assessment, we also calculated the tissue's hyperelastic parameter variation corresponding to the model presented in [11] with respect to variations in the tissue constituents' volume percentages. According to these studies, in normal cardiac tissue, the volume percentage range of the myofibril, mitochondrion, collagen, and fibroblast are at 52% - 72%, 15.5% - 30%, 0.5% - 6.59% and 7% - 13 %, respectively [29,46-47]. For infarcted cardiac tissue, the volume percentage of the collagen was altered within the range of 73% to 89% according to [41,47]. It is noteworthy that, other than the collagen, we changed the volume percentages of other constituents according to the morphological studies of infarcted cardiac tissue. However, due to very low volume contribution as well as low stiffness of those constituents compared to the collagen fibers, their alteration influence was insignificant. Hence, we focused only on the collagen fibers in this part of the sensitivity analysis.

## 2.3 Results

### 2.3.1 Normal Cardiac Tissue Modeling

The calculated Yeoh model's hyperelastic parameters of the mitochondrion, fibroblast cells and collagen fibers used to model the background part of the cardiac tissue were given in Table 2.2. The stress-strain curve resulting from the uniaxial test simulation of the background part of the tissue is illustrated in Figure 2.5.

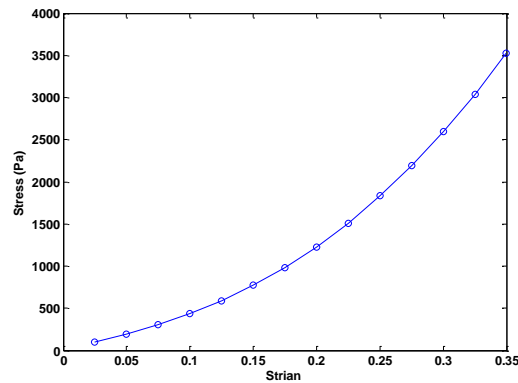


**Figure 2.5:** Stress-strain curve of background tissue of normal myocardium obtained from the proposed method.

Fitting of the stress-strain data of the background and myofibril parts of the tissue to second order Ogden model led to the hyperelastic parameters reported in Table 2.4.

**Table 2.4:** Second order Ogden hyperelastic parameters of the background tissue and myofibrils

Second Order Ogden Hyperelastic Parameters	Myofibril	Background Tissue
$\mu_1$ (Pa)	18329.00	191431.00
$\alpha_1$	0.015	0.007
$\mu_2$ (Pa)	836.88	310.12
$\alpha_2$	11.82	7.10

FE simulation of normal cardiac tissue equibiaxial test performed using the sheet sample model in conjunction with these hyperelastic parameters led to the stress-strain data illustrated in Figure 2.6. Figure 2.6 (a) and 2.6 (b) illustrate the data in both fibers and cross-fiber directions, respectively. These figures also show corresponding experimental stress-strain data of normal cardiac tissue reported in [11]. This data shows average errors of 16.17% and 8.25% in the fiber direction and cross-fiber direction, respectively.

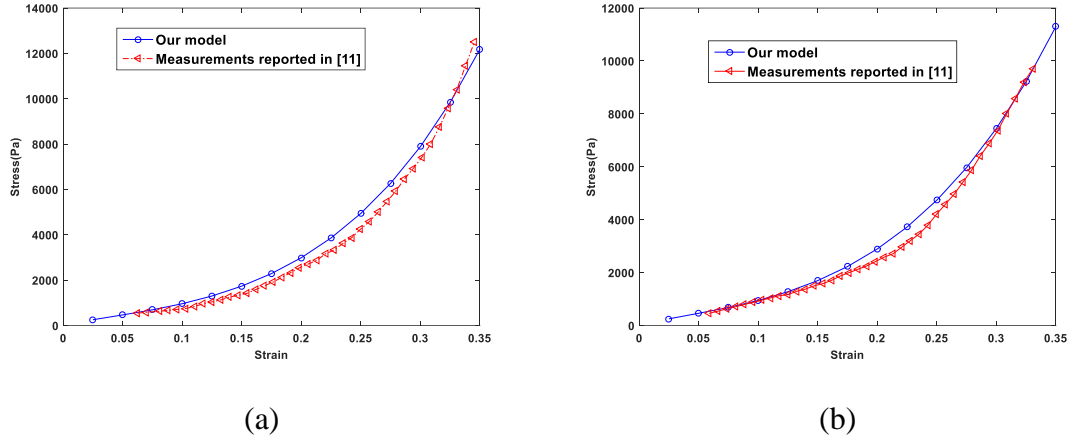


**Figure 2.6:** Stress-strain data of normal myocardial tissue along fiber direction (a) and cross-fiber direction (b) obtained from the equibiaxial test FE simulation compared to measurements reported in the literature [11].

The data in the fiber and cross-fiber directions were fitted to the hyperelastic model presented in [11], leading to the parameters reported in Table 2.5. It is noteworthy that the calculated hyperelastic parameters are in the range of the parameters presented in [11] for cardiac tissue.

**Table 2.5:** Hyperelastic parameters of normal cardiac tissue calculated from the equibiaxial stress-strain data obtained from FE simulation compared to parameters given in [11]

Hyperelastic Parameters of the Model Presented by Humphrey	Normal Tissue modeling	Parameters Given in [11]
$C_1$ ( $g/cm^2$ )	32.45	24.44
$C_2$ ( $g/cm^2$ )	64.81	54.99
$C_3$ ( $g/cm^2$ )	0.99	1.51
$C_4$ ( $g/cm^2$ )	-14.98	-18.40
$C_5$ ( $g/cm^2$ )	20.79	19.39

Results of the sensitivity analysis pertaining to normal cardiac tissue in fiber and cross-fiber directions are presented in Figures 2.7 and 2.8. As shown in these figures, the greatest range of stress-strain curves in both fiber and cross-fiber directions is observed corresponding to volume percentage changes of the myofibrils which is the major constituent of the normal cardiac tissue. This constituent shows maximum  $\Delta\sigma$  of 2.75 kPa at strain of 0.35 in fiber direction. Following the myofibrils, high ranges are observed corresponding to mitochondrion, fibroblast, and collagen where  $\Delta\sigma$ 's at 0.35 in fiber direction are 1.88 kPa, 0.72 kPa, and 0.67 kPa, respectively. Figures 2.7 and 2.8 show

higher stress values with volume percentage of collagen or myofibril changed to the upper bound value (U) while for the mitochondrion and fibroblast the contrary is seen. This is quite justified as increasing the collagen or myofibril, which have higher stiffness, leads to overall increase of the tissue stiffness. In contrast, increasing the lower stiffness constituents of mitochondrion or fibroblast leads to overall reduction of tissue stiffness as increasing these constituents' volume percentage must be associated with reduction of the collagen and myofibril volume percentages.

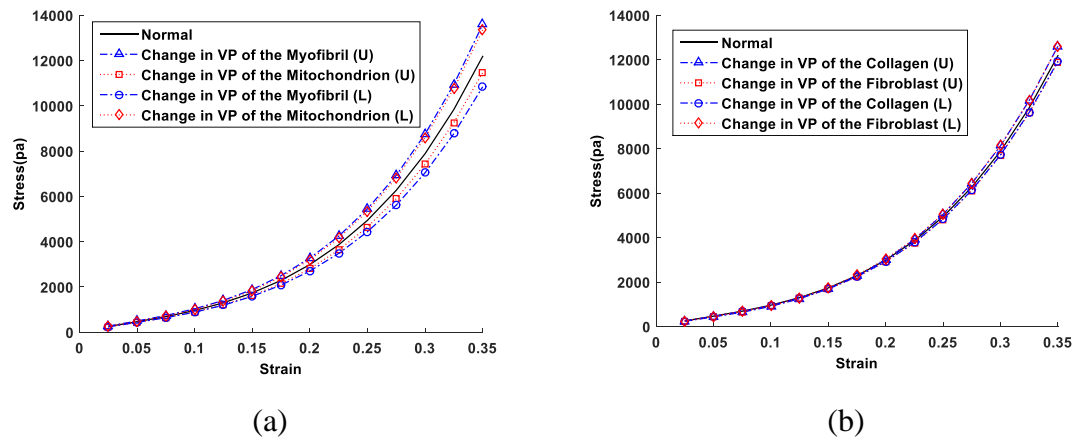


**Figure 2.7:** Stress-strain data of normal myocardial tissue along fiber direction vs. change in volume percentages (VP) of the tissue constituents (U: upper bound of VP, L: lower bound of VP). Change in VP of the myofibril and mitochondrion (a) and change in VP of the fibroblast and collagen fiber (b).

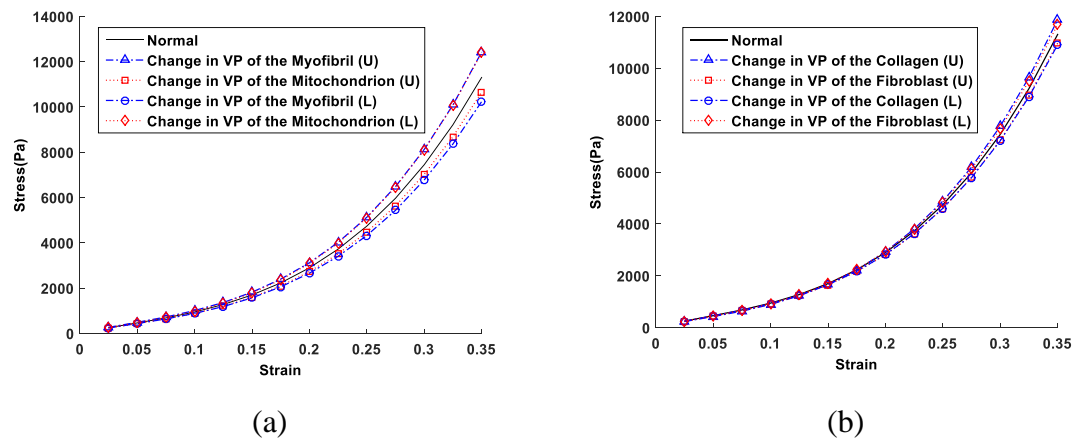




**Figure 2.8:** Stress-strain data of normal myocardial tissue along cross-fiber direction vs. Change in volume percentages (VP) of the tissue constituents (U: upper bound of VP, L: lower bound of VP). Change in VP of the myofibril and mitochondrion (a) and change in VP of the fibroblast and collagen fiber (b).

Variations of the hyperelastic parameter of the model presented in [11] over the range of the constituents volume percentage changes is presented in Table 2.6. In this table, percentages of the hyperelastic parameters variations in comparison to corresponding parameters of the normal tissue are reported.

**Table 2.6:** Percentage variations of hyperelastic parameters of normal cardiac tissue obtained by varying volume percentages (VPs) of each tissue constituent

Hyperelastic Parameters of the Model Presented by Humphrey	$\Delta C_1$ ( $g/cm^2$ ) in percentage		$\Delta C_2$ ( $g/cm^2$ ) in percentage		$\Delta C_3$ ( $g/cm^2$ ) in percentage		$\Delta C_4$ ( $g/cm^2$ ) in percentage		$\Delta C_5$ ( $g/cm^2$ ) in percentage	
	High VP	Low VP	High VP	Low VP	High VP	Low VP	High VP	Low VP	High VP	Low VP
<b>Myofibril</b>	2.40	-4.13	2.75	-3.93	-49.49	35.35	-10.35	6.34	9.91	-9.62
<b>Mitochondrion</b>	-10.72	14.7	38.71	-62.64	-13.13	-45.45	4.54	-9.41	-4.62	9.14
<b>Collagen</b>	11.43	-6.81	-76.13	47.96	-61.62	-15.15	-7.68	3.4	5.1	-2.07
<b>Fibroblast</b>	-1.2	13.41	-0.82	-62.98	-0.11	-44.44	2.07	-8.48	-4.91	3.51

### 2.3.2 Infarcted Cardiac Tissue Modeling

The 1D optimization procedure described in the Section 2.4.1, which was used to obtain the Yeoh model hyperelastic parameters of the collagen fibers led to a factor of 1.5 as, yielding the parameters given in Table 2.7.

**Table 2.7:** Yeoh hyperelastic parameters of the collagen fibers in the infarcted cardiac tissue

Yeoh Hyperelastic Parameters	Collagen Fiber
<b>C<sub>1</sub> (Pa)</b>	416.67
<b>C<sub>2</sub> (Pa)</b>	28396.97
<b>C<sub>3</sub> (Pa)</b>	4719.87

Using these parameters, stress-strain data of the background part of infarcted tissue was calculated using uniaxial test FE simulation as described earlier. This data is illustrated in Figure 2.9.

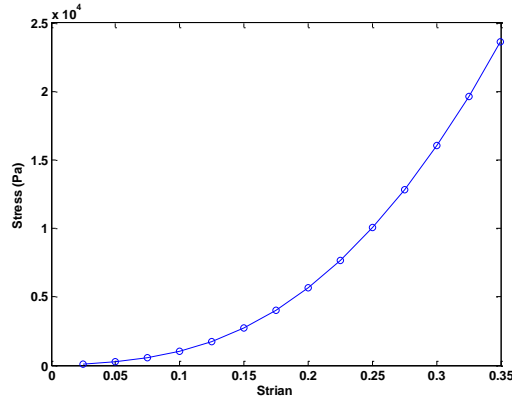


**Figure 2.9:** Stress-strain curve of background tissue of infarcted myocardium obtained from the proposed method.

For the myofibrils, we used the same parameters we obtained in modeling the normal cardiac tissue. Furthermore, for both the myofibrils and background parts, we used fifth order Ogden hyperelastic model which led to the highest agreement with experimental data. Corresponding parameters which led to the best fit are given in Table 2.8.

**Table 2.8:** Fifth order Ogden hyperelastic model parameters of the background tissue and myofibril

Fifth Order Ogden Hyperelastic Parameters	Myofibril	Background Tissue
$\mu_1$ (Pa)	834.21	279.46
$\alpha_1$	12.41	12.69
$\mu_2$ (Pa)	386.74	142.06
$\alpha_2$	0.25	12.76
$\mu_3$ (Pa)	273.43	169.45
$\alpha_3$	0.20	12.75
$\mu_4$ (Pa)	752.07	202.03
$\alpha_4$	0.18	12.78
$\mu_5$ (Pa)	53.39	269.83
$\alpha_5$	0.22	12.72

Incorporating these parameters in the uniaxial test simulation of infarcted cardiac tissue as described earlier led to the stress-strain data depicted in Figure 2.10 (a). The uniaxial stress-strain data are compared to corresponding experimental data reported in [48]. This comparison shows an average error of 10%, demonstrating the reasonable accuracy of the proposed method for infarcted tissue modeling (see Figure 2.10 (b)).

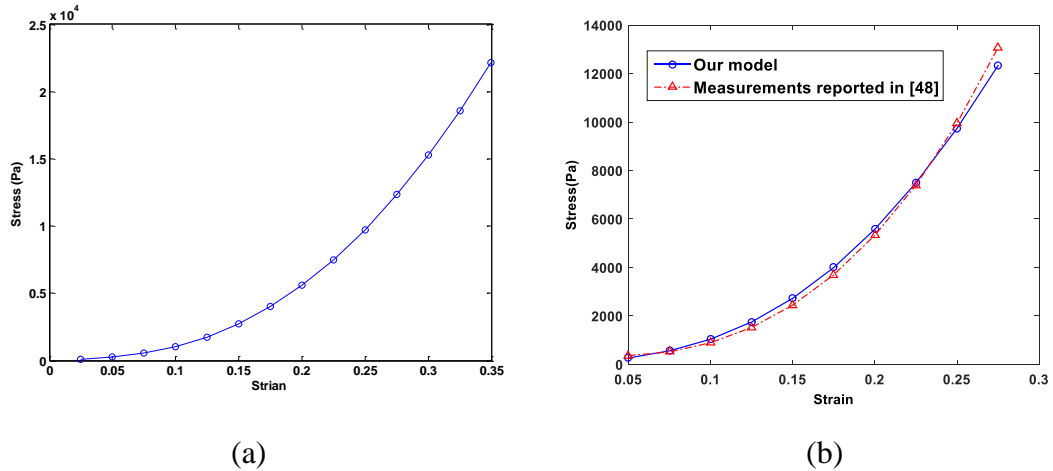


**Figure 2.10:** (a): Stress-strain data of infarcted myocardial tissue obtained from uniaxial simulation, (b): Stress-strain curve of infarcted myocardial tissue obtained from the proposed method compared to corresponding measurements.

The data obtained from uniaxial FE simulation was fitted to Yeoh, second order Polynomial, and fifth order Ogden hyperelastic models, leading to the parameters reported in Table 2.9.

**Table 2.9:** Hyperelastic parameters of the infarcted cardiac tissue

Model	Hyperelastic Parameters	Infarcted Cardiac Tissue
Yeoh	$C_1$ (Pa)	1221.45
	$C_2$ (Pa)	20236.45
	$C_3$ (Pa)	1449.49
Second order Polynomials	$C_{10}$ (Pa)	0.00
	$C_{01}$ (Pa)	500.31
	$C_{11}$ (Pa)	22452.04
	$C_{20}$ (Pa)	4673.99
	$C_{02}$ (Pa)	0.00
Fifth order Ogden	$\mu_1$ (Pa)	134.78
	$\alpha_1$	13.03
	$\mu_2$ (Pa)	116.23
	$\alpha_2$	12.97
	$\mu_3$ (Pa)	84.25
	$\alpha_3$	13.01
	$\mu_4$ (Pa)	104.28
	$\alpha_4$	13.01
	$\mu_5$ (Pa)	195.85
$\alpha_5$	12.93	

The results of the sensitivity analysis, where the variations of stress-strain data with respect to the range of variations of constituents' volume percentage were calculated, are presented

in Figure 2.11. As shown in this figure, maximum change of  $\Delta\sigma = 3.26$  kPa at strain of 0.35 occurs corresponding to change of collagen fiber volume percentage, representing the most significant change among those of other constituents.

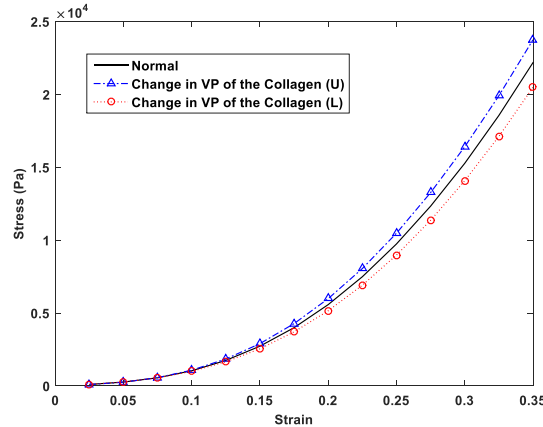


**Figure 2.11:** Stress-strain data of infarcted myocardial tissue while the volume percentages (VP) of the collagen was changed (U: upper bound of VP, L: lower bound of VP).

The variations of the Yeoh, second order Polynomial, and fifth order Ogden hyperelastic parameters with respect to changes in volume percentage of the collagen are given in Table 2.10. In this table, the percentage of the hyperelastic parameters' changes in comparison with the normal values given in Table 2.9 are reported.

**Table 2.10:** Percentage variations of infarcted cardiac tissue hyperelastic parameters due to alterations of volume percentage (VP) of collagen fibers

Model	Hyperelastic Parameters	Collagen (Low VP)	Collagen (High VP)
Yeoh	$\Delta C_1$ (Pa)	-7.86	4.87
	$\Delta C_2$ (Pa)	-7.67	8.67
	$\Delta C_3$ (Pa)	-8.81	-3.27
Second order Polynomials	$\Delta C_{10}$ (Pa)	-5.33	11.22
	$\Delta C_{01}$ (Pa)	17.13	-19.02
	$\Delta C_{11}$ (Pa)	-25.37	31.18
	$\Delta C_{20}$ (Pa)	55.49	-79.63
	$\Delta C_{02}$ (Pa)	-5.36	4.34
Fifth order Ogden	$\Delta \mu_1$ (Pa)	-6.22	3.98
	$\Delta \alpha_1$	-1.84	-1.53
	$\Delta \mu_2$ (Pa)	5.17	-5.31
	$\Delta \alpha_2$	-1.23	-0.54
	$\Delta \mu_3$ (Pa)	-16.44	-8.51
	$\Delta \alpha_3$	-2.77	-0.46

	$\Delta\mu_4$ (Pa)	-4.21	4.63
	$\Delta\alpha_4$	-1.92	-0.54
	$\Delta\mu_5$ (Pa)	3.47	36.06
	$\Delta\alpha_5$	-1.08	-0.77

## 2.4 Discussion and Conclusions

This article presents a novel method for cardiac tissue mechanics modeling. The method employs FE framework to relate the ultrastructure of cardiac tissue to its intrinsic mechanical properties. To this end, it takes into account various aspects of the passive cardiac tissue mechanics including nonlinearity and anisotropy by incorporating essential tissue constituents and their associated mechanical properties into the FE model framework. The prominence of cardiac tissue microstructural constituents in shaping its macroscopic mechanical characteristics arises from the sophisticated myocardial tissue ultrastructure which is formed by an intricate fibrous organization of diverse tissue elements [26]. Various cardiac pathologies are often caused by significant alterations in the underlying tissue constituents and their mechanical properties [26,40,49-51]. As such, the proposed technique can be effectively used to find a range of models spanning all possible cardiac tissue pathologies associated with tissue microstructure alterations. The proposed modelling technique involves two steps of modeling the background part of cardiac tissue followed by modelling the whole cardiac tissue. In each step, respective ultrastructure elements, their known properties and volume percentages were taken into account.

The technique was applied for normal cardiac tissue, leading to stress-strain curves pertaining to both fiber and cross-fiber directions. These curves were compared to cardiac tissue stress-strain data reported in [11]. For both directions good agreement was observed for the normal tissue with errors of 16.17% and 8.25% obtained in the fiber and cross-fiber direction, respectively. It is noteworthy that efforts were not made to change the volume percentage of various constituents and their parameters within acceptable range using systematic optimization algorithm to achieve minimum errors. While employing such an optimization algorithm is expected to force a higher degree of agreement, it is unnecessary in the context of this study given that there is always some variability in tissue constituents' stiffness and volume percentage parameters among patients. Overall, the errors are sufficiently low which demonstrate a solid proof of concept to the proposed modeling

technique. The fiber and cross-fiber stress-strain curves obtained from the proposed method were fitted to the hyperelastic anisotropic model presented in [11] and it was observed that the calculated parameters were in the range of the parameters reported in [11], once more demonstrating the validity of the proposed method. We also performed ad-hoc sensitivity analysis to assess the extent of tissue stress-strain curve alterations in the fiber and cross-fiber directions with respect to tissue constituent volume percentage alterations (see Figures 2.7 and 2.8). Results showed that the impact of myofibrils and mitochondria alteration are more significant than the impact of collagen fibers and fibroblasts alteration. One of the important outcomes of this work is demonstrating the significance of the mitochondria's impact on cardiac tissue mechanical behavior. It is noteworthy that relevant structural studies of cardiac tissues [23-25] typically investigated the influence of myofibrils and collagen fibers as the major players influencing cardiac tissue mechanics whereas our results reveal that the mitochondria is also a major player. This conclusion is expected because of its high volume percentage in the cardiac tissue microstructure. The sensitivity analysis was also conducted to assess the hyperelastic parameters' alterations with respect to tissue constituent changes. This was carried out in conjunction with the cardiac tissue hyperelastic model presented in [11], and it was observed that parameter alterations arising from myofibrils and mitochondria changes are more significant, which consolidates the fact that these constituents have major roles in influencing cardiac tissue mechanics.

The proposed method was also applied for modeling infarcted myocardial tissue to demonstrate its validity in predicting intrinsic mechanical properties of common pathological cardiac tissue. In the fibrotic phase after the onset of myocardial infarction, it is known that a new network of collagen fibers is deposited in the infarction area which is composed of thicker fibers with more cross-linking, both contributing to higher stiffness. This stiffness elevation is justified by the theory of spring structures mechanics which can be used to model coiled collagen fibers. The following relation was developed in [52] for the spring constant:

$$k = \frac{Gd^4}{64r^3N} \quad (2.7)$$

where  $G$  is the shear modulus of the spring material,  $d$  is the diameter of the rod from which the spring is made,  $r$  is the distance from the axis of the spring to the centroid of the rod's cross-section, and  $N$  is the number of active coils of the spring. According to this equation, the spring constant (which reflects its stiffness) is proportional to the 4<sup>th</sup> power of  $d$ . It is known that thicker collagen fibers are developed in infarction area [42-43], implying higher  $d$  values and leading to significantly higher stiffness. It is also known that more extensive cross-linking is developed among the collagen fibers in infarction tissue area [44-45]. Such elevation in cross-linking can be accounted for by considering fewer active coils ( $N$ ) for the collagen fibers, again leading to further elevation of stiffness according to the Equation (2.7). To our knowledge, no quantitative information is available to characterize the stiffness of collagen fibers developed in scar cardiac tissue. As such, we assumed that the Yeoh hyperelastic parameters ( $C_i$ 's) of collagen fibers in infarcted cardiac tissue are larger than those of normal cardiac tissue by a constant factor larger than one. This factor was determined using 1D optimization whereby it was changed systematically until the best agreement between calculated and experimental stress-strain data of infarcted cardiac tissue was achieved. The uniaxial stress-strain curve obtained as such was compared to corresponding collagenous scar tissue data reported in [52], which showed an error of 10%, demonstrating a good agreement. While multi-dimensional optimization could potentially achieve parameters leading to better agreement, it is hard to assess resulting parameters because of potential convergence to incorrect optimum values. The uniaxial stress-strain data of infarcted cardiac tissue obtained in this part of the study were fitted to Yeoh, second order Polynomial, and fifth order Ogden hyperelastic models, and corresponding hyperelastic parameters were calculated. The sensitivity of the stress-strain curve of the infarcted cardiac tissue was also investigated with respect to changes in the volume fraction of the collagen as the main and dominant component of the infarcted scar. Resulting range of the stress-strain curves of infarcted tissue was also presented in Figure 2.11 with respect to the variations in the collagen fiber content. The figure portrayed a relatively large range of stress-strain behavior especially at higher strains. Variations of the hyperelastic parameters of the scar tissue with respect to alterations in the collagen's volume percentage was also investigated which also showed relatively large changes.

The chief advantage of the proposed tissue modeling approach lies in its great flexibility in mimicking diverse cardiac tissue pathologies, since pathology spectrum pertaining to a disease can be modeled by merely altering the volume percentage and type of the tissue constituents according to severity of the pathophysiological conditions. While most of the microstructural-based techniques presented in [23-25] only consider the contribution of the myofibrils and collagen in drawing the constitutive law of the cardiac tissue, the proposed method considers other constituents of the cardiac tissue such as fibroblast and mitochondrion while it is capable of accommodating more constituents if needed. The model presented in [23] which considers a network composed of myofibril and collagen fibers is based on a 2D in-plane Kirchhoff stress-strain relation; thus it has limitations in capturing the tissue's actual 3D microstructure. The FE-based approach presented in [10,20] for modeling microscopic collagen networks in the tissue has better performance in modeling fine features of collagen fibers in the tissue microstructure. However, it requires solving a large scale nonlinear optimization problem while it considers the two parts collagen fibers and background tissue where the collagen fibers are embedded. An important advantage of the proposed technique is the utility of its straight forward concept of decomposition of cardiac tissue into the two main parts of background tissue (passive part) and myofibrils (active/passive part) where the mechanical properties of each part can be easily attained separately using the proposed approach. This tissue decomposition strategy is consistent with the Hill's model used extensively for myocardial contraction modelling. As such, the proposed model can be effectively used in conjunction with myocardial contraction models where various pathologies and their impact on cardiac mechanics can be systematically investigated. A major limitation of the proposed method is its accuracy dependence on the input parameters of the model obtained from tissue morphological analysis. These parameters include normal and pathological cardiac tissue constituents and their associated volume percentages as well as intrinsic mechanical properties. The higher the accuracy of the input parameters the higher the accuracy of the proposed composite tissue model.



## References

- [1] G. A. Holzapfel and R. W. Ogden, "Constitutive modelling of passive myocardium: a structurally based framework for material characterization," *Phil. Trans. R. Soc. A*, 367, 1902, 3445-3475, Sep. 2009.
- [2] T. S. E. Eriksson, A. J. Prassl, G. Plank, and G. A. Holzapfel, "Influence of myocardial fiber/sheet orientations on left ventricular mechanical contraction," *Math. Mech. Solids*, 1-15, May 2013.
- [3] K. B. Gupta, M. B. Ratcliffe, M. A. Fallert, L. H. J. Edmunds, and D. K. Bogen, "Changes in passive mechanical stiffness of myocardial tissue with aneurysm formation," *Circulation*, 89:2315-26, 1994.
- [4] A. Grosberg and M. Gharib, "Modeling the macro-structure of the heart: healthy and diseased," *Med. Biol. Eng. Comput.*, 47, 3, 301-311, 2009.
- [5] P. Zhang, J. M. Guccione, S. I. Nicholas, J. C. Walker, P. C. Crawford, A. Shamal, G. Acevedo-Bolton, M. A. Guttman, C. Ozturk, E. R. McVeigh, D. A. Saloner, A. W. Wallace, and M. B. Ratcliffe, "Endoventricular patch plasty for dyskinetic anteroapical left ventricular aneurysm increases systolic circumferential shortening in sheep," *J. Thorac. Cardiovasc. Surg.*, 134, 4, 1017-1024.e1, 2007.
- [6] S. C. Panda and R. Natarajan, "Finite-element method of stress analysis in the human left ventricular layered wall structure," *Med. Biol. Eng. Comput.*, 15, 1, 67-71, 1997.
- [7] D. Dagan, M. Be'ery, and A. Gefen, "Single-trabecula building block for large-scale finite element models of cancellous bone," *Med. Biol. Eng. Comput.*, 42, 4, 549-556, 2004.
- [8] V. Y. Wang, A. J. Wilson, G. B. Sands, A. A. Young, I. J. LeGrice, and M. P. Nash, "Microstructural remodelling and mechanics of hypertensive heart disease," *Functional Imaging and Modeling of the Heart*, 9126, 382-389, 2015.
- [9] D. P. Sokolis, "Passive mechanical properties and constitutive modeling of blood vessels in relation to microstructure," *Med. Biol. Eng. Comput.*, 46, 12, 1187-1199, 2008.
- [10] T. Stylianopoulos and V. H. Barocas, "Volume-averaging theory for the study of the mechanics of collagen networks," *Comput. Methods Appl. Mech. Eng.*, 196, 31, 2981-2990, 2007.
- [11] J. D. Humphrey, R. K. Strumpf, and T. C. P. Yin, "Determination of a constitutive relation for passive myocardium: II. - parameter estimation," *J. Biomech. Eng.*, 112, pp. 340-346, Aug. 1990.
- [12] D. P. Sokolis, S. Sassani, E. P. Kritharis, and S. Tsangaris, "Differential histomechanical response of carotid artery in relation to species and region: mathematical description accounting for elastin and collagen anisotropy," *Med. Biol. Eng. Comput.*, 49, 8, 867-879, 2011.

- [13] S. M. Klisch and C. Lotz, Jeffrey, "Application of a fiber-reinforced continuum theory to multiple deformations of the annulus fibrosus," *J. Biomech.*, 32, 10, 1027-1036, 1999.
- [14] S. Goktepe, S. N. S. Acharya, J. Wong, and E. Kuhl, "Computational modeling of passive myocardium," *Int. J. Numer. Method. Biomed. Eng.*, 27, 1, 1-12, 2011.
- [15] K. D. Costa, J. W. Holmes, and A. D. McCulloch, "Modelling cardiac mechanical properties in three dimensions," *Phil. Trans. R. Soc. Lond. A*, 359, 1783, 1233-1250, 2001.
- [16] P. H. M. Bovendeerd, T. Arts, J. M. Huyghe, D. H. Van Campen, and R. S. Reneman, "Dependence of local left ventricular wall mechanics on myocardial fiber orientation: a model study," *Journal of Biomechanics*, 25, 10, 1129-1140, 1992.
- [17] R. H. Keldermann, M. P. Nash, H. Gelderblom, V.Y. Wang, and A. V. Panfilov, "Electromechanical wavebreak in a model of the human left ventricle," *Am. J. Physiol. Heart Circ. Physiol.*, 299, 1, H134-H143, 2010.
- [18] V. H. Barocas and R. T. Tranquillo, "An anisotropic biphasic theory of tissue-equivalent mechanics: the interplay among cell traction, fibrillar network deformation, fibril alignment, and cell contact guidance," *J. Biomech. Eng.*, 119, 2, 137-145, 1997.
- [19] V. C. Mow, S. C. Kuei, W. M. Lai, and C. G. Armstrong, "Biphasic creep and stress relaxation of articular cartilage in compression: theory and experiments," *J. Biomech. Eng.*, 102, 1, 73-84, 1980.
- [20] B. Agoram and V. H. Barocas, "Coupled macroscopic and microscopic scale modeling of fibrillar tissues and tissue equivalents," *J. Biomech. Eng.*, 123, 4, 362-369, 2001.
- [21] N. J. Driessen, C. V. Bouten, and F. P. Baaijens, "A structural constitutive model for collagenous cardiovascular tissues incorporating the angular fiber distribution," *J. Biomech. Eng.*, 127, 3, 494-503, 2004.
- [22] K. L. Billiar and M. S. Sacks, "Biaxial mechanical properties of the native and glutaraldehyde-treated aortic valve cusp: part II-a structural constitutive model," *J. Biomech. Eng.*, 122, 4, 327-335, 2000.
- [23] M. R. Hill, M. A. Simon, D. Valdez-Jasso, W. Zhang, H. C. Champion, and M. S. Sacks, "Structural and mechanical adaptations of right ventricle free wall myocardium to pressure overload," *Ann. Biomed. Eng.*, 42, 12, 2451-2465, 2014.
- [24] D. Valdez-Jasso, M. A. Simon, H. C. Champion, and M. S. Sacks, "A murine experimental model for the mechanical behaviour of viable right-ventricular myocardium," *J. Physiol. (Lond.)*, 590, 18, 4571-4584, 2012.
- [25] C. Witzenburg, R. Raghupathy, S. M. Kren, D. A. Taylor, and V. H. Barocas, "Mechanical changes in the rat right ventricle with decellularization," *J. Biomech.*, 45, 5, 842-849, 2012.

- [26] A. M. Katz. *Physiology of the Heart*. Wolters Kluwer Health/Lippincott Williams & Wilkins Health, 2010.
- [27] A. M. Gerdes and F. H. Kasten, "Morphometric study of endomyocardium and epimyocardium of the left ventricle in adult dogs," *Am .J .Anat.*, 159, 4, 389-394, 1980.
- [28] R. R. de Souza, "Aging of myocardial collagen," *Biogerontology*, 3, 6, 325-335, 2002.
- [29] J. Schaper, E. Meiser, and G. Stammeler, "Ultrastructural morphometric analysis of myocardium from dogs, rats, hamsters, mice, and from human hearts," *Circ. Res.*, 56, 3, 377-391, 1985.
- [30] L. Yue, J. Xie, and S. Nattel, "Molecular determinants of cardiac fibroblast electrical function and therapeutic implications for atrial fibrillation," *Cardiovasc. Res.*, 89, 4, 744-753, 2011.
- [31] S. K. White, D. M. Sado, A. S. Flett, and J. C. Moon, "Characterising the myocardial interstitial space: the clinical relevance of non-invasive imaging," *Heart*, 98, 10, 773-779, 2012.
- [32] K. Rakusan and R. J. Tomanek, "Distribution of mitochondria in normal and hypertrophic myocytes from the rat heart," *J. Mol. Cell. Cardiol.*, 18, 3, 299-305, 1986.
- [33] B. A. Roeder, K. Kokini, J. E. Sturgis, J. P. Robinson, and S. L. Voytik-Harbin, "Tensile mechanical properties of three-dimensional type I collagen extracellular matrices with varied microstructure," *J. Biomech. Eng.*, 124, 2, 214-222, 2002.
- [34] G. A. Holzapfel, *Nonlinear Solid Mechanics: A Continuum Approach for Engineering*. West Sussex, England: John Wiley & Sons, 2000.
- [35] X. Shi, L. Qin, X. Zhang, K. He, C. Xiong, J. Fang, X. Fang, and Y. Zhang, "Elasticity of cardiac cells on the polymer substrates with different stiffness: an atomic force microscopy study," *Phys. Chem. Chem. Phys.*, 13, 16, 7540-7545, 2011.
- [36] D. L. Sonin, T. Wakatsuki, K. V. Routhu, L. M. Harmann, M. Petersen, J. Meyer, and J. L. Strande, "Protease-activated receptor 1 inhibition by SCH79797 attenuates left ventricular remodeling and profibrotic activities of cardiac fibroblasts," *J. Cardiovasc. Pharmacol. Ther.*, 18, 5, 460-475, 2013.
- [37] Y. Yaniv, M. Juhaszova, S. Wang, K. W. Fishbein, D. B. Zorov, and S. J. Sollott, "Analysis of mitochondrial 3D-deformation in cardiomyocytes during active contraction reveals passive structural anisotropy of orthogonal short axes," *PLoS One*, 6, 7, e21985, 2011.
- [38] S. Krauss, "Mitochondria: structure and role in respiration," *eLS*, John Wiley & Sons, Ltd, 2011.

- [39] C. A. Opitz, M. Kulke, M. C. Leake, C. Neagoe, H. Hinssen, R. J. Hajjar, and W. A. Linke, "Damped elastic recoil of the titin spring in myofibrils of human myocardium," *PNAS*, 100, 22, 12688-12693, 2003.
- [40] J. W. Holmes, T. K. Borg, and J. W. Covell, "Structure and mechanics of healing myocardial infarcts," *Annu. Rev. Biomed. Eng.*, 7, 1, 223-253, 2005.
- [41] Y. Bogatyryov, R. J. Tomanek, and E. I. Dedkov, "Structural composition of myocardial infarction scar in middle-aged male and female rats: does sex matter?," *J. Histochem. Cytochem.*, 61, 11, 833-848, 2013.
- [42] P. Whittaker, R. A. Kloner, D. R. Boughner, and J. G. Pickering, "Quantitative assessment of myocardial collagen with picosirius red staining and circularly polarized light," *Basic Res. Cardiol.*, 89, 5, 397-410, 1994.
- [43] G. M. Tabel, P. Whittaker, K. Vlachonassios, M. Sonawala, and P. A. Chandraratna, "Collagen fiber morphology determines echogenicity of myocardial scar: implications for image interpretation," *Echocardiography*, 23, 2, 103-107, 2006.
- [44] J. H. Omens, T. R. Miller, and J. W. Covell, "Relationship between passive tissue strain and collagen uncoiling during healing of infarcted myocardium," *Cardiovasc. Res.*, 33, 2, 351-358, 1997.
- [45] R. J. McCormick, T. I. Musch, B. C. Bergman, and D. P. Thomas, "Regional differences in LV collagen accumulation and mature cross-linking after myocardial infarction in rats," *Am. J. Physiol. Heart Circ. Physiol.*, 266, 1, H354-H359, 1994.
- [46] J. B. Michel, J. L. Salzmann, N. M. Ossondo, P. Bruneval, D. Barres, and J. P. Camilleri, "Morphometric analysis of collagen network and plasma perfused capillary bed in the myocardium of rats during evolution of cardiac hypertrophy," *Basic Res. Cardiol.*, 81, 2, 142-154, 1986.
- [47] K. Vandoorne, M. H. Vandsburger, T. Raz, M. Shalev, K. Weisinger, I. Biton, V. Brumfeld, C. Raanan, N. Nevo, R. Eilam, B. A. Hemmings, E. Tzahor, A. Harmelin, L. Gepstein, and M. Neeman, "Chronic Akt1 deficiency attenuates adverse remodeling and enhances angiogenesis after myocardial infarction," *Circulation: Cardiovascular Imaging*, 6, 6, 992-1000, 2013.
- [48] J. D. Laird and H. P. Vellekoop, "The course of passive elasticity of myocardial tissue following experimental infarction in rabbits and its relation to mechanical dysfunction," *Circ. Res.*, 41, 5, 715-721, 1977.
- [49] G. Ertl and S. Frantz, "Healing after myocardial infarction," *Cardiovasc. Res.*, 66, 1, 22-32, 2005.
- [50] G. Agnoletti, A. Cargnoni, L. Agnoletti, M. Di Marcello, P. Balzarini, E. Pasini, G. Gitti, P. Martina, R. Ardesi, and R. Ferrari, "Experimental ischemic cardiomyopathy: insights into remodeling, physiological adaptation, and humoral response" *Ann. Clin. Lab. Sci.*, 36, 3, 333-340, 2006.
- [51] M. L. Hubbard and C. S. Henriquez, "Microscopic variations in interstitial and intracellular structure modulate the distribution of conduction delays and block in cardiac tissue with source-load mismatch," *Europace*, 14, suppl 5, v3-v9, 2012.

- [52] E. E. Popov, *Engineering Mechanics of Solids*. Englewood Clifs, NJ: Prentice-Hall, 1990.

## Chapter 3

# A Novel Biomechanical Computational Model of the Left Ventricle using a Composite Material Approach

*The material presented in this chapter is under review at the International Journal of Engineering Science.*

### 3.1 Introduction

COMPUTATIONAL models of cardiac mechanics and electrophysiology can be utilized as effective tools in clinical systems of diagnosis and patient-specific therapy planning [1-3]. These models can assist clinicians to classify myocardial pathologies, adopt appropriate therapeutic procedures, and even predict outcome of therapies [2,4-5]. The heart function is similar to that of a mechanical pump while any pathological condition is associated with mechanical alteration that may alter its efficiency. These alterations can be quantified in terms of parameters such as ejection fraction (EF), displacement, strain, and stress fields. For instance, prolonged hypertension yields significant elevation of end-systolic wall stress and depression of fractional fiber shortening, leading to thick-walled hypertrophic ventricles which is a cardiac physiological response to the associated excessive workload [6]. Cardiac ischemia is another prevalent coronary artery disease which may be followed by myocardial infarction (MI) in acute cases. Infarcted scar immediately exhibits a mechanical response (e.g. considerably weaker contraction compared to normal tissue) [7-9]. It is subsequently replaced by stiffer fibrous tissue following fibrosis phase. Stiffer collagenous scar remaining after fibrosis amplifies mechanical stress in the infarct region, leading to irregular stretching patterns within the myocardium [7-8]. Accordingly, local and global alterations of the mechanical response of

pathological myocardium can be utilized as valuable clinical data for effective diagnosis. Such alterations are quantifiable using accurate cardiac mechanics models.

Over the past few decades, diverse computational models of cardiac mechanics were developed based on various assumptions characterizing the cardiac tissue mechanics. While linearity and isotropy have been utilized as simplifying assumptions for myocardial modeling [10-12], it is well-known that cardiac tissue can be accurately characterized by anisotropic hyperelastic models [13-15]. The majority of hyperelastic anisotropic models postulate a constitutive law in the form of an overall strain energy function of cardiac tissue [16-20]. While efficient, such models are not easily adaptable for cardiac pathologies which are associated with substantial alterations in tissue microstructure and their corresponding properties [21-25]. Recent models consider different constitutive laws for the pathological part of the myocardium. For instance, [26-27] assign different constitutive laws to regions with left ventricular (LV) aneurysm. Moreover, with advances in cardiac tissue engineering and biomaterial therapies, pathological parts (e.g. ischemic lesions) are replaced by biomaterial with different mechanical properties [28-30] to improve the heart mechanical function and prevent further remodeling. Hence, it is desirable to have cardiac mechanics models adaptable to diverse pathological and therapeutic conditions by locally assigning altered mechanical properties based on existing knowledge of corresponding tissue microstructure alteration. Conventional FE-based cardiac computational models involve complex non-linear FE algorithms which are often implemented by custom-developed computer codes [16-19]. Such models are not easily adaptable for implementation in commercial software FE packages [5, 20]. Recently, valuable endeavors have been made to implement realistic diastolic and systolic cardiac mechanics models using available off-the-shelf FE software packages [31-32]. However, such implementations require user-defined subroutines which are not publicly available for the research community. Here, we propose a novel LV mechanical model which takes into account tissue anisotropy, hyperelasticity, and active fiber's contraction forces. An important feature of the proposed model is that it can be implemented in commercial FE software packages without requiring user-defined subroutines while it is easily adaptable to both normal and pathological LV's contraction scenarios. The novelty of the model is that it treats the myocardial tissue as a composite material including a background tissue

through which microscopic reinforcement bars (fibers) are distributed to undergo variable contraction forces. The model was utilized to mimic LV diastolic and systolic mechanical behavior and its contractile performance was compared with other *in silico* models and corresponding *in vivo* measurements.

## 3.2 Materials and Methods

### 3.2.1 Composite Material Model

The LV contracts as a result of contraction force generation within the cardiac fibers, leading to blood pressure alteration applied to its endocardial surface. In fact, cardiac contraction forces work to maintain this evolving blood pressure and to continue the LV contraction necessary for pumping the blood out of its cavity. As shown in Figure 3.1 (a), in the proposed FE mechanical model cardiac tissue is decomposed into two major parts: myofiber and background tissue (non-myofiber). The myofibers' contraction forces represent the active stress distribution through the LV fibers. This is consistent with well-established models of the heart muscle such as the three-element Hill's model [18]. In this model, the myocardial tissue is mechanically simulated using two parallel elements: active element (fiber) and passive elastic element (see Figure 3.1 (b)). The active and elastic elements represent the fibers while the passive element mimics the whole tissue. According to Hill's model, active contractile stresses are developed within the active elements. This leads to contraction in both of the active (element connected in series) and passive elements (connected in parallel) since there is bonding between the fibers and background part which prevents slipping along interfaces of the tissue ultrastructural parts. As illustrated in Figure 3.1 (a), this contraction creates stresses in both of the fibers (tension) and background (compression) such that mechanical equilibrium is maintained according to the momentum balance principle [33]. This tissue decomposition provides great flexibility to model patient-specific transverse isotropy of cardiac tissue [4-5,7-8], and to assign different passive mechanical properties and active contraction inputs to each part consistent with health/pathology state. It is noteworthy that alteration of each tissue part's mechanical properties influences both parts due to their bond. Furthermore, since each part consists of a single material, it is possible to use typical constitutive equations implemented in commercial FE software packages to describe its passive behavior. This approach allows



effective modeling of pathological microstructure alteration manifested differently in each part.

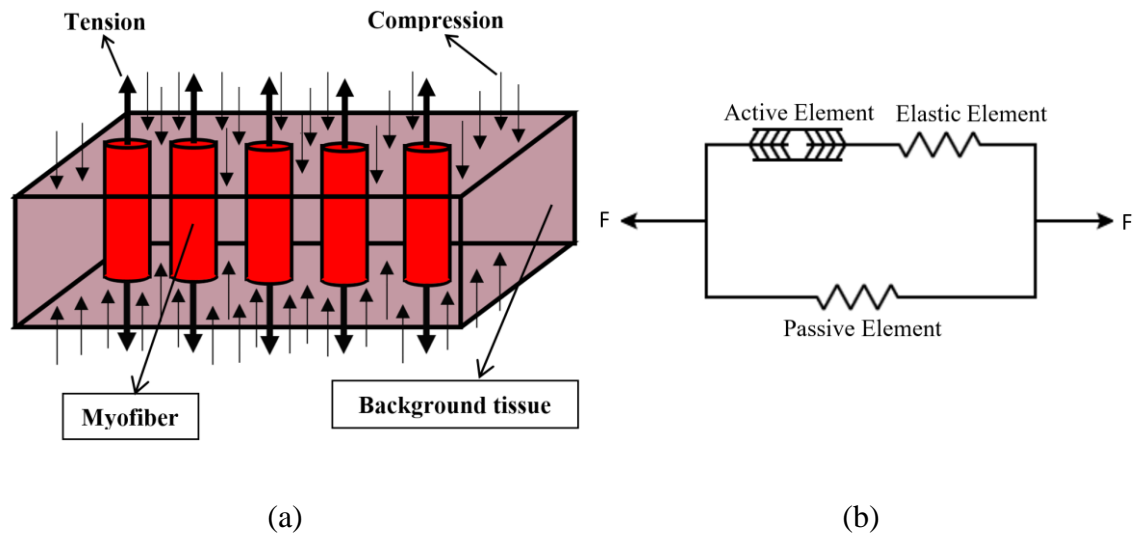


**Figure 3.1:** Schematic of composite model of cardiac tissue including two parts: myofibers and background while active contractile myofiber forces generate stresses in both parts of the tissue to maintain equilibrium according to the momentum balance principle (a), three-element Hill's model for cardiac tissue (b).

### 3.2.2 Major Elements of the LV Model

The FE based LV modeling approach is illustrated in Figure 3.2 [18]. A realistic LV geometry is used for FE simulation which may be obtained from cardiac MR image segmentation. In this work, we used realistic *in silico* geometry based on canine heart anatomy. This geometry was discretized into a FE mesh. All FE simulations presented in this study were conducted using the commercially available Abaqus/Standard FE solver [34]. In the proposed model, the myocardial tissue is considered as composite material consisting of two main parts: myofibers and background tissue. These parts are considered as building blocks of tissue in the FE model consisting of background tissue and reinforcement bars (fibers). The bars are prestressed incrementally to simulate myofibers' contraction as described in Section 3.2.3. Their orientations are in accordance with the fibrous cardiac anatomy, leading to a self-contained anisotropic model. As a result of applying prestress to the bars in each element while blood pressure is applied to the LV endocardial surface, the 3D LV model deforms. Since the LV undergoes large deformation during contraction while its tissue is intrinsically nonlinear, hyperelastic models are used

for modeling both of the background and fibers. The active contraction force is mimicked by applying longitudinal fibers' prestress along their directions. This prestress is input through ABAQUS as initial stress condition at the start of each loading increment. The blood pressure is assumed to be applied uniformly to the LV's endocardial surface. The model works based on equilibrium of the active stresses, passive stresses, and blood pressure of the LV tissue at each contraction instance of the cardiac cycle in accordance with the Cauchy's Equation of motion [33]. As shown in Figure 3.2, by applying the active stress and blood pressure to the LV model and through solving FE equations through ABAQUS, the LV's 3D displacement field can be achieved.

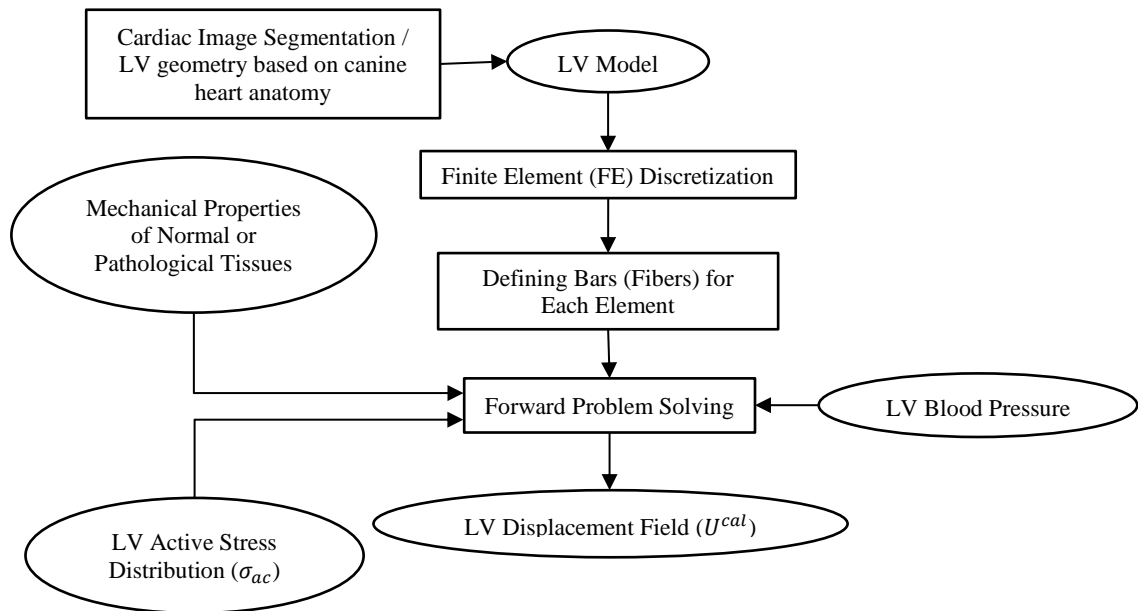


**Figure 3.2:** Flow chart illustrating biomechanical simulation of the LV.

The proposed model has three major inputs to conduct the FE modeling. The first input is endocardial LV blood pressure quantified according to the canine LV blood pressure data measured *in vivo* during a cardiac cycle [35]. The second input is time variable active fiber directional stress component which is generated according to the time-varying elastance model as described in Section 3.2.3. The third input is the mechanical properties of background tissue and myofibers.

### 3.2.3 Contraction Model and Elasticity Theory

Myocardial active fiber directional stress, which is a major input of the proposed model, is defined using the elastance model governed by the following Equation [36-37]:

$$T_0 = \frac{1}{2} T_{\max} \frac{Ca_0^2}{Ca_0^2 + ECa_{50}^2} C_t \quad (3.1)$$

where  $ECa_{50}$  is the length-dependent calcium sensitivity parameter [36-37]:

$$ECa_{50} = \frac{(Ca_0)_{\max}}{\sqrt{\exp[B(l-l_0)]-1}} \quad (3.2)$$

Here  $(Ca_0)_{\max}$ ,  $B$ ,  $l$ , and  $l_0$  are maximum peak calcium concentration, a constant, current sarcomere length, and sarcomere length at which no active tension develops, respectively.  $C_t$  is dependent on time after contraction onset,  $t$ , and  $l$  as follows [36-37]:

$$C_t = \frac{1}{2} (1 - \cos(\omega)) \quad (3.3)$$

where

$$\omega = \begin{cases} \pi \frac{t}{t_0} & \text{when } 0 \leq t < t_0 \\ \pi \frac{t-t_0+t_r}{t_r} & \text{when } t_0 \leq t < t_0+t_r \\ 0 & \text{when } t_0+t_r \leq t \end{cases} \quad (3.4)$$

Here  $t_0$  and  $t_r$  are time-to-peak tension constant and relaxation duration which is a linear function of  $l$ , i.e.  $t_r = ml + b$  where  $m$  and  $b$  are constants.  $l$  is calculated using fiber strain,  $E_{11}$ , i.e.  $l = l_R \sqrt{2E_{11} + 1}$  where  $l_R$  is the stress-free sarcomere length at reference configuration. The material constants used for our FE simulations were chosen according

to [37]:  $Ca_0 = 4.35 \mu\text{mol} / L$ ,  $(Ca_0)_{\max} = 4.35 \mu\text{mol} / L$ ,  $B = 4.75 \mu\text{m}^{-1}$ ,  $l_0 = 1.58 \mu\text{m}$ ,  $t_0 = 0.1 \text{ s}$ ,  $m = 1.0489 \text{ s} \cdot \mu\text{m}^{-1}$ ,  $b = -1.429 \text{ s}$ , and  $l_R = 1.85 \mu\text{m}$ . In this work,  $T_0$  is applied to the LV model incrementally through  $[0, t_0+t_i]$  using the above equations. This incremental active stress is applied as initial stress which leads to transfer of part of the stress to the background tissue after equilibrium is reached. The incremental approach used in ABAQUS for FE analysis under initial stresses is described in the next section. To model nonlinearity in both background tissue and myofibers, we considered the 2<sup>nd</sup> order Ogden hyperelastic model [33]:

$$\tilde{U} = \sum_{i=1}^N \frac{2\mu_i}{\alpha_i^2} (\lambda_1^{-\alpha_i} + \lambda_2^{-\alpha_i} + \lambda_3^{-\alpha_i} - 3) + \sum_{i=1}^N \frac{1}{D_i} (J_{el} - 1)^{2i} \quad (3.5)$$

where  $\alpha_i$  and  $\mu_i$  are hyperelastic coefficients, and  $\lambda_i$ s are principal stretches.

### 3.2.4 Calculation of LV Stresses under Initial Stress Condition

In the proposed method, the active stress is considered as initial stress in the LV myofibers. Assuming fiber direction along the local Z axis, this initial stress in tensor form is:

$$\tau_0 = \begin{bmatrix} 0 & 0 & 0 \\ 0 & 0 & 0 \\ 0 & 0 & T_0 \end{bmatrix} \quad (3.6)$$

where  $T_0$  is the time varying active stress as given in Equation (3.1) in the paper. To conduct FE analysis of composite hyperelastic material under initial stress ( $\tau_0$ ), one approach is founded based on deriving a strain energy function of deformation gradient  $F$  and the initial stress  $\tau_0$  in the form of  $U = U(F, \tau_0)$  [38-39]. Such strain energy functions have been derived for only few hyperelastic models with simple mathematical form (e.g. Neo-Hookean model). Derivation of such function for more complex hyperelastic models (e.g. Ogden model) is mathematically quite involved. ABAQUS follows a more general numerical approach that does not require deriving such a strain energy function, and it uses the material's original strain energy function. It follows the incremental loading method in conjunction with iterative nonlinear equations solution that ABAQUS uses to solve nonlinear FE models. This approach is described in the form of a pseudo code for

calculating stresses in LV model as follows. It is noteworthy that this code follows the composite background-rebar structure used to model the myocardial tissue in this work.

1. For current active fiber (rebar) stresses  $T_{ij}$  ( $i = 1, \dots, M$ ;  $j = 1, \dots, N$  where  $M$  and  $N$  are number of elements in the LV model and number of rebars in each element, respectively), which are calculated using Equation 1 in the paper, perform the following:
  - a. Obtain solution of the LV using the incremental loading approach by adding a very small increment  $\delta T_{ij}$  to the current loading of  $T_{ij}$ .
  - b. In each element  $i$  ( $i = 1, \dots, M$ ), calculate the start and end displacements of each fiber corresponding to  $\delta T_{ij}$  by ignoring the presence of background tissue. For this purpose, use fixed boundary conditions or current displacement estimate of the fiber's start as its start point displacement  $\delta_{ijs}$ . To calculate its end point's displacement  $\delta_{ije}$ , use the fiber's loading increment  $\delta T_{ij}$  and its tangent modulus consistent with the fiber's hyperelastic model and current  $T_{ij}$  to calculate the fiber's elongation corresponding to  $\delta T_{ij}$ . This elongation is added to the start point's displacement to obtain its end point displacement. This is performed for all fibers (rebars) in element  $i$  ( $j = 1, \dots, N$ ). It is noteworthy that fibers' start and end points displacements are calculated sequentially for the elements such that the fibers' start point displacements of the next element (for  $i = i + 1$ ) are known from the previous sequence.
  - c. Use the displacements obtained in b in conjunction with the element's shape function to calculate the element's nodal displacements corresponding to  $\delta T_{ij}$ .
  - d. At this stage, fibers' active stresses are zero as they reached their current " $l_0$ " length. This happens at the expense of compressing the background tissue, leading to disequilibrium. In order to reach equilibrium, ABAQUS uses the incremental loading approach towards  $-\delta T_{ij}$  ( $i = 1, \dots, M$ ;  $j = 1, \dots, N$ ). At a loading point  $-\alpha \delta T_{ij}$  where  $\alpha < 1$  in the incremental loading procedure, convergence towards force equilibrium cannot be achieved. The loading point prior to this point will be regarded as the solution corresponding to  $T_{ij} + \delta T_{ij}$ .

2. Set  $T_{ij}$  to  $T_{ij} + \delta T_{ij}$  and go to 1 unless  $T_{ij} + \delta T_{ij}$  has reached  $T_{ij} = T_{ij} + \Delta T_{ij}$  which is the next active stress of interest through the heart beat cycle.
3. Stop

### 3.2.4.1 Rebar Stress Calculation

To calculate the myofiber (rebar) stress using ABAQUS output which only pertain to background tissue, we start with myofiber's strain energy function  $U(I_1, I_2, I_3)$  where  $I_1$ ,  $I_2$ , and  $I_3$  are the strain invariants. For this strain energy function the Cauchy stress can be calculated using the following Equation [33]:

$$\boldsymbol{\sigma} = 2J^{-1} \left[ I_3 \frac{\partial U}{\partial I_3} \mathbf{I} + \left( \frac{\partial U}{\partial I_1} + I_1 \frac{\partial U}{\partial I_2} \right) \mathbf{B} - \frac{\partial U}{\partial I_2} \mathbf{B}^2 \right] \quad (3.7)$$

where  $\boldsymbol{\sigma}$ ,  $\mathbf{I}$ , and  $\mathbf{B}$  denote Cauchy stress tensor, identity tensor, and left Cauchy-Green deformation tensor, respectively. In addition,  $J$  is the volume ratio and  $\mathbf{B}$  is the left Cauchy-Green deformation tensor which is a function of the deformation gradient tensor  $F$ . These parameters are defined as follows [33]:

$$J = \sqrt{I_3} = \lambda_1 \lambda_2 \lambda_3 \quad (3.8)$$

$$\mathbf{B} = \mathbf{F}\mathbf{F}^T \quad (3.9)$$

where  $\lambda_i$ s represent principal stretches. Also,  $F = \nabla \vec{u} + I$  where  $I$  is the identity matrix and  $u$  is the displacement field. This tensor's components can be calculated as follows:

$$f_{ij} = \delta_{ij} + \frac{\partial u_i}{\partial x_j} \quad (3.10)$$

where  $\delta_{ij}$  is Kronecker delta and  $x_j$  denotes the  $j^{\text{th}}$  component of the coordinate system.

In the Ogden model, the strain energy function is in terms of principle stretches instead of strain scalar invariants. In this case the following derivatives need to be calculated before substituting in Equation (3.7):

$$\frac{\partial U}{\partial I_1} = \frac{1}{2} \left( \frac{1}{\lambda_1} \frac{\partial U}{\partial \lambda_1} + \frac{1}{\lambda_2} \frac{\partial U}{\partial \lambda_2} + \frac{1}{\lambda_3} \frac{\partial U}{\partial \lambda_3} \right) \quad (3.11-a)$$

$$\frac{\partial U}{\partial I_2} = \frac{1}{2} \left( \frac{1}{\lambda_1(\lambda_2^2 + \lambda_3^2)} \frac{\partial U}{\partial \lambda_1} + \frac{1}{\lambda_2(\lambda_1^2 + \lambda_3^2)} \frac{\partial U}{\partial \lambda_2} + \frac{1}{\lambda_3(\lambda_1^2 + \lambda_2^2)} \frac{\partial U}{\partial \lambda_3} \right) \quad (3.11-b)$$

$$\frac{\partial U}{\partial I_3} = \frac{1}{2\sqrt{I_3}} \left( \frac{1}{\lambda_2\lambda_3} \frac{\partial U}{\partial \lambda_1} + \frac{1}{\lambda_1\lambda_3} \frac{\partial U}{\partial \lambda_2} + \frac{1}{\lambda_1\lambda_2} \frac{\partial U}{\partial \lambda_3} \right) \quad (3.11-c)$$

Equation (3.7) can be used for rebar stress calculation with the rebars' left Cauchy-Green deformation tensor of each element calculated using Equation (3.9). The left Cauchy-Green deformation tensor obtained based on the above description is valid for the background tissue only as it is calculated using ABAQUS displacements pertaining to this tissue. Hence, it must be modified to obtain the rebar's counterpart. We assumed that the deformation field of the rebar is the same as the deformation field of the background tissue except the component in the rebar's direction. This component should be updated based on the initial stress of the rebar. We start with the strain  $\varepsilon_0$  that occurs in the rebar to achieve its zero state of stress which corresponds to  $l_0$ . This can be calculated using the rebar's 2<sup>nd</sup> order Ogden model in conjunction with the myofiber's current stress  $T_0$  calculated using Equation (3.1). As illustrated in Figure 3.3, the actual strain of the rebar is smaller than  $\varepsilon_0$  as the background part prevents it from full contraction. Assuming that the background tissue deformation is  $\Delta_b$  and that of the rebar corresponding to  $\varepsilon_0$  is  $\Delta_r$ ,  $\Delta_{r,bond}$  the rebar's actual deformation considering its bonding with the background tissue is  $\Delta_{r,bond} = \Delta_r - \Delta_b$ .

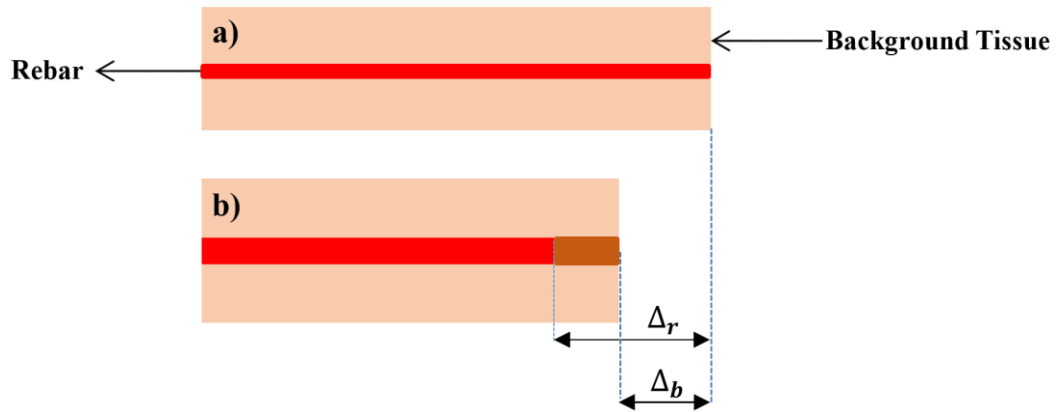


**Figure 3.3:** The rebar and background tissue in the reference state before contraction (a) and after contraction (b).

As such, the Cauchy-Green deformation tensor component of the rebar part which is in the rebar direction ( $b'_{zz}$ ) is:

$$b'_{zz} = \varepsilon_0 - b_{zz,background} \quad (3.12)$$

In developing Equation (3.12), it is assumed that the rebar is along the Z direction. The other components of the Cauchy-Green deformation tensor should be left intact as it is equal to those of the background tissue. The modified Cauchy-Green deformation tensor ( $B'$ ) is used in conjunction with Equation (3.7) to calculate the Cauchy Stress tensor of the rebars within each element.

### 3.2.5 *In silico* LV modeling

We applied the proposed technique to a canine LV *in silico* model [18] where we discretized the geometry into a FE mesh shown in Figure 3.4 (a). The fibers were simulated as bars (rebars in ABAQUS) aligned in layers in each element, occupying ~60% of its volume according to morphological measurements of the LV [40]. The rest of each element's volume was considered as non-myofiber part or background tissue where the fibers were distributed. The “rebars” orientations were incorporated into the LV geometry through alteration of the fiber helix angle from  $\sim -60^\circ$  at endocardium to  $\sim +60^\circ$  at epicardium [41-42]. To account for transmural fiber helix angle variations, the analytical model fitted to measurement data, as described in [18], was utilized.



For both of the background tissue and fibers, we applied hyperelastic models based on stress-strain data given in [43].

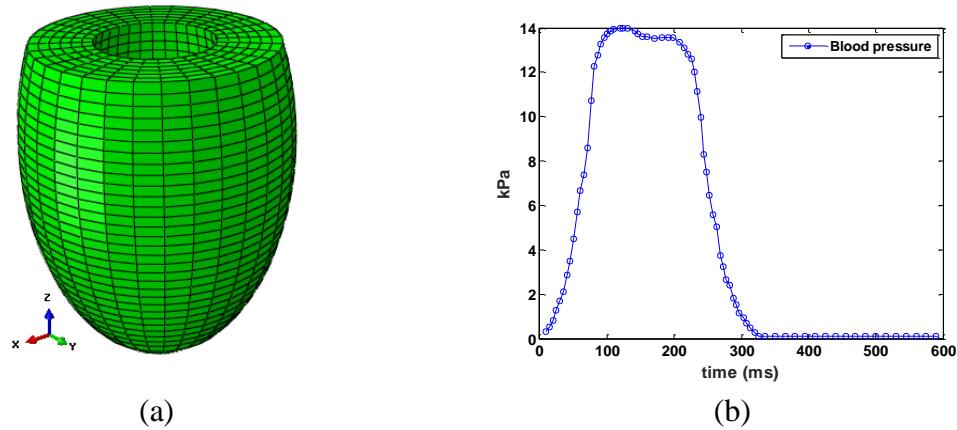


**Figure 3.4:** The *In silico* LV model constructed using finite elements (a), and blood pressure variations during a cardiac cycle [35-36].

### 3.2.5.1 Passive Inflation during Diastole

A major determinant of the passive mechanical function of the LV model is diastolic cavity pressure and volume variations. To assess these variations, following [44-46], the LV model was highly inflated using a maximum endocardial blood pressure of 3 kPa through 12 equal loading steps. For strain results comparison, blood pressure of 1 kPa was also applied [47-48].

### 3.2.5.2 Systolic LV Mechanics

Two phases were contemplated for systolic LV mechanics. The first is diastole where the LV model was inflated by 0.63 kPa blood pressure [49]. The second is systole where the myofibers contract with time-variable active stresses while the maximum isometric tension achieved at the longest sarcomere length,  $T_{\max}$  in Equation (3.1), was set to 150 kPa [37,47]. This parameter was iteratively determined such that reasonable EF value of 55% was observed. This EF value is within the normal range for a canine LV as reported in [50-51]. As indicated in [37,47], end-systole starts 350 ms after the end-diastolic instance. The contraction forces, were defined as initial stresses applied to the “rebars”. These stresses were applied incrementally in 10 separate time instances throughout a cardiac cycle according to the elastance model described in Section 3.2.3. The time-varying endocardial

LV blood pressure is illustrated in Figure 3.4 (b) where the maximum magnitude of blood pressure is  $\sim 14$  kPa [35,37,47]. This pressure was also applied incrementally in 10 separate time instances as a uniform pressure to the endocardial surface of the *in silico* model. The LV mechanical model presented here does not include the heart's atria, valves, or valve plane. As a result, the LV base is free to move and deform. Since the atria and valves hamper the deformation of the LV basal nodes, the longitudinal displacement of the LV basal nodes was restricted while the circumferential displacements of the epicardial basal nodes were also constrained, reflecting the LV model's boundary conditions. It is noteworthy that no boundary condition has been applied to the septum area where there is an interface between the LV and RV. This assumption is very common in the area of computational LV models as the lack of such a boundary condition is not expected to have a significant impact on the LV mechanical behavior due to its much thicker and more muscular structure compared to the RV wall. Such marked differences in the thickness and muscularity between the LV and RV imply minimal relative effect of the flabby RV wall on the LV mechanics.

### 3.3 Results

#### 3.3.1 Passive Inflation during Diastolic Phase

The LV volume was computed for each loading step corresponding to the 3 kPa pressure before being normalized to the unloaded volume of 40 ml. The calculated normalized pressure-volume relationship obtained using our model is shown in Figure 3.5. In this figure the pressure-volume curves obtained from another simulation study [42] and results of *ex vivo* measurements of a canine LV [45-46] are illustrated. Corresponding to the 1 kPa diastolic blood pressure, Figure 3.6 illustrates all passive strain components which are compared with those obtained from corresponding measurements [48] and another model [47]. Stress distribution through the LV model during diastolic phase was also assessed as illustrated in Figures 3.7 and 3.8. As composite material of background tissue and fiber is considered to model cardiac tissue, different stresses develop in each part that satisfy force equilibrium and deformation consistency. ABAQUS outputs stress distribution in the background tissue but not fiber stresses. Figure 3.7 illustrates transmural variations of maximum principle, radial, circumferential, and longitudinal stresses in the background

tissue. The longitudinal fiber stresses were calculated using  $T_0$  and the LV displacement field based on force equilibrium and deformation continuity at background/myofiber interface. This was further described in section 3.2.4.1. The transmural distribution of these fiber stresses along the LV wall thickness is illustrated in Figure 3.8 where the stresses at three regions of equatorial area, near base, and near apex are given.

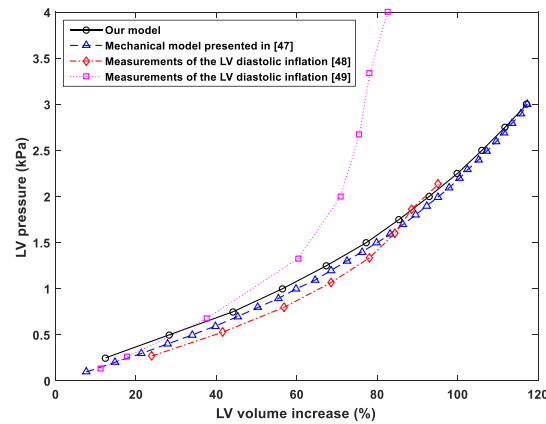
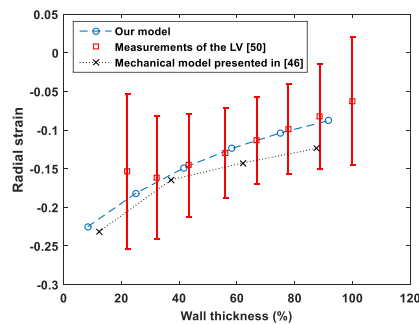
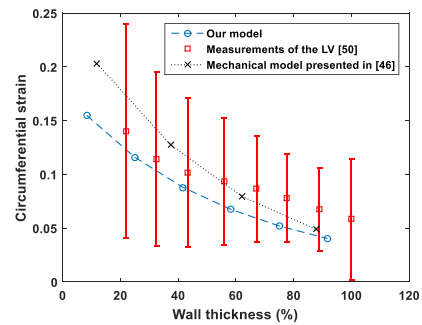


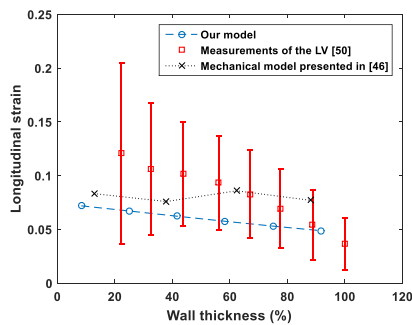
**Figure 3.5:** LV pressure-volume variations in diastolic phase.



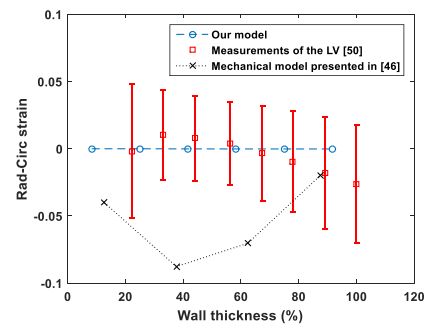
(a): Radial strain variation



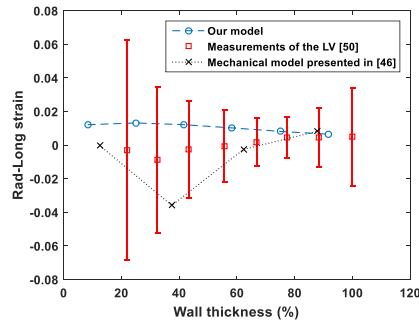
(b): Circumferential strain variation



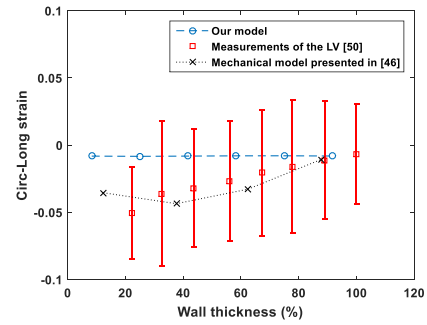
(c): Longitudinal strain variation



(d): Rad-circ. strain variation



(e): Rad-long strain variation



(f): Circ-long strain variation

**Figure 3.6:** Transmural variations of the passive strain components at the LV equatorial area from endocardium (indicated by 0) towards epicardium (indicated by 100) when a diastolic blood pressure of 1 kPa was applied to the LV model. The strains are referenced w.r.t the zero-stress unloaded configuration.

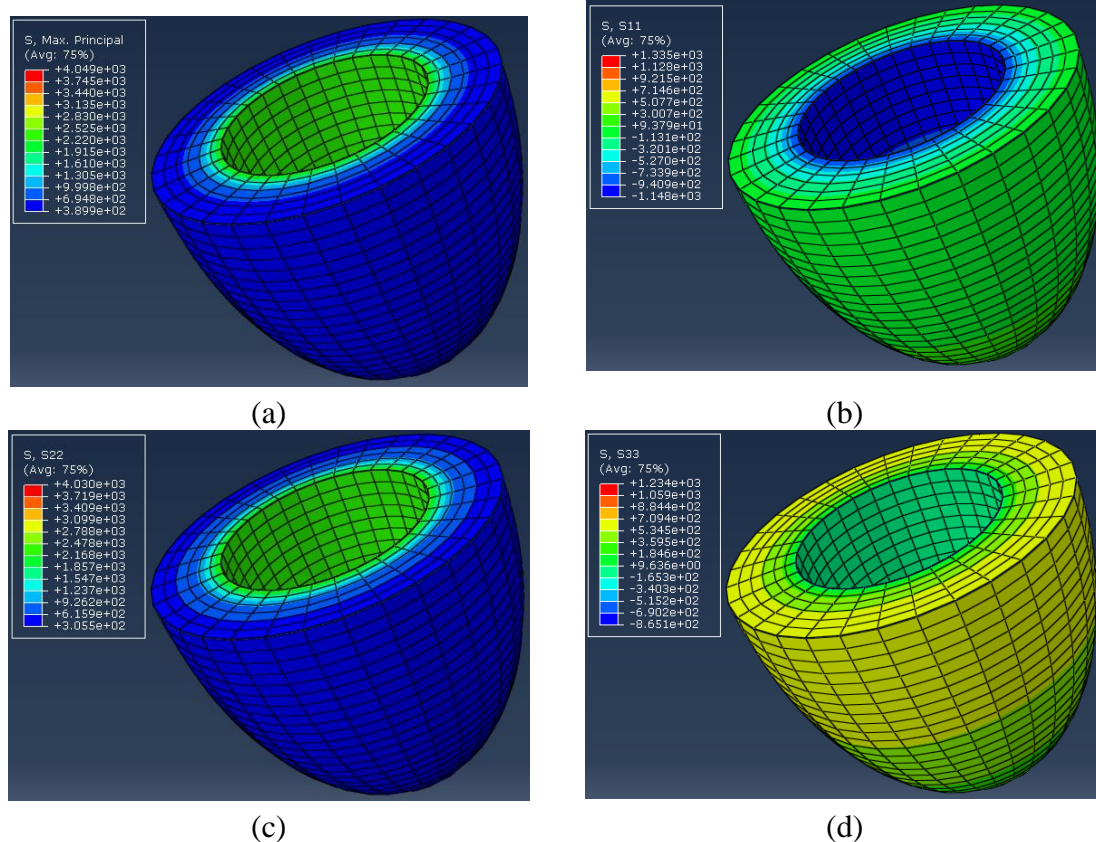


**Figure 3.7:** Transmural variations of the diastolic stress components within the background at the LV equatorial area from endocardium towards epicardium when a diastolic blood pressure of 1 kPa was applied to the LV model. Maximum principle stress (panel a), radial stress (panel b), circumferential stress (panel c), and longitudinal stress (panel d) are shown.

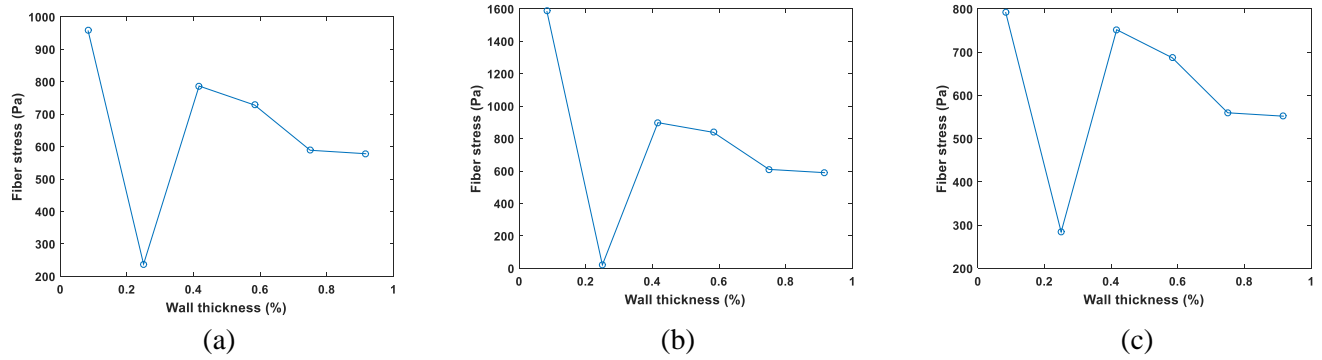
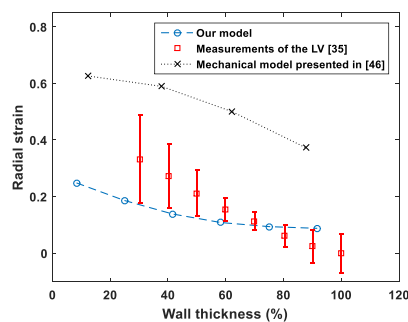


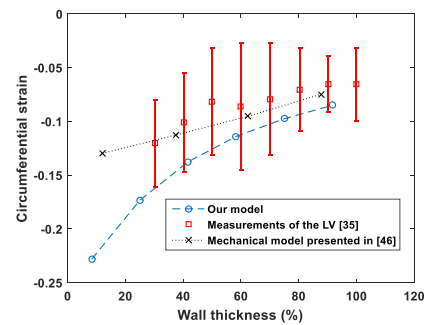
**Figure 3.8:** Transmurial variations of end-diastolic fibers stress at the equatorial area (a), transmurial variations of end-diastolic fibers stress near the base (b), and transmurial variations of end-diastolic fibers stress near the apex (c).

### 3.3.2 Systolic LV Mechanics

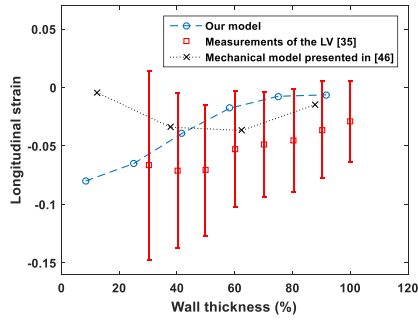
The systolic contraction of the model resulting from the time-variable loading described in Section 3.2.5.2 was evaluated by investigating all strain tensor components at end-systolic state which are illustrated in Figure 3.9. These strain components were compared with those obtained from corresponding LV function measurements [35] and the model presented in [47]. As an essential mechanical output of LV contraction, we also illustrated simulation results of stress distribution at end-systole through the LV model. Similar to diastolic phase, we presented distribution of these stresses within the background tissue part as provided by the FE solver (Figure 3.10) while the myofibers' stresses illustrated in Figure 3.11 were calculated using the FE solver outputs in conjunction with mechanical equilibrium conditions as described in section 3.2.4.1.



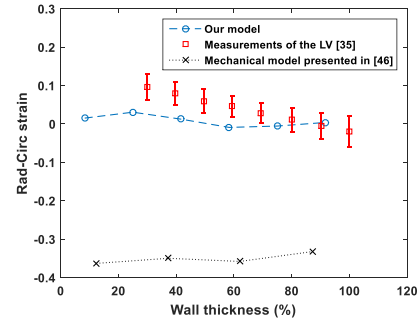
(a): Radial strain variation



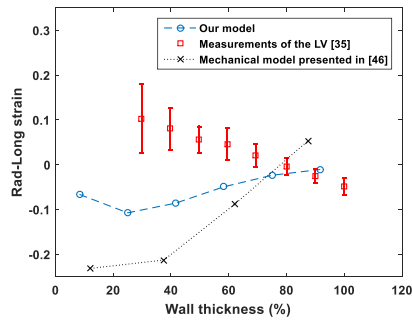
(b): Circumferential strain variation



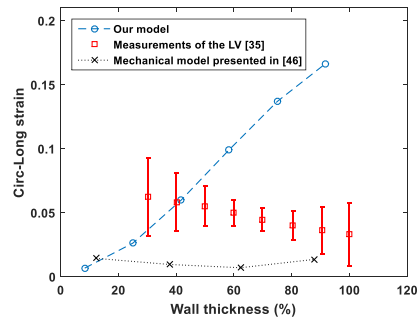
(c): Longitudinal strain variation



(d): Rad-circ. strain variation

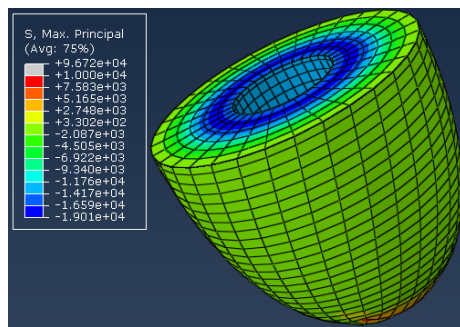


(e): Rad-long strain variation

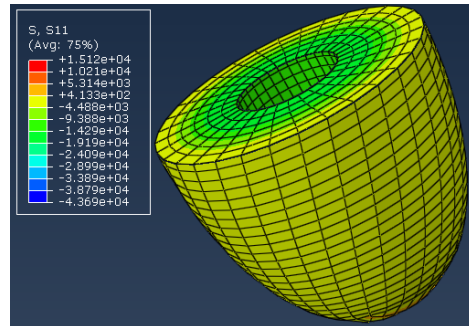


(f): Circ-long strain variation

**Figure 3.9:** Transmural variations of end-systolic strain components at the LV equatorial area from endocardium (indicated by 0) towards epicardium (indicated by 100) when time-variable active stress and blood pressure were applied to the LV model. The strains are referenced w.r.t end diastole.



(a)



(b)

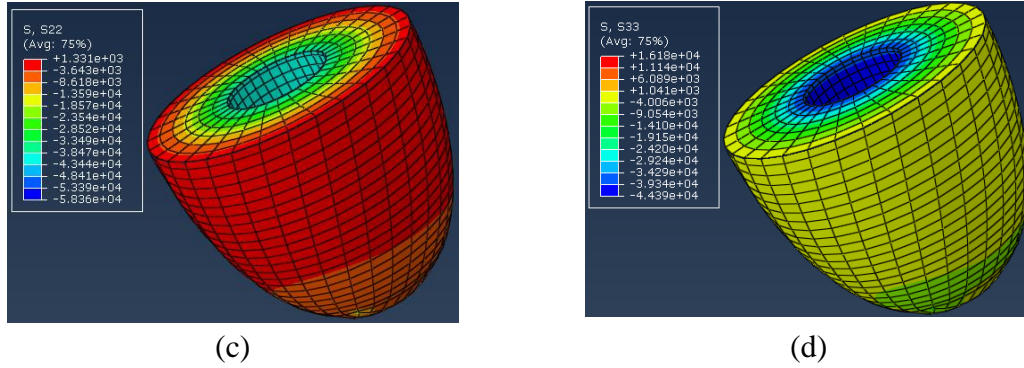


**Figure 3.10:** Transmural variations of end-systolic stress components within the background at the LV equatorial area from endocardium towards epicardium when time-variable active stress and blood pressure were applied to the LV model. Maximum principle stress (panel a), radial stress (panel b), circumferential stress (panel c), and longitudinal stress (panel d) are shown.

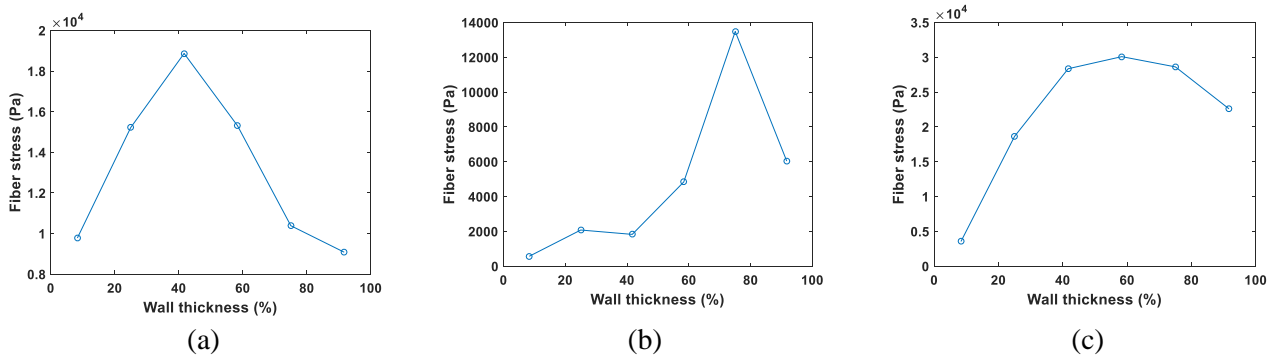


**Figure 3.11:** Transmural variations of end-systolic fibers stress at the equatorial area (a), transmural variations of end-systolic fibers stress near the base (b), and transmural variations of end-systolic fibers stress near the apex (c).

### 3.4 Discussion and Conclusions

In this article a novel approach for cardiac mechanics modeling is presented. The novelty of this model lies in decomposing the myocardial tissue into background tissue and microscopic reinforcement bars distributed throughout its volume. These “rebars” simulate myofibers where their orientation follow the LV fibrous anatomy, leading to a self-contained anisotropic model. Both of the background and myofibers parts were considered as hyperelastic materials. A major strength of the proposed model is that it can be implemented using off-the-shelf FE solvers with nonlinear analysis capability. It does not require complex custom-developed computer codes or user-defined subroutines while it incorporates all necessary mechanical complexities of the myocardial tissue. Moreover, it

is predicted that the proposed technique is more computationally efficient and less prone to divergence and computational instability as commercial FE codes are typically well integrated and optimized for high computational efficiency. The model was applied *in silico* to simulate a canine LV. Resulting parameters at diastole and systole phases were compared to corresponding canine experimental measurements and relevant LV computer models. The passive LV inflation quality was assessed based on pressure-volume variations obtained using the model illustrated in Figure 3.5. As seen in this figure, the calculated pressure-volume curve agrees reasonably well with experimental data acquired from 6 isolated potassium-arrested canine LVs [45]. These curves also show a good agreement with results obtained from Nash et al. model, especially at higher extensional blood pressures [44]. Passive transmural strain components distribution is also illustrated in Figure 3.6 where all three radial, circumferential, and longitudinal strain components agree well with the measurements and mechanical model. Moreover, the results show similar reduction or growth trends of corresponding strain components while moving from endocardium to epicardium. The good agreement achieved for pressure-volume variations and strains confirms validity of the diastolic performance of the presented LV model. The shear strain component results all fall within available measured range except circumferential-longitudinal strain component which is slightly underestimated at endocardium. It was noticed that calculated shear strain component profiles along LV thickness deviate slightly from patterns of corresponding experimental data. As indicated in [44,47,52], heterogeneity of LV tissue and imperfect anisotropy consistency maybe responsible for this deviation.

The passive stress distribution at end diastole in both parts of the cardiac tissue (i.e. background and myofiber) are shown in Figures 3.7 and 3.8. Figures 3.7 (a) and 3.7 (c) indicate that the maximum principle and circumferential stresses decrease from endocardium towards epicardium reflecting the higher influence of blood pressure loading at the endocardium. The radial stress is negative at endocardium and negligible at epicardium as observed in Figure 3.7 (b). This is reasonable since it is expected that the compressional effect of the blood pressure on the LV declines by moving from endocardial, reaching zero at epicardium consistent with boundary-conditions. The longitudinal stresses are tensile; they slightly increase from endocardium towards epicardium (see Figure 3.7



(d)). These stresses are consistent with the positive longitudinal strains which indicate LV elongation expected at diastole. The fiber stress variations are illustrated in Figures 3.8 (a), (b), and (c). It is maximum at the endocardial region and minimum at mid-wall which agrees with results presented in [31,47]. The maximum stress attained at the diastolic state in the fiber direction is 3.6 kPa which is in the range of the maximum stress reported in [31,47].

The systolic contraction of the LV model was validated by comparing all dimensional strain components distribution through the LV model (Figure 3.9). All three radial, circumferential, and longitudinal strains exhibit at least qualitative agreement while they are almost within measurement values obtained from anterior equatorial LV free wall of seven open-chest dogs reported in [35]. It is noteworthy that for radial strain, there is some insignificant overestimation at endocardial region and underestimation at epicardial region. However, considering the complexities of systolic ventricular function and comparing our systolic strains with those of the mechanical model presented in [47], confirm acceptable performance at systolic phase. Except the radial-circumferential strain component which are close to measured data, similar to other models [36-37,47], our model did not predict other shear strain components accurately.

The ventricular end-systolic stress distribution in both background tissue and myofibers was illustrated in Figures 3.10 and 3.11. The maximum principle stresses as shown in Figure 3.10 (a), increases from endocardium towards mid-wall where it has maximum value, then decreases towards epicardium. As observed in this figure, a uniform negative principle stress is generated through the midventricular area reflecting the overall contraction of the LV. The radial stress is also negative (Figure 3.10 (b)) except at the farthest epicardial region. It decreases uniformly from endocardium towards epicardium, again confirming validity of the model's contraction in the radial direction. The circumferential and longitudinal stresses (Figures 3.10 (c) and (d)) also decline from endocardium towards epicardium while their magnitude is negative (except for the most epicardial region for longitudinal stress), showing the LV model contraction in all directions. The longitudinal fiber stress (Figure 3.11) is maximum at mid-wall which is consistent with other LV models [31,41], again consolidating the validity of the proposed

model. The maximum fiber stress attained by the model is  $\sim 40$  kPa which agrees well with values reported in [31,41].

Based on the systolic and diastolic performance of the LV model, it can be concluded that the concept of decomposition of cardiac tissue into background and myofibers part is effective for simulating cardiac mechanics using off-the-shelf FE solver while it provides more control on both active response and passive properties of various parts of the tissue which is necessary for modeling various pathologies. Such flexibility is essential in developing FE-based inversion algorithm for quantification of more accurate stress distribution through realistic LV model obtained from imaging data.

## References

- [1] M. A. Hassan, M. Hamdi, and A. Noma, "The nonlinear elastic and viscoelastic passive properties of left ventricular papillary muscle of a Guinea pig heart," *J. Mech. Behav. Biomed. Mater.*, 5, 1, 99-109, 2012.
- [2] S. Marchesseau, H. Delingette, M. Sermesant, M. Sorine, K. Rhode, S. G. Duckett, C. A. Rinaldi, R. Razavi, and N. Ayache, "Preliminary specificity study of the Bestel-Clement-Sorine electromechanical model of the heart using parameter calibration from medical images," *J. Mech. Behav. Biomed. Mater.*, 20, 259-271, 2013.
- [3] K. F. Augenstein, B. R. Cowan, I. J. LeGrice, and A. A. Young, "Estimation of cardiac hyperelastic material properties from MRI tissue tagging and diffusion tensor imaging," *Medical Image Computing and Computer-Assisted Intervention – MICCAI*, LNCS 4190, 628-635, 2006.
- [4] G. Drzewiecki, J. Wang, J. K. J. Li, J. Kedem, and H. Weiss, "Modeling of mechanical dysfunction in regional stunned myocardium of the left ventricle," *IEEE Trans. Biomed. Eng.*, 43, 12, 1151-1163, 1996.
- [5] S. Goktepe and E. Kuhl, "Electromechanics of the heart: a unified approach to the strongly coupled excitation-contraction problem," *Comput. Mech.*, 45, 2-3, 227-243, 2010.
- [6] A. Christy, "Left ventricular wall mechanics in hypertension - an echocardiographic study," *Int. J. Biol. Med. Res.*, 3(1): 1267-1272, 2012.
- [7] M. Sermesant, H. Delingette, and N. Ayache, "An electromechanical model of the myocardium for cardiac image analysis and medical simulation," *INRIA Sophia Antipolis*, N° RR-5395, 2004.
- [8] A. I. Veress, W. P. Segars, B. M. W. Tsui, and G. T. Gullberg, "Incorporation of a Left Ventricle Finite Element Model Defining Infarction Into the XCAT Imaging Phantom," *IEEE Transactions on Medical Imaging*, vol. 30, no. 4, pp.915-927, 2011.
- [9] L. C. Lee, M. Genet, A. B. Dang, L. Ge, J. M. Guccione, and M. B. Ratcliffe, "Applications of computational modeling in cardiac surgery," *J. Card. Surg.*, 29(3), 293-302, 2014.
- [10] A. Nehorai and A. Jeremic, "Estimating mechanical properties of the left ventricle using dynamic modeling and magnetic resonance imaging," *Computers in Cardiology*, 25, 257-260, 1998.
- [11] B. P. Cupps, P. Moustakidis, B. J. Pomerantz, G. Vedala, R. P. Scheri, N. T. Kouchoukos, V. Davila-Roman, and M. K. Pasque, "Severe aortic insufficiency and normal systolic function: determining regional left ventricular wall stress by finite-element analysis," *Ann. Thorac. Surg.*, 76, 3, 668-675, 2003.
- [12] Z. Hu, D. Metaxas, and L. Axel, "In vivo strain and stress estimation of the heart left and right ventricles from MRI images," *Med. Image Anal.*, 7, 4, 435-444, 2003.

- [13] H. F. Choi, J. D'hooge, F. E. Rademakers, and P. Claus, "Influence of left-ventricular shape on passive filling properties and end-diastolic fiber stress and strain," *J. Biomech.*, 43, 9, 1745-1753, 2010.
- [14] H. M. Wang, H. Gao, X. Y. Luo, C. Berry, B. E. Griffith, R. W. Ogden, and T. J. Wang, "Structure-based finite strain modelling of the human left ventricle in diastole," *Int. J. Numer. Method. Biomed. Eng.*, 29, 1, 83-103, 2013.
- [15] K. D. Costa, P. J. Hunter, J. S. Wayne, L. K. Waldman, J. M. Guccione, and A. D. McCulloch, "A three-dimensional finite element method for large elastic deformations of ventricular myocardium: II—prolate spheroidal coordinates," *J. Biomech. Eng.*, 118, 4, 464-472, 1996.
- [16] S. Goktepe, S. N. S. Acharya, J. Wong, and E. Kuhl, "Computational modeling of passive myocardium," *Int. J. Numer. Method. Biomed. Eng.*, 27, 1, 1-12, 2011.
- [17] K. D. Costa, J. W. Holmes, and A. D. McCulloch, "Modelling cardiac mechanical properties in three dimensions," *Phil. Trans. R. Soc. Lond. A*, 359, 1783, 1233-1250, 2001.
- [18] P. H. M. Bovendeerd, T. Arts, J. M. Huyghe, D. H. Van Campen, and R. S. Reneman, "Dependence of local left ventricular wall mechanics on myocardial fiber orientation: a model study," *Journal of Biomechanics*, 25, 10, 1129-1140, 1992.
- [19] R. H. Keldermann, M. P. Nash, H. Gelderblom, V.Y. Wang, and A. V. Panfilov, "Electromechanical wavebreak in a model of the human left ventricle," *Am. J. Physiol. Heart Circ. Physiol.*, 299, 1, H134-H143, 2010.
- [20] H. Dal, S. Goktepe, M. Kaliske, and E. Kuhl, "A fully implicit finite element method for bidomain models of cardiac electromechanics," *Comput. Methods Appl. Mech. Eng.*, 253, 323-336, 2013.
- [21] A. M. Katz. *Physiology of the Heart*. Wolters Kluwer Health/Lippincott Williams & Wilkins Health, 2010.
- [22] J. W. Holmes, T. K. Borg, and J. W. Covell, "Structure and mechanics of healing myocardial infarcts," *Annu. Rev. Biomed. Eng.*, 7, 1, 223-253, 2005.
- [23] G. Ertl and S. Frantz, "Healing after myocardial infarction," *Cardiovasc. Res.*, 66, 1, 22-32, 2005.
- [24] G. Agnoletti, A. Cargnoni, L. Agnoletti, M. Di Marcello, P. Balzarini, E. Pasini, G. Gitti, P. Martina, R. Ardesi, and R. Ferrari, "Experimental ischemic cardiomyopathy: insights into remodeling, physiological adaptation, and humoral response" *Ann. Clin. Lab. Sci.*, 36, 3, 333-340, 2006.
- [25] M. L. Hubbard and C. S. Henriquez, "Microscopic variations in interstitial and intracellular structure modulate the distribution of conduction delays and block in cardiac tissue with source-load mismatch," *Europace*, 14, suppl 5, v3-v9. 2012.
- [26] K. Sun, N. Stander N, and C. Jhun, Z. Zhang, T. Suzuki, G. Wang, M. Saeed, A. W. Wallace, E. E. Tseng, A. J. Baker, D. Saloner, D. R. Einstein, M. B. Ratcliffe, and J. M. Guccione, "A computationally efficient formal optimization of regional

- myocardial contractility in a sheep with left ventricular aneurysm,” *ASME. J. Biomech. Eng.*, 131(11):111001-111001-10, 2009.
- [27] J. F. Wenk, K. Sun, Z. Zhang, M. Soleimani, L. Ge, D. Saloner, A. W. Wallace, M. B. Ratcliffe, and J. M. Guccione, “Regional left ventricular myocardial contractility and stress in a finite element model of posterobasal myocardial infarction,” *ASME. J. Biomech. Eng.*, 133(4):044501-044501-6, 2011.
- [28] J. F. Wenk, P. Eslami, Z. Zhang, C. Xu, E. Kuhl, J. H. Gorman III, J. D. Robb, M. B. Ratcliffe, R. C. Gorman, and J. M. Guccione, “A Novel Method for Quantifying the In-Vivo Mechanical Effect of Material Injected Into a Myocardial Infarction,” *Annals of Thoracic Surgery*, vol. 92, iss. 3, 935 – 941, 2011.
- [29] P. Zhang, J. M. Guccione, S. I. Nicholas, J. C. Walker, P. C. Crawford, A. Shamal, D. A. Saloner, A. W. Wallace, and M. B. Ratcliffe, “Left ventricular volume and function after endoventricular patch plasty for dyskinetic anteroapical left ventricular aneurysm in sheep,” *Journal of Thoracic and Cardiovascular Surgery*, vol. 130, iss. 4, 1032 – 1038, 2005.
- [30] C. Gálvez-Montón, C. Prat-Vidal, S. Roura, C. Soler-Botija, and A. Bayes-Genis, “Cardiac tissue engineering and the bioartificial heart,” *Rev. Esp. Cardiol.*, vol. 66, no. 05, 2013.
- [31] M. Genet, L. C. Lee, R. Nguyen, H. Haraldsson, G. Acevedo-Bolton, Z. Zhang, L. Ge, K. Ordovas, S. Kozerke, and J. M. Guccione, “Distribution of normal human left ventricular myofiber stress at end diastole and end systole: a target for *in silico* design of heart failure treatments,” *Journal of Applied Physiology*, 117 (2) 142-152, 2014.
- [32] M. Genet, L. C. Lee, B. Baillargeon, J. M. Guccione, and E. Kuhl, “Modeling pathologies of diastolic and systolic heart failure,” *Annals of Biomedical Engineering*, Jun. 5, 2015 [Epub ahead of print].
- [33] G. A. Holzapfel, [Nonlinear Solid Mechanics: A Continuum Approach for Engineering], Wiley, West Sussex, 141-152, 2000.
- [34] Hibbit, Karlsson, and Sorenson, *ABAQUS Theory Manual*. Pawtucket, RI, June 1998.
- [35] L. K. Waldman, D. Nosan, F. Villarreal, and J. W. Covell, “Relation between transmural deformation and local myofiber direction in canine left ventricle,” *Circulation Research.*, 63:550-62, 1988.
- [36] J. M. Guccione and A. D. McCulloch, “Mechanics of active contraction in cardiac muscle: Part I--Constitutive relations for fiber stress that describe deactivation,” *J. Biomech. Eng.*, 115(1):72-81, 1993.
- [37] J. M. Guccione, L. K. Waldman, and A. D. McCulloch, “Mechanics of active contraction in cardiac muscle: Part II--Cylindrical models of the systolic left ventricle,” *J. Biomech. Eng.*, 115(1):82-90, 1993.
- [38] M. Shams, M. Destrade, and R. W. Ogden, “Initial stresses in elastic solids: Constitutive laws and acoustoelasticity,” *Wave Motion*, 48 (7): 552-567, 2011.

- [39] A. L. Gower, P. Ciarletta, and M. Destrade, "Initial stress symmetry and its applications in elasticity," *Proc. R. Soc. A*, 471 20150448, 2015.
- [40] J. Schaper, E. Meiser, and G. Stammner, "Ultrastructural morphometric analysis of myocardium from dogs, rats, hamsters, mice, and from human hearts," *Circulation.*, 56(3), 377-391 (1985).
- [41] D. D. Streeter, M. H. Spotnitz, D. P. Patel, J. Ross, and E. H. Sonnenblick, "Fiber orientation in the canine left ventricle during diastole and systole," *Circ. Res.*, 24: 339-347, 1969.
- [42] T. Arts, P. C. Veenstra, and R. S. Reneman, "Epicardial deformation and left ventricular wall mechanisms during ejection in the dog," *Am. J. Physiol.*, 243(3):H379-90, 1982.
- [43] J. D. Humphrey, R. K. Strumpf, and T. C. P. Yin, "Determination of a constitutive relation for passive myocardium: II. - parameter estimation," *J. Biomech. Eng.*, 112, pp. 340-346, Aug. 1990.
- [44] M. P. Nash, P. J. Hunter, "Computational Mechanics of the Heart," *Journal of elasticity and the physical science of solids*, vol. 61, iss. 1, pp 113-141, 2000.
- [45] A. D. McCulloch, B. H. Smaill, and P. J. Hunter, "Regional left ventricular epicardial deformation in the passive dog heart," *Circ. Res.*, 64(4):721-33, 1989.
- [46] A. D. McCulloch, P. J. Hunter, and B. H. Smaill, "Mechanical effects of coronary perfusion in the passive canine left ventricle," *Am. J. Physiol.*, 262(2 Pt 2):H523-30, 1992.
- [47] J. M. Guccione, K. D. Costa, and A. D. McCulloch, "Finite element stress analysis of left ventricular mechanics in the beating dog heart," *J. Biomech.*, 28(10):1167-77, 1995.
- [48] J. H. Omens, K. D. May, and A. D. McCulloch, "Transmural distribution of three-dimensional strain in the isolated arrested canine left ventricle," *Am. J. Physiol.*, 261(3 Pt 2):H918-28, 1991.
- [49] F. J. Villarreal, W. Y. Lew, L. K. Waldman, and J. W. Covell, "Transmural myocardial deformation in the ischemic canine left ventricle," *Circ. Res.*, 68(2):368-81, 1991.
- [50] H. Childs, L. Ma, M. Ma, J. Clarke, M. Cocker, J. Green, O. Strohm, and M. G. Friedrich, "Comparison of long and short axis quantification of left ventricular volume parameters by cardiovascular magnetic resonance, with ex-vivo validation," *Journal of Cardiovascular Magnetic Resonance*, 13:40, 2011.
- [51] D. D. Sisson, G. B. Daniel, and A. R. Twardock, "Comparison of left ventricular ejection fractions determined in healthy anesthetized dogs by echocardiography and gated equilibrium radionuclide ventriculography," *Am. J. Vet. Res.*, 50(11):1840-7. 1989.
- [52] V. P. Novak, F. C. P. Yin, and J. D. Humphrey, "Regional mechanical properties of passive myocardium," *J. Biomechanics*, 27, 403-412, 1994.

## Chapter 4

# A Biomechanical Model of the Pathological Left Ventricle using a Composite Material Approach

*The material presented in this chapter has been submitted to Journal of Medical Engineering and Physics.*

### 4.1 Introduction

**H**EART diseases have attracted considerable attention in the medical community as the leading cause of death worldwide in all genders and ethnicities [1]. There is a wide spectrum of cardiac conditions such as rheumatic, hypertensive, ischemic, and inflammatory heart disease that can potentially hamper the critical heart role as a mechanical pump required to provide oxygen and nutrition throughout the body. Significant research efforts have been dedicated to various aspects of heart disease. Some of these efforts have been geared towards understanding of various cardiac pathologies including gaining insight into their early and late symptoms and complications, developing accurate methods for diagnosis and prognosis of these pathologies, and eventually treating them effectively and possibly least invasively [2-6]. To achieve these goals, a suite of tools are being developed including tools for mechanical modeling of pathological heart [7-10].

One of the important applications of cardiac mechanical models is to provide insight into normal heart's pump function [2-3]. These models can also provide valuable insight into how specific pathological changes ensue certain mechanical alterations in the heart, leading to specific impediment in the heart function [11-13]. For instance, a mechanical model of the canine left ventricle (LV) under ischemic states, including immediate myocardial infarction, was developed using finite element (FE) method by applying instantaneous partial or complete loss of contractility to the ischemic region of the LV [14]. This study concluded that geometrical changes of the LV is directly related to the level and size of the

ischemia within the LV wall, leading to depression of the stroke volume and ejection fraction (EF). Short QT syndrome (SQTS) is a cardiac arrhythmogenic disease which was investigated using an electromechanical model of the LV [15]. Through 3D displacements of the LV model obtained from simulations under SQTS condition, this investigation confirmed dissociation between ventricular repolarization and the end-systole mechanics which is in accordance with qualitative clinical observations.

Other than their applications in generating LV functional data covering various types of pathologies with variable severities, myocardial mechanical models are applied to devise novel computer assisted therapeutic techniques for cardiac diseases and to predict outcome of planned treatments. Heart failure is a common adverse medical incident after ischemic cardiomyopathy. It gradually progresses as a result of cardiac remodeling. The Dor procedure is a surgical procedure used for restoring LV size, shape, and wall stress by replacing infarcted LV wall with endoventricular circular patch plasty. Using an LV biomechanical model, a Dor procedure performed on a male sheep was modeled and its anticipated mechanical function was studied through mechanical simulation [16]. The simulation showed remarkable increase in the EF matching experimental data obtained six weeks after the procedure, hence confirming the effectiveness of this therapy. Other research work used similar approach to investigate the mechanical consequences of injecting biocompatible hydrogels within infarcted LV regions, demonstrating the applicability of this treatment to prevent LV remodeling by reducing the average wall stress in both infarcted and remote areas [17-18].

Given its strength in modeling arbitrary geometries and tissue intrinsic properties, cardiac mechanical models have been used for an exciting application of patient-specific clinical diagnosis and therapy planning. For this purpose medical imaging in conjunction with cardiac mechanical simulators are utilized to personalize heart mechanical models towards more accurate simulations of patients' pathologic heart [19-25]. Typical methods proposed for clinical diagnosis of heart diseases using imaging data utilize two approaches of 1) machine learning algorithms and 2) mechanical modeling in addition to inverse FE methods. In the first approach, visual clinical features such as LV wall motion, size, mass, geometry, and function characterizers such as EF pertaining to patients with known



diagnosis are identified/determined using cardiac imaging data such as ultrasound or magnetic resonance (MR) [19-22]. This processed data is used to train a mathematical function using a machine learning framework. After training and validation such function can be used to diagnose new cases. Some other studies utilized similar strategies such as Bayesian inference and Markov Chain Monte Carlo method for cardiac mechanics and electrophysiology model personalization through polynomial chaos and compressed sensing [21-22]. The second approach of utilizing inverse FE methods received significant attention over the past decade [23-28]. In [23-24,26-27], inverse FE approach was employed to match infarcted LV FE model based volume and strains with those of corresponding MR imaging data through systematically adjusting active response of the remote and border zones of cardiac tissue in the FE model. In [25,28] the same strategy was applied to adjust the active response of the cardiac tissue but a more complex non-homogeneous distribution of tissue active response with higher resolution was utilized, providing more flexibility in mimicking local variations of the tissue response. In the case of inversion algorithm schemes, the core of all presented methods is a forward mechanical model of the LV which should be run iteratively within an optimization framework. Such a model must meet two essential requirements including computational efficiency and adaptability to model a heart disease with a range of severity. In this paper, we propose a novel mechanical model of the infarcted LV. This model can be utilized to investigate cardiac function under various forms and degrees of LV infarction. Furthermore, because of its effective implementation, it is expected to be highly adaptable for a broad range of infarction forms and intensities, rendering it suitable for inversion-based strategies. The model can be implemented using off-the-shelf FE software packages. It is founded on a composite model which decomposes cardiac tissue into background tissue and myofibers modeled as bars under initial stresses. The model was applied to an *in silico* infarcted LV and results showed good agreement with data obtained through *in vivo* measurements.

## 4.2 Materials and Methods

### 4.2.1 Composite Material Model

Contraction force development within cardiac tissue fibers is the major element in the contractile function of the myocardium. Superposition of local active contraction forces

yields a considerable net shortening force through the whole myocardium which overpowers the evolving endocardial blood pressure leading to pumping the blood out of heart's cavity. Through the entire cardiac cycle, mechanical equilibrium between different forces, i.e. active contractile forces, passive tissue stresses and blood pressure, is maintained at each point within the LV. To mathematically describe the mechanical equilibrium at each point of the myocardium, in accordance with the three-element Hill's model [29] the myocardial tissue is modeled using two parallel elements: active element (fiber) and passive elastic element (see Figure 4.1). The active and elastic elements simulate the mechanical function of the fibers while the passive element represents the contribution of the background part of the tissue encompassing the fiber part. Consistent with this model, the proposed FE model decomposes the cardiac tissue into two parts of myofiber and background tissue (non-myofiber). The myofibers' contraction forces represent the active stress distribution through the LV fibers. Due to connection between fibers and background tissue, contraction in the fibers during systole leads to contraction in both parts of the tissue. As suggested by Hill's model (Figure 4.1), this contraction creates stresses in both of the fibers (tension) and background (compression) which continues until the mechanical equilibrium is reached under the well-known momentum balance principle in continuum mechanics [30]. The described tissue decomposition into passive and active (fibers) parts make it technically feasible to model cardiac tissue anisotropy in a self-contained way [4,31-33]. Moreover arbitrary intrinsic mechanical properties and active contraction force inputs can be assigned to each part of the tissue, rendering the model adaptable to model diverse pathologies. In the proposed model, the cardiac tissue strain compatibility is consistent with assuming full bonding between myofibers and background tissue. A major advantage of the tissue decomposition scheme used in the model is that each tissue part can be assigned intrinsic mechanical properties independent from the other. This is quite advantageous as it facilitates utilizing off-the-shelf FE software packages to model a wide range of pathological tissues based on our understanding of tissue ultrastructure changes resulting from the pathologies.

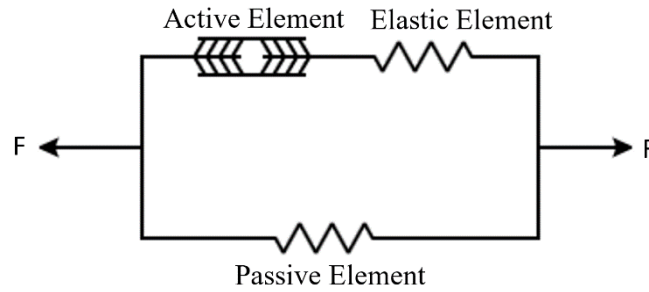


**Figure 4.1:** Three-element Hill's model for cardiac tissue.

#### 4.2.2 Major Elements of the LV Model

The flowchart of the proposed FE based model is shown in Figure 4.2. In this work, we used a realistic *in silico* LV geometry developed based on canine heart anatomy [29]. A more realistic subject-specific LV geometry may be obtained by segmenting the subject's cardiac MR or ultrasound image. The LV geometry was discretized into a number of finite elements to create the FE mesh shown in Figure 4.3. All FE simulations presented in this study were conducted using the commercially available Abaqus/Standard FE solver [34].

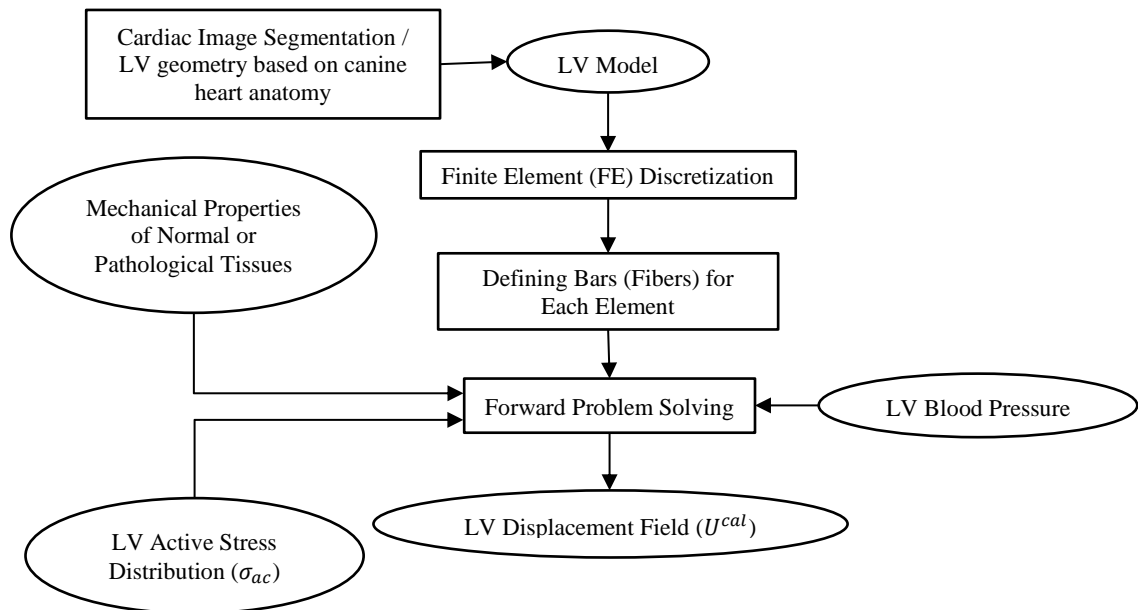


**Figure 4.2:** Flow chart illustrating biomechanical simulation of the LV.

The model was applied to an infarcted LV case using the chosen geometry, leading to the FE mesh shown in Figure 4.3 (b). This infarcted LV model was constructed by considering

an almost circular infarction within the LV wall similar to the one in [24]. The infarction area is transmural while it expands from endocardium towards epicardium [23-24]. As illustrated in Figure 4.3 (c), this *in silico* infarction model also includes myocardial thinning and remodeling which were introduced by reducing the LV wall thickness at the infarct area by about 40% in comparison with the thickness of the normal wall region [32]. A border zone surrounding the infarcted region with depressed contractile function was also introduced consistent with myocardial infarction (MI) pathological features [23-24]. The thickness of the LV wall at the border zone was reduced by about 20% compared to the normal region [32]. A cross section view of the LV with the border zone is shown Figure 4.3 (c).

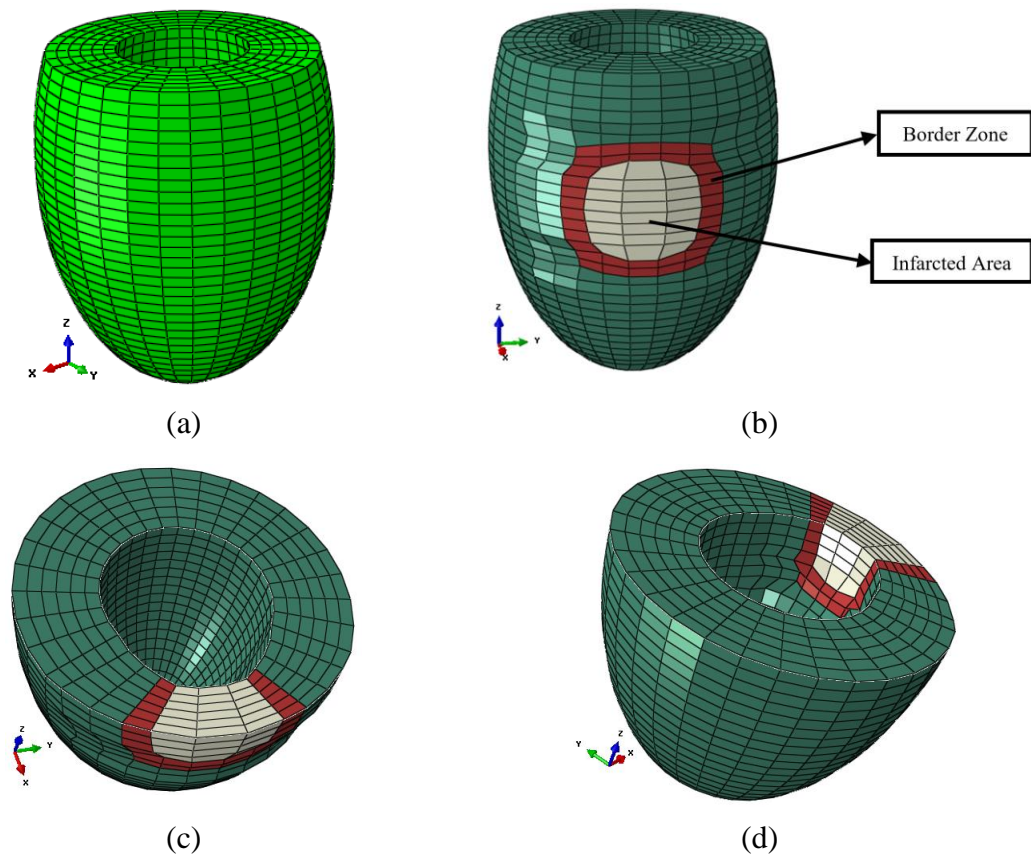


**Figure 4.3:** *In silico* normal and infarcted LV models constructed using finite elements: normal LV model (a), infarcted LV model with a circular infarcted region and border zone (b), and cross-section of the infarcted LV model with myocardial thinning from different views (c,d).

In the proposed model, the LV muscle tissue is idealized as a composite material consisting of two parts of myofibers and background tissue. These parts are utilized as the building blocks of the proposed LV finite element model. These blocks consist of fibers modeled by reinforcement rebars (fibers) and background tissue where the fibers are embedded. The rebars are prestressed incrementally to simulate myofibers' active contraction within the tissue while their orientations follow the fibrous cardiac anatomy, leading to a self-contained anisotropic model. The prestress is applied as an initial stress condition at the start of each loading increment. To incorporate large deformations and intrinsic nonlinearity into the mechanical modeling of the LV, hyperelastic models are used for modeling both of the background tissue and fibers. Blood pressure is assumed to be uniformly distributed on the LV's endocardial surface. The model works based on the well-known Cauchy's Equation of motion enforcing the equilibrium of the active stresses, passive stresses, and blood pressure of the LV tissue at each contraction instance of the cardiac cycle [30]. To conduct FE analysis, the mechanical loads of active stress and blood pressure are applied to the LV model and the FE equations are solved, leading to the LV's 3D displacement field. Accordingly, the FE LV simulation in the proposed method has three major inputs. The first is endocardial LV blood pressure quantified according to the canine LV blood pressure data measured *in vivo* during a cardiac cycle [35]. The second is time variable longitudinal active fiber stress which is governed by the time-varying elastance model presented in [36-37]. The last is the hyperelastic parameters of background tissue and myofibers. For the normal cardiac tissue, measured stress-strain data given in [38] were used to determine the hyperelastic parameters of the passive background tissue and myofibers along their direction. For the infarct, the stress-strain curves given in [39] for infarcted myocardium were used to calculate the hyperelastic parameters of the background tissue and myofibers in their directions.

#### 4.2.3 Contraction Model and Elasticity Theory

In the proposed model, the time variations of the active fiber longitudinal stress follow the elastance model which is described using the following Equation [36-37]:

$$T_0 = \frac{1}{2} T_{\max} \frac{Ca_0^2}{Ca_0^2 + ECa_{50}^2} C_t \quad (4.1)$$

Here  $T_{\max}$  and  $(Ca_0)$  are the maximum isometric tension at the longest sarcomere length and intercellular calcium concentration, respectively.  $ECa_{50}$  is the length-dependent calcium sensitivity parameter which is a function of maximum peak calcium concentration, current sarcomere length, and sarcomere length at which no active tension develops, respectively.  $C_t$  is a time-dependent parameter described as follows:

$$C_t = \frac{1}{2} (1 - \cos(\omega)) \quad (4.2)$$

where  $\omega$  depends on time after contraction onset, sarcomere length, time-to-peak tension, and relaxation duration [37]. Mathematical details of the elastance model including Equations and the values chosen for the constants of this model are given in [36-37]. Active fiber directional stress,  $T_0$ , in the proposed model is applied to the myofibers incrementally following this elastance model. This incremental active stress is exerted as initial stress to the myofibers which is partially transferred to the background tissue due to the bond between myofibers and background tissue. A description of FE analysis of the LV model under this incremental active stress using ABAQUS is given in Section 4.2.4.

Nonlinear elastic behavior has been considered for both background tissue and myofibers according to the 2<sup>nd</sup> order Ogden hyperelastic model described by the following strain energy function [30]:

$$U = \sum_{i=1}^N \frac{2\mu_i}{\alpha_i^2} (\lambda_1^{-\alpha_i} + \lambda_2^{-\alpha_i} + \lambda_3^{-\alpha_i} - 3) \quad (4.3)$$

where  $\alpha_i$  and  $\mu_i$  are hyperelastic coefficients, and  $\lambda_i$ s are principal stretches. Mechanical properties given in [38,39] for normal and infarcted cardiac tissues were fitted to the above hyperelastic model and the acquired parameters were utilized for the FE analysis.

## 4.2.4 Finite Element Analysis of LV under Incremental Initial Stresses

### 4.2.4.1 FE Analysis using Incremental Loading Scheme

In our strategy, for active cardiac contraction modeling, the active stress is applied as initial stress to the myofiber part of the tissue. The myofiber's initial stress tensor assuming myofibers along the local z-axis can be written as:

$$\tau_0 = \begin{bmatrix} 0 & 0 & 0 \\ 0 & 0 & 0 \\ 0 & 0 & T_0 \end{bmatrix} \quad (4.4)$$

where  $T_0$  is the active fiber longitudinal stress described in Equation (4.1). For computational modeling of this active stress, FE formulation of hyperelastic material undergoing initial stress ( $\tau_0$ ) can be achieved using one of two possible approaches. One is founded on a strain energy function of deformation gradient  $F$  and the initial stress  $\tau_0$  [40-41] which can be derived through a complex mathematical procedure. Apart from complexity encountered in deriving the required strain energy function, its incorporation in the ABAQUS FE solver requires coding extra subroutines before analysis can be conducted. The other approach, which fits the objective of the proposed technique, is implemented in ABAQUS and uses its incremental formulation scheme in conjunction with an iterative procedure for nonlinear FE analysis under initial stress loading. The numerical technique involved in this approach is described through the following pseudo code which is given for computing the LV fiber parts' stress:

1. Active fiber (rebar) stresses  $T_{ij}$  ( $i = 1, \dots, M; j = 1, \dots, N$  where  $M$  and  $N$  denote number of elements in the model and number of rebars in each specific element, respectively), given in Equation (4.1) are updated for the current time through the following algorithm:
  - a. Use the incremental loading approach by adding a small increment  $\delta T_{ij}$  to the fiber stress of  $T_{ij}$  and solving new FE equilibrium equations of the LV model.
  - b. Obtain displacements of the start and end of each fiber in each element resulting from stress change  $\delta T_{ij}$  while disregarding the interactions of the myofibers and

background tissue. This can be carried out for each fiber based on the hyperelastic model of the myofiber describing its stiffness.

- c. Calculate the element's nodal displacements arising from fiber stress change  $\delta T_{ij}$  using the displacements attained in step b and the element's shape functions.
  - d. With ignoring the interaction between the myofibers and background tissue in steps a through to c the myofibers are at zero state of stress while the background is compressed, leading to dissatisfaction of the LV force equilibrium equations. To restore force equilibrium, ABAQUS uses this disequilibrium state as an initial guess and incrementally changes fiber stress loading iteratively using its Newton Raphson nonlinear solver until convergence is achieved. At this stage the solution sought for the  $T_{ij} + \delta T_{ij}$  loading point is reached.
2. Update the initial fiber stress  $T_{ij}$  to  $T_{ij} + \delta T_{ij}$  and go back to step 1 unless  $T_{ij} + \delta T_{ij}$  exceeds the last active stress point in the heartbeat cycle.

Stop.

#### 4.2.4.2 Myofiber's Stress Calculation

ABAQUS merely outputs the stress of the background tissue while the rebar stress is also needed to have a more precise evaluation of the heart function. To obtain myofiber's stress, we use strain energy function of the myofibers,  $U(I_1, I_2, I_3)$ , where  $I_1$ ,  $I_2$ , and  $I_3$  are the strain invariants. As such, the myofiber's Cauchy stress can be calculated based on the strain energy function as follows [42]:

$$\boldsymbol{\sigma} = 2J^{-1} \left[ I_3 \frac{\partial U}{\partial I_3} \mathbf{I} + \left( \frac{\partial U}{\partial I_1} + I_1 \frac{\partial U}{\partial I_2} \right) \mathbf{B} - \frac{\partial U}{\partial I_2} \mathbf{B}^2 \right] \quad (4.5)$$

In the above equation  $\boldsymbol{\sigma}$  and  $\mathbf{B}$  are Cauchy stress and left Cauchy-Green strain tensor, respectively. The left Cauchy-Green strain tensor,  $\mathbf{B}$ , is a function of the deformation gradient tensor  $F$  as follows [42]:



$$B = FF^T \quad (4.6)$$

Also,  $F = \nabla \vec{u} + I$  where  $I$  is the identity matrix and  $u$  is the displacement field. Ogden strain energy function used to describe myofibers hyperelastic behavior (Equation 4.3), is in terms of principle stretches not strain scalar invariants. As such the following Equations can be utilized to obtain the derivatives of the strain energy function with respect to the scalar invariants:

$$\frac{\partial U}{\partial I_1} = \frac{1}{2} \left( \frac{1}{\lambda_1} \frac{\partial U}{\partial \lambda_1} + \frac{1}{\lambda_2} \frac{\partial U}{\partial \lambda_2} + \frac{1}{\lambda_3} \frac{\partial U}{\partial \lambda_3} \right) \quad (4.7-a)$$

$$\frac{\partial U}{\partial I_2} = \frac{1}{2} \left( \frac{1}{\lambda_1(\lambda_2^2 + \lambda_3^2)} \frac{\partial U}{\partial \lambda_1} + \frac{1}{\lambda_2(\lambda_1^2 + \lambda_3^2)} \frac{\partial U}{\partial \lambda_2} + \frac{1}{\lambda_3(\lambda_1^2 + \lambda_2^2)} \frac{\partial U}{\partial \lambda_3} \right) \quad (4.7-b)$$

$$\frac{\partial U}{\partial I_3} = \frac{1}{2\sqrt{I_3}} \left( \frac{1}{\lambda_2\lambda_3} \frac{\partial U}{\partial \lambda_1} + \frac{1}{\lambda_1\lambda_3} \frac{\partial U}{\partial \lambda_2} + \frac{1}{\lambda_1\lambda_2} \frac{\partial U}{\partial \lambda_3} \right) \quad (4.7-c)$$

Now Equation (4.5) can be used for rebar stress calculation with the rebars' left Cauchy-Green deformation tensor of each element calculated using Equation (4.6). The only component we need to use Equation (4.5) for rebar's stress calculation, is rebar's displacements to calculate rebars' left Cauchy-Green strain tensor. ABAQUS displacements outputs pertain to the background tissue while the displacement of the myofibers can be achieved by manipulation of the background tissue displacement data. The deformation field of the rebar is assumed to be the same as the deformation field of the background tissue in all directions except for the component in the rebar's direction. To obtain this component, we can first calculate the rebar deformation with ignoring the rebar and background interactions using the rebar's Ogden model and the myofiber's current stress obtained from Equation (4.1). The actual rebar deformation is smaller than the calculated deformation as the background part attaches the rebars precluding its full contraction. In fact, under equilibrium condition longitudinal rebar deformations can be attained by subtraction of the computed displacement with no background tissue effects from the background tissue displacement in the rebar direction obtained from ABAQUS

output. Assuming that the background tissue deformation is  $\Delta_b$  and that of the rebar corresponding to  $l_0$  is  $\Delta_r$ ,  $\Delta_{r,bond}$  the rebar's actual deformation is  $\Delta_{r,bond} = \Delta_r - \Delta_b$ . As such, the longitudinal Cauchy-Green deformation tensor component of the rebar is  $b'_{zz} = \varepsilon_0 - b_{zz,background}$  where  $\varepsilon_0$  corresponds to rebar full contraction corresponding to  $l_0$ .

#### 4.2.5 *In silico* Infarcted LV Modeling

The contraction of normal LV model attained by applying previously described time-variable blood pressure and active stress to the LV geometry using a similar modeling approach was investigated elsewhere [43]. For the infarcted canine LV, the geometry was first discretized into a FE mesh consisting of 6336 8-noded hexahedral elements and 13880 nodes. Further refinement of this mesh did not lead to substantial changes in the resulting strain and stress fields. After FE meshing, layers of “rebars” were distributed in each element in the healthy tissue part, mimicking the myofibers. For this part the “rebars” occupied ~60% of each element volume according to LV morphological measurements [44]. The background part of the tissue occupied the remaining element volume. The myofiber directions within the LV was determined according to the analytical helical model presented in [45-46]. As indicated earlier, Ogden hyperelastic parameters fitting the measured stress-strain data [38] was utilized to model background tissue and myofibers at non-infarcted parts. For elements in the infarct region, according to morphological studies [47], merely 5% of the tissue volume was considered to be myofibers while the rest is occupied by the background tissue (see Figure 4.4). While the myofiber orientations in the normal LV tissue follows a helix angle varying from  $\sim -60^\circ$  at endocardium to  $\sim +60^\circ$  at epicardium [45-46], the myofibers within the infarct region were aligned mainly circumferentially where the fibers helix angle was set to zero [24,48-49]. Compared to healthy LV muscle tissue, at the infarct region (hyperelastic parameters) consistent with higher stiffness were assigned to fibers and background tissue in accordance with the measurements reported in [39].

Two phases were considered for the LV function modeling including diastole and systole. In the diastolic phase, the LV model was inflated by blood pressure [50], while in the systolic phase the myofibers contract with active stresses varying with time according to

the elastance model. The maximum isometric tension at the longest sarcomere length,  $T_{\max}$  in Equation 1, was set to 150 kPa for normal LV modeling [37,51]. At the border zone, the active fiber stress was depressed by adjusting  $T_{\max}$  at 75 kPa which entails 50% reduction in comparison to normal tissue [23-24]. This parameter was set to zero at the infarct region, implying no active contraction at this part due to expected death of the majority of myocytes [23-24].

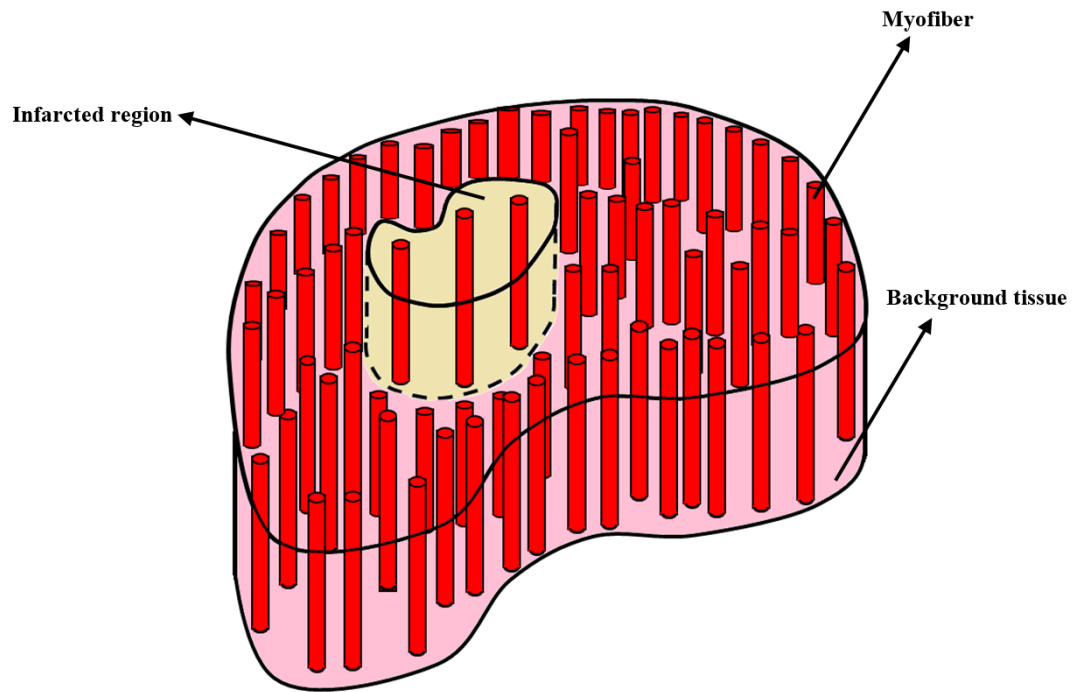


**Figure 4.4:** Infarcted region with lower volume percentage of myofibers surrounded by normal cardiac tissue with higher volume percentage of myofibers.

As indicated earlier, the active contraction forces in the proposed model, which follow the elastance model, were mimicked as initial stresses on the “rebars” which were applied incrementally to the model. Time varying endocardial LV blood pressure consistent with LV measurements illustrated in Figure 4.5 was applied incrementally to the LV endocardial surface [35,37,51]. As boundary condition of the model, the longitudinal displacements of the LV basal nodes and circumferential displacements of the epicardial basal nodes were set to zero.

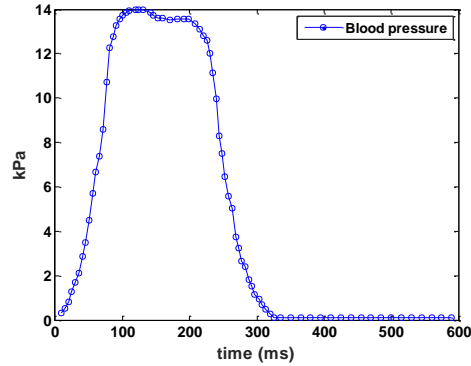


**Figure 4.5:** Blood pressure variations during a cardiac cycle [35].

### 4.3 Results

Full results of the normal canine LV model are reported in [43]. In this case EF of 58% was achieved by setting  $T_{\max}$  to 150 kPa. This EF value is within the normal range for a canine LV [52-53]. Result highlights pertaining to the normal LV model are summarized in Tables 4.1 and 4.2 where they summarize end-systolic strain and stress results, respectively.

**Table 4.1:** End-systolic radial, circumferential, and longitudinal strains in normal LV

Radial	Positive at equatorial area with a maximum value of ~30% at endocardium
Circumferential	Mainly negative with a maximum value of ~-24% at endocardium
Longitudinal	Negative at midventricular area with maximum value of ~8% at endocardium

These results agree well with those obtained from corresponding LV function measurements [35] and the mechanical model presented in [51].

**Table 4.2:** Transmural variations of end-systolic radial, circumferential, longitudinal, and fiber stresses in normal LV

Principal	Maximum is negative at the equatorial area with a value of ~20 kPa at endocardium
Radial	Negative at endocardium and positive at epicardium with greater magnitudes at endocardium while the maximum value in the background part is ~20 kPa
Circumferential	Mainly negative with large negative values at endocardium and small positive values at epicardium. The endocardial stress is ~38 kPa at midventricular area
Longitudinal	Mainly negative with large negative values at endocardium and small positive values at epicardium. The endocardial stress is ~35 kPa at midventricular area

Fiber	Maximum occurring at mid-wall are ~7 kPa, ~10 kPa, and ~24 kPa near base, at equatorial area, and near apex, respectively
-------	---

The infarcted LV contracts as a result of development of active stress within the fibrous part of the healthy cardiac tissue while the blood pressure is applied to the LV endocardial surface as described in section 4.2.5, maintaining equilibrium. For FE analysis, we considered different mechanical properties for healthy and infarcted tissue based on the stress-strain data presented in [38-39]. The second order Ogden hyperelastic model was used to fit the given data corresponding to the background tissue and myofibers for both healthy and infarcted tissues, leading to the following hyperelastic parameters which were used for the FE simulation:

**Table 4.3:** Hyperelastic parameters of the 2<sup>nd</sup> order Ogden model used for normal tissue mechanical simulation

Second Order Ogden Hyperelastic Parameters	Myofiber	Background Tissue
$\mu_1$ (Pa)	330.68	283.73
$\alpha_1$	13.21	8.81
$\mu_2$ (Pa)	0.0345	45.14
$\alpha_2$	38.96	17.73

**Table 4.4:** Hyperelastic parameters of the 2<sup>nd</sup> order Ogden model used for infarcted tissue mechanical simulation

Second Order Ogden Hyperelastic Parameters	Myofiber	Background Tissue
$\mu_1$ (Pa)	47194	41375
$\alpha_1$	0.0817	0.25
$\mu_2$ (Pa)	407.25	99.99
$\alpha_2$	37.06	31.22

The proposed FE model showed that the contraction of the infarcted LV leads to an EF value of 48%, implying over 10% reduction compared to the healthy LV. The performance of the infarcted LV model was further assessed by evaluating the three major strain components at end-systolic state which are illustrated in Figure 4.6. This figure indicates that the radial strain is tensile and non-uniformly distributed within the healthy tissue part. Moving towards the infarction region, it becomes relatively uniform with small magnitudes. The figure also shows that, in contrast to radial strain, circumferential strains in the healthy part are compressive with small spatial variability. These strains become tensile within the infarction region. Finally, the figure shows that longitudinal strains are compressive but slightly smaller in magnitude within the infarct region.

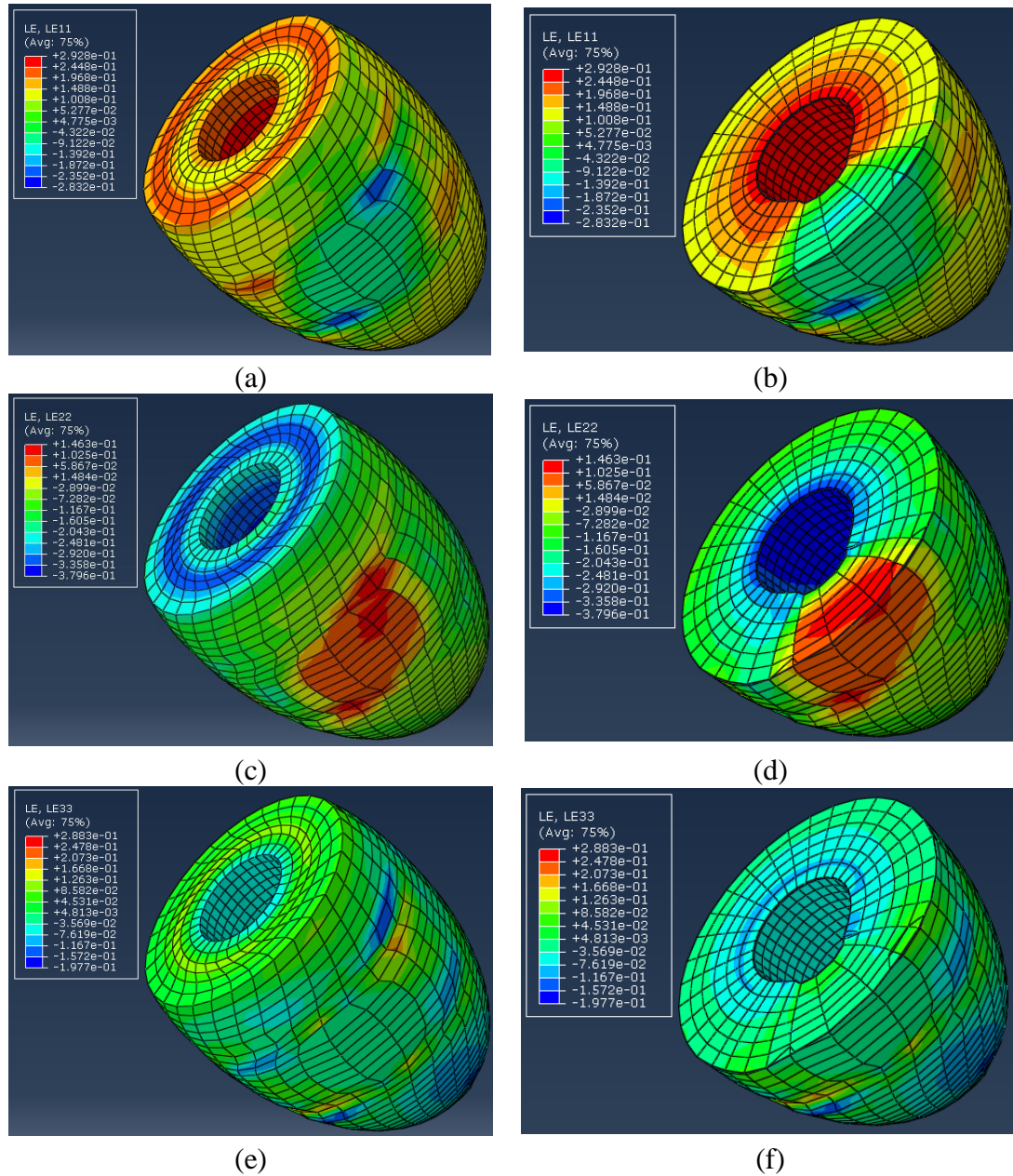


**Figure 4.6:** End-systolic strain distribution through the infarcted LV model. The strains are referenced w.r.t end diastole. Radial strain distribution (a), cross sectional view of the radial strain distribution at midventricular area (b), circumferential strain distribution (c), cross sectional view of the circumferential strain distribution at midventricular area (d), longitudinal strain distribution (e), cross sectional view of the longitudinal strain distribution at midventricular area (f).

The average values of radial, circumferential, and longitudinal strains in different regions of the LV were also calculated and reported in Table 4.5:

**Table 4.5:** Average values of end-systolic radial, circumferential, and longitudinal strains at the three regions of the infarcted LV

<b>Strain (%)</b> <b>Region</b>	Radial	Circumferential	Longitudinal
Remote (non-infarcted)	17.50	-16.18	-5.27
Border Zone	5.22	-7.55	-1.87
Infarcted	-4.31	4.48	-1.17

For comparison, corresponding circumferential strain values in different regions of the infarcted LV measured using tagged MR images in addition to the ones obtained using other mechanical models are given in the following Table [24]:

**Table 4.6:** Average values of end-systolic circumferential strains in the three regions of infarcted LV [24]

<b>Strain (%)</b> <b>Region</b>	Proposed LV FE model	Tagged MR imaging	Other LV FE model
Remote (non-infarcted)	-16.18	-14.2	-13.01
Border Zone	-7.55	-8.44	-7.16
Infarcted	4.48	2.70	4.70

For further evaluation, the end-systolic circumferential and longitudinal strains variations at the equatorial area are depicted in Figures 4.7 and 4.8. These strains are given along the circumference of the LV for the healthy (presented in Chapter 3) and infarcted LV models. For comparison, Figures 4.7 and 4.8 also illustrate strain changes obtained from measurements and other mechanical model of the LV contraction with MI [24]. It is noteworthy that the circumferential and longitudinal strain variations along the circumference pertaining to the normal model are very smooth. The positive spiky pattern of the strains pertaining to the infarcted region in the infarcted LV model is due to the lack of contraction in this region.

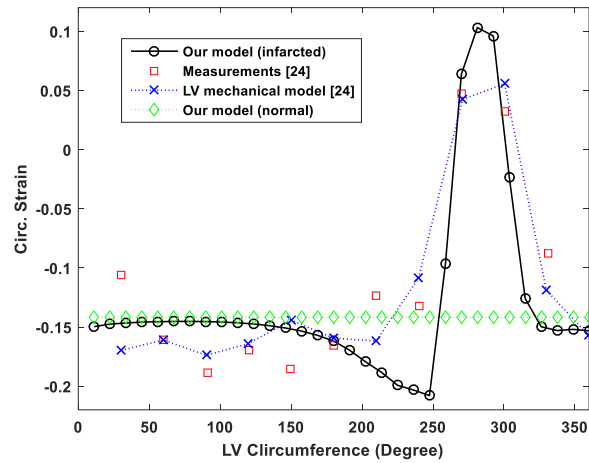


**Figure 4.7:** Circumferential strain variations with respect to the circumference of the LV at the equatorial area of the infarcted and normal models.

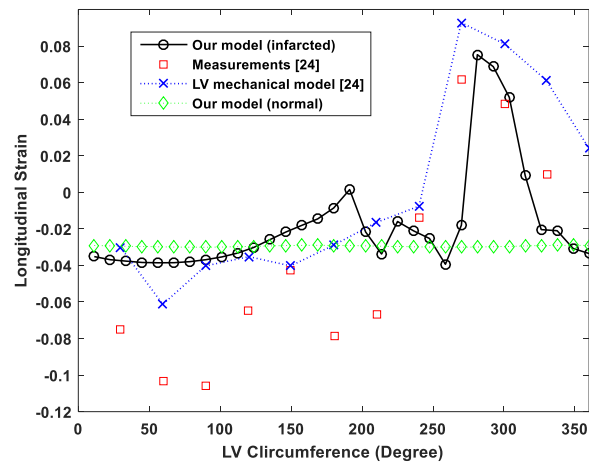


**Figure 4.8:** Longitudinal strain variations with respect to the circumference of the LV at the equatorial area of the infarcted and normal models.

For a more comprehensive performance demonstration of the proposed LV model, stress distribution at end-systole was also calculated. Distribution of the three normal stresses and the maximum principal stress components pertaining to the background tissue are shown in Figure 4.9 while the transmural variations of myofibers' longitudinal stress in the three tissue regions of healthy, border zone, and infarction are illustrated in Figure 4.10. These were calculated using the FE solver displacement outputs and  $T_0 \neq 0$  in conjunction with mechanical equilibrium conditions as described in Section 4.2.4. Figure 4.9 indicates that the maximum principal stress is mainly negative in the healthy tissue region and it becomes



tensile with little spatial variation within the infarct region. The figure also shows that the first normal stress  $S_{11}$  in the infarct region is similar in magnitude to that of healthy region but somewhat less regularly distributed. It also shows that  $S_{22}$  is significantly higher in the infarct region compared to healthy region while  $S_{33}$  exhibits only little elevation in the infarct region compared to the healthy region. Figure 4.10 illustrates the transmural variations of end-systolic fiber stresses in the infarct, border zone, and healthy regions. Figures 4.10 (a) and (b) indicate that the minimum fibers stresses in the infarct and border zone regions occur in the mid-wall region while they are close to zero and compressive, respectively. Figure 4.10 (c) demonstrates that the maximum tensile fiber stress in the healthy tissue region occurs in the mid-wall region.

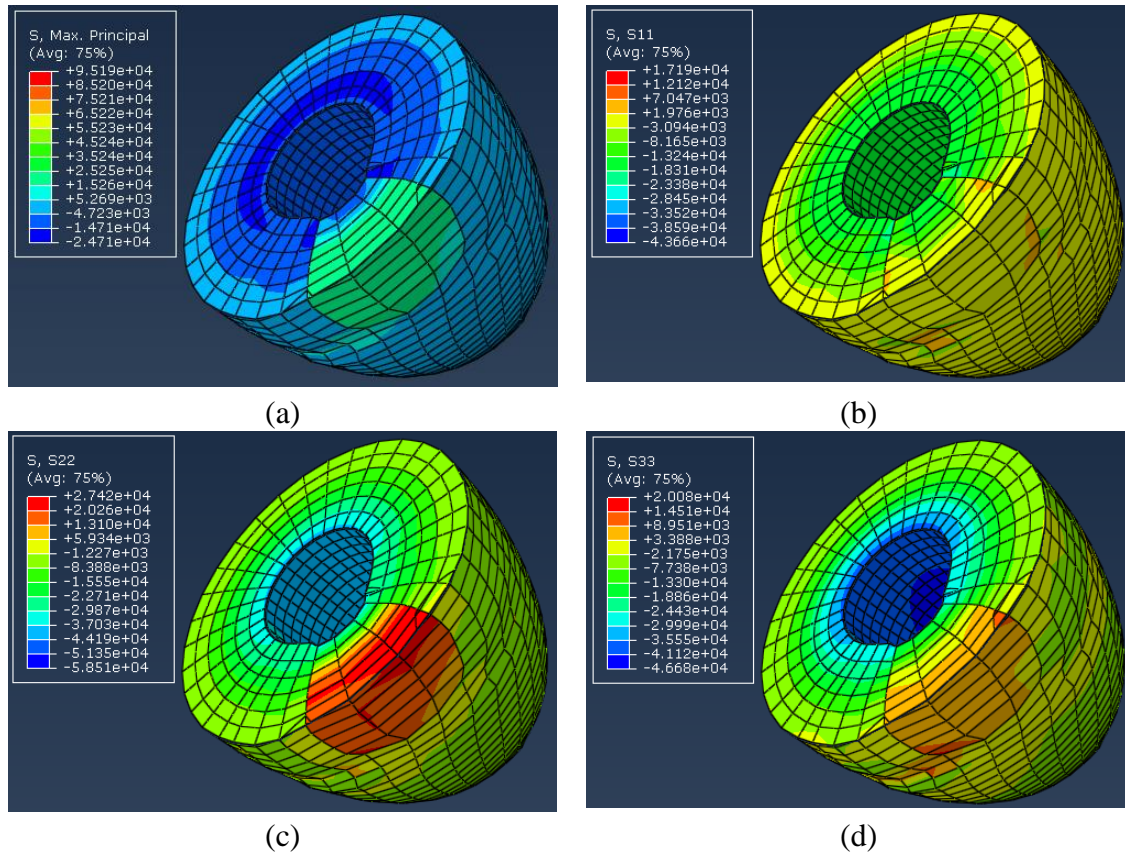


**Figure 4.9:** Transmural variations of end-systolic stress components within the background at the LV equatorial area from endocardium towards epicardium when time-variable active stress and blood pressure were applied to the infarcted LV model. Maximum principle stress (a), radial stress (b), circumferential stress (c), and longitudinal stress (d) are shown.

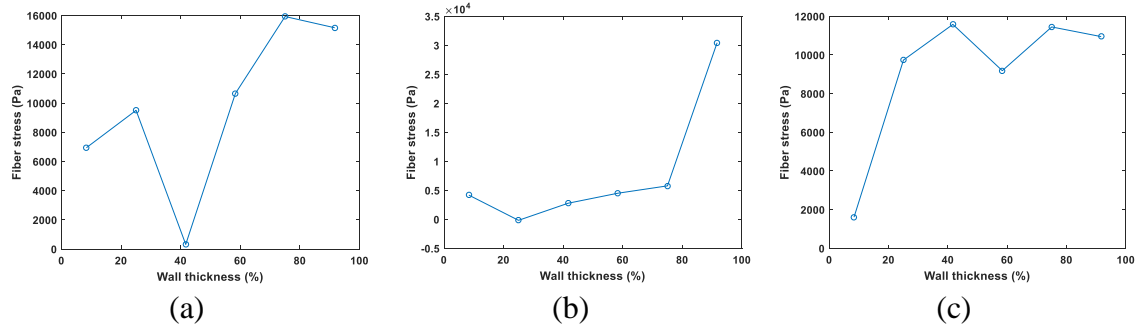


**Figure 4.10:** Transmurial variations of end-systolic fibers stress: within the infarct region (a), within the border zone (b), and within the healthy region (c).

The average fiber stresses within the infarct, border zone, and healthy regions are reported in Table 4.7:

**Table 4.7:** End-systolic average values of the fiber stress in the three regions of infarcted LV

Region	Average Fiber Stress (kPa)
Healthy	4.32
Border Zone	7.73
Infarct	5.42

## 4.4 Discussion and Conclusions

In this article a novel approach for mechanical modeling of the pathological myocardium is presented. The novel aspect of this model is that the LV muscle tissue is idealized as a composite material including two main parts of background tissue and myofibers. In the proposed model, myofiber contraction is simulated by applying initial stresses to reinforcement bars (rebars) distributed throughout the LV volume. The rebar's directions in the LV volume are adjusted based on the known spatially variable fibers orientation through the LV volume forming a self-contained anisotropy through the model. To obtain the contraction strain and stress fields FE modeling was used. In this model, both of the background and myofibers parts were considered as hyperelastic materials. Different mechanical properties have been considered for the normal and pathological tissue parts of the LV. Myofibers active stress variation through the cardiac cycle was modelled using the elastance model implemented as initial stresses applied to the rebars. For infarcted LV modeling, the maximum isometric tension at the longest sarcomere length,  $T_{\max}$  in Equation (4.1) of the elastance model was set at different values for the infarct, border zone, and healthy tissue regions. This parameter was set to 150 kPa at the normal tissue

region while lower values of zero and 75 kPa, were considered for the infarct and border zone regions, respectively. A major strength of the proposed model is that it can be implemented using off-the-shelf FE solvers with nonlinear analysis capability. It does not require complex custom-developed computer codes while it incorporates all necessary mechanical complexities of the myocardial tissue. Moreover, it is anticipated that the proposed model is computationally efficient and less prone to numerical instability and divergence issues. This stems from the effective prestressed rebar approach used to model the myofibers and model development using commercial FE solvers which are usually optimized for computation efficiency. Another key feature in the model is its easy adaptability with various cardiac pathologies since diverse mechanical parameters such as passive mechanical properties and active response of the pathological parts of the myocardium can be easily adjusted by manipulating the FE model input file without the need to modify the underlying FE codes.

To assess the capability of the proposed model, it was applied *in silico* to simulate a normal canine LV [43]. The simulation results were compared to corresponding canine experimental measurements and those of other LV computer models. The LV strain distribution at end-systolic state was evaluated. Radial strain was positive throughout the volume while decreasing from endocardium towards epicardium. This is reasonable as it is consistent with myocardial thickening at end-systolic state. The circumferential and longitudinal strains were mainly negative throughout the volume, demonstrating the LV contraction at end-systolic phase. The systolic contraction of the LV model was further validated by comparing the distribution of all three major components of the strain throughout the LV volume with measurements obtained from anterior equatorial LV free wall of seven open-chest dogs [35] and to those of LV mechanical model presented in [51], which confirmed good agreement. The ventricular end-systolic stress distribution in both background tissue and myofibers were also assessed. Negative and almost uniform distribution patterns of principal stresses were predominantly present in the midventricular area, confirmed the general trend of contraction through the LV. The directional fiber stress magnitude varied from negative values at endocardium to positive values at mid-wall and it reached maximum value of 38 kPa which is consistent with other LV models [45,54].

The performance of the model was assessed for infarcted LV where a border zone was also considered. Again, strain and stress distributions obtained from this LV model were compared with corresponding values obtained from measurements and other mechanical models of the infarcted LV. The distribution of normal components of the end-systolic strain tensor throughout the LV volume are shown in Figure 4.6. Similar to the normal case, as shown in Figures 4.6 (a) and 4.6 (b), the radial strain is tensile in the normal midventricular region while it decreases from endocardium towards epicardium. This is consistent with the myocardial thickening in the healthy part. In the infarct region, however, the radial strain are compressive while in the border zone they have smaller positive values. This is also consistent with myocardial thinning of the infarct region at end-systolic state which has been reported in the literature as a mechanical feature of infarction where active contraction within the LV wall is insignificant [55-56]. As shown in Figures 4.6 (c) and (d), the circumferential strains are compressive within the normal region of the LV as expected, representing the contractile function of the cardiac tissue at end-systole. These figures also show that the circumferential strains are tensile in the infarct regions marked by the red color in the figures. This agrees very well with the frequently described circumferential stretching of the infarcted cardiac tissue resulting from lack of contraction [23-24]. As illustrated in Figures 4.6 (e) and 4.6 (f), longitudinal strain is compressive at the healthy tissue part which indicates anticipated longitudinal contraction of the model. Its magnitude is smaller at the infarct region and border zone, proving less contraction at these regions [24,57]. For further validation, as seen in Table 4.6, average values of the circumferential strains obtained by the proposed method were compared with corresponding values acquired from tagged MR images and those obtained from LV mechanical modeling reported in [24]. Overall, there is a good agreement among results obtained for the three tissue regions, especially the healthy and border zone regions [24]. It is noteworthy that all these values are positive showing the circumferential stretching in the infarct region consistent with [24,57]. Variations of the circumferential strain with respect to LV circumference at the equatorial area where the infarct region intersects, which is shown in Figure 4.7, was investigated. This figure shows that the strain variations obtained from the proposed model are reasonably consistent with the MR tagging measurements and with those of another mechanical FE model of infarcted LV

[24]. Compared to matching our results exhibit with the MR strain measurements, the LV model presented in [24] shows better matching. However, it must be noted that the latter model was specifically constructed to be consistent with the experimental animal model. Circumferential variations of the longitudinal strain at the equatorial area with the MI is also depicted in Figure 4.8 where they are compared with results of the MR measurements and LV mechanical model presented in [24]. This figure shows that our model exhibits reasonable agreement with the measurements especially within the infarcted region where the longitudinal strain becomes positive, again consolidating the validity of the proposed model. The ventricular end-systolic stress distribution in both background tissue and myofibers are shown in Figures 4.9 and 4.10. Figure 4.9 (a) illustrates the volumetric distribution of background tissue maximum principal stresses, which shows increase from large negative values at endocardium towards small positive values at epicardium in the healthy tissue region. A mainly uniformly distributed compressive principal stress in the healthy region is consistent with the contraction pattern expected in this part. Figure 4.9 (a) also shows development of tensile principle stress in the infarct region, demonstrating the tissue extension in that part due to lack of active contraction. The radial background stress in the normal areas of the LV model is also negative compressive as illustrated in Figure 4.9 (b) except at the most epicardial portions similar to the normal LV case. In the infarct region, the radial background stress is mainly tensile, especially by moving toward the epicardium, reflecting tissue stretching in that region which is consistent with lack of active contraction in that region. The circumferential and longitudinal stresses (Figures 4.9 (c) and (d)) are also mainly compressive in the healthy midventricular region consistent with normal LV contraction. In the border zone and infarct regions, however, these stresses are tensile while slightly non-uniform in both of the infarct and border zone regions, particularly the circumferential stresses, which is again reasonably consistent with little or lack of active contraction in those regions. Figure 4.10 illustrates the directional fiber stress variations at midventricular regions pertaining to healthy, infarct and border zone. As illustrated in Figures 4.10 (a) and (b), these fiber stresses increase from endocardium to epicardium in both of the infarct and border zone regions consistent with what is reported in [24]. The fiber stresses in the border zone are higher compared to the infarct region as illustrated in Figure 4.10 and Table 4.7. This agrees very well with the corresponding fiber

stress distribution presented in [18,24], consolidating the validity of the presented simulation. The maximum fiber stress obtained by the proposed model, which occurs at the border zone, is ~40 kPa which is within the range of values reported in [24]. As shown in Figure 4.10 (c), the fiber stress in the healthy tissue region is much lower compared to both of the infarct and border zone regions, confirming the higher fiber stresses in the infarct region which is consistent with similar observations tied to cardiac remodeling as reported in the literature [17-18,23-24]. Our results indicate that the maximum value of fibers stress in the healthy region occurs in mid-wall region which is also consistent with the literature.

Based on the results obtained from the proposed model and their reasonable consistency with corresponding data obtained from MR tagging measurement or other FE models, it can be concluded that the proposed approach of cardiac tissue decomposition into passive background and active myofibers parts is highly effective as it makes possible utility of off-the-shelf FE solvers for accurate cardiac mechanical modeling. While potentially computationally efficient, this approach facilitates straight-forward adaptability to both myofiber active stress characteristics and passive properties of various parts of the tissue which is quite essential for effective modeling of various cardiac pathologies. Such adaptability is a major requirement for developing FE-based inversion algorithm to accomplish more accurate active stress distribution in realistic LV models obtained from imaging data.

## References

- [1] World Health Organization (WHO), [www.who.org](http://www.who.org).
- [2] S. Marchesseau, H. Delingette, M. Sermesant, M. Sorine, K. Rhode, S. G. Duckett, C. A. Rinaldi, R. Razavi, and N. Ayache, "Preliminary specificity study of the Bestel-Clement-Sorine electromechanical model of the heart using parameter calibration from medical images," *J. Mech. Behav. Biomed. Mater.*, 20, 259-271, 2013.
- [3] M. L. McCain and K. K. Parker, "Mechanotransduction: the role of mechanical stress, myocyte shape, and cytoskeletal architecture on cardiac function," *European Journal of Physiology*, 462(1): 89-104, 2011.
- [4] G. Drzewiecki, J. Wang, J. K. J. Li, J. Kedem, and H. Weiss, "Modeling of mechanical dysfunction in regional stunned myocardium of the left ventricle," *IEEE Trans. Biomed. Eng.*, 43, 12, 1151-1163, 1996.
- [5] A. Christy, "Left ventricular wall mechanics in hypertension - an echocardiographic study," *Int. J. Biol. Med. Res.*, 3(1): 1267-1272, 2012.
- [6] H. Jin, E. R. Chemaly, A. Lee, C. Kho, L. Hadri, R. J. Hajjar, and F. G. Akar, "Mechanoelectrical remodeling and arrhythmias during progression of hypertrophy," *FASEB J.*, 24:451-463, 2010.
- [7] J. Dou, L. Xia, D. Deng, Y. Zang, G. Shou, C. Bustos, W. Tu, F. Liu, and S. Crozie, "A study of mechanical optimization strategy for cardiac resynchronization therapy based on an electromechanical model," *Computational and Mathematical Methods in Medicine*, Vol. 2012, 2012.
- [8] M. Genet, L. C. Lee, B. Baillargeon, J. M. Guccione, and E. Kuhl, "Modeling pathologies of diastolic and systolic heart failure," *Annals of Biomedical Engineering*, 44(1): 112-127, 2015.
- [9] L. C. Lee, J. F. Wenk, L. Zhong, D. Klepach, Z. Zhang, L. Ge, M. B. Ratcliffe, T. I. Zohdi, E. Hsu, J. L. Navia, G. S. Kassab, and J. M. Guccione, "Analysis of patient-specific surgical ventricular restoration: importance of an ellipsoidal left ventricular geometry for diastolic and systolic function," *J. Appl. Physiol.*, 115(1): 136-44. 2013.
- [10] H. F. Choi, F. E. Rademakers, and P. Claus, "Left-ventricular shape determines intramyocardial mechanical heterogeneity," *Am. J. Physiol. Heart Circ. Physiol.*, 301(6): H2351-61. 2011.
- [11] E. J. Howard and J. H. Omens, "Distributions of myocyte stress, strain, and work in normal and infarcted ventricles," in P. Kohl, F. Sachs, M. R. Franz (Eds), [Cardiac Mechano-Electric Feedback and Arrhythmias], Oxford: Oxford University Press, 442-449, 2011.
- [12] J. Luo, K. Fujikura, S. Homma, and E. E. Konofagou, "Myocardial elastography at both high temporal and spatial resolution for the detection of infarcts," *Ultrasound Med. Biol.*, 33(8): 1206-23, 2007.

- [13] M. Schwarzl, S. Huber, H. Maechler, P. Steendijk, S. Seiler, M. Truschnig-Wilders, T. Nestelberger, B. M. Pieske, and H. Posta, “Left ventricular diastolic dysfunction during acute myocardial infarction: Effect of mild hypothermia,” *Resuscitation.*, 83(12): 1503–1510, 2012.
- [14] M. Perl and A. Horowitz, “Mechanical model for the simulation of ischaemia and infarction of the left ventricle,” *Medical and Biological Engineering and Computing*, 25(3): 284-288, 1987.
- [15] I. Adeniran, J. C. Hancox, and H. Zhang, “*In silico* investigation of the short QT syndrome, using human ventricle models incorporating electromechanical coupling,” *Front Physiol.*, 4: 166, 2013.
- [16] P. Zhang, J. M. Guccione, S. I. Nicholas, J. C. Walker, P. C. Crawford, A. Shamal, D. A. Saloner, A. W. Wallace, and M. B. Ratcliffe, “Left ventricular volume and function after endoventricular patch plasty for dyskinetic anteroapical left ventricular aneurysm in sheep,” *J. Thorac. Cardiovasc. Surg.*, 130(4): 1032-8, 2005.
- [17] X. J. Jiang, T. Wang, X. Y. Li, D. Q. Wu, Z. B. Zheng, J. F. Zhang, J. L. Chen, B. Peng, H. Jiang, C. Huang C, and X. Z. Zhang, “Injection of a novel synthetic hydrogel preserves left ventricle function after myocardial infarction,” *J. Biomed. Mater. Res. A.*, 90(2): 472-7, 2009.
- [18] J. F. Wenk, P. Eslami, Z. Zhang, C. Xu, E. Kuhl, J. H. Gorman, J. D. Robb, M. B. Ratcliffe, R. C. Gorman, and J. M. Guccione, “A novel method for quantifying the in-vivo mechanical effect of material injected into a myocardial infarction,” *Ann. Thorac. Surg.*, 92(3):935-41, 2011.
- [19] V. Sudarshan V, U. R. Acharya, E. Y. Ng, C. S. Meng, R. S. Tan, and D. N. Ghista, “Automated identification of infarcted myocardium tissue characterization using ultrasound images: a review,” *IEEE Rev. Biomed. Eng.*, 8:86-97, 2015.
- [20] X. Zhang, B. R. Cowan, D. A. Bluemke, J. P. Finn, C. G. Fonseca, A. H. Kadish, D. C. Lee, J. A. Lima, A. Suinesiaputra, A. A. Young, and P. Medrano-Gracia, “Atlas-based quantification of cardiac remodeling due to myocardial infarction,” *PLoS One.*, 9(10): e110243, 2014.
- [21] E. Konukoglu, J. Relan, U. Cilingir, B. H. Menze, P. Chinchapatnam, A. Jadidi, H. Cochet, M. Hocini, H. Delingette, P. Jaïs, M. Haïssaguerre, N. Ayache, and M. Sermesant, “Efficient probabilistic model personalization integrating uncertainty on data and parameters: Application to eikonal-diffusion models in cardiac electrophysiology,” *Prog. Biophys. Mol. Biol.*, 107(1):134-46, 2011.
- [22] D. Neumann, T. Mansi, B. Georgescu, A. Kamen, E. Kayvanpour, A. Amr, F. Sedaghat-Hamedani, J. Haas, H. Katus, B. Meder, J. Hornegger, D. Comaniciu, and S. less, “Robust image-based estimation of cardiac tissue parameters and their uncertainty from noisy data,” *Medical Image Computing and Computer-Assisted Intervention*, 8674: 9-16, 2014.
- [23] K. Sun, N. Stander, C. S. Jhun, Z. Zhang, T. Suzuki, G. Y. Wang, M. Saeed, A. W. Wallace, E. E. Tseng, A. J. Baker, D. Saloner, D. R. Einstein, M. B. Ratcliffe, and J. M. Guccione, “A computationally efficient formal optimization of regional



- myocardial contractility in a sheep with left ventricular aneurysm,” *J. Biomech. Eng.*, 131(11): 111001, 2009.
- [24] J. F. Wenk, K. Sun, Z. Zhang, M. Soleimani, L. Ge, D. Saloner, A. W. Wallace, M. B. Ratcliffe, and J. M. Guccione, “Regional left ventricular myocardial contractility and stress in a finite element model of posterobasal myocardial infarction,” *J. Biomech. Eng.*, 133(4): 044501, 2011.
- [25] C. A. Linte, M. Wierzbicki, T. M. Peters, and A. Samani, “Towards a biomechanics-based technique for assessing myocardial contractility: an inverse problem approach,” *Comput. Methods Biomech. Biomed. Engin.*, 11(3): 243-55, 2008.
- [26] A. I. Hassaballah, M. A. Hassan, A. N. Mardi, and M. Hamdi, “An inverse finite element method for determining the tissue compressibility of human left ventricular wall during the cardiac cycle,” *PLoS One.*, 8(12): e82703, 2013.
- [27] H. Delingette, F. Billet, K. C. Wong, M. Sermesant, K. Rhode, M. Ginks, C. A. Rinaldi, R. Razavi, and N. Ayache, “Personalization of cardiac motion and contractility from images using variational data assimilation,” *IEEE Trans. Biomed. Eng.*, 59(1): 20-4, 2012.
- [28] L. C. Lee, J. F. Wenk, D. Klepach, Z. Zhang, D. Saloner, A. W. Wallace, L. Ge, M. B. Ratcliffe, and J. M. Guccione, “A novel method for quantifying in-vivo regional left ventricular myocardial contractility in the border zone of a myocardial infarction,” *J. Biomech. Eng.*, 133(9): 094506, 2011.
- [29] P. H. M. Bovendeerd, T. Arts, J. M. Huyghe, D. H. Van Campen, and R. S. Reneman, “Dependence of local left ventricular wall mechanics on myocardial fiber orientation: a model study,” *Journal of Biomechanics*, 25, 10, 1129-1140, 1992.
- [30] G. A. Holzapfel, [Nonlinear Solid Mechanics: A Continuum Approach for Engineering], Wiley, West Sussex, 141-152, 2000.
- [31] S. Goktepe and E. Kuhl, “Electromechanics of the heart: a unified approach to the strongly coupled excitation-contraction problem,” *Comput. Mech.*, 45, 2-3, 227-243, 2010.
- [32] A. I. Veress, W. P. Segars, B. M. W. Tsui, and G. T. Gullberg, “Incorporation of a Left Ventricle Finite Element Model Defining Infarction Into the XCAT Imaging Phantom,” *IEEE Transactions on Medical Imaging*, vol. 30, no. 4, pp.915-927, 2011.
- [33] M. Sermesant, H. Delingette, and N. Ayache, “An electromechanical model of the myocardium for cardiac image analysis and medical simulation,” *INRIA Sophia Antipolis*, N° RR-5395, 2004.
- [34] Hibbit, Karlsson, and Sorenson, *ABAQUS Theory Manual*. Pawtucket, RI, June 1998.
- [35] L. K. Waldman, D. Nosan, F. Villarreal, and J. W. Covell, “Relation between transmural deformation and local myofiber direction in canine left ventricle,” *Circulation Research.*, 63:550-62, 1988.

- [36] J. M. Guccione and A. D. McCulloch, "Mechanics of active contraction in cardiac muscle: Part I--Constitutive relations for fiber stress that describe deactivation," *J. Biomech. Eng.*, 115(1):72-81, 1993.
- [37] J. M. Guccione, L. K. Waldman, and A. D. McCulloch, "Mechanics of active contraction in cardiac muscle: Part II--Cylindrical models of the systolic left ventricle," *J. Biomech. Eng.*, 115(1):82-90, 1993.
- [38] J. D. Humphrey, R. K. Strumpf, and T. C. P. Yin, "Determination of a constitutive relation for passive myocardium: II. - parameter estimation," *J. Biomech. Eng.*, 112, pp. 340-346, Aug. 1990.
- [39] K. B. Gupta, M. B. Ratcliffe, M. A. Fallert, L. H. J. Edmunds, and D. K. Bogen, "Changes in passive mechanical stiffness of myocardial tissue with aneurysm formation," *Circulation*, 89:2315-26, 1994.
- [40] M. Shams, M. Destrade, and R. W. Ogden, "Initial stresses in elastic solids: Constitutive laws and acoustoelasticity," *Wave Motion*, 48 (7): 552-567, 2011.
- [41] A. L. Gower, P. Ciarletta, and M. Destrade, "Initial stress symmetry and its applications in elasticity," *Proc. R. Soc. A*, 471 20150448, 2015.
- [42] G. A. Holzapfel, [Nonlinear Solid Mechanics: A Continuum Approach for Engineering], Wiley, West Sussex, 2000.
- [43] Seyyed M. H. Haddad and Abbas Samani, "A novel biomechanical computational model of the left ventricle using a composite material approach," Summited to *the Journal of the Biomechanical Engineering*, under review.
- [44] J. Schaper, E. Meiser, and G. Stammner, "Ultrastructural morphometric analysis of myocardium from dogs, rats, hamsters, mice, and from human hearts," *Circulation.*, 56(3), 377-391 (1985).
- [45] D. D. Streeter, M. H. Spotnitz, D. P. Patel, J. Ross, and E. H. Sonnenblick, "Fiber orientation in the canine left ventricle during diastole and systole," *Circ. Res.*, 24: 339-347, 1969.
- [46] T. Arts, P. C. Veenstra, and R. S. Reneman, "Epicardial deformation and left ventricular wall mechanisms during ejection in the dog," *Am. J. Physiol.*, 243(3):H379-90, 1982.
- [47] Y. Bogatyryov, R. J. Tomanek, and E. I. Dedkov, "Structural composition of myocardial infarction scar in middle-aged male and female rats: does sex matter?," *J. Histochem. Cytochem.*, 61, 11, 833-848, 2013.
- [48] Moonly, S. Experimental and computational analysis of left ventricular aneurysm mechanics. University of California, San Francisco with University of California; Berkeley, San Francisco, CA, 2003.
- [49] K. D. Costa, J. W. Holmes, and A. D. McCulloch, "Modelling cardiac mechanical properties in three dimensions," *Phil. Trans. R. Soc. Lond. A*, 359: 1233-1250, 2001.

- [50] F. J. Villarreal, W. Y. Lew, L. K. Waldman, and J. W. Covell, "Transmural myocardial deformation in the ischemic canine left ventricle," *Circ. Res.*, 68(2):368-81, 1991.
- [51] J. M. Guccione, K. D. Costa, and A. D. McCulloch, "Finite element stress analysis of left ventricular mechanics in the beating dog heart," *J. Biomech.*, 28(10):1167-77, 1995.
- [52] H. Childs, L. Ma, M. Ma, J. Clarke, M. Cocker, J. Green, O. Strohm, and M. G. Friedrich, "Comparison of long and short axis quantification of left ventricular volume parameters by cardiovascular magnetic resonance, with ex-vivo validation," *Journal of Cardiovascular Magnetic Resonance*, 13:40, 2011.
- [53] D. D. Sisson, G. B. Daniel, and A. R. Twardock, "Comparison of left ventricular ejection fractions determined in healthy anesthetized dogs by echocardiography and gated equilibrium radionuclide ventriculography," *Am. J. Vet. Res.*, 50(11):1840-7. 1989.
- [54] M. Genet, L. C. Lee, R. Nguyen, H. Haraldsson, G. Acevedo-Bolton, Z. Zhang, L. Ge, K. Ordovas, S. Kozerke, and J. M. Guccione, "Distribution of normal human left ventricular myofiber stress at end diastole and end systole: a target for *in silico* design of heart failure treatments," *Journal of Applied Physiology*, 117 (2) 142-152, 2014.
- [55] M. G. Sutton and N. Sharpe, "Left ventricular remodeling after myocardial infarction: pathophysiology and therapy," *Circulation*, 101(25): 2981-8, 2000.
- [56] H. Hammerman, R. A. Kloner, E. J. Schoen, E. J. Jr Brown, S. Hale, and E. Braunwald, "Indomethacin-induced scar thinning after experimental myocardial infarction," *Circulation*, 67(6): 1290-5, 1983.
- [57] H. Ashikaga, S. R. Mickelsen, D. B. Ennis, I. Rodriguez, P. Kellman, H. Wen, and E. R. McVeigh, "Electromechanical analysis of infarct border zone in chronic myocardial infarction," *Am. J. Physiol. Heart Circ. Physiol.*, 289(3): H1099-105, 2005.

## Chapter 5

# Human Left Ventricle Biomechanics using Medical Imaging Data and Composite Material Mechanics Approach

### 5.1 Introduction

**Q**UANTITATIVE understanding of cardiac mechanics under normal and pathophysiological conditions is vital for many medical applications. It can pave the way for in-depth understanding of the heart physiology under normal and pathological conditions and better comprehension of the genesis of cardiac mechanical function alterations resulting from cardiac conditions [1-2]. Such understanding can be exploited to utilize observed mechanical alterations as quantitative measures for diagnosis, prognosis, and even effective treatment of cardiac diseases [3-6]. In-depth comprehension of cardiac mechanics of both systole and diastole phases are often necessary to interpret symptoms associated with various cardiac conditions [7-8]. Some cardiac abnormalities and dysfunctions, however, pertain to abnormalities in one of the phases [7,9]. In such cases, data of that phase can be utilized for effective diagnosis and therapy purposes. Heart failure is a serious and widespread cardiac condition which could possibly lead to death. It occurs when the heart cannot pump enough blood and oxygen to support normal function of all organs in the body. Clinically, it is accompanied by increase in tissue water content and decrease in tissue perfusion in different parts of the body [9]. According to recent statistics in developed countries, ~2% of adults are diagnosed with heart failure while 6–10% of adults over the age of 65 have this cardiac condition [10-11]. Heart failure arises from two major types of cardiac disorders, i.e. diastolic and systolic dysfunctions. Systolic dysfunctions are the most common causes of mortal heart failures, however, epidemiological studies reveal that more than 50% of heart failure patients suffer from diastolic dysfunctions while they have normal systolic function and EF [12–13]. Diastolic dysfunction is a clinical term which refers to a wide range of cardiac conditions when the

diastolic phase is protracted, slowed, or incomplete [9,14]. It is typically caused by diverse conditions such as myocardial infarction, hypertension, atrial fibrillation, heart valve disease, overuse of alcohol, presence of infection, cardiomyopathy, etc. Long-term diastolic dysfunctions can lead to abnormal LV relaxation, filling, diastolic distensibility, or diastolic stiffness typically followed by diastolic heart failure. The latter occurs when the LV cannot receive sufficient blood volume within the diastolic phase under normal blood pressure to preserve an acceptable level of stroke volume in the systolic phase [9,14]. Among the above diastolic failure mechanisms, diastolic stiffness is a highly important and prevalent mechanism. Quantitative assessment of this mechanism is feasible using LV deformation imaging data of diastole in conjunction with inverse problem framework. Such framework can be utilized to estimate LV tissue stiffness using the imaging data. Such inverse problem framework requires a robust cardiac mechanics forward model that can be used effectively for this application. This forward model should ideally include tissue anisotropy and hyperelasticity in accordance with its microstructure [15-16]. Conventional cardiac mechanics models utilize different constitutive laws for simulation of the passive behavior of the cardiac tissue [15-18]. While the majority of these constitutive laws assume transversely anisotropy for cardiac tissue [15-16], some more complex constitutive laws contemplate orthotropic material properties [17-18] which are based on this hypothesis that the myocardial fibers are organized within bundles of fiber layers that are bound together by endomysial collagen [19]. These constitutive laws cannot be implemented easily using most of available FE solvers, hence highly complex custom-developed nonlinear FE codes have been implemented to fill this gap [20-21]. Furthermore, such hyperelastic anisotropic constitutive laws impose high computational burden to the inversion-based FE algorithms where the forward model must be run iteratively. These issues render the hyperelastic anisotropic constitutive laws less appealing, specifically in comparison with the cardiac mechanics model presented in Chapters 3 and 4 where an effective composite material model was introduced to mimic anisotropy. In this chapter, we use the forward model concept of cardiac mechanics which was introduced in Chapters 3 and 4 to investigate the diastolic phase mechanics of a healthy volunteer. The LV geometry of this subject was developed using MRI data. This study includes preliminary assessment of the proposed model to estimate blood pressure and cardiac tissue stiffness properties in the diastolic

phase. This part was carried out using a simplified inverse problem scheme where an ad-hoc optimization approach as utilized.

## 5.2 Materials and Method

### 5.2.1 Image Acquisition

Cardiac MR imaging is used to obtain images with high resolution to delineate cardiac tissue, particularly endocardial and epicardial contours, accurately without the need for additional contrast improvement and noise reductions techniques. Accordingly, MR is considered as the preferred imaging modality for high-quality dynamic cardiac image acquisition which is typically utilized to construct subject-specific FE models of the heart and its individual compartments such as LV. As such, in this research we used cardiac MR image data to acquire accurate geometry of a human subject LV. For this purpose, a set of 4D cardiac MR image data including 20 3D cardiac volumes (time frames) of a healthy human was acquired. The 3D volumes were acquired through 20 equal time steps during a cardiac cycle while the time interval between each two consecutive frames was 50 ms. The MR imaging procedure was carried out using a 1.5 T GE CVi scanner (GE medical systems, WI, USA) where a fast cine SPGR pulse sequence in the coronal plane was utilized with NEX = 4 and flip angle of  $20^\circ$ . This led to an image matrix of  $256 \times 128$  with eight views per segment. The resulting 3D cardiac volumes have an in-plane resolution of  $1.5 \text{ mm}^2$  with 75 coronal slices of 1.5 mm spatial space. Each time frame of the image dataset was obtained with a complete breath-hold to minimize motion artifacts and noise in the final MR images [22]. Figure 5.1 shows the MR image of the myocardium at start diastole where the myocardium is almost at its static state.

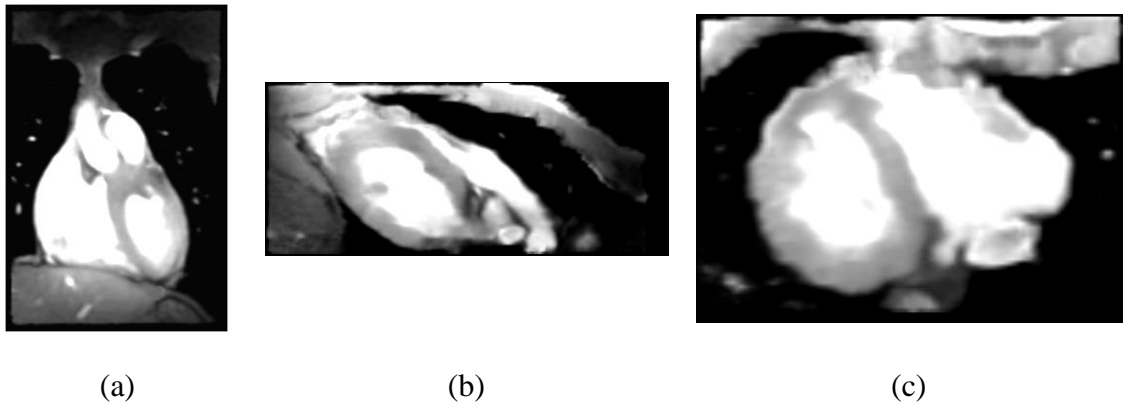


**Figure 5.1:** 3D Cardiac MR image of a healthy human subject at the start-diastole: coronal view (a), sagittal view (b), and axial view (c).

### 5.2.2 Left Ventricle Model Construction

The 3D volume pertaining to the start diastole corresponds to the state where the myocardium is relaxed, hence it was considered to represent the reference geometry of the myocardium (LV) for the mechanical model construction. It is noteworthy that at this time frame the heart is relatively static and, as such, motion artefacts are minimized allowing for the subsequent LV segmentation with high accuracy. Through manual segmentation of the start diastole frame, the LV geometry was extracted while the segmentation was performed in both short axis and long axis slices to minimize errors pertaining to segmentation, especially errors of delineating the endocardial and epicardial boundaries. The entire segmentation process was performed using the Editor module in 3D Slicer software where the endocardial and epicardial contours were segmented slice by slice [23]. After segmenting the LV boundaries in the MR image slices, the 3D model of the LV was generated using the Model Maker module of 3D Slicer software [23]. To remove uneven lines from the LV model boundaries, which were regarded as segmentation artifacts, the 3D model was smoothed using Laplacian filter. The result of the segmentation process and corresponding 3D LV model are illustrated in Figures 5.2 and 5.3, respectively.

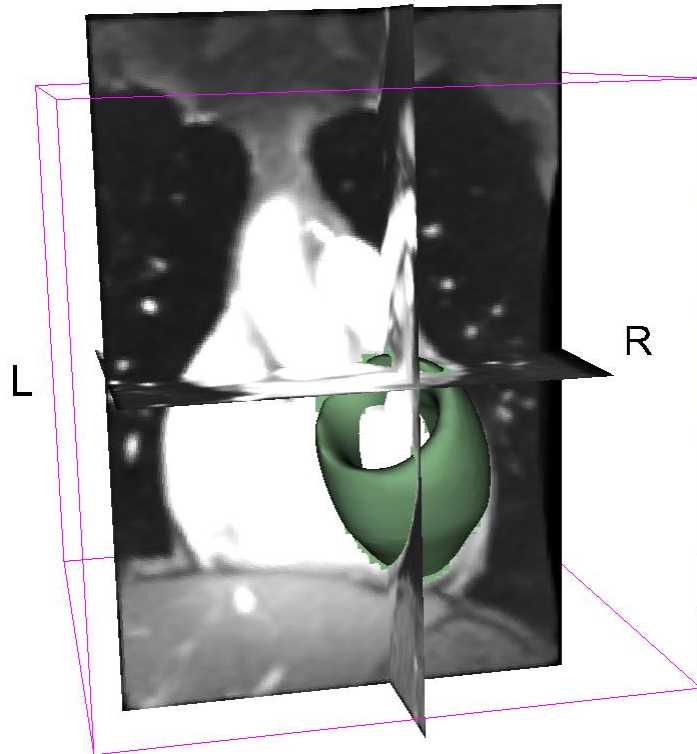


**Figure 5.2:** 3D surface model of the healthy subject's LV obtained from MR image slices segmentation (shown using green color) which is superimposed onto arbitrary 3 orthogonal slices of the 3D MR image pertaining to start diastole.

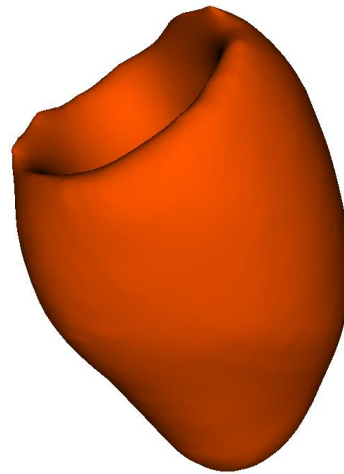


**Figure 5.3:** 3D LV model of the healthy subject at start diastole constructed by MR image segmentation.

The 3D LV model obtained from segmentation was discretized into hexahedral elements using the IA-FEMesh module in 3D slicer [24]. It is noteworthy that the FE mesh resolution



was adjusted such that enough elements were embedded within the LV wall to account for transmural variations of the helix fiber angle which play a crucial role in mimicking anisotropy through the model, hence insuring mesh convergence. The resulting FE mesh obtained from this procedure is illustrated in Figure 5.4.

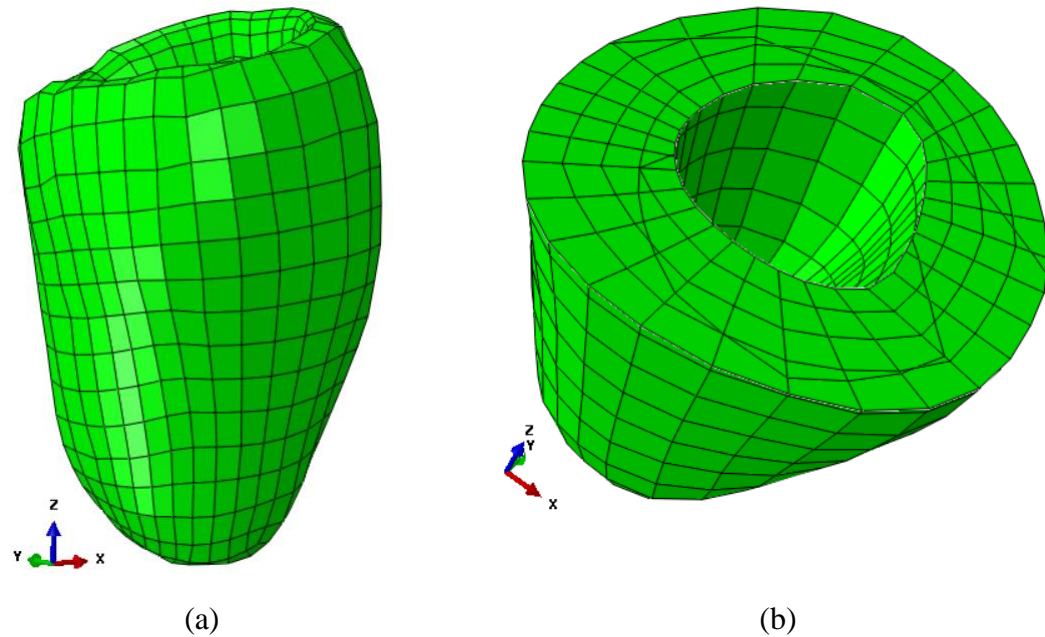


**Figure 5.4:** FE model of the human subject LV: whole LV model view (a) and the model's short axis cross section view (b).

### 5.2.3 Composite Material Model of the Cardiac Tissue

In the diastolic phase, the ventricular blood pressure descends considerably from high values occurring in the systolic phase as a result of the relaxation of the myofibers and ejection of the blood out of the LV cavity. This reduction persists until the ventricular pressure reaches a level lower than that of the left atrium. At this instance, the mitral valve opens, establishing a steady blood flow from the left atrium towards the LV. Afterwards, the ventricular pressure increases gradually as a consequence of filling of the LV cavity which continues until the end-diastolic phase where the LV cavity is fully inflated by blood. As such, during this phase the myocardial tissue within the LV undergoes passive deformation caused by endocardial blood pressure [7,12,25]. In the diastolic phase, consistent with the Hill's model and the fibrous microstructure of the myocardial tissue, the cardiac tissue can be decomposed into the two major parts of myofiber and background

tissue (non-myofiber) part. This tissue decomposition arises from the well-known difference in passive mechanical properties of the myofiber and non-myofiber part of the tissue [15-18], which requires considering different passive material models for each of these tissue parts. As indicated in Chapters 3 and 4, the full mechanical bond between these two tissue parts is considered, hence stress developments in each part affects stress distribution within the other part such that mechanical equilibrium is maintained according to the momentum balance principle [26]. The described composite model of the cardiac tissue follows the actual myocardial tissue fibrous structure. It lends itself well for considering arbitrary passive mechanical properties for each part of the tissue in accordance with the healthy/pathological condition of the diastolic phase. It is noteworthy that alteration of the mechanical properties of any of the two tissue parts influences the overall properties of the whole tissue. The major advantage of this tissue decomposition is that since each tissue part is composed of a single material, classic isotropic hyperelastic constitutive laws available in typical off-the-shelf FE solvers can be used to model that part. Consequently, the issue of using complex hyperelastic anisotropic constitutive laws for modeling cardiac tissue is circumvented. This feature increases the computational efficiency of the presented cardiac mechanics model.

#### 5.2.4 Major Elements of the Left Ventricle Model

The flow chart of the presented LV mechanical model is shown in Figure 5.5. The FE model of the LV geometry obtained from segmenting the MR image at start diastole is illustrated in Figure 5.4. All FE simulations presented in this study were conducted using quasi static module of the commercially available Abaqus/Standard FE solver [27]. As indicated earlier, the composite material approach used in the model considers myofibers and background tissue parts. As such, the hexahedral finite elements which are regarded as building blocks of tissue in the FE model consist of two major materials: background tissue and rebars (fibers). The orientations of the rebars, which mimic the myofibers, model anisotropy of the cardiac tissue in accordance with the fibrous LV structure. In fact, systematic dispersal of the rebars in different directions consistent with the LV anatomy induces a self-contained transverse isotropy to the FE LV model. During diastole phase, the LV cavity is filled with blood leading to LV blood pressure elevation as the blood

volume increases in the LV cavity. As such, through passive diastolic inflation, the increasing endocardial blood pressure pushes the LV wall tissue outward while no significant contraction is developed within myofibers [7,12,25]. Figure 5.6 shows a typical instance of the active stress variations along a sarcomere of length  $1.7 \mu m$  during a cardiac cycle [28]. As observable in this figure, the active stress is insignificant after the start-diastole instance ( $400 ms$ ). Based on this mechanical description of the diastole phase, the only significant load applied to the LV is the blood pressure which is modeled as a uniform pressure acting on the LV endocardial surface. Similar to the cardiac mechanics model presented in Chapter 3 and 4, hyperelastic models were used for simulating the mechanical behavior of both of the background tissue and myofibers. This is due to the fact that even in the diastole phase the LV undergoes large deformations during inflation while its tissue is intrinsically nonlinear. Parameters of these models were used as the mechanical properties of the background tissue and myofibers for FE simulations. The model described here is developed to simulate the LV diastole phase mechanics based on equilibrium of blood pressure and passive stresses throughout differential material points of the LV composite tissue at each instance of the phase. This equilibrium was mathematically enforced by satisfying the Cauchy's Equation of motion [26]. The 3D displacements field of the LV model was calculated through solving these equilibrium equations using Abaqus FE solver (Dassault Systèmes Simulia Corp., Providence, RI, USA). The LV model's boundary conditions included restricting the longitudinal displacements of the basal nodes while the circumferential displacements of the epicardial basal nodes were set to zero.

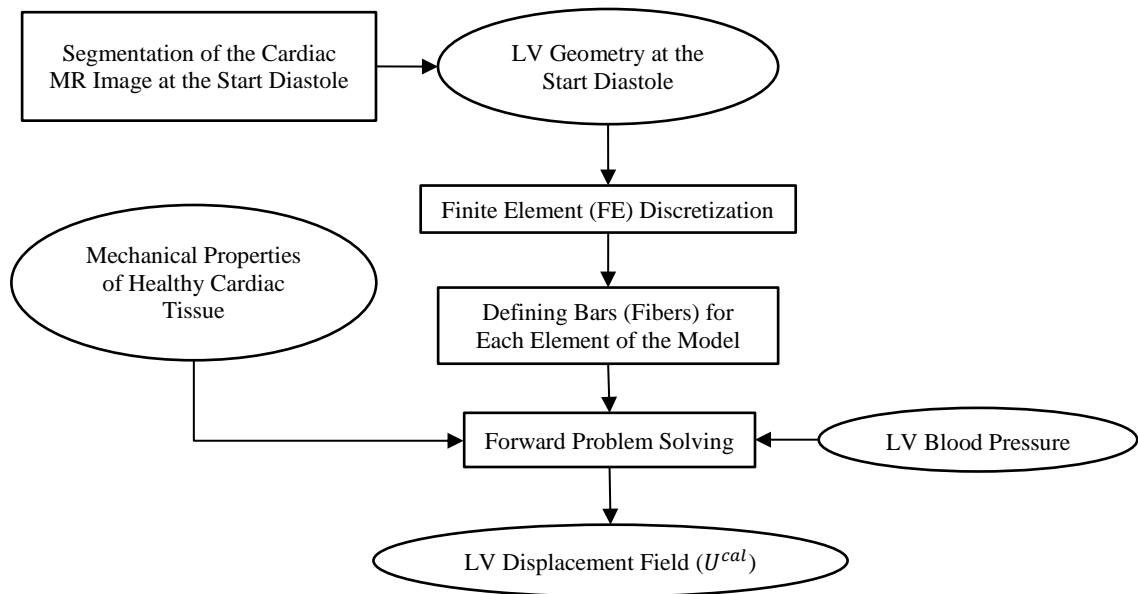


**Figure 5.5:** Flow chart illustrating biomechanical simulation of the LV at the diastolic phase.

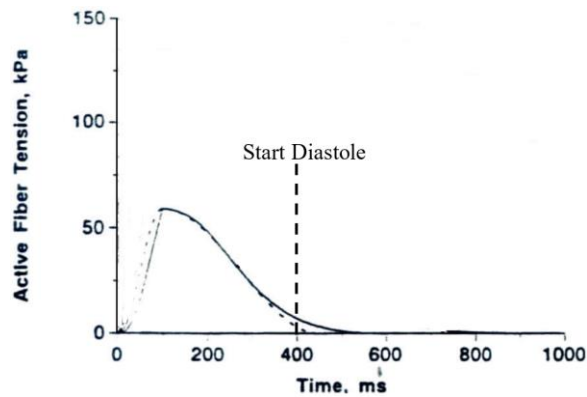


**Figure 5.6:** Active stress variations along a sarcomere of length  $1.7 \mu\text{m}$  during a cardiac cycle [28].

### 5.2.5 Anisotropy of the FE-based Left Ventricle Model

The fibers within the FE-based LV model introduced in Figure 5.4 were simulated by rebars aligned within layers in each element. The fibers occupied  $\sim 60\%$  of the volume of the elements according to morphological studies of the LV tissue composition [29]. The remaining 40% was filled by a non-myofiber material (background tissue). Anisotropy of

the LV model was simulated by altering the helix angle fiber, as the major parameter defining the fiber orientation in 3D space, by moving from endocardium towards epicardium. Hence, the helix angles of the fibers were changed linearly from  $\sim -40^\circ$  at epicardium to  $\sim +66^\circ$  at endocardium according measurements of human LV fiber orientation obtained from a database developed using LV DT-MRI of a cohort of healthy subjects [30].

### 5.2.6 Ad-hoc Inversion-based Approach for End-diastolic LV Blood Pressure Estimation

To estimate the LV diastolic blood pressure of the subject, we altered the pressure and hyperelastic parameters of the background tissue and myofibers iteratively following an ad-hoc scheme such that the best match was achieved between measured and calculated end-diastolic geometries. The calculated geometry was computed using the proposed forward model described in Section 5.2.4. The measured LV geometry was acquired from the 4D MR image dataset of the cardiac cycle and through segmentation of the end-diastolic 3D volume. As an initial guess of the mechanical properties of both of the background tissue and myofibers, we utilized a 2<sup>nd</sup> order Ogden hyperelastic model based on the cardiac tissue stress-strain data given in [31]. This Ogden hyperelastic model is described using the following strain-energy function [26]:

$$\tilde{U} = \sum_{i=1}^N \frac{2\mu_i}{\alpha_i^2} (\lambda_1^{-\alpha_i} + \lambda_2^{-\alpha_i} + \lambda_3^{-\alpha_i} - 3) + \sum_{i=1}^N \frac{1}{D_i} (J_{el} - 1)^{2i} \quad (5.1)$$

where  $\alpha_i$  and  $\mu_i$  are the hyperelastic model coefficients, and  $\lambda_i$ s are principal stretches. The initial guess of the blood pressure was considered to vary between 400 Pa to 1600 Pa which is the diastolic blood pressure range of a healthy human according to reported measurements of the LV diastolic function [32]. It is noteworthy that the forward model only provides the deformed configuration of the LV resulting from the diastolic blood pressure. The final LV configuration obtained from mechanical LV simulations, however, includes significant rigid body motion. To account for this rigid body motion, iterative closest point (ICP) algorithm was performed to achieve the best alignment of the calculated and measured LV geometries [33].

## 5.2.7 Performance Evaluation of the LV Mechanical Model at End Diastole

Through the ad-hoc optimization scheme described in the previous section the optimum mechanical properties of the myofibers and background tissue as well as the optimum diastolic pressure which led to the best match between the calculated and measured end-diastolic geometries were attained. The calculated mechanical properties and blood pressure were applied to the start-diastole LV geometry, which represent the reference configuration, to obtain corresponding stress and strain distribution through the LV geometry. For further validation of the proposed model, distributions of the calculated stresses and strains were assessed and validated by comparing with measurements and other mechanical models of the LV diastolic function.

## 5.3 Results

### 5.3.1 Ad-hoc Optimization

During the ad-hoc optimization procedure described in Section 5.2.6 we observed less sensitivity to changes in the mechanical properties of the myofibers and background tissue. As such, only small changes were made to the mean stress-strain data presented in [31] for healthy cardiac tissue samples. It is noteworthy that the stress-strain data utilized for FE simulation as the optimum mechanical properties were within the range of the measurements reported in [31]. The optimum hyperelastic parameters of the 2<sup>nd</sup> order Ogden model for both background tissue and myofibers obtained from the ad-hoc optimization process is reported in Table 5.1. Accordingly, our primary target during optimization was to optimize the magnitude of the endocardial LV blood pressure such that the best match is attained between the deformed LV geometry as the output of the FE simulation and the one obtained from segmentation of the end-diastolic image. For quantitative assessment of the performance of the ad-hoc optimization, the ICP algorithm was utilized to measure the differences between the calculated and measured LV surface, including endocardial and epicardial surfaces. It should be noted that the ICP algorithm compensates for the rigid body motion of the LV which arises from body and respiratory motions which are not accounted for in the LV mechanical model. Errors matching surfaces obtained by the ICP are reported in the Table 5.2.

**Table 5.1:** Optimum hyperelastic parameters of the 2<sup>nd</sup> order Ogden model used for diastolic LV mechanical simulation

Second Order Ogden Hyperelastic Parameters	Myofiber	Background Tissue
$\mu_1$ (Pa)	335.41	278.06
$\alpha_1$	13.08	8.55
$\mu_2$ (Pa)	0.0331	44.24
$\alpha_2$	38.18	17.02

**Table 5.2:** Variations of the surface matching errors obtained from the ICP algorithm with variable end-diastolic blood pressure values

End-Diastolic Blood Pressure (Pa)	ICP error in root mean squared of the Euclidean distance between surfaces of the measured and Calculated LV Geometries (mm)
400	3.1657
600	3.0773
800	3.0433
1000	3.1178
1200	3.2698
1400	3.3694
1600	3.3989

According to Table 5.2, the best match between measured and calculated geometry with the minimum ICP error was achieved corresponding to blood pressure value of  $p = 800$  Pa. The two surfaces of the measured and calculated LV geometry at the optimum blood pressure and mechanical properties are illustrated in Figure 5.7.

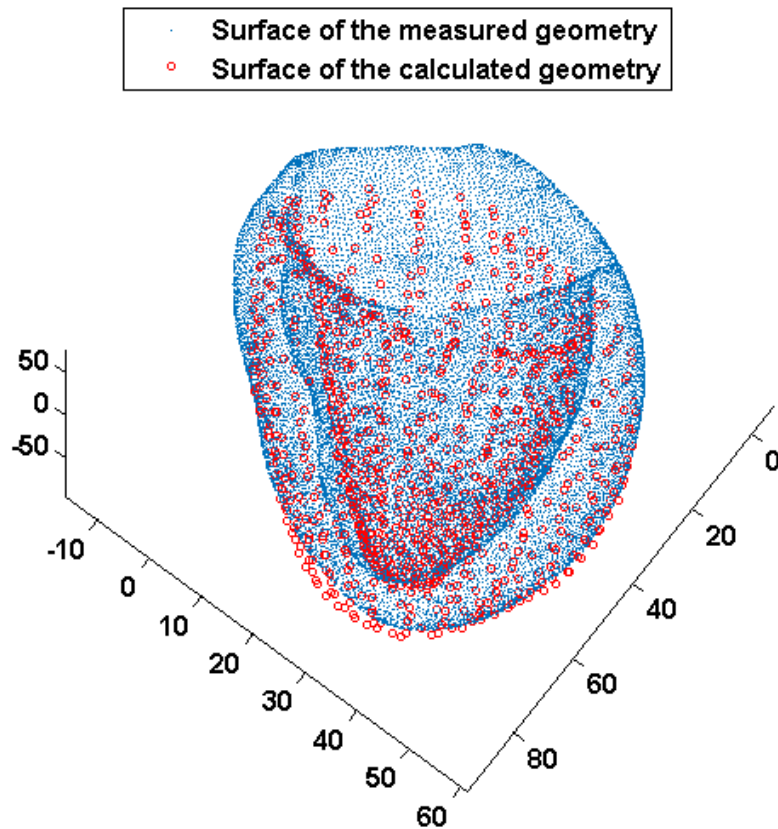


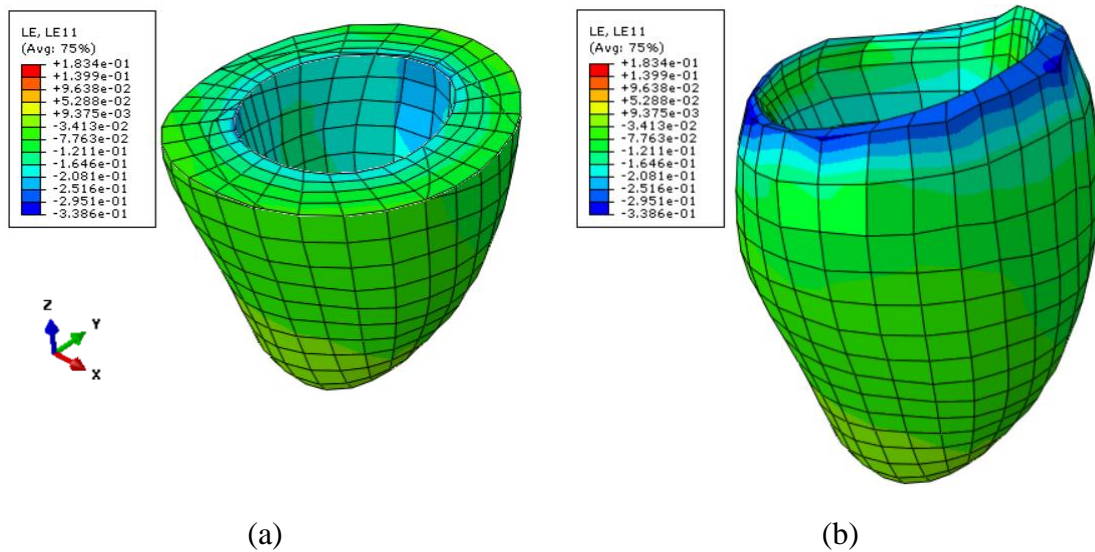
**Figure 5.7:** Surfaces of the calculated and measure LV geometries at the end-diastolic state corresponding to the best match achieved through ad-hoc optimization.

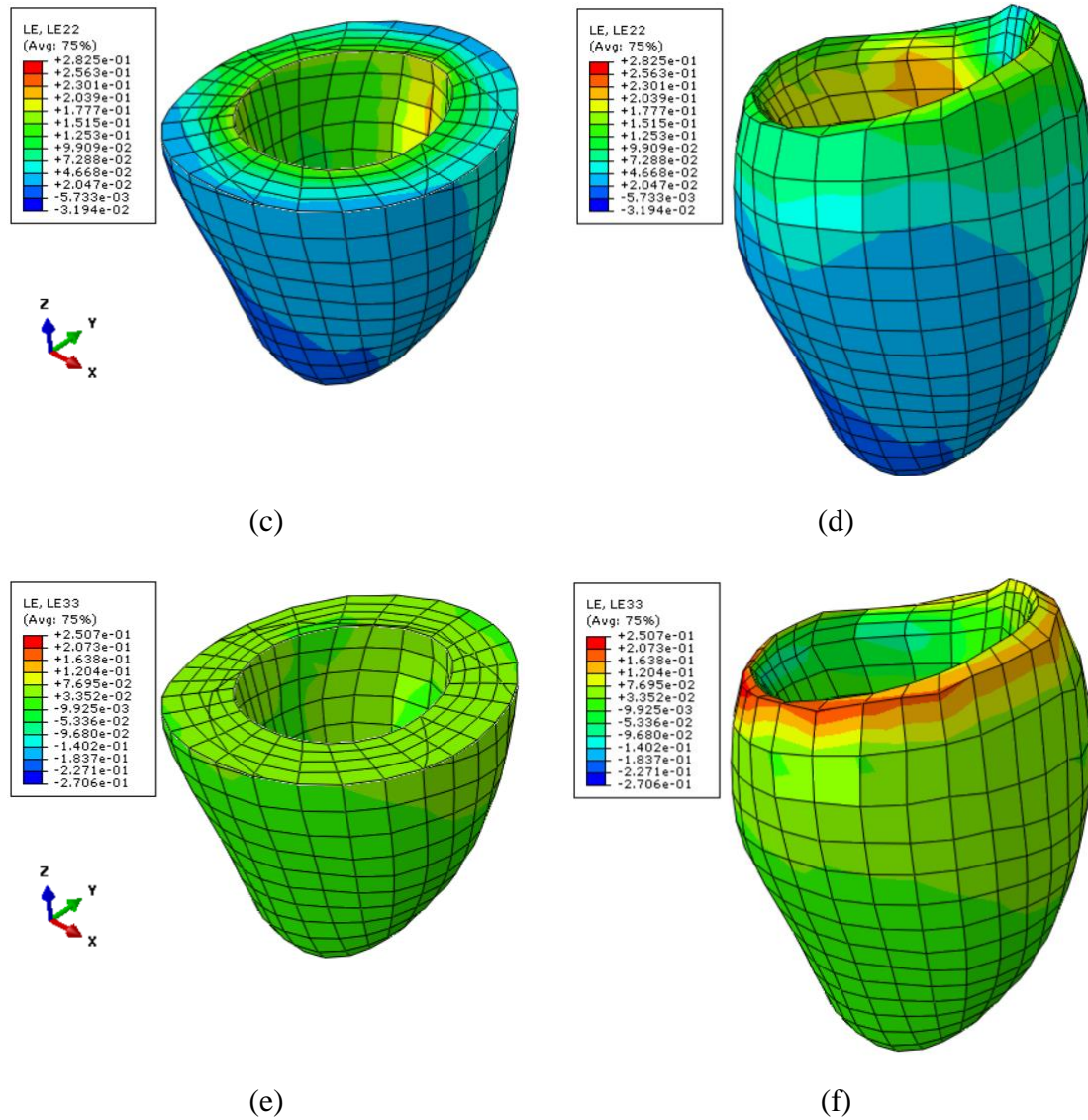
### 5.3.2 Diastolic LV Mechanical Model with Optimum Parameters

After calculating the optimum values of the diastolic blood pressure and tissue hyperelastic parameters, the accuracy of the LV mechanical simulation corresponding to these optimum parameters was assessed. One important geometric measure is the midventricular diameter of the LV at the end-diastolic state. This was calculated at 41.1 mm which is within the normal range of human LV diameter (i.e. 36 mm to 56 mm [34]), indicating good performance of the model. Another measure of LV diastolic mechanics is end-diastolic strain distribution through the LV model which was also investigated. Figure 5.8 shows the normal strains' distribution through the LV volume at the end-diastolic state corresponding to the blood pressure value of  $p = 800$  Pa. The main feature of these strain distributions is that the radial strain (Figure 5.8 (a)) is mostly negative at the midventricular region while the other two strain components, i.e. circumferential (Figure 5.8 (c)) and



longitudinal (Figure 5.8 (e)), are mostly positive. This is consistent with both measurements and simulation results of other LV diastole mechanics models [35-36]. The negative radial strain values reflect the compressional effect of the blood pressure in the radial direction that leads to thinning of the LV wall while approaching the maximum dilation of the LV volume at the end-diastole phase. The positive values of the circumferential and longitudinal strains illustrate dilation of the model by stretching strains in circumferential and longitudinal directions. As shown in Figure 5.8 (a) the end-diastolic radial strain at the midventricular area changes from -16.4% to -7.76% while moving from endocardium towards epicardium. It is also evident that the equatorial circumferential strain decreases from 17.77% at the endocardium to 4.6% at the epicardium (Figure 5.8 (c)) while the equatorial longitudinal strain varies from 7.6% at endocardium to 3.3% at epicardium (Figure 5.8 (e)).

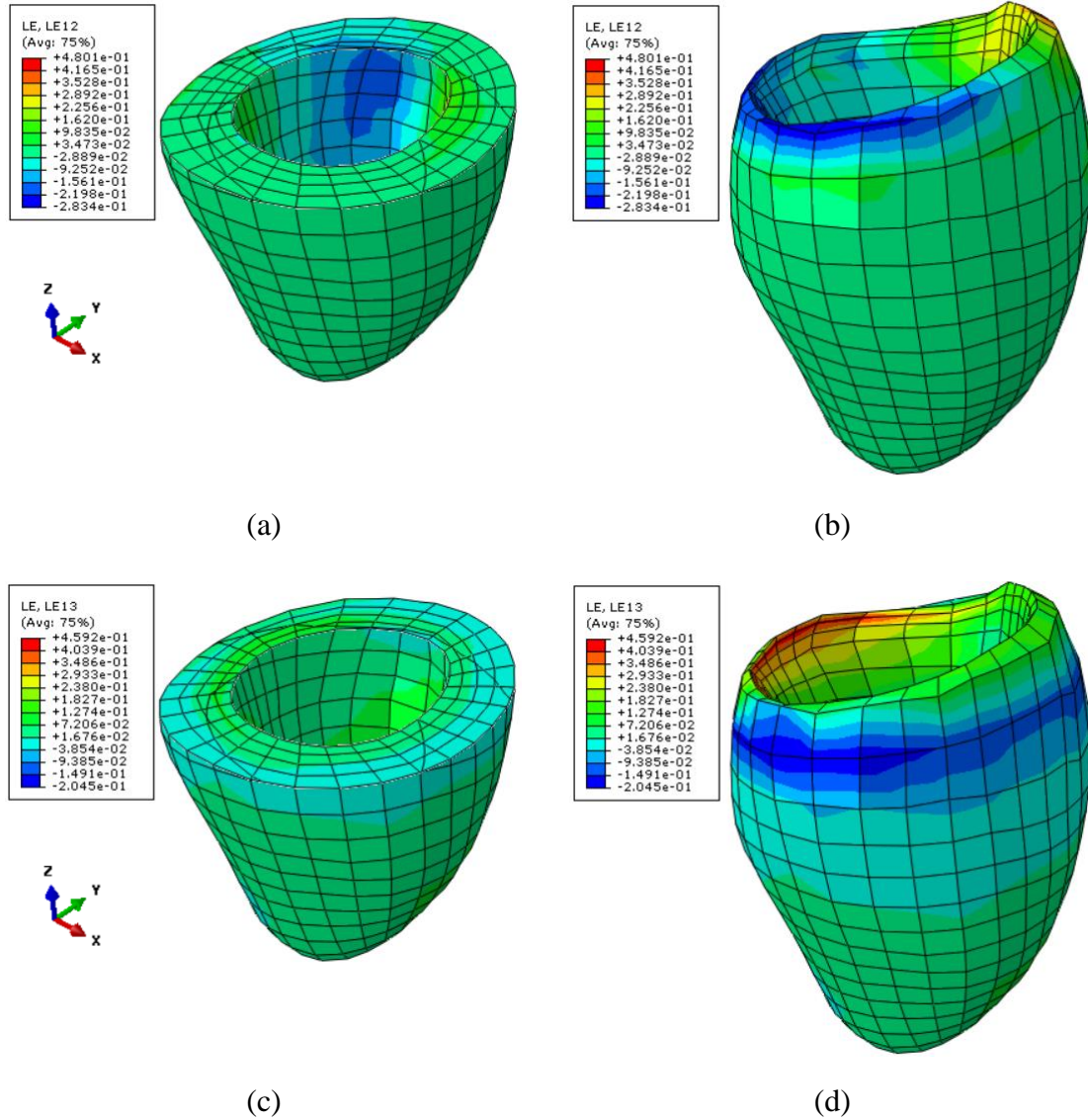


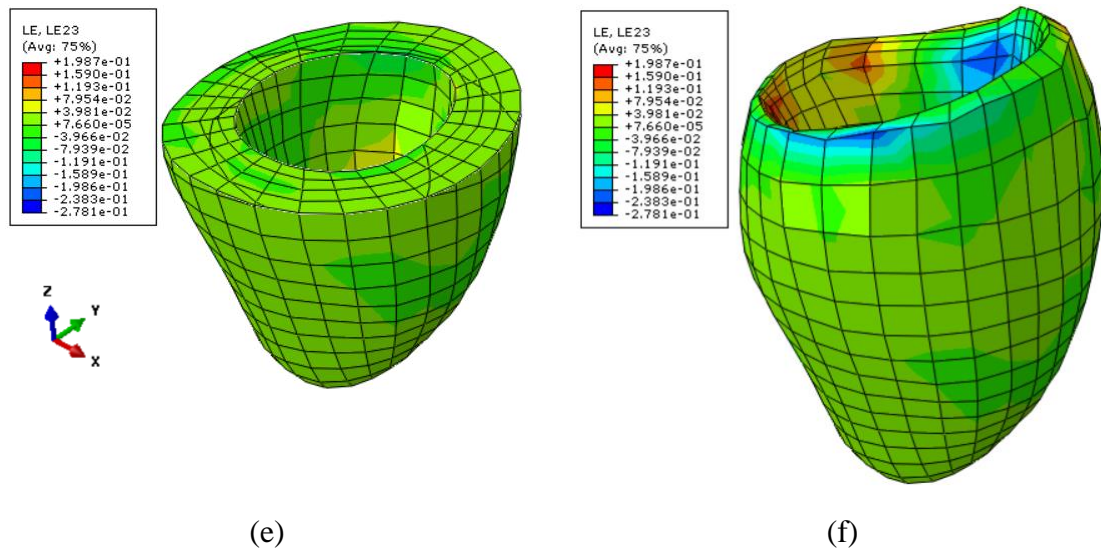


**Figure 5.8:** Normal strains distributions through the LV volume at the end-diastolic state: cross-sectional views of the radial strain distribution (a) along with the whole radial strain distribution (b), cross-sectional view of the circumferential strain distribution (c) along with the whole circumferential strain distribution (d), cross-sectional view of the longitudinal strain distribution (e) along with the whole longitudinal strain distribution (f).

For further investigation of the performance of the end-diastolic simulation, shear strains distributions within the LV model are also illustrated in Figure 5.9. The midventricular radial-circumferential strain is positive across the LV wall as shown in Figure 5.9 (a) while it varies from  $\sim 9.8\%$  at endocardium to  $\sim 2\%$  at epicardium. The equatorial radial-longitudinal strain varies from  $\sim 5\%$  to  $\sim -2\%$  by moving from endocardium to epicardium (Figure 5.9 (c)). Furthermore, the circumferential-longitudinal strain transmurally changes

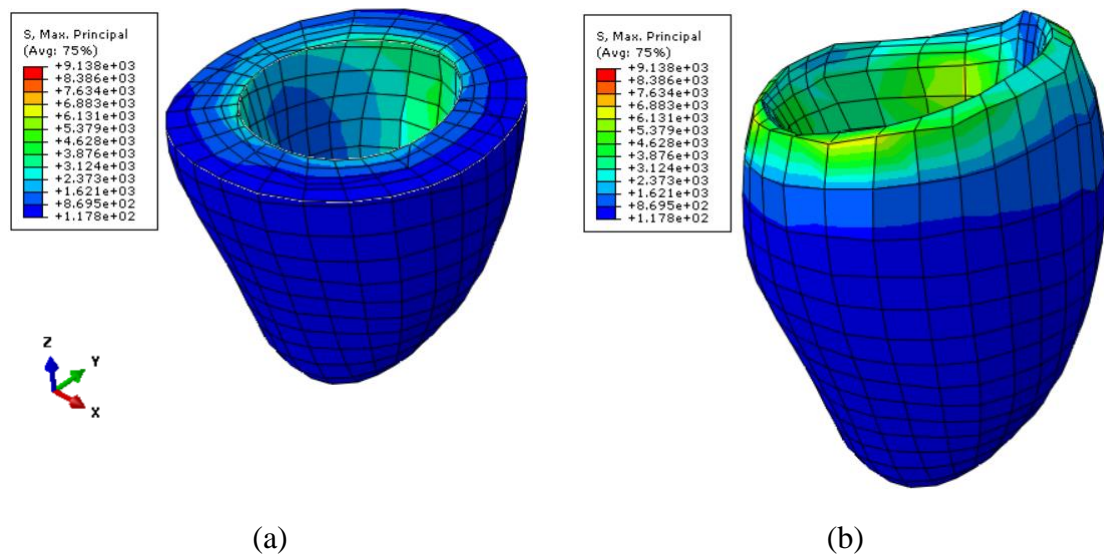
from  $\sim -3.9\%$  to  $\sim 1\%$  (Figure 5.9 (e)). The validity of these strain distributions comparing with measurements and with simulations obtained from other LV mechanical models will be discussed in the Discussion and Conclusions section.

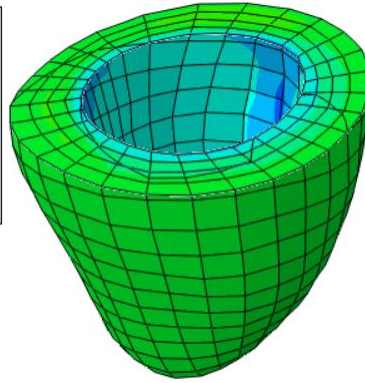
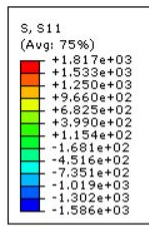




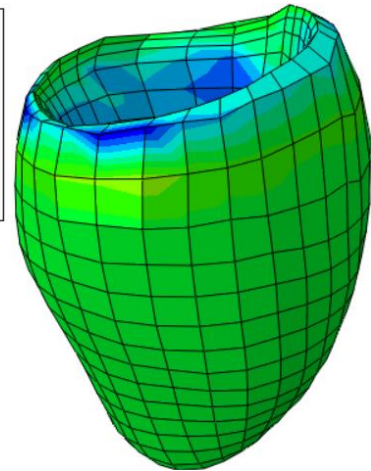
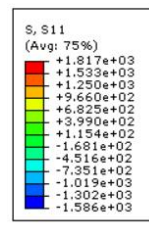
**Figure 5.9:** Shear strains distributions through the LV volume at the end-diastolic state: cross-sectional view of the rad-circ. strain distribution (a) along with the whole rad-circ. strain distribution (b), cross-sectional view of the rad-long strain distribution (c) along with the whole rad-long strain distribution (d), cross-sectional view of the circ.-long strain distribution (e) along with the whole circ.-long strain distribution (f).

For further assessment, we illustrate the LV tissue stress distributions at end diastole phase in Figure 5.10. The major feature of all of these stresses is that all of their maximum principal, radial, circumferential, and longitudinal stress components except the endocardial radial stresses are positive. This is consistent with the dilation of the LV model.

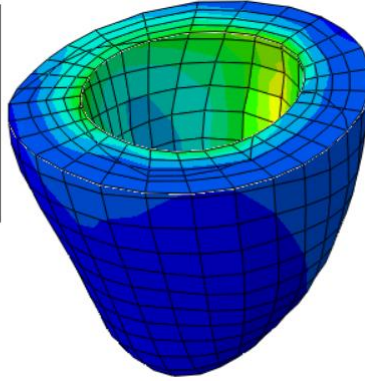
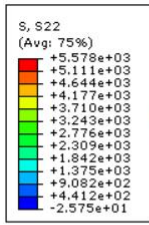




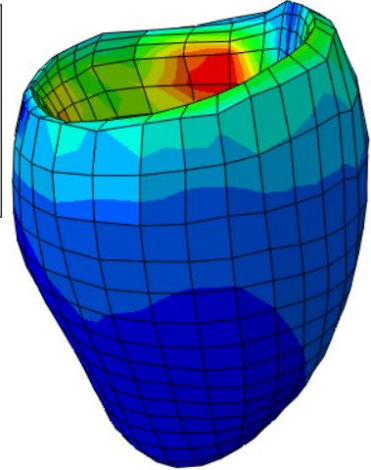
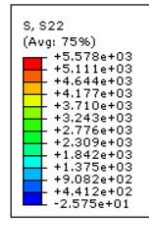
(c)



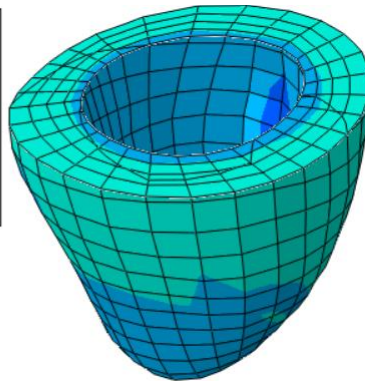
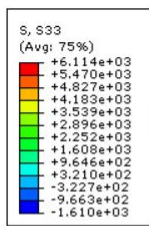
(d)



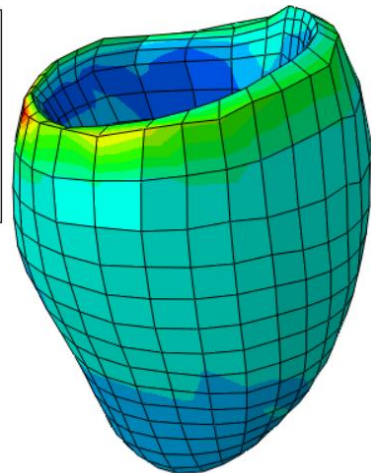
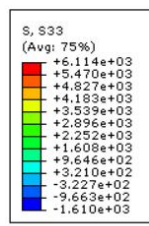
(e)



(f)



(g)



(h)



**Figure 5.10:** Distribution of the background tissue stresses through the LV model at the end-diastolic state: cross-sectional view of the maximum principal stress distribution (a) along with the whole maximum principal stress distribution (b), cross-sectional view of the radial stress distribution (c) along with the whole radial stress distribution (d), cross-sectional view of the circumferential stress distribution (e) along with the whole circumferential stress distribution (f), cross-sectional view of the longitudinal stress distribution (g) along with the whole longitudinal stress distribution (h).

## 5.4 Discussion and Conclusions

In this chapter the LV diastolic function was simulated using the mechanical modeling approach presented in Chapters 3 and 4. In this method, a human subject LV geometry at the start diastole was acquired from MR image segmentation. This geometry was used for mechanical modeling of the LV during the passive inflation at the diastolic phase. Accordingly, the research work conducted in this chapter can be considered as a step forward towards more realistic modeling of the LV since a realistic geometry of the human LV was utilized. In the proposed mechanical model, a composite material model was considered for the LV muscle tissue. As such the tissue was decomposed into myofibers (microscopic reinforcement bars) and background tissue. These components were distributed throughout the tissue volume consistent with the LV anatomy and morphological analysis of fibrous structure of the LV muscle tissue. Distribution of the “rebars” in the LV geometry in fact reflects the fibrous structure of the cardiac tissue. For simulation of the mechanical behavior of the background tissue and myofibers, hyperelastic models were considered. As a result of applying the diastolic blood pressure to the LV endocardial surface, the model was inflated while both parts of the cardiac tissue underwent passive deformation. The proposed model has this special merit that it is implementable using off-the-shelf FE solvers without any need for further FE module coding. Since a well validated and computationally efficient commercial FE solver was utilized for our simulations, we were able to conduct the simulations presented in this work with high efficiency while divergence and instability issues were rarely encountered.

To demonstrate the effectiveness of the proposed model in simulating natural deformation of the LV during diastole phase, we used an ad-hoc optimization scheme to adjust the diastolic blood pressure and stiffness parameters of the LV muscle tissue parts (myofibers

and background tissue) such that the LV surface, including both endocardial and epicardial surfaces, of the calculated end-diastolic LV model has the best match with that of the measured end-diastolic LV geometry obtained from segmentation of the MR image. It is noteworthy that the LV mechanical model accounts for tissue deformation only and it does not consider the LV rigid motion arising from body and respiratory motions. As such, the ICP algorithm was used to eliminate the rigid motion through finding the best surface alignment before surface matching can be assessed. The ICP algorithm calculates the surface matching error, providing a reasonable cost function optimization which was used to find the subject's blood pressure at the end diastole phase non-invasively. Through an ad-hoc optimization procedure, both of the diastolic pressure and tissue hyperelastic parameters were varied to obtain the best surface match. However, the variations of hyperelastic parameters were bounded within a small range to reflect high certainty of their measured values. Using this optimization procedure, the diastolic blood pressure was determined at 800 Pa while the determined mechanical properties were slightly different from the ones corresponding to average stress-strain data given in [31]. This reinforces the validity of the proposed method as calculated optimum parameters pertaining to both diastolic blood pressure and mechanical properties of the myofibers and background tissue are within the normal range of the LV measurements [31-32].

The performance of the LV model was further evaluated by investigating the distribution of the end-diastolic strains within the LV model while the optimum values of blood pressure (800 Pa) and mechanical properties were used for mechanical simulation. Figure 5.8 shows the distribution of the normal strain through the model. As observed in Figure 5.8 (a), the radial strain is mainly negative through the model reflecting the thinning of the LV model by approaching to the end-diastolic phase while blood pressure is increasing [7,35-37]. It is also evident that the magnitude of the radial strains decreases by moving from endocardium towards epicardium, reflecting the greater compressional effect of the blood pressure in the radial direction on the endocardial surface [7,35-37]. The end-diastolic radial strain at the midventricular area changes from -16.4% to -7.76% by moving from endocardium towards epicardium (Figure 5.8 (a)). This is consistent with other mechanical models of the LV diastolic inflation [7] in which the radial strain changes from -14% to -9% in the same region. These values are also in a fairly good agreement with

measurements of the LV diastolic function [36] where the transmural radial strain alterations is reported at -18% to -12%. The circumferential strain in our model is mainly positive (contrary to the radial strain), reflecting the circumferential dilation of the model caused by the blood pressure (Figure 5.8 (c)) [7,35-37]. The circumferential strain magnitude declines from 17.77% at the endocardium to 4.6% at the epicardium, showing greater extensional influence of the blood pressure near the endocardial region. This is in a good agreement with measurements of the human LV dilation [37] where the transmural variations of the radial strains is reported to vary from 15% to 7%. Other LV mechanical models (e.g. [38]) reported circumferential strain variations from endocardium to epicardium is 15% to 9%, showing good consistency with our model. Similar to the circumferential strain, longitudinal strain has a positive strain distribution through the model while varies from ~7.6% at endocardium to ~3.3% at epicardium at the equatorial area (see Figure 5.8 (e)). These strain alterations are normal since it shows the dilation of the model while the greater stretches occur near the endocardium where the LV tissue is in close contact with the blood pool and is affected more by its dilatational effect [7,35-38]. Quantitatively, these strain values are in good accordance with the measurements of the LV diastolic function [36] where it changes from 12% to 3.6% by moving from endocardium towards epicardium. It is also in a fairly good agreement with other mechanical models of the LV dilatation [38] in which the longitudinal strain alters from 8.5% to 7.6% transmurally which is tensional across the LV wall. On the whole, the quantitative assessment of the transmural end-diastolic normal strain variations within the LV wall in our model agrees very well with those reported from measurements and other mechanical models of the LV dilation, reinforcing the validity of the proposed model. Furthermore, the diameter of the dilated LV at the end-diastolic instance was calculated at 41.1 mm which was within the normal range of the end-diastolic diameter of the human LV based on values reported in the literature [34], once more providing evidence of reliable performance of the proposed LV FE model.

The shear strain distribution within the LV model at the end-diastolic instance was also probed as another measure of performance of the model during diastole phase. It is noteworthy that capturing shear strain variations of the LV accurately is more challenging as this strain is more sensitive to heterogeneous anisotropic tissue properties. This



sensitivity has led to higher diversity in values reported by both experimental and mechanical modeling studies of the LV diastolic function [7,35-38]. The radial-circumferential strain is positive through the LV wall and at the midventricular region while it varies from  $\sim 9.8\%$  at endocardium to  $\sim 2\%$  at epicardium as illustrated in Figure 5.9 (a). This agrees fairly well with other validated mechanical models of the LV at the diastolic phase [12] especially in predicting positive values of the strain through the LV wall. The radial-longitudinal strain also changes from  $\sim 5\%$  at endocardium to  $\sim -2\%$  at epicardium, showing good agreement with the LV mechanical model presented in [12] which reports that this strain component varies from  $4\%$  to  $-2\%$  transmurally (see Figure 5.9 (c)). The circumferential-longitudinal strain also changes from  $\sim -3.9\%$  to  $\sim 1\%$  from endocardium to epicardium (see Figure 5.9 (e)), showing a good agreement with the mechanical model presented in [35], while this shear strain changes from  $-3\%$  to zero by moving from endocardium towards epicardium. Other mechanical models of the LV have reported results which show fairly good agreement with our results [7,12,39]. It also agrees well with measurements presented in [36] for LV dilation which shows a variation of the  $-5\%$  to  $-0.5\%$  from endocardium to epicardium. Overall, it can be concluded that the shear strain components in the presented LV model at the end-diastolic instance is also consistent with values reported from experimental and other mechanical modeling studies of the LV, again consolidating the validity of the FE LV simulation conducted in this chapter.

The passive stress distributions at end diastole in the background tissue which was produced by Abaqus software are shown in Figure 5.10. The maximum principle stress distribution through the model is illustrated by Figure 5.10 (a) and (b). The major observation of this stress component is the positive stress distribution throughout the LV volume which indicates tensile stress distribution throughout the model as a result of the dilating blood pressure. The maximum value of this stress at midventricular area is  $\sim 3.5$  kPa at endocardium which is in the range of the LV tissue stress values reported for end diastole [25,35]. The radial stress distribution were shown in Figures 5.10 (c) and (d). As observed in Figure 5.10 (c) at the equatorial area, the radial stress changes from positive tensional values at endocardium towards very small negative compressional values at epicardium, reflecting expected reduction of the dilatational effect of the blood pressure by moving towards epicardium. The circumferential and longitudinal stress distributions

through the LV model are illustrated in Figures 5.10 (e), (f), (g), and (h). Both of these stresses are mainly positive, reflecting the LV model expansion resulting from the dilating blood pressure. Overall, the stress distributions presented in Figure 5.9 are in good agreement with other mechanical models of the LV, again reinforcing the validity of the proposed LV model.

In this chapter we used an ad-hoc method to estimate the blood pressure and tissue mechanical properties. This was done as the main purpose of this study is to demonstrate the accuracy and effectiveness of the proposed cardiac mechanical model based on composite material model of the cardiac tissue to capture the LV diastolic phase mechanics. For more effective assessment systematic optimization can be utilized to provide more accurate estimate of the blood pressure and tissue mechanical properties. It should be emphasized that while a rough ad-hoc method was utilized to estimate tissue stiffness and diastolic blood pressure, the performance of the LV diastolic mechanical simulations at the calculated optimum values was consistent with other mechanical models and measurements of the LV diastolic function available in the literature. This was concluded based on quantitative and qualitative evaluations of the LV strain and stress distributions as well as end diastolic diameter at the end of the diastolic phase.

## References

- [1] M. Sermesant, H. Delingette, and N. Ayache, “An electromechanical model of the myocardium for cardiac image analysis and medical simulation,” *INRIA Sophia Antipolis*, N° RR-5395, 2004.
- [2] A. I. Veress, W. P. Segars, B. M. W. Tsui, and G. T. Gullberg, “Incorporation of a Left Ventricle Finite Element Model Defining Infarction Into the XCAT Imaging Phantom,” *IEEE Transactions on Medical Imaging*, vol. 30, no. 4, pp.915-927, 2011.
- [3] S. Marchesseau, H. Delingette, M. Sermesant, M. Sorine, K. Rhode, S. G. Duckett, C. A. Rinaldi, R. Razavi, and N. Ayache, “Preliminary specificity study of the Bestel-Clement-Sorine electromechanical model of the heart using parameter calibration from medical images,” *J. Mech. Behav. Biomed. Mater.*, 20, 259-271, 2013.
- [4] K. F. Augenstein, B. R. Cowan, I. J. LeGrice, and A. A. Young, “Estimation of cardiac hyperelastic material properties from MRI tissue tagging and diffusion tensor imaging,” *Medical Image Computing and Computer-Assisted Intervention – MICCAI*, LNCS 4190, 628-635, 2006.
- [5] G. Drzewiecki, J. Wang, J. K. J. Li, J. Kedem, and H. Weiss, “Modeling of mechanical dysfunction in regional stunned myocardium of the left ventricle,” *IEEE Trans. Biomed. Eng.*, 43, 12, 1151-1163, 1996.
- [6] P. Zhang, J. M. Guccione, S. I. Nicholas, J. C. Walker, P. C. Crawford, A. Shamal, D. A. Saloner, A. W. Wallace, and M. B. Ratcliffe, “Left ventricular volume and function after endoventricular patch plasty for dyskinetic anteroapical left ventricular aneurysm in sheep,” *J. Thorac. Cardiovasc. Surg.*, 130(4): 1032-8, 2005.
- [7] A. I. Veress, G. T. Gullberg, and J. A. Weiss, “Measurement of strain in the left ventricle during diastole with cine-MRI and deformable image registration,” *J. Biomech. Eng.*, 127(7): 1195-207, 2005.
- [8] S. D. Colan, “Mechanics of left ventricular systolic and diastolic function in physiologic hypertrophy of the athlete heart,” *Cardiol Clin.*, 10(2): 227-40, 1992.
- [9] M. R. Zile and D. L. Brutsaert, “New concepts in diastolic dysfunction and diastolic heart failure: Part I: diagnosis, prognosis, and measurements of diastolic function,” *Clinical Cardiology: New Frontiers: Circulation.*, 105: 1387-1393, 2002.
- [10] J. J. McMurray and M. A. Pfeffer, “Heart failure,” *The Lancet*, vol. 365, iss. 9474, pp. 1877-1889, 2005.
- [11] W. A. Newman, *Dorland's Illustrated Medical Dictionary*. Philadelphia, PA: Saunders, 2007.
- [12] H. M. Wang, H. Gao, X. Y. Luo, C. Berry, B. E. Griffith, R. W. Ogden, and T. J. Wang, “Structure-based finite strain modelling of the human left ventricle in diastole,” *Int. J. Numer. Method. Biomed. Eng.*, 29, 1, 83-103, 2013.

- [13] W. J. Paulus, C. Tschöpe, J. E. Sanderson, C. Rusconi, F. A. Flachskampf, F. E. Rademakers, P. Marino, O. A. Smiseth, G. D. Keulenaer, A. F. Leite-Moreira, A. Borbely, I. Edes, M. L. Handoko, S. Heymans, N. Pezzali, B. Pieske, K. Dickstein, A. G. Fraser, and D. L. Brutsaert, “How to diagnose diastolic heart failure: a consensus statement on the diagnosis of heart failure with normal left ventricular ejection fraction by the heart failure and echocardiography associations of the European society of cardiology,” *European Heart Journal*, 28 (20): 2539-2550, 2007.
- [14] M. R. Zile and D. L. Brutsaert, “New concepts in diastolic dysfunction and diastolic heart failure: Part II: causal mechanisms and treatment,” *Clinical Cardiology: New Frontiers: Circulation.*, 105: 1387-1393, 2002.
- [15] H. F. Choi, J. D’hooge, F. E. Rademakers, and P. Claus, “Influence of left-ventricular shape on passive filling properties and end-diastolic fiber stress and strain,” *J. Biomech.*, 43, 9, 1745-1753, 2010.
- [16] M. Genet, L. C. Lee, B. Baillargeon, J. M. Guccione, and E. Kuhl, “Modeling pathologies of diastolic and systolic heart failure,” *Annals of Biomedical Engineering*, Jun. 5, 2015.
- [17] V. Gurev, T. Lee, J. Constantino, H. Arevalo, and N. A. Trayanova, “Models of cardiac electromechanics based on individual hearts imaging data: image-based electromechanical models of the heart,” *Biomech. Model. Mechanobiol.*, 10(3): 295-306, 2011.
- [18] T. P. Usyk, R. Mazhari, and A. D. McCulloch, “Effect of laminar orthotropic myofiber architecture on regional stress and strain in the canine left ventricle,” *Journal of elasticity and the physical science of solids*, vol. 61, iss. 1, pp. 143-164, 2000.
- [19] I. J. LeGrice, B. H. Smaill, L.Z. Chai, S. G. Edgar, J. B. Gavin, and P. J. Hunter, “Laminar structure of the heart: ventricular myocyte arrangement and connective tissue architecture in the dog,” *Am. J. Physiol.*, 269(2 Pt 2): H571-82, 1995.
- [20] S. Goktepe and E. Kuhl, “Electromechanics of the heart: a unified approach to the strongly coupled excitation-contraction problem,” *Comput. Mech.*, 45, 2-3, 227-243, 2010.
- [21] H. Dal, S. Goktepe, M. Kaliske, and E. Kuhl, “A fully implicit finite element method for bidomain models of cardiac electromechanics,” *Comput. Methods Appl. Mech. Eng.*, 253, 323-336, 2013.
- [22] J. Moore, M. Drangova, M. Wierzbicki, J. Barron, and T. M. Peters, “A high resolution dynamic heart model based on averaged MRI data,” *In Proceedings of the Medical Image Computing and Computer-Assisted Interventions – MICCAI*, vol. 2878, 2003.
- [23] A. Fedorov, R. Beichel, J. Kalpathy-Cramer, J. Finet, J. C. F. Robin, S. Pujol, C. Bauer, D. Jennings, F. Fennessy, M. Sonka, J. Buatti, S. Aylward, J. V. Miller, S. Pieper, and R. Kikinis, “3D Slicer as an image computing platform for the

- quantitative imaging network,” *Magnetic Resonance Imaging*, vol. 30, iss. 9, pp. 1323-1341, 2012.
- [24] N. M. Grosland, K. H. Shivanna, V. A. Magnotta, N. A. Kallemeyn, N. A. DeVries, S. C. Tadepalli, and C. Lisle, “IA-FEMesh: An open-source, interactive, multiblock approach to anatomic finite element model development,” *Computer Methods and Programs in Biomedicine*, vol. 94, iss. 1, pp. 96-107, 2009.
- [25] M. Genet, L. C. Lee, R. Nguyen, H. Haraldsson, G. Acevedo-Bolton, Z. Zhang, L. Ge, K. Ordovas, S. Kozerke, and J. M. Guccione, “Distribution of normal human left ventricular myofiber stress at end diastole and end systole: a target for *in silico* design of heart failure treatments,” *Journal of Applied Physiology*, 117 (2) 142-152, 2014.
- [26] G. A. Holzapfel, [Nonlinear Solid Mechanics: A Continuum Approach for Engineering], Wiley, West Sussex, 141-152, 2000.
- [27] Hibbit, Karlsson, and Sorenson, *ABAQUS Theory Manual*. Pawtucket, RI, June 1998.
- [28] J. M. Guccione, L. K. Waldman, and A. D. McCulloch, “Mechanics of active contraction in cardiac muscle: Part II--Cylindrical models of the systolic left ventricle,” *J. Biomech. Eng.*, 115(1):82-90, 1993.
- [29] J. Schaper, E. Meiser, and G. Stammner, “Ultrastructural morphometric analysis of myocardium from dogs, rats, hamsters, mice, and from human hearts,” *Circulation.*, 56(3), 377-391 (1985).
- [30] H. Lombaert, J. M. Peyrat, P. Croisille, S. Rapacchi, L. Fanton, F. Cheriet, P. Clarysse, I. Magnin, H. Delingette, and N. Ayache, “Human atlas of the cardiac fiber architecture: study on a healthy population,” *IEEE Trans. Med. Imaging.*, 31(7): 1436-47, 2012.
- [31] J. D. Humphrey, R. K. Strumpf, and T. C. P. Yin, “Determination of a constitutive relation for passive myocardium: II. - parameter estimation,” *J. Biomech. Eng.*, 112, pp. 340-346, Aug. 1990.
- [32] Table 30-1 in: A. G. Trudie, M. E. Klingensmith, E. C. Li, and C. G. Sean, *The Washington manual of surgery Glasgow*. Philadelphia: Wolters Kluwer Health/Lippincott Williams & W.ilkins, 2008.
- [33] P. J. Besl, N. D. McKay, “A method for registration of 3-D shapes,” *IEEE Trans. on Pattern Analysis and Machine Intelligence*, 14(2): 239–256, 1992.
- [34] Page 41 in: O'Connor and Simon, *Examination Medicine (The Examination)*. Edinburgh: Churchill Livingstone, 2009.
- [35] J. M. Guccione, K. D. Costa, and A. D. McCulloch, “Finite element stress analysis of left ventricular mechanics in the beating dog heart,” *J. Biomech.*, 28(10):1167-77, 1995.
- [36] J. H. Omens, K. D. May, and A. D. McCulloch, “Transmural distribution of three-dimensional strain in the isolated arrested canine left ventricle,” *Am. J. Physiol.*, 261(3 Pt 2):H918-28, 1991.

- [37] A. J. Sinusas, X. Papademetris, R. T. Constable, D. P. Dione, M. D. Slade, P. Shi, and J. S. Duncan, "Quantification of 3-D regional myocardial deformation: shape-based analysis of magnetic resonance images," *Am. J. Physiol. Heart Circ. Physiol.*, 281(2): H698-714, 2001.
- [38] J. M. Guccione, A. D. McCulloch, and L. K. Waldman, "Passive material properties of intact ventricular myocardium determined from a cylindrical model," *J. Biomech. Eng.*, 113(1): 42-55, 1991.
- [39] K. May-Newman, J. H. Omens, R. S. Pavelec, and A. D. McCulloch, "Three-dimensional transmural mechanical interaction between the coronary vasculature and passive myocardium in the dog," *Circulation Research*, 74(6):1166-1178, 1994.

# Chapter 6

## Conclusion and Future Work

### 6.1 Conclusion

**D**IFFERENT aspects of the LV mechanics were investigated in this research where the major focus was to develop an LV mechanics model using a novel approach. Two levels of biomechanical modeling pertaining to the myocardium were tackled through the investigations presented in this dissertation. The first level involved developing a framework to characterize intrinsic mechanical properties of healthy and pathological myocardial tissue based on its microstructure. The second level involved studying the LV mechanics at health and disease state. As explained in Chapter 1, myocardial tissue has a very sophisticated microstructure, including various constituents such as myofibers, mitochondria, and collagen fibers. These constituents have been adeptly organized within a fibrous structure to accomplish the contractile performance required to push out the blood with sufficient pressure out of ventricular cavities. Moreover, diverse cardiac pathophysiological conditions are known to change the type, mechanical properties, and organization of the tissue constituents, which leads to overall alteration in the heart mechanical function characterized by EF, stroke volume, and pressure-volume curve. As such the microscopic organization of cardiac tissue plays a crucial role in generating the overall mechanical performance of the myocardium. Connecting the overall macroscopic performance of the cardiac tissue to the tissue constituents' organization is of interest to the medical community as it aids gaining insight into how tissue pathology leads to measurable symptoms pertaining to heart disease. This can be accomplished effectively using computational biomechanics technique. In the area of cardiac mechanics and specifically LV mechanics, there are a few methods presented in the literature. However, none of them are implementable using commercial FE software packages, unless additional custom-developed codes are augmented as subroutines. This arises from the fact that

myocardial contractile function modeling involves hyperelastic anisotropic mechanical tissue models with the cardiac myofibers which need to be modeled as active elements generating contraction. These intricate features are not available in typical modules of commercially available FE software packages. Current FE models idealize cardiac tissue as a mono-phase material with hyperelasticity and anisotropy as its major mechanical properties. Another possible approach follows a composite material idealization which is capable of idealizing cardiac tissue anisotropy more effectively by incorporating actual myofiber orientation with high accuracy. This approach is expected to lead to a model that mimic cardiac mechanics characteristics with improved accuracy. This approach also offers high adaptability and ease of modeling various pathologies at cardiac tissue level. As such, our research was geared towards a number of major objectives which were tackled through different chapters of this thesis. In the first stage of our research we developed a novel cardiac tissue mechanical model for accurate quantification of the cardiac tissue intrinsic mechanical properties. This model takes into account all major cardiac tissue constituents and their associated mechanical properties to acquire the overall intrinsic properties of cardiac tissue. This tissue model is capable of accounting for cardiac tissue microstructural alterations in terms of composition, types, and volume distributions of each constituent corresponding to various pathologies. In the next stage of our investigation, a novel mechanical model of the LV was developed based on a composite tissue material model. This model considers all aspects and complexities of cardiac mechanics including anisotropy, hyperelasticity, and active contraction forces. The model was developed based on the composite material tissue approach of cardiac tissue. A highly important feature of this model is that it can be implemented using commercial FE software packages. The advantage of this feature is two-fold; one is possibility of its development with minimal efforts and paving the way for its wide availability to the research community and the other is its stability and computational efficiency built in most commercial FE solvers. The model was employed to simulate both a normal and a pathological LV mechanics during a complete heartbeat, to demonstrate its adaptability for heart disease mechanical simulation. The presented cardiac mechanics model is computationally efficient as it is fully implementable using commercial FE solvers, therefore, it is attractive for FE inversion-based approaches. Accordingly, for a preliminary assessment of this model towards FE



inversion-based applications, the model was applied to a human LV model constructed using MR imaging data. Using this model, an ad-hoc optimization scheme was used to estimate the LV tissue muscle stiffness parameters and blood pressure of the diastole phase. The studies conducted in this research were presented in four chapters. The highlights of research achievements and results from these studies are presented briefly in the following sections.

### 6.1.1 Chapter 2: A Novel Micro-to-Macro Approach for Cardiac Tissue Mechanics

A novel approach for characterizing cardiac tissue mechanics under normal and various pathological conditions was proposed in this chapter where hyperelasticity and anisotropy were modeled. This approach is based on the cardiac tissue composition and organization of its microstructural tissue constituents. To develop cardiac tissue constitutive model following this approach, two major parts were considered for the tissue: 1) the background tissue including the three major constituents of mitochondria, collagen fibers and myofibroblasts, and 2) myofibrils. The major cardiac tissue constituents were chosen carefully based on morphological studies of the cardiac tissue which are available in the literature. The variations of type, volume percentage, and organization of the cardiac tissue constituents which are consistent with the pathophysiological state of the tissue is known to determine variations of cardiac tissue intrinsic properties. To obtain the tissue constitutive model following the proposed strategy, FE tissue samples of composite models pertaining to normal and pathological tissues were constructed by combining the tissue constituents as infinitesimal elements with different mechanical properties distributed throughout the samples' volumes. The FE models were employed to simulate necessary uniaxial or biaxial mechanical tests to obtain corresponding stress vs. strain data. In the proposed approach, a two-step FE simulation was devised. In the first step, mechanical properties of the background tissue (non-myofiber part) and myofibers of the cardiac tissue were quantified in terms of hyperelastic parameters. In the second step, a self-contained anisotropic hyperelastic composite model of the whole cardiac tissue consisting of the two background and myofiber parts was constructed and used for biaxial and uniaxial FE

simulations. The major outcome of this two-step FE simulation is the overall intrinsic properties of cardiac tissue (stress-strain curve) in terms of its microstructural constituents.

The technique was applied for normal cardiac tissue, leading to stress-strain datasets pertaining to both fiber and cross-fiber directions. These datasets were compared to measured cardiac tissue stress-strain datasets available in the literature and good agreement was observed. Moreover, the biaxial stress-strain datasets obtained in this study were fitted to the hyperelastic anisotropic models of normal cardiac tissue available in the literature and, as expected, the calculated parameters were in the range of parameters reported in the literature. Ad-hoc sensitivity analysis was also conducted to assess variations of the tissue stress-strain characteristics with respect to changes in the volume percentages of the tissue constituents. It was observed that the stress-strain characteristics are more sensitive to the myofibrils and mitochondria alterations. The significance of the mitochondria's volume contribution alterations on cardiac tissue mechanical behavior is very interesting, and it arises from its high volume contribution to the cardiac tissue. It is noteworthy that most of the structural analysis merely investigate the influence of myofibrils and collagen fibers as the major players in determining the overall cardiac tissue mechanics. We also evaluated the hyperelastic parameters' alterations with respect to tissue constituent changes as another measure of sensitivity, and once more the parameter alterations due to myofibrils and mitochondria changes were found to be more substantial. This agrees with our previous findings of the stress-strain relationship sensitivity analysis.

Our method was also applied for modeling infarcted cardiac tissue as an important instance of cardiac pathological tissue. In our analysis of the MI mechanics, due to well-known development of the thick collagen fibers with more cross-linking within the infarct area, collagen fibers with stiffer mechanical properties were used. As such, the stiffness of the collagen fibers were adjusted such that a stress-strain curve with a good agreement between our results and experimental data (errors smaller than 10%) was achieved. The uniaxial stress-strain data of infarcted cardiac tissue obtained from the proposed method was also fitted to Yeoh, second order Polynomial, and fifth order Ogden hyperelastic models to compute the corresponding hyperelastic parameters. These hyperelastic parameters are very important since they can be utilized as input parameters for mechanical simulations

of the heart and LV with MI. The sensitivity of the stress-strain relationship to volume fraction variations of tissue constituents was also investigated, and it was observed that collagen fibers as the main constituent of the infarcted scar with the highest volume contribution plays a more important role in determining the cardiac tissue mechanics with MI. As another measure of sensitivity, infarcted cardiac tissue's hyperelastic parameters variations by change in the collagen's volume percentage was evaluated. Our results demonstrated significant changes due to these alterations, once more confirming the importance of collagen fiber network and its decisive effect in characterizing the intrinsic characteristics of infarcted cardiac tissue.

### 6.1.2 Chapter 3: A Novel Biomechanical Computational Model of the Left Ventricle using a Composite Material Approach

In this chapter, a novel mechanical model of the LV was presented. The model was devised based on a composite material model of the cardiac tissue. Based on this composite model, cardiac tissue is decomposed into two major parts a background tissue in which the microscopic reinforcement rebars (fibers) are distributed. This composite model is consistent with the cardiac physiology, its fibrous structure, and available mechanical models of the cardiac tissue such as Hill's model. In such models, typically two major parts are considered for the tissue: a mechanically active/passive part (myofibers) and a passive part (background tissue). The model was implemented using nonlinear FE approach and applied to an *in silico* geometry of a canine LV. To conduct the FE analysis, LV geometry was discretized into a FE mesh. The elements of this model were built as a composite material including two major constructive material (tissues): myofibers and background tissue. Myofibers were distributed through the elements of the FE LV model such that their directions were consistent with the fibrous structure of the LV anatomy based on the mathematical helical model presented in the literature. This element-based directional myofibers dispersal results in a self-contained anisotropy for the model which agrees with the realistic LV fiber orientations. To account for nonlinearity of the cardiac tissue as a major attribute of its passive behavior especially considering the large deformations though the myocardium, hyperelastic material model was considered for both myofibers and background tissue. Taking this description of the proposed model into consideration, both

aspects of the cardiac passive mechanics, i.e. hyperelasticity and anisotropy, were incorporated into our model. To model another important mechanical aspect of the cardiac mechanics, i.e. active myofibers stress, the elements' rebars were prestressed incrementally to simulate time-variable myofibers' contraction according to the well-known elastance model. Blood pressure alterations were also simulated by exerting a time-dependent uniform pressure to the endocardial surface of the model quantified according to available ventricular blood pressure data acquired during a cardiac cycle.

The performance of the LV contractile function, which was constructed based on abovementioned method, was evaluated in both diastolic and systolic phases. As an important feature of the LV passive inflation, the LV model was pressurized by an incremental blood pressure up to 3 kPa while no significant active contractile stress was applied to the rebars. The pressure-volume characteristic curve obtained from our model was compared with experimental measurements of the LV contraction as well as other mechanical models presented in the literature, confirming the validity of our model. Passive transmural strain components through the model at end diastolic state were also evaluated. Our results indicated similar variations in all six components of the passive strains by moving from endocardium towards epicardium to those presented by other valid mechanical simulations of the LV, properly validating the diastolic performance of our model. The passive stress distribution through both parts of the tissue, i.e. background tissue and myofibers, at the end diastolic state agrees very well with stress distributions presented in other research works. The values of the fiber stress attained by our approach at the diastolic state also were in the range of stresses reported by other validated models, confirming the accuracy of our simulation.

The LV model contraction at end systolic state was also investigated by comparing all six components of the strains through the LV model with the measurements as well as other mechanical models of the LV. All normal strains, i.e. radial, circumferential, and longitudinal strains, were found to be within the range of measurements reported for the strains within the anterior equatorial LV free wall. The calculated normal strains also demonstrated a very good agreement with other validated mechanical model of the LV. With radial strain, our results show slightly higher near endocardium and slightly lower

near epicardium. However, these strains are on par with other validated mechanical models. In case of shear strain components, due to the high level of complexity of the LV contraction arising from its heterogeneity and geometrical irregularities, similar to other validated mechanical models of the LV our model did not provide shear strain values close to the measured data for all three components of the shear strains. However, considering the radial-circumferential strain resulting from our simulation, which is almost within the range of the measured data, the performance of the presented model is quite acceptable. The end-systolic stress distributions resulting from our simulation in both background tissue and myofibers were also assessed. They showed that the maximum principle, radial, circumferential, and longitudinal stresses are mainly negative except within some small portions of the LV model, confirming the overall contraction within the model. It was also observed that the longitudinal fiber stress in the proposed model varies from negative values at endocardium to positive values at epicardium while the maximum values occur at mid-wall. These results are consistent with other LV models, again reinforcing the validity of the proposed model. The maximum value of fiber stress achieved by our model is also in the range of values reported by other validated mechanical models of the LV. In conclusion, considering the performance of the presented LV model in both systolic and diastolic phases, composite material model for cardiac tissue decomposition can be considered as an effective approach for cardiac mechanical simulations. This tissue decomposition strategy offers an outstanding opportunity to use off-the-shelf FE software packages which are usually computationally cost-effective with better convergence characteristics for modeling both passive and active aspects of cardiac mechanics. The model developed in this chapter can be considered as a core element for inversion-based finite element algorithms which are implemented by FE commercial software packages.

### 6.1.3 Chapter 4: A Biomechanical Model of the Pathological Left Ventricle using a Composite Material Approach

In Chapter 3, the LV mechanical model was applied to a normal LV geometry. In Chapter 4, to investigate the performance of our model under pathological conditions, we utilized this model for pathological LV modeling. For this purpose an infarcted region was considered at the equatorial area of the LV model with a border zone enclosing it consistent

with known MI related tissue changes. The passive mechanical properties of the infarct region were changed such that the stiffness is higher in accordance with mechanical testing data pertaining to infarcted cardiac tissue. Fiber orientation within the infarct region was adjusted mostly in the circumferential direction consistent with known MI pathological alteration reported for cardiac ischemic scars. Similar to the normal LV model, the elastance model was used to account for time variations of the myofibers' active stress during a cardiac cycle. The same parameters were assigned for the elastance model within the healthy regions of the infarcted LV model. However, the maximum isometric tension at the longest sarcomere length, which is an essential parameter of the elastance model, was set to zero and to half of the value used for healthy tissue at the infarct region and border zone, respectively, in accordance with other validated mechanical models of the infarcted LV. It is noteworthy that setting maximum isometric tension at the longest sarcomere length to zero at the infarct region implies zero contraction at this part which is expected due to the death of the majority of the cardiomyocytes. All other parameters and loadings of the infarcted model were similar to those used for normal LV mechanical model presented in Chapter 3.

The LV model with MI was evaluated by investigating the distribution of normal strains at end-systolic state. It was observed that while stretching radial strain occurred at the normal midventricular areas as a sign of myocardial thickening at this parts, negative compressional strains developed at the infarct region, reflecting the well-known MI related thinning at this area. As another sign of infarction, the circumferential strain was positive at the infarct region consistent with other mechanical simulations of the infarcted LV. This was mainly because of depression of the contractile power of the tissue at this area, whereas it was negative within the normal LV parts due to their normal contraction. Longitudinal strains were also mainly negative in the healthy parts of the midventricular area while, similar to the other normal strain components, they were less negative and even positive at the infarct region and border zone compliant with lack of contraction at these parts. The average values of the circumferential strains obtained by our method were also compared with the ones of tagged MR images and LV mechanical models to reinforce the validity of the proposed model. The stress distribution through our LV model at end-systolic state in both background tissue and myofibers were also investigated for further evaluations. All

stress components within the background tissue including maximum principle, radial, circumferential, and longitudinal strain components were mainly negative in the healthy parts, reflecting the compressional behavior of the tissue at these parts. These strains took less negative values or small positive values especially in case of circumferential stresses at both infarcted region and border zone, reflecting the depression of the contraction at these parts. Consistent with other LV mechanical simulation with MI, fiber stress distribution also showed elevation of the stresses from endocardium to epicardium at both the infarct area and border zone. The highest values of fiber stress occurred at the border zone consistent with values reported by other MI mechanics studies. The maximum value of fiber stresses in our model was ~40 kPa which is in the range of values reported by other validated mechanical model of the infarcted LV, once more reinforcing the validity of our model. Overall, the performance of the model in simulating contraction of infarcted LV, especially at end systolic state consolidated the validity of the cardiac tissue composite concept for fast and easily adaptable modeling of LV mechanics under pathological conditions. Similar to the healthy LV case, the model was implemented using off-the-shelf commercial FE solver without any need for further subroutine coding, making it widely available to the research community for use and further development.

#### 6.1.4 Chapter 5: Human Left Ventricle Biomechanics Using Medical Imaging Data and Composite Material Mechanics Approach

LV tissue stiffening is regarded as a common diastolic dysfunction which gradually results into depression of the LV contractile function, and eventually leading to heart failure. Consequently, quantification of the LV tissue stiffness in the diastolic phase is of great importance to determine cardiac tissue stiffening as a symptom of diastolic dysfunction in diastolic heart patients. To tackle this problem using a simplified inversion-based strategy, the mechanical model presented in Chapters 3 and 4 was applied for diastolic mechanical simulation of the human LV. To this end, human MR image data of a complete cardiac cycle was acquired. To obtain start-diastolic LV FE model, the LV geometry was acquired by segmenting the MR image data pertaining to the start-diastolic frame. The LV model was discretized into a FE mesh composed of hexahedral element. Next, the cardiac mechanics model presented in Chapter 3 was applied to the FE model to simulate dilation

of the LV by moving from start-diastolic instance to the end-diastolic instance. Similar to Chapters 3 and 4, composite material model including two main parts myofibers (rebars) and background tissue was used for the finite elements within the LV model. Myofiber orientations were also incorporated into the LV model by changing the fiber helix angle from endocardium towards epicardium according to data pertaining to human LV fiber direction obtained from DT-MRI technique. Again, similar to Chapters 3 and 4, hyperelastic models were considered for both background tissue and myofibers to account for large deformations and intrinsic nonlinearity of the cardiac tissue during LV passive filling. Since no significant contraction occurs during the diastole phase, no active properties were considered for cardiac myofibers. Our model takes into account all aspects of the cardiac passive mechanics including anisotropy and hyperelasticity which are needed for accurate diastolic mechanics simulation of the LV. The described forward model was utilized to adjust passive mechanical properties of the cardiac tissue and blood pressure such that the best match was achieved between calculated and measured LV geometries. It is noteworthy that the measure LV geometry was obtained from segmenting the end-diastolic MR image frame while the calculated LV geometry was determined using forward LV model's displacements output. The matching procedure was accomplished using an ad-hoc optimization scheme.

While the optimization scheme led to a blood pressure value of 0.8 kPa, it led to only small alteration of the tissue mechanical properties of the myofibers and background tissue from the initialized values adapted from the literature. It is noteworthy that the calculated values of the mechanical properties and blood pressure were within the range of reported LV measurements data pertaining to healthy subjects, consolidating the validity of the proposed cardiac mechanics model in conjunction with the ad-hoc inversion-based strategy. Furthermore, the diameter of the dilated LV model resulting from the LV mechanics model run with the optimal stiffness and blood pressure parameters was ~41 mm, which is again within the range of measurements reported for normal human subjects. Further validation of the model involved the strain and stress distributions of the LV model at the end-diastolic state attained using the optimal stiffness and blood pressure values. The results confirmed that all normal strains' distributions including radial, circumferential, and longitudinal strain distributions were within the range of corresponding data obtained from



measurements pertaining to healthy subjects. The results indicated that the equatorial end-diastolic radial strain is negative through the model, reflecting the well-known myocardial thinning during diastolic expansion. They also showed that both circumferential and longitudinal strains are positive, confirming the passive LV dilation due to the endocardial blood pressure. These results confirm good agreement with corresponding measurements of the LV diastolic function, consolidating the validity of the proposed model. The shear strain components at the end-diastolic state except radial-circumferential strain component were both quantitatively and qualitatively consistent with corresponding measured data and data reported from other LV mechanics models, which again strengthen the validity of the proposed model. The stress distribution throughout the dilated LV model was also assessed. All stress components in the background tissue including maximum principle, radial, circumferential, and longitudinal stresses except very epicardial stresses were positive throughout the model, reflecting the expected tensile effect of the dilating blood pressure on the LV. The maximum value of the maximum principle stress was about 3.5 kPa which is in the range of those obtained from other diastolic LV mechanical models. Overall, the end-diastolic stresses' distributions throughout the LV model are in good accordance with other validated mechanical models of the LV, confirming the reliable performance of the proposed LV mechanics model in the diastole phase.

## 6.2 Future Directions

The forward mechanical model of the LV presented in Chapters 3 and 4 of this thesis can be considered as a core element to be run iteratively within an inverse FE problem framework towards diverse patient-specific diagnosis and therapy planning applications. One interesting application of the inverse FE problem method which uses our forward mechanical model and cardiac imaging data is assessing the severity of myocardial infarction. For this purpose, infarct region and border zone as well as displacement field of the LV model can be acquired from various imaging modalities such as MR imaging and/or US data pertaining to cardiac cycles of the MI patient. The proposed mechanical model of the infarcted LV can be used in conjunction with the geometry obtained from MR imaging data and the methods described in Chapters 3 and 4 of this thesis. Quantitative assessment of the infarction severity, involves setting the maximum isometric tension at the longest

sarcomere length ( $T_{\max}$  in Equation (3.1) of Chapter 3) as a variable in the model to be determined iteratively through an optimization algorithm. As such, initial guess values of this parameter can be initialized in the optimization algorithm for different regions including the normal regions, infarct regions, and border zones. The optimization algorithm changes these values systematically with the aim of achieving the best match between the LV's displacement field obtained from our mechanical simulation and the corresponding one obtained from MR imaging data. Values of this parameter, especially at the infarct region and border zone can be used as indicators of the acuteness of the infarction. Very low values of  $T_{\max}$  (e.g. values close to zero) at the infarcted region, may indicate nonviable cardiomyocytes at this region. In such a case, clinicians may determine that there would be no chance of recovery of the cardiomyocytes in this region using revascularization therapies and vice versa. Accordingly, this computational scheme along with cardiac imaging technique may aid cardiologists to decide appropriate and effective therapeutic strategies for the MI patients.

### 6.3 Closing Remarks

Diverse cardiac mechanics models of normal and pathological heart have been developed during the recent decades. The major goal of all of these developments is to achieve accurate computer-based techniques aimed at diagnosis and treatment of different cardiac conditions. Taking into account the complexities of the heart mechanics, these models were implemented using intricate nonlinear FE algorithms which are not implemented in available commercial FE software packages. The mechanical model of the LV presented in this work is implementable using conventional FE software without need to any custom-developed codes. The presented model was implemented using a novel composite material model of the cardiac tissue and can be considered as a step forward towards wide accessibility of computational tools for patient-specific diagnosis and therapies. The presented model is easily adaptable to diverse cardiac pathological conditions by easy adjustment of the passive and active mechanical properties through different parts of the LV geometry, rendering this model even more attractive for clinical applications. For preliminary assessment of the suitability of this model for FE inversion-based cardiac mechanics characterization towards patient-specific diagnosis and therapy planning, the

model was also utilized within an ad-hoc optimization framework. In this framework, the passive LV tissue stiffness parameters and diastolic blood pressure were successfully determined, confirming the merits of the proposed model for such applications.

Another important contribution of this research is development of an effective technique to estimate cardiac tissue intrinsic properties on its microstructural constituents. As such a novel FE-based cardiac tissue mechanics model was developed in which type, volume percentage, and organization of the tissue constituents can be easily changed according to the physiology of the normal and pathological cardiac tissue to obtain the sought tissue intrinsic properties. It was also observed that volume percentage, type, and organization of the major cardiac tissue constituents affect the overall cardiac tissue intrinsic properties significantly. This cardiac tissue model can be used as a highly effective alternative to using uniaxial and biaxial mechanical testing while it is capable to catalogue a wide range of pathologies without the need of scarce cardiac tissue samples. As such it can be considered as another step forward in the field of cardiac mechanics modeling by providing required inputs for such simulations.

## Appendices

# Curriculum Vitae

Name: Seyyed Mohammad Hassan Haddad

## Education

- 2011 – 2016  
**Western University, London, Canada**  
Ph.D. Graduate Program in Biomedical Engineering
- 2002 – 2005  
**University of Tehran, Tehran, Iran**  
M.Sc. in Electrical Engineering, Minor in Communications - Fields
- 1997 – 2002  
**Amirkabir University of Technology (Tehran Polytechnic), Tehran, Iran**  
B.Sc. in Electrical Engineering, Minor in Communications

## Honors and Awards

- **Western Graduate Research Scholarship (WGRS)**, Biomedical Engineering Graduate Program, Western University, London, Ontario, Canada, 2011- 2015.
- **Research Grants for Ph.D. Studies**, Western University, London, Ontario, Canada, 2011- 2016.
- **Canadian Institute of Health Research (CIHR) Fellowship**, Vascular Training Program in Biomedical Engineering Graduate Program, Western University, London, Ontario, Canada, 2011 – 2013.
- **Conference Travel Award**, Biomedical Engineering Graduate Program, Western University, London, Ontario, Canada, 2015.
- **Research Grants for B.Sc. Studies**, National Farsi Text to Speech (TTS) Research Project, Amirkabir University of Technology (Tehran Polytechnic), 2000.

## Research Experience

- **Graduate Research Assistant (GRA)**, Biomedical Engineering Graduate Program, Western University, London, Ontario, Canada, 2011- 2016.
- **Graduate Research Assistant (GRA)**, New Biomaterials for Post-Mastectomy / Lumpectomy Breast Reconstruction, Western University, London, Ontario, Canada, 2015.
- **Canadian Institute of Health Research (CIHR) Scholar**, Vascular Training Program in Biomedical Engineering Graduate Program, Western University, London, Ontario, Canada, 2011 – 2013.
- **Graduate Research Assistant (GRA)**, Time-domain Electromagnetic Research Group, Center of Excellence on Applied Electromagnetic Systems, School of Electrical and Computer Engineering, University of Tehran, Tehran, Iran, 2004 – 2011.
- **Undergraduate Research Assistant**, National Farsi Text to Speech (TTS) Research Project, Amirkabir University of Technology (Tehran Polytechnic), Tehran, Iran, 2000.

## Teaching Experience

- **Graduate Teaching Assistant (GTA)** for “Human and Animal Biomechanics” course, Biomedical Engineering Graduate Program, Western University, London, Ontario, Canada, Fall 2013, Fall 2014, and Fall 2015.
- **Graduate Teaching Assistant (GTA)** for “Advanced Image Processing and Analysis” graduate course, Department of Electrical and Computer Engineering, Isfahan University of Technology, Isfahan, Iran, Winter 2012.
- **Graduate Teaching Assistant (GTA)** for “Electric Circuits and Electromechanics” course, Biomedical Engineering Graduate Program, Western University, London, Ontario, Canada, Winter 2015.
- **Graduate Teaching Assistant (GTA)** for “Electrical Laboratory II” course, Biomedical Engineering Graduate Program, Western University, London, Ontario, Canada, Winter 2012, Winter 2013, Winter 2014, and Winter 2016.
- **Graduate Teaching Assistant (GTA)** for “Electrical Laboratory I” course, Biomedical Engineering Graduate Program, Western University, London, Ontario, Canada, Fall 2012.

- **Graduate Teaching Assistant (GTA)** for “Electric Circuits I” course, Biomedical Engineering Graduate Program, Western University, London, Ontario, Canada, Fall 2011.
- **University Instructor** for “Engineering Mathematics”, “Signals & Systems”, “Communications I”, and “English Language in Electrical Engineering” courses, Department of Electrical and Computer Engineering (ECE), Shahabdanesh Institute of Higher Education, Qom, Iran, 2008 – 2011.
- **University Instructor** for “General Physics II” course, Faculty of Science, Department of Physics, University of Qom, Qom, Iran, 2006 – 2008.

## Publications

### Peer-Reviewed Journal Papers

- **S. M. H. Haddad** and A. Samani, “A novel micro-to-macro approach for cardiac tissue mechanics,” accepted for publication in the *Journal of the Computer Methods in Biomechanics and Biomedical Engineering*, Jul. 2016.
- **S. M. H. Haddad**, E. Omid, L. E. Flynn, and A. Samani, “Comparative biomechanical study of using decellularized human adipose tissues for post-mastectomy and post-lumpectomy breast reconstruction,” *Journal of Mechanical Behavior of Biomedical Materials*, Vol. 57, pp. 235-245, 2016.
- **S. M. H. Haddad**, M. Ghaffari-Miab, and R. Faraji-Dana, “Transient analysis of thin-wire structures above a multilayer medium using complex-time Green’s functions,” *IET Microwaves, Antennas & Propagation*, Vol. 4, Iss. 11, pp. 1937–1947, 2010.

### Submitted Journal Papers

- **S. M. H. Haddad** and A. Samani, “A novel biomechanical computational model of the left ventricle using a composite material approach,” submitted to the *International Journal of the Engineering Science*, 2016.
- **S. M. H. Haddad** and A. Samani, “A biomechanical model of the pathological left ventricle using a composite material approach,” submitted to the *Journal of Medical Engineering and Physics*, 2016.

### Conference Papers

- **S. M. H. Haddad**, M. Drangova, J. A. White, and A. Samani, “Towards a myocardial contraction force reconstruction technique for heart disease

assessment and therapy planning,” *Proc. SPIE* 9038, Medical Imaging 2014: Biomedical Applications in Molecular, Structural, and Functional Imaging, San Diego, California, USA, 2014.

- **S. M. H. Haddad**, M. Drangova, J. A. White, and A. Samani, “Towards myocardial contraction force image reconstruction for heart disease assessment and intervention planning,” *Proc. SPIE* 9417, Medical Imaging 2015: Biomedical Applications in Molecular, Structural, and Functional Imaging, Orlando, Florida, USA, 2015.
- **S. M. H. Haddad**, M. Drangova, J. A. White, and A. Samani, “A novel micro-to-macro approach for cardiac tissue mechanics,” *7th World Congress Biomechanics (WCB)*, Boston, USA, 2104.
- **S. M. H. Haddad**, M. Drangova, J. A. White, and A. Samani, “A novel mechanical model of the left ventricle for cardiac contraction force reconstruction applications,” *13<sup>th</sup> World Congress of Medical Physics & Biomedical Engineering*, Toronto, Ontario, Canada, 2015.
- **S. M. H. Haddad**, E. Omid, L. E. Flynn, and A. Samani, “Simulation of implantation of decellularized human adipose tissues and hyaluronic acid fillers for post-mastectomy and post-lumpectomy patients,” *13th International Symposium on Computer Methods in Biomechanics and Biomedical Engineering (CMBBE)*, Montreal, Canada, 2015.